ACCSCIENCE PUBLISHING

Advances in Radiotherapy & Nuclear Medicine

ISSN: 3060-8554 (Print)
ISSN: 2972-4392 (Online)
Volume 3 · Issue 1
March 2025

ACCSCIENCE PUBLISHING

Advances in Radiotherapy & Nuclear Medicine

Print ISSN: 3060-8554
Online ISSN: 2972-4392

Advances in Radiotherapy & Nuclear Medicine is a peer-reviewed and open-access journal that aims to publish and disseminate novel research in the breadth of radiation oncology, physics, and biology.

The journal aims to advance our understanding in the radiotherapy and provide a platform to oncologists and physicians to showcase their findings in original fundamental and clinical research as well as to present new ideas that highlight the changes in the radiation oncological clinical practice.

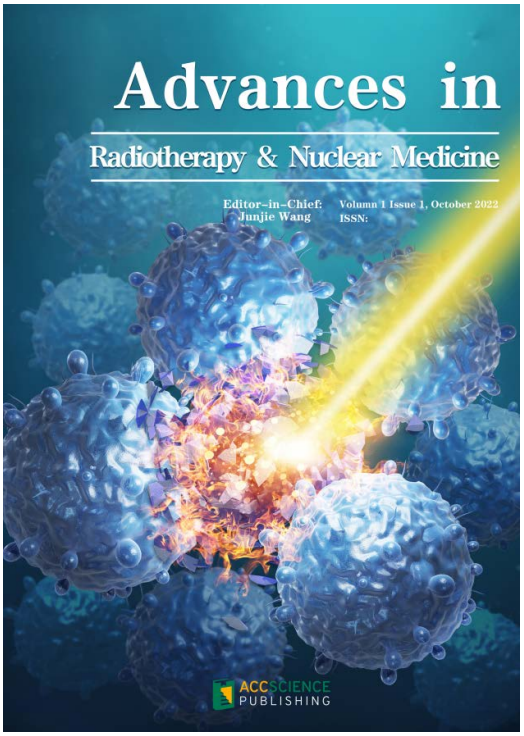

About the Publisher

AccScience Publishing is a publishing company based in Singapore. We publish a range of high-quality, open-access, peer-reviewed journals and books from a broad spectrum of disciplines.

Contact Us

Managing Editor
arnm.office@accscience.sg

AccScience Publishing
8 Burn Road, #15-03 Trivex, Singapore 369977.

Volume 3 • Issue 1 • March 2025
ISSN 3060-8554 (print) ISSN 2972-4392 (online)

Advances in Radiotherapy & Nuclear Medicine

ACCSCIENCE PUBLISHING

Access Science Without Barriers

ADVANCES IN RADIOTHERAPY & NUCLEAR MEDICINE

ISSN: 3060-8554 (print)
ISSN: 2972-4392 (online)

Editorial and Production Credits

Publisher: AccScience Publishing
Managing Editor: Freda Wang
Production Editor: Sharmila Velapasamy
Article Layout and Typeset: Sinjore Technologies (India)

For all advertising queries, contact arnm.office@accscience.sg.

Supplementary file

Supplementary files of articles can be obtained at https://accscience.com/journal/ARNM/3/1.

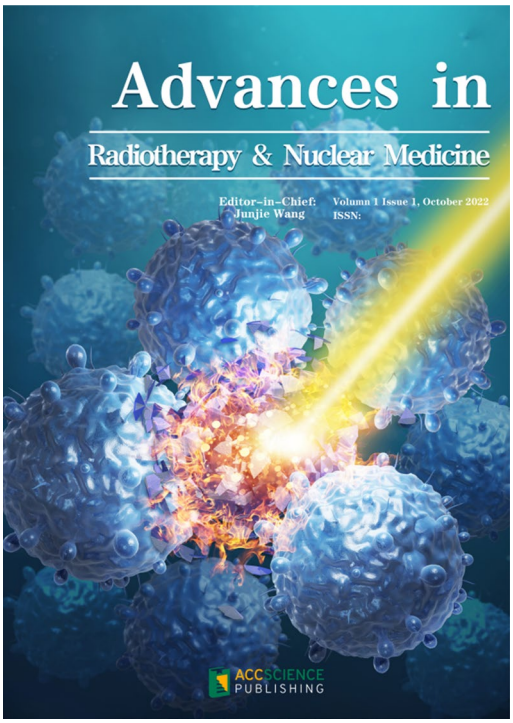

Advances in Radiotherapy & Nuclear Medicine

Editorial Board

Youth Editorial Board Members

*Editorial Board Members as of March 20, 2025

ACCSCIENCE PUBLISHING

Volume 3 | Issue 1 | March 2025 | Page 1 – 108 |

Advances in Radiotherapy & Nuclear Medicine

https://accscience.com/journal/ARNM

CONTENTS

ACCSCIENCE PUBLISHING

Advances in Radiotherapy & Nuclear Medicine

REVIEW ARTICLE

Different diagnostic methods for biliary tract cancer: A review

Zakariya Abdi Yakub[1], David Aebisher[1], Paweł Woźnicki[1], Justyna Magdalena Łabądź[2], Angelika Myśliwiec[2], Klaudia Dynarowicz[2], and Dorota Bartusik-Aebisher[2]*

[1]Department of Photomedicine and Physical Chemistry, Medical College of The Rzeszów University, Rzeszów, Subcarpathian, Poland

[2]Department of Biochemistry and General Chemistry, Medical College of The Rzeszów University, Rzeszów, Subcarpathian, Poland

Abstract

Cholangiocarcinoma (CCA) is a primary malignant tumor originating from the epithelium of the bile duct mucosa. It is the second most common primary tumor of the liver and biliary tract. Based on tumor location, CCA is classified as intrahepatic and extrahepatic. Clinical diagnosis relies on imaging techniques (ultrasonography, computed tomography [CT], magnetic resonance imaging [MRI]), while the final diagnosis is confirmed through histopathological examination of biopsy, brush swab, or post-operative samples. Imaging plays a critical role in diagnosing, staging, and guiding the treatment of biliary cancers. Key imaging methods include magnetic resonance cholangiopancreatography (MRI with MRCP), endoscopic retrograde cholangiopancreatography, endoscopic ultrasound (EUS), and positron emission tomography (PET). Selecting the most suitable diagnostic tool is challenging due to the distinct properties of each method, which are tailored to different diseases and stages of diagnosis or treatment. For example, MRCP provides superior visualization of biliary tract narrowing/dilatation compared to direct cholangiography (ERC) and is more effective in assessing tumor extent. Ultrasound is useful for initial evaluation of bile duct and gallbladder tumors and for identifying bile duct dilatation. CT is effective for detecting focal lesions and staging cancer progression, while MRI is considered the gold standard for tumor visualization. EUS offers a detailed assessment of extrahepatic bile ducts, gallbladder, hepatic hilar structures, local lymph nodes, and vessels. Although ERC allows biopsy or smear collection, it does not assess tumor extent. PET is valuable for detecting distant metastases, monitoring treatment efficacy, and evaluating recurrence. This review focuses on the role of various imaging techniques in the diagnosis, staging, treatment response prediction, and therapy of CCA.

Keywords: Cholangiocarcinoma; Biliary tract cancer; Image-guided therapeutics

***Corresponding author:**
Dorota Bartusik-Aebisher
(dbartusikaebisher@ur.edu.pl)

Citation: Yakub ZA, Aebisher D, Woźnicki P, *et al*. Different diagnostic methods for biliary tract cancer: A review. *Adv Radiother Nucl Med*. 2025;3(1):1-16. doi: 10.36922/arnm.4557

Received: August 16, 2024

Revised: October 28, 2024

Accepted: November 18, 2024

Published online: January 7, 2025

1. Introduction

Cholangiocarcinoma (CCA) is an epithelial-origin neoplasm arising from the mucosa of the bile ducts.[1,2] Histologically, it is predominantly adenocarcinoma.[3] After hepatocellular carcinoma (HCC), CCA is the second most common primary

malignancy of the liver and biliary tract.[4] Despite advances in diagnosis and treatment, the incidence of new cases and mortality from this disease continues to rise steadily.[5,6] Depending on the tumor's location, CCA is classified into intrahepatic cholangiocarcinoma (iCCA) and extrahepatic cholangiocarcinoma (eCCA), which is further divided into perihilar cholangiocarcinoma (pCCA) and distal forms.[7,8] Histologically, conventional perihilar and distal bile duct carcinomas are typically mucin-producing adenocarcinomas or papillary tumors, while intrahepatic bile duct carcinomas exhibit greater heterogeneity and can be subclassified based on the extent or size of the bile duct involved.[9] The incidence of CCA is relatively low in Western countries. However, it is notably higher in regions such as China and Thailand. CCA also exhibits geographic concentration, with clusters found in northern India, Japan, and several South American countries. On the other hand, the incidence of iCCA has been steadily rising, particularly in Western nations. Epidemiological data from developed countries, such as the United Kingdom and the Unites States of America, demonstrate a steady increase in the incidence of iCCA over the past three decades. Global incidence rates of CCA vary significantly across regions. The highest rates are observed in Asia, with northeastern Thailand reporting the greatest age-standardized incidence. In Western countries, the incidence is lower, although Italy has the highest rate in the West. Mortality patterns for iCCA and eCCA show distinct regional trends. Over the past decade, iCCA mortality has notably increased in most European countries, particularly in Western Europe, with the highest rates observed in Ireland, the United Kingdom, Portugal, and Spain.

The Baltic countries, particularly Latvia and Lithuania, have experienced the most dramatic increases in iCCA mortality. Since 2008, nearly all European countries have seen an upward trend in iCCA mortality, except for Austria. In North America, iCCA mortality has also risen in both the United States and Canada, with similar trends in Oceania (Australia and New Zealand) and the Middle East (Israel and Turkey). East Asia continues to report higher iCCA mortality rates, although the sharp increases seen in other regions have not been observed.[10]

Risk factors for the development of CCA include primary sclerosing cholangitis, biliary cysts, liver malformations, choledocholithiasis (especially secondary to chronic cholangitis), smoking, diabetes mellitus, older age, certain hereditary diseases (such as Lynch syndrome and cystic fibrosis), and infestations of the parasitic flukes *Clonorchis sinensis*, *Opisthorchis viverrini*, and *Opisthorchis felineus*.[11-14] However, the majority of patients with biliary tract cancer do not have any known or suspected risk factors and are often diagnosed at an advanced stage of the disease.[15,16] Symptoms of biliary tract cancer include cholestatic jaundice, pruritus, abdominal discomfort and pain, liver enlargement, unexplained weight loss, nausea and vomiting, fever, a palpable tumor in the right hypogastric area, and Courvoisier's sign – a painless, enlarged, palpable through the abdomen gallbladder, typically indicative of tumors located peripherally from the junction of the cystic duct and the common hepatic duct.[17,18] The onset of jaundice and pruritus often signifies significant tumor progression. In most patients at this stage, the tumor is inoperable, and the median survival time is typically <12 months from diagnosis.[19-22] The progression of CCA is further aggravated by its dense stromal environment, which contains numerous cancer-associated fibroblasts that support tumor growth.[11] Surgical resection or liver transplantation remains the only treatment offering long-term, disease-free survival.[23,24] Although the 1-year survival rate for CCA patients has improved over time, the 5-year survival rate has not shown any significant change, remaining below 5%.[25] To reduce cancer-related mortality, it is essential to identify preventable risk factors and implement surveillance strategies in high-risk populations.[21] The diagnosis of CCA typically involves a combination of liver function tests, tumor marker tests, imaging techniques such as ultrasound, computed tomography (CT), magnetic resonance imaging (MRI) combined with magnetic resonance cholangiopancreatography (MRCP), endoscopic retrograde cholangiopancreatography (ERCP), and biopsy for histological confirmation.[26,27] Imaging studies play a crucial role in assessing the extent of the lesion and determining resectability, with multi-detector CT (MDCT) used for overall staging and ERCP for local evaluation.[28] Despite technological advances, diagnosing CCA remains challenging, and up to 20% of biliary strictures may yield indeterminate results despite extensive evaluation.[29,30] Therefore, optimal management requires the integration of clinical information, imaging, cytological and histological studies, and rapid multidisciplinary assessment.[15,31] Histopathological biopsy remains the gold standard for diagnosis, including MRCP, endoscopic ultrasound (EUS), ERCP, and cholangioscopy, which have improved diagnostic accuracy.[16]

This paper aims to examine the role of various imaging methods – ultrasonography (USG), CT, MRI, direct cholangiography (ERC), EUS, and positron emission tomography (PET) – in the diagnosis, staging, treatment response prediction, and therapy of biliary tract cancer. The range of diagnostic tools is extensive, with each method offering distinct advantages and disadvantages (Figure 1). The choice of diagnostic approach is often determined by

the attending physician and the patient's specific condition. These imaging methods have been extensively studied for several decades, yet emerging techniques continue to provide new insights into the changes occurring in the patient's body. Therefore, this review highlights the most commonly used methods and discusses the types of changes that can be observed through each technique.

2. Diagnostic methods for biliary tract cancer

2.1. Ultrasound

USG is a non-invasive, widely accessible diagnostic tool commonly available in most medical facilities. It offers a simple procedure without any harmful side effects, making it a highly favorable option for initial assessment. Over recent years, intestinal USG has gained increasing prominence, particularly in diagnosing inflammatory bowel diseases. Due to its numerous benefits, USG is now considered as valuable as more complex imaging techniques, such as CT. Unlike CT, USG does not expose patients to ionizing radiation, further enhancing its appeal.

During an ultrasound of the large intestine, clinicians can detect not only changes within the intestinal wall but also abnormalities beyond it. Key indicators, such as variable echogenicity and increased Color-Doppler signals, may suggest excessive blood supply to tissue or decreased intestinal peristalsis. These features make USG a useful tool for assessing disease activity, identifying complications, characterizing stenoses, and evaluating treatment effectiveness. In addition, USG aids in evaluating blood vessels in the digestive system and detecting fluid in the peritoneal cavity. It can also reveal changes in the lymph nodes of the abdominal mesentery.

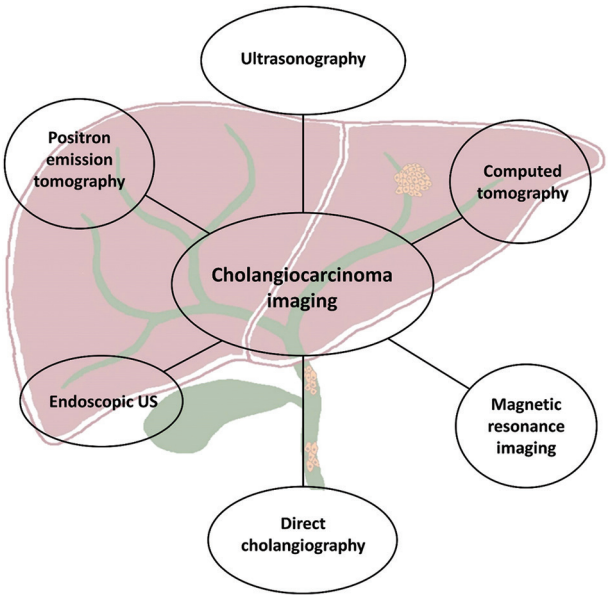

Figure 1. A map of cholangiocarcinoma imaging techniques
Abbreviation: US: Ultrasound.

Ultrasound is one of the safest methods for diagnosing digestive system issues, as its non-invasive nature allows for frequent repetition over short intervals without posing any significant health risks to patients. The primary limitation, however, is the lack of a standardized protocol for measuring and analyzing parameters during an ultrasound examination. Transabdominal ultrasound can confirm biliary dilation and exclude cholelithiasis, as well as detect masses in the liver.[32] This technique is valuable in the early detection of biliary tract cancer.[33] It is particularly useful for the initial evaluation of tumor masses within the bile ducts and gallbladder. On USG, intrahepatic bile duct cancer can often appear as a mass lesion.[34] eCCAs are typically echogenic, but they can still be demonstrated and characterized using ultrasound.[34] Moreover, this examination allows for simple visualization of papillary tumors and nodular ductal carcinomas of the biliary tract.[35,36] The extent of biliary tract involvement can be assessed based on the location of the tumor and the distribution of biliary obstruction.[34] However, the specificity of ultrasound remains unknown. A 5-year population-based study conducted in Thailand showed that USG can detect premalignant lesions and resectable biliary tract cancer at an early stage. For this reason, it is recommended as the first screening tool for biliary tract cancer in patients aged ≥40 years in endemic areas.[37] Technical improvements, such as the use of contrast-enhanced ultrasound (CEUS) and the ability to perform both transabdominal ultrasound and EUS, further expand the potential of this imaging method in evaluating luminal and extraluminal masses in the diagnosis of biliary tract cancer.[38] Rayubkul *et al.*[33] showed that ultrasound screening for gallbladder cancer improves early detection and may reduce the need for expensive or invasive diagnostic procedures. Similarly, Thinkhamrop *et al.*[39] found that ultrasound findings were strongly associated with CCA, particularly in patients diagnosed with biliary dilation and liver masses. In their study, of the 1,880 people who underwent ultrasound and had a pathological diagnosis of CCA, the overall detection rate was 35.74%. The detection rate for those with liver masses was 54.85%, and for those with dilated bile duct, it was 62.01%. Ultrasound is also useful for guiding needle biopsy of intrahepatic lesions.[36] Advances in Doppler imaging and three-dimensional ultrasound have further enhanced the application of ultrasound in evaluating the biliary system. CEUS, which combines traditional ultrasound with a contrast agent, has emerged as a valuable tool.[40,41]

Elastography is another non-invasive technique that assesses tissue stiffness by measuring changes in organ and focal tissue characteristics. Transient elastography and real-time elastography are commonly used to image changes in the bile ducts.

The principle of elastography involves assessing the distribution of tissue elasticity, which is then converted into an image of the elastic modulus, known as an elastogram. This technique measures tissue deformation caused by static or dynamic stress, allowing for the estimation of tissue stiffness and the differentiation between benign and malignant changes.

Elastography is also valuable for visualizing, localizing, and diagnosing various nodules, as well as pancreatic and liver masses.[42] While traditional USG is often utilized to detect liver lesions, it is typically considered less precise than CT, MRI, or histology. The combination of these modalities is considered the gold standard for patient evaluation. However, the introduction of CEUS has significantly improved the detection and characterization of liver lesions by providing superior visualization of the microvasculature, thereby enhancing its diagnostic accuracy.[43]

Ultrasound, and more recently CEUS, is often the first method employed to assess biliary lesions. CEUS enables the visualization of microcirculation in liver metastases, allowing for the monitoring of changes in tumor perfusion following local ablation or new antiangiogenic therapies.

2.2. CT

Over the past few years, CT imaging has evolved from single-detector scanners to MDCT technology, enabling the acquisition of high-resolution images in seconds.[44] Multidetector row CT is now the imaging modality of choice for evaluating and staging CCA,[45] due to its high spatial and temporal resolution and widespread availability.[45,46] CT allows for the detection of tumor masses, the definition of local enlargement of cavitary tumors, the assessment of blood vessel invasion and adjacent organ involvement, and the identification of metastatic disease, including lymph node and abdominal metastases.[38,45-47] This method is more accurate than ultrasound for detecting biliary tract cancer,[38] which is why CT is used in up to 90% of patients with suspected biliary tract cancer.[38] Multiphase CT protocols, including late arterial phase and portal vein phase scanning, are now recommended for the primary staging of biliary tract cancer.[40,48] Moreover, this diagnostic test can differentiate between types of CCA. Nam *et al.*[49] showed that pre-operative MDCT features of intrahepatic mass-forming CCAs can help distinguish between small-duct and large-duct types. Contrast administration greatly improves tumor visibility, with tumors often being barely visible without it.[38] The appearance of biliary tract cancer on CT scans depends on the tumor's location within the biliary system,[48] with intrahepatic bile duct carcinomas being particularly heterogeneous on CT scans.[50]

The accuracy of MDCT in imaging bile duct involvement is 86%, although it tends to significantly underestimate the extent of longitudinal involvement.[45] CT and contrast-enhanced CT can perform precise multidirectional assessments of bile duct and vascular involvement, which helps accurately predict tumor resectability and facilitates successful tumor resection.[32,51-53] Studies have shown that in the primary stage of intrahepatic biliary tract cancer, CT is more sensitive than MRI in detecting extrahepatic invasion and vascular involvement.[54] Specifically, CT exhibited 84% sensitivity and 93% specificity in detecting hepatic artery involvement, while the accuracy of detecting portal vein involvement was 87%.[45] Infiltration of adjacent structures, particularly the hepatoduodenal ligament, duodenum, transverse colon, liver, and lymph nodes, often indicates the inoperability of the cancer.[48] CT arteriography and CT venography are reconstructed using various techniques to visualize the vascular anatomy, assist in surgical planning, and reduce the risk of complications.[45] Park *et al.*[55] demonstrated that CT imaging of vascularization can serve as a non-invasive, accessible, and valuable prognostic indicator for the treatment of iCCA. A study involving 345 patients developed a pre-operative model for predicting post-operative outcomes in massive intrahepatic biliary tract cancer and showed that CT, along with clinical and radiomic features, can be useful for this purpose.[56] Furthermore, a deep learning model based on CT imaging, developed by Wakiya *et al.*,[57] exhibited high predictive performance in forecasting early post-operative recurrence of iCCA. Moreover, volumetric scanning techniques can assess the liver volume and residual function before surgery, helping to prevent post-operative small-size syndrome.[58] A new CT technique, functional CT volume perfusion imaging, may be valuable in assessing treatment responses to targeted therapies or antiangiogenic drugs by demonstrating changes in tumor vascularization.[59] The sensitivity of CT in detecting lymph node metastases is 61%, with a specificity of 88%.[45] For evaluating distant metastases, CT shows a sensitivity of 67% and a specificity of 94%. However, the accuracy of CT in assessing the progression of extrahepatic biliary tract cancer remains unestablished. A key challenge in this regard is determining the extent of tumor spread beyond the bile duct wall and its potential involvement with adjacent anatomical structures.[48] Liver Imaging Reporting and Data System (LI-RADS®) was created to standardize the reporting and data collection of CT and

MR imaging for HCC. LI-RADS emerges as an essential tool in the management of liver tumors. CT remains one of the primary tools in cancer diagnostics, particularly useful for imaging bone structures. This examination enables the detection of tumors and metastases, precise planning of radiotherapy (allowing for focused radiation delivery), and monitoring of treatment response, including the reduction or growth of tumors.[60]

2.3. MRI

MRI is the non-invasive method of choice for detection, pre-operative staging, and follow-up on biliary tract cancer.[61-64] When combined with MRCP, MRI is optimal for evaluating bile ducts both above and below their strictures. It also allows the identification of intrahepatic mass lesions. The primary role of MRI in biliary tract cancer is to confirm or establish the diagnosis, assess the possibility of resection, and aid in differential diagnosis.[64-66] MRCP is considered one of the most advanced imaging technologies and offers several advantages over CT.[63] Due to their high tissue contrast and multifaceted capabilities, MRI and MRCP are effective in detecting and preoperatively evaluating patients with biliary tract cancer, allowing detailed examination of all involved structures, such as the bile ducts, vessels, and liver parenchyma.[64] MRCP has demonstrated the highest sensitivity and specificity (92% and 76%, respectively) in identifying the extension of pCCA.[64] The role of MRI in diagnosing CCA has been well-established through numerous studies. For example, Xu *et al.*[67] showed that MRI could differentiate CCA from metastatic colorectal cancer. Moreover, as demonstrated in a study by Zhang *et al.,*[68] MRI texture signatures can serve as a potential predictive biomarker for immunophenotyping and overall survival in patients with iCCA.[68] The utility of MRI in predicting therapeutic response was also tested by Sheng *et al.*,[69] who found that contrast-enhanced MRI performed before treatment could predict therapeutic response in advanced iCCA to systemic therapy. They also determined that the best predictive value was achieved by a combined model incorporating key MRI features. Similar findings were reported by Koh *et al.*,[70] who showed that hepatobiliary phase MRI images could serve as a prognostic factor after surgery for massive intrahepatic bile duct carcinomas, likely due to the fibrous component of the tumor stroma. MRI can also predict survival and prognosis in patients with eCCA. In a study involving 78 patients with histopathologically confirmed cancer, Wang *et al.*[71] demonstrated that MRI could be used to predict survival and prognosis in these patients. In addition, Xin *et al.*[72] showed that high-resolution MRI images have excellent capability in assessing the extent of pCCA and its vascular invasion. The pattern of arterial MRI enhancement may also serve as a prognostic marker in the pre-operative evaluation of patients with resectable intrahepatic mass-forming bile duct cancer, as demonstrated by Min *et al.*[73]

On dynamic MR images, biliary tract cancer shows moderate peripheral enhancement, followed by progressive and concentric filling of the tumor with contrast material. Contrast accumulation within the tumor on delayed MRI phases suggests peripheral bile duct cancer.[64] Massive intraductal lesions may appear hypointense or isointense on T1-weighted (T1W) images relative to the liver parenchyma. On T2-weighted (T2W) images, tumors may show variable hyperintensity, as the signal intensity depends on the severity of necrosis, hemorrhage, fibrosis, and mucinous material within the tumor.[61] Central hypointensity may correspond to fibrosis.[64] The degree of tumor hyperintensity also depends on the tumor subtype: adenocarcinoma is characterized by higher signal intensity, especially when well-differentiated, while squamous cell carcinomas are characterized by lower signal intensity. In some cases, the tumor may appear as an isointense mass on both T1W and T2W images.[74] pCCAs exhibit similar signal intensity patterns to peripheral tumors on both T1W and T2W images. On MRCP images, pCCA appears as moderately irregular thickening of the bile duct wall (≥5 mm) with symmetric widening of the intrahepatic bile ducts.[64] The typical appearance of massive iCCA consists of irregular annular enhancement in the arterial phase, followed by progressive central enhancement in the portal vein and delayed phase. An atypical presentation, such as hypervascular massive iCCA, can also occur and may be attributed to different pathological features.[75]

The quality of MRCP imaging is largely independent of the operator, but careful technique is required to obtain accurate results. MRCP imaging can be compromised by previous biliary drainage, as this procedure may lead to the collapse of the biliary tree. The combination of MRCP and MR angiography can provide valuable information on the involvement of vascular structures at the hilum. Compared to ERCP, MRCP is a more sophisticated and commonly used technique for identifying tumor location and assessing the resectability of a pCCA.[63] However, the use of MRI in standard diagnostic protocols has some limitations. These limitations include the high cost of the examination, failure to detect microcalcifications, and the possibility of false-positive results, often due to difficulty distinguishing malignant from benign tumors. Other problems include patient-related issues, such as claustrophobia (which can be problematic for both children and adults), various contraindications, such as metal implants or permanent makeup, and potential allergic reactions to contrast agents.

2.4. Invasive techniques

Endoscopic diagnosis is essential for most patients with CCA.[76,77] The diagnostic performance of these methods depends on the tumor's location, as well as the knowledge and experience of the endoscopist. ERCP and EUS remain the most commonly used endoscopic diagnostic tools.[76] However, endoscopy should be preceded by an evaluation of disease severity using cross-sectional imaging, as cholangitis requiring immediate drainage occurs in only 10% of patients at the time of their initial presentation.[78] Other technologies, such as fluorescence in situ hybridization, single-slice cholangioscopy, confocal laser endomicroscopy, and intraductal ultrasound, are also increasingly being utilized.[76]

Direct ERC is critical in the evaluation and treatment of CCA and often serves as an essential diagnostic tool.[79,80] This procedure determines the anatomy of the biliary tract, enables biopsy collection from the lesion or lancet smear for cytological evaluation, and functions therapeutically in biliary stricture dilation and stenting.[79,80] However, ERC cannot determine the full extent of the tumor.[80] Detection of a dominant stricture, with or without accompanying proximal bile duct dilation or the presence of a polypoid lesion, indicates the presence of pCCA. These findings should prompt further cytologic evaluation using bile duct brushing.[79] Tissue collection through brush cytology and tick biopsy allows for cytological and/or histological confirmation of the disease.[77] Conventional cytology obtained through ERCP is suboptimal due to limited sensitivity, though it remains the gold standard with high specificity.[81] ERC is particularly useful for determining tumor staging, assessing the extent of infiltration into extrahepatic and perihepatic lesions, and planning various medical interventions.[80,81] Despite the diagnostic advantages of ERC imaging, a study by Kalaitzakis *et al.*[82] showed that many patients with immunoglobulin G4-associated cholangitis can be misdiagnosed with biliary tract cancer. During ERC, biliary obstruction can be relieved by placing a stent or drainage catheter, which offers palliation for patients with an inoperable condition.[80]

EUS is an alternative to ERC for diagnosing biliary tract cancer.[83] This technique allows for accurate evaluation of extrahepatic bile ducts, the gallbladder, hepatic hilar structures, regional lymph nodes, and adjacent vessels.[84] EUS plays a critical role in the diagnosis and staging of biliary tract cancer, especially in assessing inoperable periampullary bile duct cancer for potential liver transplantation.[85] However, there is still a lack of data regarding the precise role of EUS in diagnosing biliary tract cancer in patients with unspecified extrahepatic biliary strictures.[86] EUS has a tumor detection rate of 94% in patients with CCA, although it has a significantly higher detection rate for distal tumors (100%) compared to proximal tumors (83%).[79] Tissue sampling from extrahepatic localized primary tumors using EUS is typically reserved for inoperable or metastatic CCAs, particularly for distal stenosis or mass CCAs.[87] EUS-guided biopsy of tumors or lymph nodes is a highly sensitive diagnostic method. In a study of 263 patients, the accuracy of EUS-guided fine-needle aspiration (EUS-FNA) compared with ERC-based tissue sampling was 76.1% versus 60.5%, with diagnostic sensitivities of 73.6% for EUS-FNA and 56.5% for ERC.[84] Onda *et al.*[88] suggest that EUS-FNA could be used as a first-line diagnostic method, although its exact usefulness remains to be fully verified. EUS can assess the status of regional lymph nodes and the local extent of eCCA. Although ERC, with or without brushing and biopsy, remains the primary choice for diagnosing CCA, EUS-FNA plays an important role in clinical practice. EUS-FNA can be performed not only to collect tissue samples from tumors but also from enlarged lymph nodes.[89] The method provides slightly better results than ERCP in diagnosing biliary tract cancer.[90] The information from EUS can be used to guide patient care and improve outcomes, though it can also be used in ways that compromise patient well-being.[85] A study by De Jong *et al.*[91] demonstrated that EUS with tissue harvesting can be useful in patients with potentially resectable pCCA based on pre-operative cross-sectional imaging, regardless of lymph node enlargement. A modification of ultrasound technology allows for the placement of an intraductal high-frequency ultrasound (IDUS) probe. Although certain features, such as irregular wall thickening, may strongly suggest malignant neoplasm, IDUS currently lacks the capability to acquire tissue samples.[92]

2.5. PET/CT

PET is a non-invasive imaging method that provides functional images by detecting the uptake of the radiolabeled 18F-fluorodeoxyglucose (FDG) in cancer cells. Over the past decade, integrated PET and CT (PET/CT) imaging systems have enabled the acquisition of both anatomical and functional images.[64] FDG-PET in oncology is performed with the patient fasting and at rest, which enhances the uptake of the tracer in tumor cells while minimizing its uptake by skeletal muscle.[93] PET and PET/CT are now considered the standard methods for staging various malignancies and have also proven valuable in the diagnosis and staging of biliary tract cancer.[63] A meta-analysis of the diagnostic accuracy of FDG-PET in detecting primary biliary tract cancer demonstrated that the combined sensitivity and specificity of FDG-PET were 95% and 83% for intrahepatic cancer, 84% and 95%

for perihilar cancer, and 76% and 74% for extrahepatic cancer, respectively.[94] In a recent study, PET exhibited 90% sensitivity and 78% specificity for diagnosing pCCA.[63] Another study on the clinical role of 18-FDG PET-CT in patients with suspected and potentially operable biliary tract cancer found a sensitivity of 84.0% and a specificity of 79.3% for this imaging modality. In this study, PET-CT showed no significant difference in detecting different morphological tumor types: Periampullary infiltrating, intraductal growing, or mass-forming.[95,96] Furthermore, data from a scientific study indicated that PET can reliably detect nodular bile duct cancer >1 cm in size.[95] However, PET-CT has shown limited reliability in evaluating regional lymph node metastases, with a sensitivity of 12% and specificity of 96%.[95] PET is a useful imaging test for diagnosing distant metastases, monitoring treatment responses, and detecting recurrence.[93,96-98] It can identify metastatic lymph nodes, distant metastases, or clarify indeterminate lesions, especially in patients with primary sclerosing cholangitis.[96] However, due to its low sensitivity (<70%), PET should only be considered in selected cases. In fact, distant metastases are more accurately identified by CT, while EUS remains the gold standard for lymph node evaluation.[96] Fiz *et al.* demonstrated that PET-based radiomics for iCCA can predict pathological data and enable reliable pre-operative prognostic assessment. The combined clinical and radiomic models outperformed purely clinical pre-operative models and provided results comparable to post-operative models.[99] To enhance the diagnostic performance of PET/CT imaging in iCCA, it can be combined with MRI, as demonstrated by Jiang *et al.*[100] Another emerging technology in CCA imaging is simultaneous PET and MRI (PET/MRI). Theoretically, PET/MRI may be advantageous in this context by combining the functional information from FDG-PET with the high contrast resolution of MRI to assess ductal involvement, although no significant studies have yet evaluated PET/MRI for this purpose. This technique may be particularly useful in differentiating CCA from HCC.[101] PET, particularly in combination with PET/CT or PET/MRI, is increasingly being used to assess the molecular characteristics of malignant tumors in the hepato-pancreato-biliary system (Table 1). In cases of suspected or confirmed HCC or biliary tract tumors, PET is performed using 11C-labeled acetate. This imaging method is crucial for evaluating tumor progression and staging before making therapeutic decision-making. Testing with 11C-labeled acetate is also recommended to rule out potential metastases in distant organs, as PET demonstrates higher sensitivity, accuracy, and specificity in detecting metastases.

The strong interaction between radioisotopes and tumor cells, such as increased glucose consumption and DNA synthesis, underscores PET's important role. P*Et al*lows for

Table 1. Selected studies evaluating the use of magnetic resonance imaging in diagnosing cholangiocarcinoma

Authors	Title	Year of publication	Conclusions
Wang *et al.*[71]	The value of an MRI-based radiomics model in predicting the survival and prognosis of patients with eCCA	2024	MRI radiomics model can be used to predict survival and prognosis in patients with eCCA
Xu *et al.*[67]	MRI-based radiomics nomogram for preoperatively differentiating intrahepatic mass-forming cholangiocarcinoma from resectable colorectal liver metastases	2023	MRI can differentiate cholangiocarcinoma from metastatic colorectal cancer
Sheng *et al.*[69]	Contrast-enhanced MRI could predict the response of systemic therapy in advanced iCCA	2022	Pre-treatment contrast-enhanced MRI can be used to predict therapeutic response to systemic therapy for advanced iCCA
Zhang *et al.*[68]	iCCA: MRI texture signature as predictive biomarkers of immunophenotyping and survival	2021	MRI texture signature may serve as a potential predictive biomarker for immunophenotyping and overall survival in patients with iCCA
Xin *et al.*[72]	Hilar cholangiocarcinoma: Value of high-resolution enhanced MRI for pre-operative evaluation	2020	High-resolution MRI (HR-MRI) can predict the ability of cholangiocarcinoma to invade the vasculature
Min *et al.*[73]	Intrahepatic mass-forming cholangiocarcinoma: Arterial enhancement patterns at MRI and prognosis	2019	MRI arterial enhancement pattern may serve as a prognostic marker in the pre-operative evaluation of patients with resectable intrahepatic bile duct cancer presenting as masses
Koh *et al.*[70]	Intrahepatic mass-forming cholangiocarcinoma: prognostic value of pre-operative gadoxetic acid-enhanced MRI	2016	Hepatobiliary phase MRI images may be a prognostic factor after surgery for intrahepatic massive bile duct carcinomas

Abbreviations: MRI: Magnetic resonance imaging; eCCA: Extrahepatic cholangiocarcinoma; CCA: Cholangiocarcinoma; iCCA: Intrahepatic cholangiocarcinoma.

the assessment of the tumor's metabolic activity, detection of metastases throughout the body, including those too small to be detected by CT or MRI, and combining this functional information with anatomical imaging for a more comprehensive view.

Modern diagnostic imaging integrates multiple advanced techniques to provide a comprehensive understanding of pathological changes. Combined imaging systems, such as PET/CT and PET/MRI, allow for simultaneous anatomical (CT, MRI) and metabolic (PET) assessment of tumors. This approach is particularly valuable for accurately localizing lesions, evaluating their aggressiveness, and determining tumor spread. For instance, PET/CT not only reveals the size of a brain tumor but also identifies the most metabolically active areas, directly influencing therapy planning – surpassing the capabilities of CT imaging alone.[102] It is worth noting that before PET/CT examination, the histological features of tissues and inflammatory conditions should be assessed, taking into account specific clinical features and complications related to the treatment.[103]

In addition, other complementary methods should be considered, such as initial diagnostic approaches, like laboratory tests and morphological imaging techniques that assess the metabolic changes in tissues.[104]

PET is also one of the diagnostic methods that enable the assessment of disease stage (including lymph nodes and distant metastases) and the identification of relapse in patients with biliary tract cancer. It primarily aids in treatment planning, particularly in cases of distant metastases, which are frequently assessed. The role of PET in diagnosing the primary tumor, however, remains a subject of debate. Although its diagnostic range is broad, ongoing studies are still analyzing the effectiveness of PET compared to other methods.[105]

PET, utilizing various tracers, is an advanced functional imaging technique that is increasingly recognized for its value and cost-effectiveness in the pre-operative staging of numerous cancers. By capitalizing on the metabolic characteristics of tumors, PET can detect occult metastatic disease that might be missed or appear ambiguous on standard cross-sectional imaging. This capability can significantly alter disease staging and influence treatment decisions.[106] Traditional radiological examinations, such as abdominal X-ray, oral cholecystography, and intravenous or infusion ERC, are now rarely used due to advances in technology and the development of innovative diagnostic methods. An overview X-ray of the abdominal cavity is typically performed where there is suspicion of air in the bile ducts, for example, following surgeries that involve anastomosis between the bile ducts and the digestive tract, or to confirm a diagnosis of a porcelain gallbladder. Meanwhile, cholecystography is a radiological examination of the gallbladder. Cholecystography, once considered the standard test for suspected cholelithiasis, is now rarely used due to its low diagnostic value. At present, for gallbladder diseases, USG of the bile ducts (hepatobiliary USG) is the preferred imaging method. If cholecystography is still deemed necessary, the procedure involves administering a contrast agent to the patient – either orally (typically in the form of dragees, known as oral cholecystography) or intravenously (intravenous cholecystography). The contrast agent enters the bloodstream and is secreted through the liver into the bile. Subsequently, a series of X-rays are taken of the gallbladder, cystic duct, and common bile ducts (biliary ducts), although the latter is usually not well-visualized. The bile, along with the contrast agent, outlines the gallbladder, allowing the assessment of its location, shape, and size, and helping to detect possible obstructions, such as stones. In cases of cholecystitis, the characteristic feature is the absence of visualization of the gallbladder. As for ERC, the term refers to various methods used to examine the bile ducts and pancreas, including retrograde, percutaneous, intraoperative, and post-operative techniques. ERC is often performed in conjunction with cholecystography, a radiographic examination of the gallbladder. Table 2 summarizes the imaging methods used in biliary tract cancer.

2.6. Advanced imaging techniques

Digital cholangioscopy is a valuable technique that enables direct endoscopic visualization of the biliary tree, facilitating optical diagnosis, targeted biopsy, and therapeutic interventions. Its applications encompass both diagnostic and therapeutic roles.

Diagnostic indications include: (i) evaluating indeterminate biliary strictures; (ii) clarifying unclear filling defects; (iii) staging CCA; (iv) assessing ampullary tumors for extension into the common bile duct; (v) investigating unexplained bile duct dilation; (vi) exploring cystic lesions of the biliary tree; (vii) diagnosing unexplained hemobilia; and (viii) managing post-transplant biliary complications.

Therapeutic indications include: (i) lithotripsy for difficult stones; (ii) retrieving migrated stents; (iii) removing foreign bodies; (iv) assisting in guidewire placement; (v) transpapillary gallbladder drainage; and (vi) endoscopic tumor ablation therapy.

One of the most well-established and widely studied applications of digital cholangioscopy is the diagnosis of indeterminate biliary strictures and the performance of intraductal lithotripsy for challenging bile duct stones. The adverse events associated with digital cholangioscopy are similar to those of ERCP, with no significant increase in

Table 2. Characteristics of common diagnostic methods for biliary tract cancer

Ultrasonography	CT	MRI	Positron emission tomography	Endoscopic US	Direct cholangiography
Enables confirmation of biliary tract dilatation and exclusion of gallstones and liver masses	Used to assess and determine the stage of advancement of bile duct cancer	MRI combined with magnetic resonance cholangiopancreatography is optimal for assessing the bile ducts both above and below their strictures	Now considered the standard method for staging various malignancies and has also proven useful in the diagnosis and staging of biliary tract cancer	Enables accurate assessment of the extrahepatic bile ducts, gallbladder, liver hilum structures, regional lymph nodes, and vessels	Essential in the evaluation and treatment of CCA, often serving as a crucial tool for diagnosis
Useful for the initial assessment of tumor masses in the bile ducts and gallbladder	Characterized by high spatial and temporal resolution	Useful for confirming or establishing the diagnosis, as well as assessing the possibility of resection and differential diagnosis	Its sensitivity and specificity ranges are the broadest among all diagnostic methods	Tumor detection rate of 94% in CCA patients	Determines the anatomy of the bile ducts and allows for biopsy or smear test from the site of damage
Facilitates easy visualization of papillary tumors and nodular ductal carcinomas of the biliary tract	More accurate than an ultrasound	Its usage alone is insufficient to determine the correct surgical strategy	Sensitivity drops to 12% and specificity to 96% when assessing metastases to regional lymph nodes	Can assess the status of regional lymph nodes and the local extent of extrahepatic cholangiocarcinoma	Functions as a therapeutic tool for dilating and placing stents in biliary tract strictures
Accuracy ranges from 87% to 96%	Performed in 90% of patients with suspected bile duct cancer	Has the best sensitivity (92%) and specificity (76%) compared to CT	PET-based radiomics of iCCA can predict pathological findings and enable reliable pre-operative prognostic assessment	The information obtained can be used to guide patient care and improve outcomes	Particularly useful in determining the stage of cancer progression and the extent of extrahepatic and perihepatic lesion invasion
Can be used to guide needle biopsy of intrahepatic lesions	Characterized by relatively low sensitivity (61%) and specificity (88%) in detecting lymph node metastases	Allows examination of all relevant structures, including the bile ducts, vessels, and liver parenchyma			

Abbreviations: CCA: Cholangiocarcinoma; CT: Computed tomography; EUS: Endoscopic ultrasound; MRI: Magnetic resonance imaging; PET: Positron emission tomography; US: Ultrasound; iCCA: Intrahepatic cholangiocarcinoma.

complication rates. Digital cholangioscopy is regarded as a safe and effective complement to standard ERCP, with advancements in digital technology addressing many of the limitations observed in earlier generations of cholangioscopes.[107]

Digital cholangioscopy provides high-quality, direct visualization of biliary lesions and enables precise, targeted biopsies. Key cholangioscopic features suggestive of malignancy include dilated, tortuous tumor vessels, infiltrative strictures with irregular margins and partial lumen occlusion, an uneven surface, and areas prone to easy bleeding.

An emerging application of digital cholangioscopy is the mapping of biliopancreatic neoplasia. This technology allows for the precise visual delineation of neoplastic margins within the biliary and pancreatic ducts, thereby improving the accuracy of malignancy staging. As a result, enhanced visualization can significantly impact and alter surgical planning. Digital cholangioscopy provides a safe and effective method for pre-operative assessment of the extent of biliopancreatic neoplasia, including surgical decisions in a considerable number of cases.[108]

Gene panel testing, in combination with advanced genomic mutation analysis using next-generation sequencing (NGS) or similar technologies, enables the simultaneous detection of multiple genomic alterations. These methods are essential for identifying cancer-related mutations in individual patients and facilitating the development of personalized treatment plans. Typically, a gene panel test focuses on a selection of genes that are critical for predicting responses to medication and prognosis, thereby aiding in more accurate medical diagnoses.

These panels can assess a wide range of genomic alterations, including mutations, deletions, insertions, gene fusions, and duplications, by analyzing multiple transcripts

simultaneously. As diagnostic and therapeutic strategies continue to advance, the depth and scope of information provided by gene panel testing expand, leading to a more precise and effective integration of genetic data into patient care.[109]

Typically, the amount of DNA required for a gene panel test ranges from 10 to 500 ng, with the proportion of tumor cells in the sample playing a crucial role in maintaining the accuracy and quality of the test results. Ensuring an adequate percentage of tumor cells is essential for reliable genomic analysis and mutation detection.[110]

In clinical practice, tumor panel assays detect drug-targetable mutations in approximately 10 – 15% of pancreatic cancers and 40 – 50% of CCAs. As a result, the use of multigene tumor NGS is strongly recommended for identifying actionable mutations in CCA, enabling more personalized and targeted treatment approaches.

Radiomics is currently considered a distinct branch of science focused on developing methods for analyzing diagnostic images (from MRI, CT, or nuclear medicine) to better characterize pathological changes. These methods rely on complex computer algorithms.[111]

Radiomics can be used to detect tissue characteristics, particularly in evaluating variations such as shape or heterogeneity during treatment or surveillance. In oncology, the assessment of tissue heterogeneity is of particular interest, as genomic analyses have shown that the degree of tumor heterogeneity is a prognostic determinant of survival and a challenge to cancer control.

Recent studies have demonstrated the potential benefits of radiomics in non-invasive prediction of pathological type and long-term survival in patients undergoing resectable treatment.[112]

The combination of radiomics with artificial intelligence (AI) is another example of how new technologies are being applied in diagnostics. AI refers to systems that can accurately derive results and conclusions from large datasets using advanced computational algorithms. It encompasses various learning algorithms, including machine learning and, more recently, deep learning.[113]

Radiomics can be applied to a range of imaging techniques, including CT, MRI, PET, X-ray, and ultrasound. There are numerous acquisition techniques in use today, and the choice of method can significantly impact radiomics analyses. Differences in acquisition and image processing can lead to inconsistent results in radiomics analyses of independent datasets, which represents one of the primary challenges in the field. The main goal of radiomics is to identify the most stable and accurate radiomics models that can be applied to images obtained using different protocols. Radiomics is widely used in the diagnostic, prognostic, and predictive evaluation of CCA, offering valuable insights into clinical indicators that can be measured or predicted.[114,115]

3. Summary

As mentioned earlier, bile duct cancer rarely produces early symptoms, which is why it is frequently diagnosed at an advanced stage.[17] The disease is commonly identified late, primarily due to non-specific symptoms.[116]

Early diagnosis and timely treatment of CCA are essential for improving treatment outcomes in patients. Early diagnostic methods and recognition of symptoms preceding these aggressive tumors are invaluable. It is worth mentioning that non-specific symptoms (e.g., general weakness, lack of appetite, nausea, or abdominal pain) can prolong the diagnostic process for an extended period.[89]

Symptoms attributed to bile duct cancer may also be indicative of other conditions. For example, upper abdominal pain can be caused by various factors and does not necessarily point to bile duct cancer. Consequently, an increasing number of patients seek medical attention only when the disease is already in an advanced stage. Due to these factors, early diagnosis of bile duct cancer is rare, and the prognosis often depends on the speed of diagnosis and the initiation of treatment. Therefore, it is important that individuals in high-risk groups undergo regular check-ups.[117]

Improving early diagnosis remains a key area for development. One of the major challenges is the late detection of bile duct cancer. The future direction for progress lies in the development of more effective early diagnostic methods. Innovative improvements in imaging techniques, including diagnostics based on tumor markers, are also being explored.[118]

Doctors report that in 8 out of 10 cases, bile duct cancer is diagnosed too late and is often found at an advanced, inoperable stage.

In the case of HCC, the US is highly specific but lacks sufficient sensitivity to detect HCC in many patients with liver cirrhosis, which limits its effectiveness in surveillance programs. The diagnostic performance of CT is comparable, while MRI offers greater sensitivity. However, the accuracy of ultrasound, spiral CT, and MRI in diagnosing HCC in patients with chronic liver disease has not been systematically evaluated. It is estimated that MRI has a sensitivity of 81% and specificity of 85%, which is higher than that of ultrasound but lower than that of CT. These findings highlight the individualized nature

of diagnostic decision-making. Given the absence of standardized treatment regimens, a combined diagnostic approach is often necessary. Therefore, further research and development of a comprehensive review of diagnostic methods for specific biliary tract diseases should be pursued in the future.[119]

4. Conclusion

Imaging plays a crucial role in the management of CCA. It serves several purposes: First, enabling a confident diagnosis; second, characterizing and staging the tumor, which is essential for planning optimal therapy; and third, predicting treatment response and overall patient survival. Despite the availability of numerous imaging methods, the diagnosis of CCA remains challenging. To date, no single imaging modality has been established as the most optimal for this tumor. Advancements in modern imaging technologies, particularly USG, CT, and MRI, aim to improve the accuracy of distinguishing CCA from other biliary diseases. However, further research is needed to assess the accuracy of various imaging techniques, especially emerging intraductal methods. An interesting avenue for development would be to leverage the strengths of the imaging methods described above and create a diagnostic algorithm that maximizes imaging accuracy. Moreover, the integration of these methods could not only enhance the precision of CCA detection but also aid in making more effective therapeutic decisions, ultimately improving patient prognosis.

Acknowledgments

None.

Funding

None.

Conflict of interest

The authors declare no conflicts of interest.

Author contributions

Conceptualization: Zakariya Abdi Yakub, Justyna Magdalena Łabądź, David Aebisher, Paweł Woźnicki, Klaudia Dynarowicz, Angelika Myśliwiec, Dorota Bartusik-Aebisher

Writing – original draft: Justyna Magdalena Łabądź, David Aebisher, Paweł Woźnicki, Klaudia Dynarowicz, Dorota Bartusik-Aebisher

Writing – review & editing: Zakariya Abdi Yakub, Justyna Magdalena Łabądź, David Aebisher, Paweł Woźnicki, Klaudia Dynarowicz, Angelika Myśliwiec, Dorota Bartusik-Aebisher

Ethics approval and consent to participate

Not applicable.

Consent for publication

Not applicable.

Availability of data

Data are available within the article.

References

1. Labib PL, Goodchild G, Pereira SP. Molecular pathogenesis of cholangiocarcinoma. *BMC Cancer*. 2019;19(1):185.

   doi: 10.1186/s12885-019-5391-0

2. Blechacz BR, Gores GJ. Cholangiocarcinoma. *Clin Liver Dis*. 2008;12(1):131-150, ix.

   doi: 10.1016/j.cld.2007.11.003

3. Sempoux C, Jibara G, Ward SC, *et al*. Intrahepatic cholangiocarcinoma: New insights in pathology. *Semin Liver Dis*. 2011;31:49-60.

   doi: 10.1055/s-0031-1272839

4. Yazici C, Niemeyer DJ, Iannitti DA, Russo MW. Hepatocellular carcinoma and cholangiocarcinoma: An update. *Expert Rev Gastroenterol Hepatol*. 2014;8(1):63-82.

   doi: 10.1586/17474124.2014.852468

5. Acalovschi M. Cholangiocarcinoma: Risk factors, diagnosis and management. *Rom J Intern Med*. 2004;42(1):41-58.

6. Vithayathil M, Khan SA. Current epidemiology of cholangiocarcinoma in Western countries. *J Hepatol*. 2022;77(6):1690-1698.

   doi: 10.1016/j.jhep.2022.07.022

7. Khan AS, Dageforde LA. Cholangiocarcinoma. *Surg Clin North Am*. 2019;99(2):315-335.

   doi: 10.1016/j.suc.2018.12.004

8. Krasinskas AM. Cholangiocarcinoma. *Surg Pathol Clin*. 2018;11(2):403-429.

   doi: 10.1016/j.path.2018.02.005

9. Kendall T, Verheij J, Gaudio E, *et al*. Anatomical, histomorphological and molecular classification of cholangiocarcinoma. *Liver Int*. 2019;39 (Suppl 1):7-18.

   doi: 10.1111/liv.14093

10. Qurashi M, Vithayathil M, Khan SA. Epidemiology of cholangiocarcinoma. *Eur J Surg Oncol*. 2023;2023:107064.

    doi: 10.1016/j.ejso.2023.107064

11. Rizvi S, Gores GJ. Pathogenesis, diagnosis, and management of cholangiocarcinoma. *Gastroenterology*. 2013; 145(6):1215-1229.

doi: 10.1053/j.gastro.2013.10.013

12. Khan SA, Tavolari S, Brandi G. Cholangiocarcinoma: Epidemiology and risk factors. *Liver Int*. 2019;39 Suppl 1:19-31.

doi: 10.1111/liv.14095

13. Cadamuro M Strazzabosco M. Inflammatory pathways and cholangiocarcinoma risk mechanisms and prevention. *Adv Cancer Res*. 2022;156:39-73.

doi: 10.1016/bs.acr.2022.02.001

14. Patel T. Cholangiocarcinoma. *Nat Clin Pract Gastroenterol Hepatol*. 2006;3(1):33-42.

15. Esnaola NF, Meyer JE, Karachristos A, Maranki JL, Camp ER, Denlinger CS. Evaluation and management of intrahepatic and extrahepatic cholangiocarcinoma. *Cancer*. 2016;122(9):1349-1369.

doi: 10.1002/cncr.29692

16. Surya H, Abdullah M, Nelwan EJ, *et al*. Current updates on diagnosis and management of cholangiocarcinoma: From surgery to targeted therapy. *Acta Med Indones*. 2023;55(3):361-370.

17. Banales JM, Marin JJ, Lamarca A, *et al*. Cholangiocarcinoma 2020: The next horizon in mechanisms and management. *Nat Rev Gastroenterol Hepatol*. 2020;17(9):557-588.

doi: 10.1038/s41575-020-0310-z

18. Razumilava N, Gores GJ. Classification, diagnosis, and management of cholangiocarcinoma. *Clin Gastroenterol Hepatol*. 2013;11(1):13-21.e1; quiz e3-4.

doi: 10.1016/j.cgh.2012.09.009

19. Razumilava N, Gores GJ. Cholangiocarcinoma. *Lancet*. 2014;383(9935):2168-2179.

doi: 10.1016/S0140-6736(13)61903-0

20. Sarcognato S, Sacchi D, Fassan M, *et al*. Cholangiocarcinoma. *Pathologica*. 2021;113(3):158-169.

doi: 10.32074/1591-951X-252

21. Izquierdo-Sanchez L, Lamarca A, La Casta A, *et al*. Cholangiocarcinoma landscape in Europe: Diagnostic, prognostic and therapeutic insights from the ENSCCA Registry. *J Hepatol*. 2022;76(5):1109-1121.

doi: 10.1016/j.jhep.2021.12.010

22. Gatto M, Bragazzi MC, Semeraro R, *et al*. Cholangiocarcinoma: Update and future perspectives. *Dig Liver Dis*. 2010;42(4):253-260.

doi: 10.1016/j.dld.2009.12.008

23. Oliverius M, Havlůj L, Hajer J, Soumarová R, Hrudka J, Gürlich R. Surgery for cholangiocarcinoma. *Cas Lek Cesk*. 2019;158(2):73-77.

doi: 10.1111/liv.14089

24. Giovinazzo F, Pascale MM, Cardella F, *et al*. Current perspectives in liver transplantation for perihilar cholangiocarcinoma. *Curr Oncol*. 2023;30(3):2942-2953.

doi: 10.3390/curroncol30030225

25. Mosconi S, Beretta GD, Labianca R, Zampino MG, Gatta G, Heinemann V. Cholangiocarcinoma. *Crit Rev Oncol Hematol*. 2009;69(3):259-270.

doi: 10.1016/j.critrevonc.2008.09.008

26. Fábrega-Foster K, Ghasabeh MA, Pawlik TM, Kamel IR. Multimodality imaging of intrahepatic cholangiocarcinoma. *Hepatobiliary Surg Nutr*. 2017;6:67-78.

doi: 10.21037/hbsn.2016.12.10

27. Blechacz B, Komuta M, Roskams T, Gores GJ. Clinical diagnosis and staging of cholangiocarcinoma. *Nat Rev Gastroenterol Hepatol*. 2011;8(9):512-522.

doi: 10.1038/nrgastro.2011.131

28. Kawashima H, Ohno E, Ishikawa T, *et al*. Endoscopic management of perihilar cholangiocarcinoma. *Dig Endosc*. 2022;34(6):1147-1156.

doi: 10.1111/den.14317

29. Hamaoka M, Kozaka K, Matsui O, *et al*. Early detection of intrahepatic cholangiocarcinoma. *Jpn J Radiol*. 2019;37(10):669-684.

doi: 10.1007/s11604-019-00860-0

30. Coronel M, Lee JH, Coronel E. Endoscopic ultrasound for the diagnosis and staging of biliary malignancy. *Clin Liver Dis*. 2022;26(1):115-125.

doi: 10.1016/j.cld.2021.08.010

31. Saleh M, Virarkar M, Bura V, *et al*. Intrahepatic cholangiocarcinoma: Pathogenesis, current staging, and radiological findings. *Abdom Radiol (NY)*. 2020; 45(11):3662-3680.

doi: 10.1007/s00261-020-02559-7

32. Yao D, Kunam VK, Li X. A review of the clinical diagnosis and therapy of cholangiocarcinoma. *J Int Med Res*. 2014;42(1):3-16.

doi: 10.1177/0300060513505488

33. Rayubkul J, Laohasiriwong W, Thinkhamrop B, Mahato RK, Khantikeo N, Pongpanich S. Prevalence of suspected cholangiocarcinoma based on ultrasonography screening and its associated factors in Northeastern Thailand. *Kathmandu Univ Med J (KUMJ)*. 2022;20(79):254-259.

34. Hann LE, Greatrex KV, Bach AM, Fong Y, Blumgart LH. Cholangiocarcinoma at the hepatic hilus: Sonographic findings. *AJR Am J Roentgenol*. 1997;168(4):985-989.

doi: 10.2214/ajr.168.4.9124155

35. Bloom CM, Langer B, Wilson SR. Role of US in the detection, characterization, and staging of cholangiocarcinoma. *Radiographics*. 1999;19(5):1199-1218.

doi: 10.1148/radiographics.19.5.g99se081199

36. Robledo R, Muro A, Prieto ML. Extrahepatic bile duct carcinoma: US characteristics and accuracy in demonstration of tumors. *Radiology*. 1996;198(3):869-873.

doi: 10.1148/radiology.198.3.8628885

37. Sungkasubun P, Siripongsakun S, Akkarachinorate K, *et al*. Ultrasound screening for cholangiocarcinoma could detect premalignant lesions and early-stage diseases with survival benefits: A population-based prospective study of 4,225 subjects in an endemic area. *BMC Cancer*. 2016;16:346.

doi: 10.1186/s12885-016-2390-2

38. Chung YE, Kim MJ, Park YN, *et al*. Varying appearances of cholangiocarcinoma: Radiologic-pathologic correlation. *Radiographics*. 2009;29(3):683-700.

doi: 10.1148/rg.293085729

39. Thinkhamrop K, Khuntikeo N, Chamadol N, Suwannatrai AT, Phimha S, Kelly M. Associations between ultrasound screening findings and cholangiocarcinoma diagnosis in an at-risk population. *Sci Rep*. 2022;12(1):13513.

doi: 10.1038/s41598-022-17794-9

40. Dietrich CF, Tannapfel A, Jang HY, Kim TK, Burns PN, Dong Y. Ultrasound imaging of hepatocellular adenoma using the new histology classification. *Ultrasound Med Biol*. 2019;45:1-10.

doi: 10.1016/j.ultrasmedbio.2018.06.015

41. Xu HX. Contrast-enhanced ultrasound in the biliary system: Potential uses and indications. *World J Radiol*. 2009;1(1):37-44.

doi: 10.4329/wjr.v1.i1.37

42. Conti CB, Cavalcoli F, Fraquelli M, Conte D, Massironi S. Ultrasound elastographic techniques in focal liver lesions. *World J Gastroenterol*. 2016;22(9):2647-2656.

doi: 10.3748/wjg.v22.i9.2647

43. Massironi S, Conte D, Sciola V, *et al*. Contrast-enhanced ultrasonography in evaluating hepatic metastases from neuroendocrine tumours. *Dig Liver Dis*. 2010;42(9):635-641.

doi: 10.1016/j.dld.2010.01.009

44. Ringe KI, Wacker F. Radiological diagnosis in cholangiocarcinoma: Application of computed tomography, magnetic resonance imaging, and positron emission tomography. *Best Pract Res Clin Gastroenterol*. 2015;29(2):253-265.

doi: 10.1016/j.bpg.2015.02.004

45. Kim SY. Preoperative radiologic evaluation of cholangiocarcinoma. *Korean J Gastroenterol*. 2017;69(3):159-163.

doi: 10.4166/kjg.2017.69.3.159

46. Raghavan K, Jeffrey RB, Patel BN, DiMaio MA, Willmann JK, Olcott EW. MDCT diagnosis of perineural invasion involving the celiac plexus in intrahepatic cholangiocarcinoma: Preliminary observations and clinical implications. *AJR Am J Roentgenol*. 2015;205(6):W578-584.

doi: 10.2214/AJR.15.14607

47. Zhu Y, Mao Y, Chen J, Qiu Y, Wang Z, He J. Preoperative computed tomography features of intrahepatic cholangiocarcinoma for predicting lymph node metastasis and overall survival. *J Comput Assist Tomogr*. 2019;43(5):729-735.

doi: 10.1097/RCT.0000000000000922

48. Olthof SC, Othman A, Clasen S, Schraml C, Nikolaou K, Bongers M. Imaging of cholangiocarcinoma. *Visc Med*. 2016;32(6):402-410.

doi: 10.1159/000453009

49. Nam JG, Lee JM, Joo I, *et al*. Intrahepatic mass-forming cholangiocarcinoma: Relationship between computed tomography characteristics and histological subtypes. *J Comput Assist Tomogr*. 2018;42(3):340-349.

50. Aherne EA, Pak LM, Goldman DA, *et al*. Intrahepatic cholangiocarcinoma: Can imaging phenotypes predict survival and tumor genetics? *Abdom Radiol (NY)*. 2018;43(10):2665-2672.

doi: 10.1007/s00261-018-1505-4

51. Chen HW, Lai EC, Pan AZ, Chen T, Liao S, Lau WY. Preoperative assessment and staging of hilar cholangiocarcinoma with 16-multidetector computed tomography cholangiography and angiography. *Hepatogastroenterology*. 2009;56(91-92):578-583.

52. Kim HJ, Lee DH, Lim JW, Ko YT. Multidetector computed tomography in the preoperative workup of hilar cholangiocarcinoma. *Acta Radiol*. 2009;50(8):845-853.

doi: 10.1080/02841850903092366

53. Endo I, Matsuyama R, Mori R, *et al*. Imaging and surgical planning for perihilar cholangiocarcinoma. *J Hepatobiliary Pancreat Sci*. 2014;21(8):525-532.

doi: 10.1002/jhbp.75

54. Zhang Y, Uchida M, Abe T, Nishimura H, Hayabuchi N, Nakashima Y. Intrahepatic peripheral cholangiocarcinoma: Comparison of dynamic CT and dynamic MRI. *J Comput Assist Tomogr*. 1999;23(5):670-677.

doi: 10.1097/00004728-199909000-00004

55. Park HM, Jang HY, Lee DE, *et al*. Prognostic impact of tumor vascularity on CT in resectable intrahepatic cholangiocarcinoma. *HPB (Oxford)*. 2022;24(3):359-369.

doi: 10.1016/j.hpb.2021.06.424

56. Park HJ, Park B, Park SY, *et al*. Preoperative prediction of postsurgical outcomes in mass-forming intrahepatic cholangiocarcinoma based on clinical, radiologic, and radiomics features. *Eur Radiol*. 2021;31(11):8638-8648.

doi: 10.1007/s00330-021-07926-6

57. Wakiya T, Ishido K, Kimura N, *et al*. CT-based deep learning enables early postoperative recurrence prediction for intrahepatic cholangiocarcinoma. *Sci Rep.* 2022;12(1):8428.

doi: 10.1038/s41598-022-12604-8

58. Bliznakova K, Kolev N, Buliev I, *et al*. Computer aided preoperative evaluation of the residual liver volume using computed tomography images. *J Digit Imaging*. 2015;28(2):231-239.

doi: 10.1007/s10278-014-9737-5

59. Sainani NI, Catalano OA, Holalkere NS, Zhu AX, Hahn PF, Sahani DV. Cholangiocarcinoma: Current and novel imaging techniques. *Radiographics*. 2008;28(5):1263-1287.

doi: 10.1148/rg.285075183

60. Fred HL. Drawbacks and limitations of computed tomography: Views from a medical educator. *Tex Heart Inst J*. 2004;31(4):345-348.

61. Vilgrain V, Van Beers BE, Flejou JF, *et al*. Intrahepatic cholangiocarcinoma: MRI and pathologic correlation in 14 patients. *J Comput Assist Tomogr*. 1997;21(1):59-65.

doi: 10.1097/00004728-199701000-00012

62. Jhaveri KS, Hosseini-Nik H. MRI of cholangiocarcinoma. *J Magn Reson Imaging*. 2015;42(5):1165-1179.

doi: 10.1002/jmri.24810

63. Zhimin G, Noor H, Jian-Bo Z, Lin W, Jha RK. Advances in diagnosis and treatment of hilar cholangiocarcinoma--a review. *Med Sci Monit*. 2013;19:648-656.

doi: 10.12659/MSM.889379

64. Manfredi R, Barbaro B, Masselli G, Vecchioli A, Marano P. Magnetic resonance imaging of cholangiocarcinoma. *Semin Liver Dis*. 2004;24(2):155-164.

doi: 10.1055/s-2004-828892

65. Masselli G, Gualdi G. Hilar cholangiocarcinoma: MRI/MRCP in staging and treatment planning. *Abdom Imaging*. 2008;33(4):444-451.

doi: 10.1007/s00261-007-9281-6

66. Kim DW, Kim SY, Yoo C, Hwang DW. Update on biliary cancer imaging. *Radiol Clin North Am*. 2022;60(5):825-842.

doi: 10.1016/j.rcl.2022.05.001

67. Xu Y, Ye F, Li L, *et al*. MRI-based radiomics nomogram for preoperatively differentiating intrahepatic mass-forming cholangiocarcinoma from resectable colorectal liver metastases. *Acad Radiol*. 2023;30(9):2010-2020.

doi: 10.1016/j.acra.2023.04.030

68. Zhang J, Wu Z, Zhao J, *et al*. Intrahepatic cholangiocarcinoma: MRI texture signature as predictive biomarkers of immunophenotyping and survival. *Eur Radiol*. 2021;31(6):3661-3672.

doi: 10.1007/s00330-020-07524-y

69. Sheng R, Huang X, Jin K, *et al*. Contrast-enhanced MRI could predict response of systemic therapy in advanced intrahepatic cholangiocarcinoma. *Eur Radiol*. 2022;32(8):5156-5165.

doi: 10.1007/s00330-022-08679-6

70. Koh J, Chung YE, Nahm JH, *et al*. Intrahepatic mass-forming cholangiocarcinoma: Prognostic value of preoperative gadoxetic acid-enhanced MRI. *Eur Radiol*. 2016;26(2):407-416.

doi: 10.1007/s00330-015-3846-5

71. Wang L, Liu J, Zeng Y, Shu J. The value of an MRI-based radiomics model in predicting the survival and prognosis of patients with extrahepatic cholangiocarcinoma. *Cancer Med*. 2024;13(1):e6832.

doi: 10.1002/cam4.6832

72. Xin Y, Liu Q, Zhang J, *et al*. Hilar cholangiocarcinoma: Value of high-resolution enhanced magnetic resonance imaging for preoperative evaluation. *J Cancer Res Ther*. 2020;16(7):1634-1640.

doi: 10.4103/jcrt.JCRT_140_20

73. Min JH, Kim YK, Choi SY, *et al*. Intrahepatic mass-forming cholangiocarcinoma: Arterial enhancement patterns at MRI and prognosis. *Radiology*. 2019;290(3):691-699.

doi: 10.1148/radiol.2018181485

74. Vanderveen KA, Hussain HK. Magnetic resonance imaging of cholangiocarcinoma. *Cancer Imaging*. 2004;4(2):104-115.

doi: 10.1102/1470-7330.2004.0018

75. Kovač JD, Janković A, Đikić-Rom A, Grubor N, Antić A, Dugalić V. Imaging spectrum of intrahepatic mass-forming cholangiocarcinoma and its mimickers: How to differentiate them using MRI. *Curr Oncol*. 2022;29(2):698-723.

doi: 10.3390/curroncol29020061

76. Singh A, Siddiqui UD. The role of endoscopy in the diagnosis and management of cholangiocarcinoma. *J Clin Gastroenterol.* 2015;49(9):725-737.

doi: 10.1097/MCG.0000000000000390

77. Voigtländer T, Lankisch TO. Endoscopic diagnosis of cholangiocarcinoma: From endoscopic retrograde cholangiography to bile proteomics. *Best Pract Res Clin Gastroenterol*. 2015;29(2):267-275.

doi: 10.1016/j.bpg.2015.02.005

78. Vogel A, Wege H, Caca K, Nashan B, Neumann U. The diagnosis and treatment of cholangiocarcinoma. *Dtsch Arztebl Int*. 2014;111(44):748-754.

doi: 10.3238/arztebl.2014.0748

79. Rizvi S, Gores GJ. Current diagnostic and management options in perihilar cholangiocarcinoma. *Digestion*. 2014;89(3):216-224.

doi: 10.1159/000360791

80. Cowling MG, Adam AN. Internal stenting in malignant biliary obstruction. *World J Surg*. 2001;25(3):355-359; discussion 359-361.

doi: 10.1007/s002680020384

81. Rizvi S, Eaton J, Yang JD, Chandrasekhara V, Gores GJ. Emerging technologies for the diagnosis of perihilar cholangiocarcinoma. *Semin Liver Dis*. 2018;38(2):160-169.

doi: 10.1055/s-0038-1655775

82. Kalaitzakis E, Levy M, Kamisawa T, *et al*. Endoscopic retrograde cholangiography does not reliably distinguish IgG4-associated cholangitis from primary sclerosing cholangitis or cholangiocarcinoma. *Clin Gastroenterol Hepatol*. 2011;9(9):800-803.e2.

doi: 10.1016/j.cgh.2011.05.019

83. Chaves, J., Fernandez, Y., Viesca, M., Arvanitakis, M. Using Endoscopy in the Diagnosis of Pancreato-Biliary Cancers. Cancers (Basel). 2023 Jun 28;15(13):3385.

84. Jo JH, Cho CM, Jun JH, *et al*. Same-session endoscopic ultrasound-guided fine needle aspiration and endoscopic retrograde cholangiopancreatography-based tissue sampling in suspected malignant biliary obstruction: A multicenter experience. *J Gastroenterol Hepatol*. 2019;34(4):799-805.

doi: 10.1111/jgh.14528

85. Levy MJ, Heimbach JK, Gores GJ. Endoscopic ultrasound staging of cholangiocarcinoma. *Curr Opin Gastroenterol*. 2012;28(3):244-252.

doi: 10.1097/MOG.0b013e32835005bc

86. Strongin A, Singh H, Eloubeidi MA, Siddiqui AA. Role of endoscopic ultrasonography in the evaluation of extrahepatic cholangiocarcinoma. *Endosc Ultrasound*. 2013;2(2):71-76.

doi: 10.4103/2303-9027.117690

87. Orzan RI, Pojoga C, Agoston R, Seicean R, Seicean A. Endoscopic ultrasound in the diagnosis of extrahepatic cholangiocarcinoma: What do we know in 2023? *Diagnostics (Basel)*. 2023;13(6):1023.

doi: 10.3390/diagnostics13061023

88. Onda S, Ogura T, Kurisu Y, *et al*. EUS-guided FNA for biliary disease as first-line modality to obtain histological evidence. *Therap Adv Gastroenterol*. 2016;9(3):302-312.

doi: 10.1177/1756283X15625584

89. Shin DW, Moon SH, Kim JH. Diagnosis of cholangiocarcinoma. *Diagnostics (Basel)*. 2023;13(2):233.

doi: 10.3390/diagnostics13020233

90. Harewood GC. Endoscopic tissue diagnosis of cholangiocarcinoma. *Curr Opin Gastroenterol*. 2008; 24(5):627-630.

doi: 10.1097/MOG.0b013e32830bf7e1

91. De Jong DM, van de Vondervoort S, Dwarkasing RS, *et al*. Endoscopic ultrasound in patients with resectable perihilar cholangiocarcinoma: Impact on clinical decision-making. *Endosc Int Open*. 2023;11(2):E162-E168.

doi: 10.1055/a-2005-3679

92. Nguyen K, Sing JT Jr. Review of endoscopic techniques in the diagnosis and management of cholangiocarcinoma. *World J Gastroenterol*. 2008;14(19):2995-2999.

doi: 10.3748/wjg.14.2995

93. Büsing KA, Schönberg SO, Brade J, Wasser K. Impact of blood glucose, diabetes, insulin, and obesity on standardized uptake values in tumors and healthy organs on 18F-FDG PET/CT. *Nucl Med Biol*. 2013;40(2):206-213.

doi: 10.1016/j.nucmedbio.2012.10.014

94. Annunziata S, Caldarella C, Pizzuto DA, *et al*. Diagnostic accuracy of fluorine-18-fluorodeoxyglucose positron emission tomography in the evaluation of the primary tumor in patients with cholangiocarcinoma: A meta-analysis. *Biomed Res Int*. 2014;2014:247693.

doi: 10.1155/2014/247693

95. Anderson CD, Rice MH, Pinson CW, Chapman WC, Chari RS, Delbeke D. Fluorodeoxyglucose PET imaging in the evaluation of gallbladder carcinoma and cholangiocarcinoma. *J Gastrointest Surg*. 2004;8(1):90-97.

doi: 10.1016/j.gassur.2003.10.003

96. Kim JY, Kim MH, Lee TY, *et al*. Clinical role of 18F-FDG PET-CT in suspected and potentially operable cholangiocarcinoma: A prospective study compared with conventional imaging. *Am J Gastroenterol*. 2008;103(5):1145-1151.

doi: 10.1111/j.1572-0241.2007.01710.x

97. Breitenstein S, Apestegui C, Clavien PA. Positron emission tomography (PET) for cholangiocarcinoma. *HPB (Oxford)*. 2008;10(2):120-121.

doi: 10.1080/13651820801992583

98. Lee Y, Yoo IR, Boo SH, Kim H, Park HL, Hyun OJ. The role of F-18 FDG PET/CT in intrahepatic cholangiocarcinoma. *Nucl Med Mol Imaging*. 2017;51(1):69-78.

doi: 10.1007/s13139-016-0440-y

99. Fiz F, Masci C, Costa G, *et al*. PET/CT-based radiomics of mass-forming intrahepatic cholangiocarcinoma improves prediction of pathology data and survival. *Eur J Nucl Med Mol Imaging*. 2022;49(10):3387-3400.

doi: 10.1007/s00259-022-05765-1

100. Jiang L, Tan H, Panje CM, Yu H, Xiu Y, Shi H. Role of 18F-FDG PET/CT imaging in intrahepatic cholangiocarcinoma. *Clin Nucl Med*. 2016;41(1):1-7.

doi: 10.1097/RLU.0000000000000998

101. Guniganti P, Kierans AS. PET/MRI of the hepatobiliary

system: Review of techniques and applications. *Clin Imaging*. 2021;71:160-169.

doi: 10.1016/j.clinimag.2020.10.056

102. Vaquero JJ, Kinahan P. Positron emission tomography: Current challenges and opportunities for technological advances in clinical and preclinical imaging systems. *Annu Rev Biomed Eng*. 2015;17:385-414.

doi: 10.1146/annurev-bioeng-071114-040723

103. Arslan E, Çermik TF. PET/CT variants and pitfalls in liver, biliary tract, gallbladder and pancreas. *Semin Nucl Med*. 2021;51(5):502-518.

doi: 10.1053/j.semnuclmed.2021.04.006

104. Lan L, Zhang S, Xu T, *et al*. Prospective comparison of 68Ga-FAPI versus 18F-FDG PET/CT for tumor staging in biliary tract cancers. *Radiology*. 2022;304(3):648-657.

doi: 10.1148/radiol.213118

105. Lamarca A, Barriuso J, Chander A, *et al*. 18F-fluorodeoxyglucose positron emission tomography (18FDG-PET) for patients with biliary tract cancer: Systematic review and meta-analysis. *J Hepatol*. 2019;71(1):115-129.

doi: 10.1016/j.jhep.2019.01.038

106. Goel S, Aggarwal A, Iqbal A, Gupta M, Rao A, Singh S. 18-FDG PET-CT should be included in preoperative staging of gall bladder cancer. *Eur J Surg Oncol*. 2020;46(9):1711-1716.

doi: 10.1016/j.ejso.2020.04.015

107. Karagyozov P, Boeva I, Tishkov I. Role of digital single-operator cholangioscopy in the diagnosis and treatment of biliary disorders. *World J Gastrointest Endosc*. 2019;11(1):31-40.

doi: 10.4253/wjge.v11.i1.31

108. Feng Y, Liang Y, Liu Y, *et al*. Digital cholangioscopy-assisted, direct visualization-guided, radiation-free, endoscopic retrograde intervention for cholelithiasis: Technical feasibility, efficacy, and safety. *Surg Endosc*. 2024;38(3):1637-1646.

doi: 10.1007/s00464-024-10684-3

109. Wakai T, Nagahashi M, Shimada Y, Prasoon P, Sakata J. Genetic analysis in the clinical management of biliary tract cancer. *Ann Gastroenterol Surg*. 2020;4(4):316-323.

doi: 10.1002/ags3.12334

110. Kato S. Tumour-agnostic therapy for pancreatic cancer and biliary tract cancer. *Diagnostics (Basel)*. 2021;11(2):252.

doi: 10.3390/diagnostics11020252

111. Mayerhoefer ME, Materka A, Langs G, *et al*. Introduction to radiomics. *J Nucl Med*. 2020;61(4):488-495.

doi: 10.2967/jnumed.118.222893

112. Liu QP, Tang J, Chen YZ, *et al*. Immuno-genomic-radiomics to predict response of biliary tract cancer to camrelizumab plus GEMOX in a single-arm phase II trial. *JHEP Rep*. 2023;5(7):100763.

doi: 10.1016/j.jhepr.2023.100763

113. Koçak B, Durmaz EŞ, Ateş E, Kılıçkesmez Ö. Radiomics with artificial intelligence: A practical guide for beginners. *Diagn Interv Radiol*. 2019;25(6):485-495.

doi: 10.5152/dir.2019.19321

114. Bo Z, Chen B, Yang Y, *et al*. Machine learning radiomics to predict the early recurrence of intrahepatic cholangiocarcinoma after curative resection: A multicentre cohort study. Eur J *Nucl Med Mol Imaging*. 2023;50(8):2501-2513.

doi: 10.1007/s00259-023-06184-6

115. Gupta P, Kambadakone A, Sirohi B. Editorial: Role of imaging in biliary tract cancer: Diagnosis, staging, response prediction and image-guided therapeutics. *Front Oncol*. 2024;14:1387531.

doi: 10.3389/fonc.2024.1387531

116. Fernandez Y, Viesca M, Arvanitakis M. Early diagnosis and management of malignant distal biliary obstruction: A review on current recommendations and guidelines. *Clin Exp Gastroenterol*. 2019;12:415-432.

doi: 10.2147/CEG.S195714

117. Cha JM, Kim MH, Jang SJ. Early bile duct cancer. *World J Gastroenterol*. 2007;13(25):3409-3416.

doi: 10.3748/wjg.v13.i25.3409

118. Bao F, Liu J, Chen H, Miao L, Xu Z, Zhang G. Diagnosis biomarkers of cholangiocarcinoma in human bile: An evidence-based study. *Cancers (Basel)*. 2022;14(16):3921.

doi: 10.3390/cancers14163921

119. Colli A, Fraquelli M, Casazza G, *et al*. Accuracy of ultrasonography, spiral CT, magnetic resonance, and alpha-fetoprotein in diagnosing hepatocellular carcinoma: A systematic review. *Am J Gastroenterol*. 2006;101(3):513-23.

doi: 10.1111/j.1572-0241.2006.00467.x

ACCSCIENCE PUBLISHING

Advances in Radiotherapy & Nuclear Medicine

REVIEW ARTICLE

Treatment consensus for locally advanced cervical cancer

Ping Jiang[1†], Zhuhui Yuan[1†], Lichun Wei[2], Fengju Zhao[3], Xiangkun Yuan[4], Yipeng Song[5], Jing Bai[6], Xiaofan Li[7], Baosheng Sun[8], Lijuan Zou[9], Sha Li[10], Yuhua Gao[11], Yanhong Zhuo[12], Song Gao[13], Qin Xu[14], Xiaohong Zhou[15], Hong Zhu[16], Yunyan Zhang[17*], Zi Liu[18*], and Junjie Wang[1*]

[1]Department of Radiation Oncology, Cancer Center of Peking University Third Hospital, Peking University Third Hospital, Haidian District, Beijing, China

[2]Department of Radiotherapy, Xijing Hospital, The Fourth Military Medical University of People's Liberation Army, Xi'an, Shaanxi, China

[3]Radiotherapy Center, Gansu Province Maternal and Child Health Hospital/Gansu Province Central Hospital, Lanzhou, Gansu, China

[4]Department of Radiation Oncology, Hebei Cangzhou Integrated Traditional Chinese and Western Medicine Hospital, China

[5]Department of Oncology, Yantai Yuhuangding Hospital, Yantai, China

[6]Department of Radiation Oncology, Baotou Tumor Hospital, Baotou, China

[7]Department of Radiation Oncology, Peking University Cancer Hospital, Beijing, China

[8]Department of Radiotherapy, Jilin Province Cancer Hospital, Changchun, China

[9]The Second Hospital Affiliated to Dalian Medical University, Dalian, China

[10]Department of Radiation Oncology, 940 Hospital of the Joint Logistics Support Force of The Chinese People's Liberation Army, Lanzhou, Gansu, China

[†]*These authors contributed equally to this work.*

***Corresponding authors:**
Yunyan Zhang
(Zhangyunyan_1972@163.com)
Zi Liu
(liuzmail@163.com)
Junjie Wang
(junjiewang@pku.edu.cn)

Citation: Jiang P, Yuan Z, Wei L, *et al*. Treatment consensus for locally advanced cervical cancer. *Adv Radiother Nucl Med*. 2025;3(1):17-27.
doi: 10.36922/arnm.4032

Received: June 24, 2024

Revised: November 23, 2024

Accepted: December 17, 2024

Published online: January 13, 2025

Abstract

Concurrent chemoradiotherapy (CCRT) involves the simultaneous administration of chemotherapy and radiotherapy, in which low-dose chemotherapy enhances the effectiveness of radiotherapy. This combined approach mitigates tumor recurrence and metastasis, ultimately improving patient prognosis. The primary mechanism behind the increased radiosensitivity induced by concurrent chemotherapy involves inhibiting tumor cell repair and the complementary effects of chemotherapy and radiotherapy on different phases of the cell cycle. Despite CCRT application in patients with locally advanced cervical cancer (LACC), the 5-year survival rate remains at 60%. To improve treatment efficacy, a series of exploratory investigations have been conducted, encompassing the integration of targeted therapy, immunotherapy, and utilization of immunomodulatory agents in neoadjuvant protocols preceding CCRT. Although targeted therapies and immunomodulators represent efficacious interventions for LACC management, the scarcity of robust, large-scale evidence-based data necessitates the undertaking of multicenter prospective randomized Phase III clinical trials and dissemination of high-quality publications to elevate the standard of evidence-based medicine. This consensus acts as a valuable resource for clinicians and researchers, highlighting recent seminal evidence-based studies and the evolving landscape of clinical research on targeted and immunomodulatory agents.

Keywords: Immunotherapy; Targeted therapy; Concurrent chemoradiotherapy; Locally advanced cervical cancer

[11]Obstetrics and Gynecology Radiation Ward, Liaoning Province Cancer Hospital and Institute (Cancer Hospital of China Medical University), Dadong District, Shenyang, Liaoning, China
[12]Department of Radiation Oncology, Zhangzhou Hospital, Teaching Hospital of Fujian Medical University, Zhangzhou, Fujian, China
[13]Department of Obstetrics and Gynecology, Shengjing Hospital Affiliated to China Medical University, Shenyang, Liaoning, China
[14]Department of Gynecology, Fujian Provincial Cancer Hospital, Fuzhou, China
[15]Department of Radiation Oncology, Jiamusi Cancer Hospital, Jiamusi, China
[16]Department of Oncology, Xiangya Hospital, Central South University, Changsha, Hunan, China
[17]Department of Gynecology, The Affiliated Tumor Hospital of Harbin Medical University, Baojian Road 6, Nangang District, Harbin, China
[18]Department of Radiation Oncology, The First Affiliated Hospital of Xi'an Jiaotong University, Xi'an, Shaanxi, China

1. Introduction

Cervical cancer, a prevalent gynecological malignant tumor, ranks as the second most common female malignancy in China.[1] According to the 2020 global cancer statistics analysis report, over 600,000 new cases of cervical cancer are recorded globally, with over 340,000 deaths. Notably, 85% of these cases were identified in developing countries. In China, approximately 110,000 new cases and 60,000 deaths are recorded annually.[1-3] Despite significant advances in the diagnostic accuracy and therapeutic efficacy of cervical cancer in recent years, 37% of patients are still diagnosed at locally advanced stages.[4]

The International Federation of Gynecology and Obstetrics (FIGO) defines locally advanced cervical cancer (LACC) narrowly as stage IB3/IIA2 and broadly as stage IB3-IVA (as per the 2018 FIGO stage). LACC has a propensity for distant metastasis even after undergoing standard concurrent chemoradiotherapy (CCRT), resulting in a 3-year overall survival (OS) rate of only 72%. This is attributed to large local tumor size and high-risk factors, such as lymph node metastasis and paravaginal infiltration.[5]

In recent years, targeted drugs and immunotherapy have significantly progressed. The LACC working group, comprising gynecologic tumor oncologists and radiation oncologists, has developed a Chinese expert consensus on combining targeted and immunological drugs with CCRT for treating LACC. This consensus aims to provide a reliable reference and academic guidance for clinical practice.

2. Methods

The consensus process commenced with the application of the estimate-talk-estimate methodology.[6,7] A multicenter panel comprising 20 health professionals involved in the diagnosis, treatment, and follow-up of LACC was assembled. This panel included two medical oncologists, 15 radiation oncologists, and three gynecologists. Each panelist independently identified the most pertinent issues (or items) related to the use of targeted and immunological agents in combination with CCRT for LACC treatment, which merited attention and discussion. These issues were subsequently harmonized and categorized by the facilitator into six items, which were presented to the panel members during a virtual meeting. To achieve consensus, the harmonized items were thoroughly discussed. Then, each board member individually formulated one or more statements addressing each of the six agreed-upon items. In a second meeting, the panel members reviewed and further deliberated on the harmonized statements, ultimately agreeing on eight statements. The grading of recommendations, assessment, development, and evaluation framework was utilized to assess the evidence levels and recommendation grades. Levels of evidence were classified as high, medium, low, and very low, whereas recommendations were categorized as strong or weak (Table 1).

3. Results

3.1. Targeted drug combined with CCRT for LACC treatment

3.1.1. Combination therapy involving anti-vascular endothelial growth factor (VEGF) antibody

Anti-VEGF antibodies inhibit tumor proliferation by suppressing angiogenesis and inducing endothelial cell apoptosis. Bevacizumab, a humanized immunoglobulin G1 monoclonal antibody targeting VEGF, serves as the primary treatment for recurrent metastatic cervical cancer when used alongside chemotherapy. Its efficacy has also been investigated in LACC cases. In the RTOG 0417 trial,[8] a Phase II study incorporating CCRT and bevacizumab for LACC treatment included 60 patients with sizable tumors (n = 49 were evaluated), resulting in a 3-year OS rate of 81.3%, a disease-free survival (DFS) rate of 68.7%, and a locoregional lymph node failure rate of 23.2%. However, 36.7% of participants reported significant adverse effects (grade 3, 26.5%; grade 4, 10.2%). Given the limited sample size of the RTOG0417 trial and the observed clinical toxicities, caution is advised when considering bevacizumab combined with CCRT in patients with LACC and substantial tumor burden (Table 2).

Table 1. Grading of evidence quality and consensus recommendation strength

Evidence level	Definition
Evidence quality grade	
High	Future research is unlikely to significantly change the credibility of existing efficacy evaluations
Medium	Future research may have a significant effect on existing efficacy evaluations, potentially altering the credibility of the results
Low	Future research is likely to have a significant effect on existing efficacy evaluations, with a higher likelihood of changing the credibility of the results
Very low	Evaluation of any efficacy is highly uncertain
Consensus recommendation grade	
Strong	Clearly indicates that the benefits of the intervention outweigh the harms or vice versa
Weak	Uncertainty in the balance of benefits and harms or evidence, regardless of its quality, shows a balance between benefits and harms

- Level of evidence: Low
- Grade of recommendation: Weak.

3.1.2. Combination therapy involving recombinant human vascular endothelial inhibitors

Recombinant human vascular endothelial inhibitor impedes the migration of vascular endothelial cells, thereby preventing tumor neoangiogenesis and cutting off the nutrient supply to the tumor, which hinders its growth and metastasis. For example, Endostar, primarily used for treating advanced non-small cell lung cancer (NSCLC), has been recently utilized in managing LACC treatment. In a Phase II randomized controlled trial (n = 116), the trial group exhibited 1- and 2-year progression-free survival (PFS) rates of 91.4% and 80.8%, respectively, surpassing those of the control group at 82.1% and 63.5%, respectively; however, the difference was not significant (P = 0.091). Both groups demonstrated analogous safety profiles.[9] Another randomized controlled trial revealed a higher complete response rate (CRR) in the experimental group (83% vs. 65%, $P < 0.05$), with no significant differences in objective response rate (ORR) or disease control rate (DCR) (93% vs. 90% and 95% vs. 95%; $P > 0.05$) compared with the control group.[10] The experimental group experienced higher frequencies of infections (50% vs. 18%), hypertension (16% vs. 2%), and neutropenia (68% vs. 44%). Despite the limited sample size, low evidence level, and lack of long-term follow-up data (e.g., 3-year PFS and OS), patients may be advised to consider participation in clinical trials.

- Level of evidence: Low
- Grade of recommendation: Weak.

3.1.3. Combination therapy involving anti-epidermal growth factor receptor (EGFR) antibodies

EGFR monoclonal antibodies suppress the malignant biological behaviors of tumor cells by recognizing the extracellular segment of the EGFR receptor and competing with the ligand for binding. This action involves blocking the ligand binding site of EGFR, disrupting receptor phosphorylation, impeding activation, and inhibiting the signaling pathway. Cetuximab and nimotuzumab are two frequently employed pharmaceuticals targeting EGFR.

Cetuximab is a human-mouse chimeric anti-EGFR monoclonal antibody that competitively interacts with EGFR to inhibit tumor cell growth by impeding intracellular proliferative signals. It can be utilized for the treatment of head and neck squamous cell carcinoma and metastatic colorectal cancer. Research investigating the efficacy of cetuximab in treating LACC is ongoing. In a Phase II randomized controlled study involving 78 participants with a median 31-month follow-up, a combination of cetuximab with CCRT for LACC revealed 2-year DFS rate of 63% (95% confidence interval [CI], 49 – 80%) compared with 76% (95% CI, 63 – 91%) in the control group, with non-significant between-group differences (P = 0.18).[11] The experimental group exhibited a 2-year OS rate of 83% (95% CI, 72 – 96%), appearing similar to 87% (95% CI, 76 – 98%) in the control group. Both groups exhibited comparable safety profiles, and no grade ≥3 adverse events occurred.

In 2022, a Phase I feasibility study was conducted, involving 21 participants who received varying cetuximab doses (250 or 200 mg/m^2) in combination with CCRT (cisplatin, 30 or 40 mg/m^2).[12] The study reported 5-year PFS and OS rates of 57.5% and 58.5%, respectively. Notably, when administering cetuximab at 250 mg/m^2 combined with CCRT (cisplatin, 30 mg/m^2), only one patient was diagnosed with dose-limiting toxicity (DLT, grade 4 renal failure), and other patients demonstrated tolerability. However, the study primarily concentrated on toxicology and provided limited evidence of efficacy; thus, cetuximab has not been recommended for treating patients with LACC.

- Level of evidence: Low (cetuximab)
- Grade of recommendation: Weak (cetuximab).

Nimotuzumab is utilized for treating stage III/IV nasopharyngeal carcinoma that expresses EGFR, and Phase III studies on LACC are ongoing. Patients diagnosed with LACC receive nimotuzumab, and measuring EGFR expression is recommended in facilities where available. No discernible variations in efficacy and safety based on pathology type were observed. The trial group receiving nituzumab with CCRT comprised 147 participants,

Table 2. Clinical studies of targeted drugs in combination with CCRT for LACC

Classification	Drug name	Researcher	Study type	No. of cases	RT	Follow-up (Mo.)	Efficacy	Adverse reactions/events
Anti-VEGFR	Bevacizumab	Schefter *et al.*[8]	Phase II single-arm	60	EBRT	45	3-year OS, DFS, and LRF of 81.3%, 68.7%, and 23.2%, respectively	36.7% of patients experienced grade ≥3 adverse events (26.5% with grade 3, 10.2% with grade 4)
Recombinant human endostatin	Endostar	Lu *et al.*[9]	Phase II randomized controlled	116	IMRT	22	1-year PFS 91.4% *vs.* 82.1%; 2-year PFS 80.8% *vs.* 63.5%	Similar safety profiles
Recombinant human endostatin	Endostar	Shu *et al.*[10]	Phase II randomized controlled	91	IMRT	NA	CRR 83% *vs.* 65%	Higher incidence of neutropenia (68% vs. 44%), hypertension (16% vs. 2%), and infections (50% vs. 18%) noted in the experimental group
Anti-EGFR monoclonal antibody	Cetuximab	De la Rochefordiere *et al.*[11]	Phase II randomized controlled	78	EBRT, IMRT	31	2-year OS 83% *vs.* 87%; 2-year DFS 63% *vs.* 76%	Similar safety profiles
Anti-EGFR monoclonal antibody	Cetuximab	Fracasso *et al.*[12]	Phase I study	21	EFRT	NA	5-year PFS rate and OS rate 57.5% and 58.5% respectively	Well-tolerated by most patients
Anti-EGFR monoclonal antibody	Nimotuzumab	Wang *et al.*[13]	Phase III study	291	IMRT, VMAT	Ongoing	ORR 86.3% *vs.* 76.3%	Similar safety profiles
Anti-EGFR monoclonal antibody	Nimotuzumab	Qu *et al.*[14]	Phase II study	122	IMRT, VMAT	Ongoing	CRR 42.6%, PRR 45.0%	Majority of drug-related adverse reactions were Grades 1–2
Anti-EGFR monoclonal antibody	Nimotuzumab	Yuan *et al.*[15]	Meta-analysis	393	IMRT	NA	Significant improvements in experimental group CRR, ORR, and 3-year OS	Similar safety profiles

Abbreviations: CRR: Complete response rate; DCR: Disease control rate; DFS: Disease-free survival; DMFS: Distant metastasis-free survival; EBRT: External beam radiotherapy; EFRT: Extended-field radiotherapy; EGFR: Epidermal growth factor receptor; IMRT: Intensity-modulated radiotherapy; LACC: Locally advanced cervical cancer; LRF: Locoregional failure; mOS: Median overall survival; NA: Not applicable; ORR: Objective response rate; OS: Overall survival; PFS: Progression-free survival; PRR: Partial response rate; RT: Radiotherapy; SAE: Severe adverse events; VEGFR: Vascular endothelial growth factor; VMAT: Volumetric modulated arc therapy.

whereas the control group included 144 participants.[13] The ORRs in the two groups were 86.3% and 76.3%, respectively, exhibiting a significant difference ($P = 0.028$). Notably, no significant variance ($P > 0.05$) was noted in the incidence of grade ≥3 adverse events between the two groups.

In this prospective multicenter single-arm Phase II trial,[14] 122 older patients with cervical cancer who were ineligible for chemotherapy received nituzumab combined with radiotherapy. The partial response rate (PRR), ORR, DCR, and CRR were 45.0% (55/122), 87.7% (107/122), 92.6% (113/122), and 42.6% (52/122), respectively, with Grade 1 – 2 adverse events being the most common. A meta-analysis involving 393 patients indicated that the nimotuzumab plus CCRT group displayed significantly improved CRR (RR = 1.34, 95% CI 1.08 – 1.65, $P = 0.007$), ORR (RR = 1.30, 95% CI 1.16 – 1.44, $P < 0.05$), and 3-year OS rate (RR = 1.27, 95% CI 1.06 – 1.51, $P = 0.008$) compared with the radiotherapy group.[15] Notably, the incidence of adverse events, such as leukopenia, gastrointestinal reactions, radiation cystitis, and radiation proctitis, did not exhibit significant differences between the two groups ($P > 0.05$). The evidence supports the safety and clinical benefits of nimotuzumab in combination with CCRT, exhibiting positive short-term efficacy outcomes, such as ORR and favorable long-term survival (e.g., 3-year OS rate). The recommended nimotuzumab dosage is 200 – 400 mg once weekly for 6 weeks.

- Level of evidence: Medium (nimotuzumab)
- Grade of recommendation: Strong (nimotuzumab).

3.2. Integration of ICIs with CCRT in LACC treatment

The integration of ICIs with CCRT in LACC treatment represents significant progress over the last decade. ICIs have revolutionized the management of malignant tumors and reshaped the tumor therapy landscape. The potential of ICIs in cervical cancer treatment has remarkably attracted the attention of clinicians. By inhibiting T-cell activation and cytokine production, ICIs reactivate T-cell-mediated cytotoxicity and enhance antitumor immune responses by impeding immunological checkpoints and ligand binding. To ensure precise medication dosing, programmed death ligand-1 (PD-L1) and tumor mutation burden testing are recommended before initiating ICIs along with CCRT (Table 3).

Nivolumab, a human monoclonal antibody targeting the PD-1 receptor, is the pioneering ICI to receive approval. It has demonstrated efficacy in conditions, such as advanced gastric cancer, recurrent or metastatic squamous head and neck cancer, and locally advanced or metastatic NSCLC. During the 2022 ASCO congress, a Phase I clinical trial investigating nivolumab in combination with CCRT to treat LACC ($n = 16$) unveiled its findings.[16] The trial reported an impressive ORR of 93.8% (15/16), CRR of 50% (8/16), and PRR of 43.75% (7/16). The 2-year PFS rate was 75% (95% CI 56.5 – 99.5%). Among 15 patients evaluable for DLT, three experienced DLT, consisting of two cases of Grade 3 hypotension and one case of Grade 3 acute renal injury. No fatalities occurred during the DLT evaluation. Given that the outcomes of a Phase I trial with a small sample size have yet to be substantiated by comprehensive data from a large randomized controlled

Table 3. Clinical studies of immunotherapy drugs in combination with CCRT for LACC

Drug name	Researcher	Study type	No. of cases	RT	Follow-up (Mo.)	Efficacy	Adverse reactions/events
Atezolizumab	Mayadev *et al.*[29]	Phase I study	40	EFRT	20	A Arm ORR 69%, 2-year DFS 79%; B Arm ORR 40%, 2-year DFS 59%	3 DLT cases, 7 cases of grade ≥3 adverse reactions
Nivolumab	Rodrigues *et al.*[16]	Phase I study	16	Not reported	23.8	ORR 93.8%, CRR 50%, PRR 43.75%, 2-year PFS 75%	3 DLT cases
Camrelizumab	Xiao *et al.*[17]	Phase II study	25	IMRT	Not reported	CRR 28%, ORR 96.0%, DCR 100%	16% incidence of grade ≥3 adverse reactions
Durvalumab	Monk *et al.*[22]	Phase III study	714	EBRT	18.5	1-year PFS 76.0% versus 73.3%	Overall rate of grade ≥3 adverse reactions 28% versus 23%
Pembrolizumab	Duska *et al.*[23]	Phase II Study	88	IMRT, EBRT	9.2	NA	88% incidence of ≥2-grade TRAEs
Pembrolizumab	Lorusso *et al.*[24]	Phase III study	1060	EBRT	17.9	2-year PFS 67.8% versus 57.3%, 2-year OS 87.2% versus 80.8%	67.0% versus 60.0% incidence of grade ≥3TRAEs

Abbreviations: CRR: Complete response rate; DCR: Disease control rate; DFS: Disease-free survival; DLT: Dose-limiting toxicity; EBRT: External beam radiotherapy; EFRT: Extended-field radiotherapy; IMERT: Intensity-modulated external radiotherapy; IMRT: Intensity-modulated radiotherapy; LACC: Locally advanced cervical cancer; LRF: Locoregional failure; mOS: Median overall survival; ORR: Objective response rate; OS: Overall survival; PFS: Progression-free survival; SAE: Severe adverse events; TRAE: Treatment-related adverse events.

clinical study, nivolumab is not recommended for treating patients with LACC.

- Level of evidence: Low (nivolumab)
- Grade of recommendation: Weak (nivolumab).

Cedelizumab, a humanized anti-PD-1 monoclonal antibody initially developed by a Chinese company, can be employed in the treatment of Hodgkin's lymphoma, hepatocellular carcinoma (HCC), esophageal cancer, and advanced lung cancer. A Phase II study investigating the combination of cedelizumab with CCRT in patients with LACC was presented at the 2022 ESMO congress.[17] The study outcomes were CRR, ORR, and DCR of 28% (7/25), 96.0% (24/25), and 100% (25/25), respectively. Among the immune-related adverse events, reactive capillary hyperplasia was the most prevalent (92.0%), followed by enterocolitis (80.0%) and anemia (56.0%), with severity Grades 1 – 2. Severe adverse events affected 16.0% of participants (4 out of 25). Further studies are needed to collect long-term survival data.

- Level of evidence: Low (cedelizumab)
- Grade of recommendation: Weak (cedelizumab).

Durvalumab, a humanized monoclonal antibody, targets PD-L1 to inhibit its engagement with PD-1 and CD8, thereby impeding tumor immune evasion and provoking immune responses. It is also employed as a frontline therapy for SCLC, advanced biliary tract cancer, unresectable locally advanced or metastatic bladder cancer, and advanced HCC.[18-21] A recent Phase III trial assessed the efficacy of durvalumab in treating LACC. The primary endpoint of the CALLA trial,[22] a multicenter double-blind study, was PFS in 714 patients with high-risk LACC who were randomized to receive durvalumab or placebo alongside CCRT. The 2023 follow-up data from the CALLA trial revealed that neither group achieved a median PFS. The 12-month PFS rate for the durvalumab group was 76.0% (95% CI, 71.3 – 80.0), whereas the placebo group reached 73.3% (95% CI, 68.4 – 77.5).[22] Notably, in both groups anemia (20% [76/385] with durvalumab and 15% [56/384] with placebo) and leukopenia (10% [39/385] with durvalumab vs. 13% [49/384] with placebo) were the most prevalent Grade 3 – 4 adverse events. Furthermore, serious adverse events were reported in 23% (89/385) of placebo recipients and 28% (106/384) of durvalumab recipients. The integration of immunotherapy with CCRT in treating LACC has not been endorsed based on the disappointing results of the Phase III study.

- Level of evidence: Low (durvalumab)
- Grade of recommendation: Strong (durvalumab).

Pembrolizumab is approved for managing melanoma, NSCLC, esophageal cancer, head and neck squamous carcinoma, and metastatic colorectal cancer with high microsatellite instability or deficient mismatch repair genes. In 2020, a Phase II randomized trial was performed to evaluate the safety of pembrolizumab combined with CCRT for treating LACC. Group A received pembrolizumab post-CCRT, whereas Group B received pembrolizumab plus CCRT.[23] Among 88 patients, 52 completed the treatment regimen as per the findings. Adverse events of grade ≥2 linked to therapy were noted in 88% of cases. No significant difference was found in the occurrence of grade ≥1 severe diarrhea between the two groups (63% in group A vs. 68% in group B). Notably, two patients experienced three instances of dose-limiting adverse events.

The results of the midterm analysis from a Phase III randomized controlled clinical trial investigating pembrolizumab combined with CCRT for LACC treatment were unveiled at the 2023 ESMO congress.[24] The study encompassed 1060 patients with high-risk LACC, who were diagnosed using the 2014 FIGO as having clinical stages IB2–IIB with lymph node metastases or stages III–IV irrespective of lymph node involvement, where PD-1 testing was not obligatory. The average follow-up time was 17.9 months. The trial group exhibited a 2-year PFS rate of 67.8%, whereas the control group showed 57.3% (hazard ratio [HR] = 0.70 [95% CI, 0.55–0.89; P = 0.0020]). The 2-year OS rate was 80.8% (95% CI, 74.8 – 85.5%) and 87.2% (95% CI, 82.4 – 90.8%) in the trial and control groups, respectively. Grade ≥3 adverse events occurred in 67.0% of the trial group compared with 60.0% in the control group. The Phase III trial indicated the therapeutic potential of pembrolizumab for patients with high-risk LACC, illuminating novel insights for immunotherapy in conjunction with CCRT. However, comprehensive long-term follow-up data are eagerly anticipated. Encouraging patient participation in clinical trials is crucial, and vigilance toward the adverse effects of immunotherapy in combination with CCRT is vital. The recommended administration involves 200 mg of pembrolizumab alongside CCRT every 3 weeks for five cycles, followed by 400 mg every 6 weeks for a total of 15 cycles.

- Level of evidence: high (pembrolizumab)
- Grade of recommendation: Strong (pembrolizumab)

3.3. Induction chemotherapy (IC) before CCRT in LACC

A randomized, controlled Phase III trial involving 500 patients with LACC was presented at the 2023 ESMO Congress to assess the safety and efficacy of IC preceding CCRT.[25] The average follow-up time was extended to 64 months. The study incorporated a CCRT control arm and an IC/CCRT arm (comprising 6 weeks of carboplatin plus paclitaxel at 80 mg/m^2). At 5 years, OS rates were 80% and 72% for the control and IC/CCRT groups,

respectively (HR 0.61; 95% CI, 0.40 – 0.91, $P = 0.04$), and 5-year PFS rates were 73% and 64% for the IC/CCRT and control groups, respectively (HR 0.65; 95% CI, 0.46 – 0.91, $P = 0.013$). Grade ≥3 adverse events occurred in 59% and 48% of patients in the respective groups. The findings underscored the significant enhancement in PFS and OS among patients with LACC using IC preceding CCRT, demonstrating its feasibility and clinical benefit of this treatment approach.

- Level of evidence: High
- Expert consensus: Strong.

3.4. ICIs before CCRT in LACC

Atezolizumab, a PD-L1 monoclonal antibody, was approved for treating metastatic triple-negative breast cancer, advanced bladder cancer, SCLC, and metastatic NSCLC.[26-28] Findings from a phase I trial combining atezolizumab with CCRT in patients with LACC and lymph node metastases ($n = 40$) were presented in the 2022 SGO meeting.[29] The study comprised two cohorts: (a) administering one cycle of atezolizumab before CCRT, followed by two cycles during CCRT, resulted in an ORR of 69% and a 2-year DFS rate of 79%. (b) Conversely, when three atezolizumab cycles were administered during CCRT, the ORR decreased to 40% with 2-year DFS rate of 59%. Notably, 8% of the participants experienced DLTs, including thrombocytopenia, immune-related colitis, and non-immune-associated colitis. Notably, seven patients experienced grade ≥3 adverse events. Given the trial's Phase I nature and limited sample size, the clinical outcomes were deemed low. Future studies are warranted to further explore the potential of neoadjuvant immunotherapy.

- Level of evidence: Low (atezolizumab)
- Expert consensus level: Weak (atezolizumab).

The synergistic potential of combining CTLA-4 inhibitors with PD-1 inhibitors was well-documented. PD-1 and CTLA-4 collaborate to impede T-cell activation and reduce CD28 co-stimulation. Using a combination of PD-1 and CTLA-4 inhibitors, the suppressive immunological status of effector T cells can be alleviated, diminishing the influences of regulatory T cells on T effector cells and facilitating the activation of effector T cells. In a Phase II study involving 40 patients with LACC of FIGO 2018 stages IB3-IVA, an anti-PD-1 monoclonal antibody was paired with an anti-CTLA-4 monoclonal antibody.[30] The induction regimen included a 2-week treatment plan of nivolumab (3 mg/kg on days 1 and 15) alongside ipilimumab (1 mg/kg on day 1), a CTLA-4 monoclonal antibody, and CCRT. Throughout the subsequent 6-month maintenance phase, a cumulative nivolumab dose of 480 mg was administered >28 days. The CRR was 0% after induction with ICIs, 62.5% following CCRT, and 82.5% after the study. Notably, three patients experienced grade ≥3 ICI-related adverse effects. Dual immunotherapy holds significant promise in clinical research; however, careful evaluation is imperative because of the increasing adverse events linked with combination therapies, until strong evidence of therapeutic benefit is established.

- Level of evidence: Low (nivolumab)
- Expert consensus Level: Weak (nivolumab)
- Level of evidence: Low (ipilimumab)
- Expert consensus: Weak (ipilimumab)

A prospective Phase II study of camrelizumab in the neoadjuvant setting for LACC conducted across multiple centers employed an open-label, single-arm design.[31] The study enrolled 83 patients, involving 78 subjects who underwent evaluation. The induction regimen comprised one cycle of cisplatin (75 – 80 mg/m^2, intravenously) alongside albumin-bound paclitaxel (260 mg/m^2, intravenously), followed by two cycles of camrelizumab infusion (200 mg, intravenously, every 3 weeks), separated by 3-week intervals. Patients exhibiting stable or progressive disease proceeded to CCRT, whereas those achieving PR or CR underwent radical surgery. In June 2023, the study achieved a primary endpoint ORR of 100%, in which 14 patients achieved CR (17.95%), 64 with PR (82.05%), and 30 exhibited pathological complete response (pCR, 39.47%). In addition, 17 (22.37%) patients necessitated postoperative adjuvant therapy. During IC, 35 (44.87%) patients experienced grade ≥3 adverse events. After the initial publication, data up to December 2023 revealed an ORR of 98% among 83 patients, in which 16 (19%) achieved CR and 67 (79%) demonstrated PR.[32] Lymphopenia (25%), neutropenia (12%), and leukopenia (8%) were the most prevalent grade 3 – 4 therapy-related adverse events observed during neoadjuvant chemoimmunotherapy. Notably, no severe or treatment-related fatalities were reported. The study demonstrated that the incorporation of camrelizumab with neoadjuvant chemotherapy for LACC treatment resulted in significant ORR and pCR rates, along with manageable toxicity levels, potentially reducing the necessity for postoperative adjuvant therapy. Nevertheless, the limited sample size underscores the need for further extensive clinical investigations.

- Level of evidence: Low (camrelizumab)
- Expert consensus degree: Weak (camrelizumab).

3.5. Maintenance therapy with ICIs after CCRT in patients with LACC

The NRG-GOG9929 trial[33] represented the pioneering investigations into the post-CCRT maintenance treatment of ipilimumab in patients with LACC with lymph node metastases. The trial aimed to achieve the

Table 4. Ongoing Phase II-III studies of LACC combining CCRT with targeted immunotherapy

Title	Phase	Country/region	NCT registration number
Nimotuzumab Combined with CCRT for LACC: A Randomized, Controlled, Open-Label, Multicenter Study	Phase III	Third Hospital of Peking University, China	NCT04678791
AK104/Placebo Combined with CCRT for LACC	Phase III	Peking Union Medical College Hospital, China	NCT05235516
Tislelizumab Combined with CCRT for LACC	Phase II	First Affiliated Hospital of Guangxi Medical University, China	NCT05588219
Sintilimab Combined with CCRT for LACC	Phase II	Affiliated Hospital of Xuzhou Medical University, China	NCT05105672
Tirapazamine Combined with CCRT for LACC	Phase II	Tianjin Medical University, China	NCT05084677
Carilizumab Combined with CCRT for IB2-IIIB Cervical Cancer	Phase II	Beijing, China	NCT05311566
Volrustomig/Placebo Combined with CCRT for High-Risk LACC (eVOLVE-Cervical Trial)	Phase III	AstraZeneca, United States	NCT06079671
Atezolizumab Combined with CCRT for LACC with Lymph Node Positivity	Phase I	Birmingham Cancer Center, United States	NCT03738228
Tirapazamine Combined with CCRT for LACC	Phase I	Third Hospital of Peking University, China	NCT04368273
TSR-042 as Maintenance Therapy after High-risk LACC CCRT Treatment (ATOMICC Trial)	Phase II	La Fe Hospital, Spain	NCT03833479

Source: ClinicalTrials.gov; As of November 2023.
Abbreviations: LACC: Locally advanced cervical cancer; CCRT: Concurrent chemoradiotherapy.

maximum tolerated dose and ensure safety. Among 32 enrolled participants, 21 underwent treatment. Patients received ipilimumab at two different dosages: 3 and 10 mg/kg, which were administered every 3 weeks for a total of four cycles. The study revealed that a fraction of patients faced challenges tolerating ipilimumab as a maintenance therapy post-CCRT, and 2 out of 21 patients experienced Grade 3 toxicities. The results of the Phase I trial demonstrated a 12-month PFS rate of 81% and a 12-month OS rate of 90%. Notably, a Phase I investigation indicated a significant upregulation in T-cell-inducible co-stimulatory factor expression, whereas CCRT induced an increase in PD-1 expression in both CD4+ and CD8+ T cells. Moreover, the study hinted at radiation therapy triggering immunogenic cell death, potentially enhancing T-cell activation.[33]

The best maintenance therapy after CCRT is still debated and no clear consensus has been reached on whether immune-targeted therapy, targeted therapy, or immunotherapy should be utilized.

- Level of evidence: Low (ipilimumab)
- Expert consensus: Weak (ipilimumab).

3.6. Current clinical studies on CCRT combined with targeted immunotherapy in LACC

In November 2023, nine Phase I–III clinical trials were listed as investigational on ClinicalTrials.gov. Notably, Phase III studies for cardenolide, volrustomig, and nimotuzumab are ongoing. Cardenolide and volrustomig are PD-1/CTLA-4 dual antibodies, whereas nimotuzumab is the only targeted agent being evaluated in an ongoing Phase III trial (Table 4).

4. Conclusion

This consensus synthesizes evidence-based medical data regarding the use of targeted and immunological agents in conjunction with CCRT for LACC management. However, some limitations must be addressed. Regarding targeted agents, all clinical studies were either Phase II trials or meta-analyses. Conversely, in immunotherapy, two were Phase III clinical studies; however, their findings exhibited inconsistency. The evolutionary nature of evidence-based medicine presents that the current treatment landscape may evolve with ongoing advancements. After multiple rounds of thorough review and refinement, the expert consensus committee synthesized the current clinical research with practical clinical applications. They presented a consensus on the level and degree of available evidence, which resulted in the creation of this comprehensive consensus framework.

Acknowledgments

None.

Funding

This consensus was supported by the Key Specialization Project of Beijing Natural Science Foundation (Grant No. Z2008), the Clinical Scientist Training Program at Peking University (Grant No. BMU2023PYJH009), Clinical Key Project Innovation Project Class A at the Third Hospital of Peking University (Grant No. BYSYZD2021011), and the National Clinical Key Specialization Construction Project Special Fund (2021).

Conflict of interest

Junjie Wang is the Editor-in-Chief and Ping Jiang is the Editorial Board Member of this journal, but was not in any way nvolved in the editorial and peer-review process conducted for this paper, directly or indirectly. Separately, other authors declared that they have no known competing financial interests or personal relationships that could have influenced the work reported in this paper.

Author contributions

Conceptualization: Junjie Wang, Ping Jiang, Zi Liu, Yunyan Zhang
Writing–original draft: Ping Jiang, Zhuhui Yuan
Writing–reviewing & editing: All authors

Ethics approval and consent to participate

Not applicable.

Consent for publication

Not applicable.

Availability of data

Data for this study can be obtained from the cited original articles.

References

1. National Cancer C, Cervical Cancer Expert Committee of National Cancer Quality Control C. Quality control index for standardized diagnosis and treatment of cervical cancer in China (2022 edition). *Zhonghua Zhong Liu Za Zhi*. 2022;44(7):615-622.

   doi: 10.3760/cma.j.cn112152-20220511-00328

2. Erratum: Global cancer statistics 2018: GLOBOCAN estimates of incidence and mortality worldwide for 36 cancers in 185 countries. *CA Cancer J Clin*. 2020;70(4):313.

   doi: 10.3322/caac.21609

3. Singh D, Vignat J, Lorenzoni V, *et al*. Global estimates of incidence and mortality of cervical cancer in 2020: A baseline analysis of the WHO Global Cervical Cancer Elimination Initiative. *Lancet Glob Health*. 2023;11(2):e197-e206.

   doi: 10.1016/S2214-109X(22)00501-0

4. Monk BJ, Tan DSP, Hernandez Chagui JD, *et al*. Proportions and incidence of locally advanced cervical cancer: A global systematic literature review. *Int J Gynecol Cancer*. 2022;32(12):1531-1539.

   doi: 10.1136/ijgc-2022-003801

5. Liu H, Ma X, Sun C, *et al*. Concurrent chemoradiotherapy followed by adjuvant chemotherapy versus concurrent chemoradiotherapy alone in locally advanced cervical cancer: A systematic review and meta-analysis. *Front Oncol*. 2022;12:997030.

   doi: 10.3389/fonc.2022.997030

6. Gustafson DH, Shukla RK, Delbecq A, Walster GW. A comparative study of differences in subjective likelihood estimates made by individuals, interacting groups, Delphi groups, and nominal groups. *Organ Behav Hum Perform*. 1973;9(2):280-291.

   doi: 10.1016/0030-5073(73)90052-4

7. Gallego D, Bueno S. Exploring the application of the Delphi method as a forecasting tool in information systems and technologies research. *Technol Anal Strateg Manag*. 2014;26(9):987-999.

   doi: 10.1080/09537325.2014.941348

8. Schefter T, Winter K, Kwon JS, *et al*. RTOG 0417: Efficacy of bevacizumab in combination with definitive radiation therapy and cisplatin chemotherapy in untreated patients with locally advanced cervical carcinoma. *Int J Radiat Oncol Biol Phys*. 2014;88(1):101-105.

   doi: 10.1016/j.ijrobp.2013.10.022

9. Lu H, Wu Y, Liu X, *et al*. Endostar, an antiangiogenesis inhibitor, combined with chemoradiotherapy for locally advanced cervical cancer. *Oncol Res*. 2022;28(9):929-944.

   doi: 10.3727/096504021X16318716607908

10. Shu H, Dong Y, Xu Z, *et al*. The efficacy and safety of continuous intravenous endostar treatment combined with concurrent chemoradiotherapy in patients with locally advanced cervical squamous cell carcinoma: A randomized controlled trial. *Front Oncol*. 2021;11:723193.

    doi: 10.3389/fonc.2021.723193

11. De la Rochefordiere A, Kamal M, Floquet A, *et al*. PIK3CA pathway mutations predictive of poor response following standard radiochemotherapy ± cetuximab in cervical cancer patients. *Clin Cancer Res*. 2015;21(11):2530-2537.

    doi: 10.1158/1078-0432.CCR-14-2368

12. Fracasso PM, Duska LR, Thaker PH, *et al*. An exploratory study of neoadjuvant cetuximab followed by cetuximab and chemoradiotherapy in women with newly diagnosed locally

advanced cervical cancer. *Am J Clin Oncol*. 2022;45(7): 286-293.

doi: 10.1097/COC.0000000000000926

13. Wang J, Jiang P, Wei L, *et al*. 759P Nimotuzumab combined with concurrent chemo-radiotherapy in patients with locally advanced cervical squamous cell carcinoma: A randomized, controlled, open-label, multicenter study. *Ann Oncol*. 2023;34:S518-S519.

14. Qu A, Wang J, Zhuo Y, *et al*. 760P Efficacy and safety of nimotuzumab plus radiotherapy for elderly patients with locally advanced cervical squamous cell carcinoma. *Ann Oncol*. 2023;34:S519.

15. Yuan Y, Chen J, Fang M, *et al*. Nimotuzumab combined with chemoradiotherapy for the treatment of cervical cancer: A meta-analysis of randomized controlled trials. *Front Oncol*. 2022;12:994726.

doi: 10.3389/fonc.2022.994726

16. Rodrigues M, Vanoni G, Loap P, *et al*. Nivolumab plus chemoradiotherapy in locally-advanced cervical cancer: The NICOL phase 1 trial. *Nat Commun*. 2023;14(1):3698.

doi: 10.1038/s41467-023-39383-8

17. Xiao Y, Cheng H, Wang L, Yang L, Yu X. 562P Camrelizumab plus concurrent chemoradiotherapy for locally advanced cervical cancer: Preliminary results of a single-arm, open-label, phase II trial. *Ann Oncol*. 2022;33:S805.

18. Patel TH, Brewer JR, Fan J, *et al*. FDA approval summary: Tremelimumab in combination with durvalumab for the treatment of patients with unresectable hepatocellular carcinoma. *Clin Cancer Res*. 2024;30(2):269-273.

doi: 10.1158/1078-0432.CCR-23-2124

19. Powles T, van der Heijden MS, Castellano D, *et al*. Durvalumab alone and durvalumab plus tremelimumab versus chemotherapy in previously untreated patients with unresectable, locally advanced or metastatic urothelial carcinoma (DANUBE): A randomised, open-label, multicentre, phase 3 trial. *Lancet Oncol*. 2020;21(12): 1574-1588.

doi: 10.1016/S1470-2045(20)30541-6

20. Oh DY, Ruth He A, Qin S, *et al*. Durvalumab plus gemcitabine and cisplatin in advanced biliary tract cancer. *NEJM Evid*. 2022;1(8).

doi: 10.1056/EVIDoa2200015

21. Paz-Ares L, Dvorkin M, Chen Y, *et al*. Durvalumab plus platinum-etoposide versus platinum-etoposide in first-line treatment of extensive-stage small-cell lung cancer (CASPIAN): A randomised, controlled, open-label, phase 3 trial. *Lancet*. 2019;394(10212):1929-1939.

doi: 10.1016/S0140-6736(19)32222-6

22. Monk BJ, Toita T, Wu X, *et al*. Durvalumab versus placebo with chemoradiotherapy for locally advanced cervical cancer (CALLA): A randomised, double-blind, phase 3 trial. *Lancet Oncol*. 2023;24(12):1334-1348.

doi: 10.1016/S1470-2045(23)00479-5

23. Duska LR, Scalici JM, Temkin SM, *et al*. Results of an early safety analysis of a study of the combination of pembrolizumab and pelvic chemoradiation in locally advanced cervical cancer. *Cancer*. 2020;126(22):4948-4956.

doi: 10.1002/cncr.33136

24. Lorusso D, Xiang Y, Hasegawa K, *et al*. LBA38 Pembrolizumab plus chemoradiotherapy for high-risk locally advanced cervical cancer: A randomized, double-blind, phase III ENGOT-cx11/GOG-3047/KEYNOTE-A18 study. *Ann Oncol*. 2023;34:S1279-S1280.

25. McCormack M, Rincón DG, Eminowicz G, *et al*. LBA8 A randomised phase III trial of induction chemotherapy followed by chemoradiation compared with chemoradiation alone in locally advanced cervical cancer: The GCIG INTERLACE trial. *Ann Oncol*. 2023;34:S1276.

26. Herbst RS, Giaccone G, de Marinis F, *et al*. Atezolizumab for first-line treatment of PD-L1-selected patients with NSCLC. *N Engl J Med*. 2020;383(14):1328-1339.

doi: 10.1056/NEJMoa1917346

27. Emens LA, Adams S, Barrios CH, *et al*. First-line atezolizumab plus nab-paclitaxel for unresectable, locally advanced, or metastatic triple-negative breast cancer: IMpassion130 final overall survival analysis. *Ann Oncol*. 2021;32(8):983-993.

doi: 10.1016/j.annonc.2021.05.355

28. Powles T, Duran I, van der Heijden MS, *et al*. Atezolizumab versus chemotherapy in patients with platinum-treated locally advanced or metastatic urothelial carcinoma (IMvigor211): A multicentre, open-label, phase 3 randomised controlled trial. *Lancet*. 2018;391(10122): 748-757.

doi: 10.1016/S0140-6736(17)33297-X

29. Mayadev J, Zamarin D, Deng W, *et al*. Safety and immunogenicity of anti PD-L1 (Atezolizumab) given as an immune primer or concurrently with extended field chemoradiotherapy for node positive locally advanced cervical cancer: An NRG oncology trial (024). *Gynecol Oncol*. 2022;166:S18-S19.

doi: 10.1016/S0090-8258(22)01242-2

30. Ray-Coquard IL, Kaminsky-Forrett MC, Ohkuma R, *et al*. *In situ* immune impact of nivolumab + ipilimumab combination before standard chemoradiation therapy (RTCT) for FIGO IB3-IVA in patients (pts) with cervical squamous carcinoma: COLIBRI trial, a GINECO study. *J Clin Oncol*. 2023;41:5501.

doi: 10.1200/JCO.2023.41.16_suppl.5501

31. Chen J, Han Y, Hu Y, *et al.* Neoadjuvant camrelizumab plus chemotherapy for locally advanced cervical cancer (NACI Study): A study protocol of a prospective, single-arm, phase II trial. BMJ Open 2023;13(5):e067767.

doi: 10.1136/bmjopen-2022-067767

32. Li K, Chen J, Hu Y, *et al*. Neoadjuvant chemotherapy plus camrelizumab for locally advanced cervical cancer (NACI study): A multicentre, single-arm, phase 2 trial. *Lancet Oncol*. 2024;25(1):76-85.

doi: 10.1016/S1470-2045(23)00531-4

33. Mayadev JS, Enserro D, Lin YG, *et al*. Sequential ipilimumab after chemoradiotherapy in curative-intent treatment of patients with node-positive cervical cancer. *JAMA Oncol*. 2020;6(1):92-99.

doi: 10.1001/jamaoncol.2019.3857

ACCSCIENCE PUBLISHING

Advances in Radiotherapy & Nuclear Medicine

REVIEW ARTICLE

Targeting EZH2 to mitigate immune checkpoint resistance in *ARID1A*-deficient triple-negative breast cancer

Lauren Lukas[1]*, Hye Ri Han[1], Evanthia T. Roussos Torres[2], Aaron G. Baugh[2], Oliver Bell[3], Jason C. Ye[1], Kenneth Wong[1], Vyshnavi Pachipulusu[4], Hualin Zhang[1], and Alan L. Epstein[4]

[1]Department of Radiation Oncology, Norris Comprehensive Cancer Center, Keck School of Medicine, University of Southern California, Los Angeles, California, United States of America

[2]Department of Medicine, Division of Medical Oncology, Norris Comprehensive Cancer Center, Keck School of Medicine, University of Southern California, Los Angeles, California, United States of America

[3]Department of Biochemistry and Molecular Medicine, Keck School of Medicine, University of Southern California, Los Angeles, California, United States of America

[4]Department of Pathology, Keck School of Medicine, University of Southern California, Los Angeles, California, United States of America

(This article belongs to the *Special Issue: Novel developments in cancer therapy utilizing combinatorial approaches of radiotherapy and immunotherapy*)

***Corresponding author:**
Lauren Lukas
(llukas@usc.edu)

Citation: Lukas L, Han HR, Torres ETR, *et al*. Targeting EZH2 to mitigate immune checkpoint resistance in *ARID1A*-deficient triple-negative breast cancer. *Adv Radiother Nucl Med*. 2025;3(1):28-45. doi: 10.36922/arnm.5132

Received: October 13, 2024

1st revised: December 11, 2024

2nd revised: December 24, 2024

Accepted: December 25, 2024

Published online: January 16, 2025

Abstract

Immune checkpoint inhibitors (ICIs) have shown promise in treating triple-negative breast cancer (TNBC), but resistance to these therapies remains a significant challenge. AT-rich interactive domain 1A (*ARID1A*), a component of the SWItch/Sucrose Non-Fermentable chromatin remodeling complex, is frequently mutated in TNBC and is associated with increased programmed cell death ligand 1 expression, which contributes to immune evasion. Paradoxically, this mutation may make TNBC potentially more responsive to ICIs. Chromatin-mediated gene expression requires a balance between *ARID1A* and enhancer of zeste homolog 2 (EZH2), a histone methyltransferase, and *ARID1A* deficiency results in enhanced EZH2 activity, contributing to various oncologic processes. Epigenetic modulation through EZH2 inhibition could exploit the synthetic lethality between *ARID1A* deficiency and EZH2 activity, which may reduce the immunosuppressive tumor microenvironment and enhance infiltration and activity of cytotoxic T-cells within the tumor, thereby synergizing with immune checkpoint inhibition. This review explores the potential of EZH2 inhibition as a therapeutic strategy to overcome immune checkpoint resistance in *ARID1A*-deficient TNBC. In addition, the role of *ARID1A* deficiency as a radiosensitizer is also discussed in the context of combination therapy strategies.

Keywords: Epigenetic; Immunotherapy; Triple-negative breast cancer; Combination therapy; Radiotherapy

1. Background

Triple-negative breast cancer (TNBC) is defined by the absence of estrogen receptor and progesterone receptor expression, as well as the amplification of the human epithelial growth factor receptor 2. TNBC is a heterogeneous disease comprising subtypes such as basal-like (BL1 and BL2), mesenchymal (M), and luminal androgen receptors.[1] Each TNBC subtype is associated with different transcriptional patterns and immune cell compositions. Notably, M-subtype tumors exhibit high mutational loads, genomic instability, lack of immune cells, low programmed cell death ligand 1 (PD-L1) expression, decreased global DNA methylation, and transcriptional repression of genes responsible for antigen presentation.[1] The presence of immune cells has been associated with survival; tumors with fewer immune cells have displayed a trend toward shorter progression-free intervals, whereas tumors with greater stromal immune cells have shown a lower risk of recurrence.[1-3] Variations in immune cell composition and genetic susceptibilities specific to different subtypes indicate potential new treatment approaches for TNBC to enhance the efficacy of immunotherapy.[1] For example, deletions of DNA repair genes and members of the BRG1-associated factors, SWItch/Sucrose Non-Fermentable (SWI/SNF) complex, are more commonly observed in M-subtype TNBC tumors.[1] The SWI/SNF complex regulates chromatin structure and is one of the most frequently mutated protein complexes in human cancers.[4,5] It has also been found that SWI/SNF has a role in regulating anti-tumor immunity.[6] Research indicates approximately 30% of breast tumors exhibit genetic alterations in one or more SWI/SNF subunits, such as the AT-rich interactive domain 1A gene (*ARID1A*), and these gain- and loss-of-function mutations are linked to the initiation and progression of cancer.[4] Low expression levels of *ARID1A* are found in 78% of TNBCs and are associated with poor prognosis.[4,7] The loss of *ARID1A* expression presents a challenge for therapeutic targeting, highlighting the necessity to uncover therapeutic vulnerabilities in *ARID1A*-deficient tumors.[6] *ARID1A* deficiency has been shown to variably enhance PD-L1 expression, but the overall impact on immune cell populations can vary. While *ARID1A* deficiency may promote an immune response, it does not guarantee an increase in tumor-infiltrating lymphocytes (TILs) across all tumor types.[8,9] For example, Sun *et al.*[10] demonstrated increased infiltration of $CD4^+$ T cells and Th17 cells, along with enhanced CD8 effector and antigen presentation signatures in *ARID1A*-deficient gastric cancer.[10] Conversely, Jung *et al.*[11] found that low *ARID1A* expression was associated with decreased CD8 T-cell infiltration in ovarian clear cell carcinoma, suggesting that blocking PD-L1 is unlikely to result in a T-cell response.[11] Table 1 lists key clinical studies of immunotherapy in *ARID1A*-deficient tumors.

Although the effectiveness of immune checkpoint inhibitors (ICIs) in breast cancer is less pronounced than that seen in other tumor types, and most patients with TNBC ultimately develop resistance to these agents,[12] *ARID1A*-deficiency in TNBC has been shown to increase chromatin accessibility and gene expression of nucleophosmin 1, which in turn further activates PD-L1 transcription.[13] Elevated PD-L1 levels could render this subgroup more responsive to ICIs; however, *ARID1A* deficiency was also found to inhibit $CD8^+$ T cells, contributing to adaptive immune resistance in TNBC.[13] Using xenograft models, Chen *et al.*[13] demonstrated that TNBC with low *ARID1A* expression-induced PD-L1 elevation was associated with reduced tumor volume and pulmonary metastasis when treated with atezolizumab (anti-PD-L1), compared to *ARID1A*-high TNBC. This occurred despite insufficient anti-tumor immune infiltrates, especially $CD8^+$ T cells.[13] Notably, atezolizumab significantly increased the $CD45^+CD8^+$ T-cell population in the *ARID1A*-deficient tumors.[13] Tumor tissues from patients with metastatic TNBC treated with pucotenlimab (anti-PD-1) with gemcitabine and cisplatin were analyzed for *ARID1A* deficiency and PD-L1 expression as part of the CTR20191353 clinical trial.[13] Kaplan–Meier progression-free survival (PFS) analysis based on *ARID1A* and PD-L1 expression demonstrated that patients with low *ARID1A* expression had significantly longer PFS.[13] The longest PFS observed was 615 days in the *ARID1A*-low/PD-L1-high subgroup.[13]

Given these findings of PD-L1 elevation but low anti-tumor immune infiltrates, exploration of combination therapies to further enhance the effects of ICIs in *ARID1A*-deficient TNBC through immune stimulation is warranted. Therapeutic strategies for *ARID1A*-mutant breast cancer include inhibition of enhancer of zeste homolog 2 (EZH2).[4] EZH2 is an enzymatic catalytic subunit of polycomb repressive complex 2 (PRC2), one of two main polycomb group complexes that mediate gene silencing mainly through modulating chromatin structure.[14-16] EZH2 induces trimethylation of lysine 27 of histone H3 (H3K27me3)[17] and deposition of H3K27me3 at target genes signals for polycomb repressive complex 1 recruitment, which in turn enforces transcriptional silencing through compaction of chromatin.[18] Targeting epigenetic regulators such as EZH2 may enhance tumor immunogenicity, improve immune cell function, and modulate the immunosuppressive tumor microenvironment (TME) to synergize with immunotherapy.[19] EZH2 contributes to cancer progression through various mechanisms,

Table 1. Key clinical studies of immunotherapy in AT-rich interactive domain 1A-deficient tumors

Reference	Tumor type	Study design	Key findings
Chen *et al.*[13]	TNBC	Cohort study	Kaplan–Meier PFS analysis based on *ARID1A* and PD-L1 expression demonstrated that patients with low *ARID1A* expression had a significantly longer PFS
Duran *et al.*[117]	Metastatic lung adenocarcinoma with *ARID1A* mutations	Case report	19-month partial response maintained with nivolumab
Goswami *et al.*[118]	Metastatic urothelial carcinoma	Cohort study	*ARID1A* mutation and CXCL13 expression as combinatorial biomarkers in baseline tumor tissues suggested improved OS compared to either single biomarker from immunotherapy
Li *et al.*[119]	Gastrointestinal cancer	Cohort study	Improved OS with immunotherapy in *ARID1A*-mutated cancers versus *ARID1A*-wildtype cancers
Pignata *et al.*[120]	Advanced endometrial cancer	Pre-planned transitional analysis of the MITO END-3 randomized trial	Improved treatment effect with avelumab with *ARID1A* mutation
Sun *et al.*[8]	NSCLC	Cohort study	More responders (CR+PR+SD) with *ARID1A* mutation (50 vs. 19%, *P*=0.045); trend for median survival with *ARID1A* mutation (6.8 vs. 5.5 months, *P*=0.313)
Sun *et al.*[10]	Gastric cancer	Cohort study	*ARID1A*-deficiency associated with improved OS with immunotherapy (HR: 0.39; 95% CI: 0.15 – 0.98, *P*=0.044)
Zhou *et al.*[121]	Solid tumors (gastric, endometrial, NSCLC, cholangiocarcinoma, esophageal, urothelial, ovarian, colon, breast, and pancreatic cancer)	Retrospective study	*ARID1A* mutations (majority inactivating) associated with longer median overall survival after immunotherapy (51 vs. 41 months)

Abbreviations: *ARID1A*: AT-rich interactive domain 1A; CI: Confidence interval; CR: Complete response; HR: Hazard ratio; NSCLC: Non-small cell lung carcinoma; OS: Overall survival; PD-L1: Programmed cell death ligand 1; PFS: Progression-free survival; PR: Partial response; SD: Stable disease; TNBC: Triple-negative breast cancer.

including mutations antagonizing the SWI/SNF chromatin remodeling complex.[20] This contribution raises the possibility of synthetic lethality, as both *ARID1A* and EZH2 can silence the PI3K-interacting protein 1 gene (*PIK3IP1*) and subsequently promote cell proliferation and anti-apoptotic effects through PI3K/AKT signaling.[20] Low *ARID1A* expression leads to unbalanced EZH2 activity, which is hypothesized to drive tumorigenesis.[20] Inhibition of EZH2 has been shown to upregulate PIK3IP1 expression in *ARID1A*-deficient ovarian cancer cells, thereby suppressing cell growth by inhibiting PI3K/AKT signaling as depicted in Figure 1.[21]

2. Enhancer of zeste homolog 2 in TNBC

Epigenetic modulations in TNBC encompass several key processes: DNA methylation (inactivation of gene transcription), hypomethylation (gene activation), histone acetylation (transcriptional activation), and histone methylation (transcriptional inhibition).[16] Histone methylation is modulated by methyltransferases, such as EZH2. High expression of EZH2 has been found across various cancer types, including breast, prostate, bladder, colon, lung, pancreas, sarcoma, and lymphoma, and is strongly associated with the TNBC phenotype.[22,23] In breast cancer, EZH2 overexpression promotes initiation, invasion, and metastasis.[24] Studies using human breast tissue samples have shown that EZH2 expression is low in normal epithelium but increases with the degree of atypia.[24] EZH2 levels increase progressively from atypical ductal hyperplasia to ductal carcinoma *in situ* and invasive carcinomas, with the highest expression observed in distant metastases.[25] High levels of EZH2 in primary breast carcinomas are significantly linked to estrogen receptor-negative status, which is indicative of poor tumor differentiation and acts as an independent biomarker for patient survival.[24]

The canonical mechanism by which EZH2 contributes to cancer development and progression is primarily attributed to H3K27me3-mediated transcriptional silencing; however, non-canonical functions of EZH2 have also been reported.[24] Imbalances in methyltransferases, such as EZH2, can lead to histone methylation dysregulation, which subsequently alters chromatin structure and gene expression.[16] Enhanced EZH2 activity has been associated with tumor cell proliferation and metastasis in various subtypes of breast cancer through the

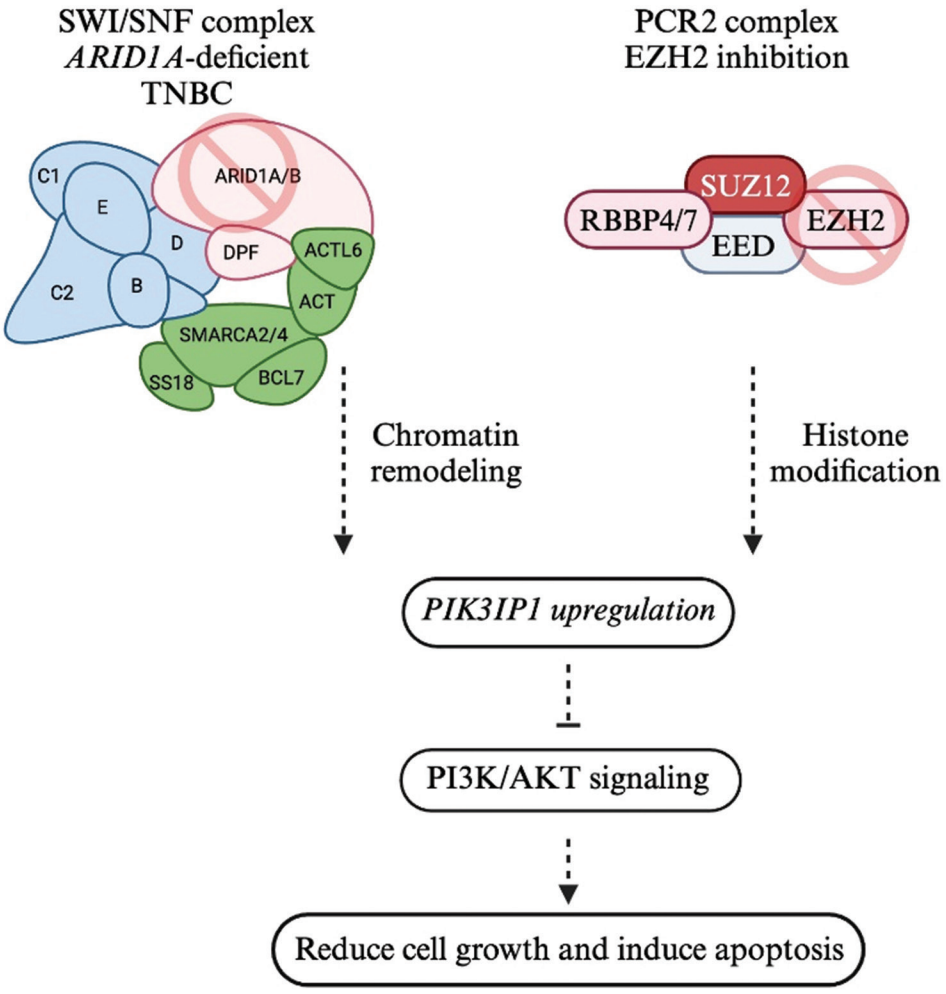

Figure 1. Enhancer of zeste homolog 2 (EZH2) and AT-rich interactive domain 1A (*ARID1A)* synthetic lethality. Synthetic lethality is due to antagonistic roles played by methyltransferase EZH2 and chromatin remodeler SWI-like gene *ARID1A*, in regulating target gene *PIK3IP1*.[21] In the context of *ARID1A* mutation, *PIK3IP1* is upregulated by EZH2 inhibition and contributes to synthetic lethality by inhibiting PI3K/AKT signaling.[21] Created in BioRender by Lukas, L. (https://BioRender.com/y06c279).

silencing of tumor suppressor genes, such as *RUNX3*,[16,26] *FOXC1* in luminal B breast cancer,[16,27] *FOXO3*,[16,28,29], and *CDKN1c*, also known as p57.[16,28,30] In TNBC, EZH2-mediated H3K27me3 gene silencing includes repression of *TIMP2* transcription, resulting in increased activity of matrix metalloproteinase 2 and matrix metalloproteinase 9, which enhances the invasive capacity of TNBC cells.[22] EZH2 also suppresses the epithelial-mesenchymal transition suppressor gene *CDH1*.[31] In addition, EZH2-mediated epigenetic inactivation of FOSB promotes TNBC cell proliferation by inactivating the p53 pathway.[32] EZH2 accelerates cell invasion through transcriptional silencing of the metastasis suppressor Raf-1 kinase inhibitor protein.[31] Overexpression of EZH2 increases the level of H3K27me3 and inhibits expression of *FOXC1*.[33] Although TNBC cell lines with low *FOXC1* expression were reported to be more sensitive to doxorubin,[33] simultaneous delivery of EZH2-targeting siRNA by vortex magnetic nanorods – potentially increasing *FOXC1* expression – synergistically improved doxorubicin efficacy in TNBC.[34] Although EZH2-mediated silencing of genes is the typical mechanism of the PRC2 complex, H3K27me3 can also be associated with transcriptional upregulation.[35] EZH2 promotes *KRT14* transcription by attenuating the binding of repressor SP1 to its promoter, thereby facilitating TNBC migration, invasion, and peritoneal metastasis.[35] Examples of EZH2-mediated H3K27me3 transcriptional silencing in TNBC are shown in Figure 2.

Beyond its H3K27me3-mediated effects on gene transcription through its role within the PRC2 complex, EZH2 has also been identified as a transcriptional activator of several genes.[36,37] In TNBC, these non-canonical effects

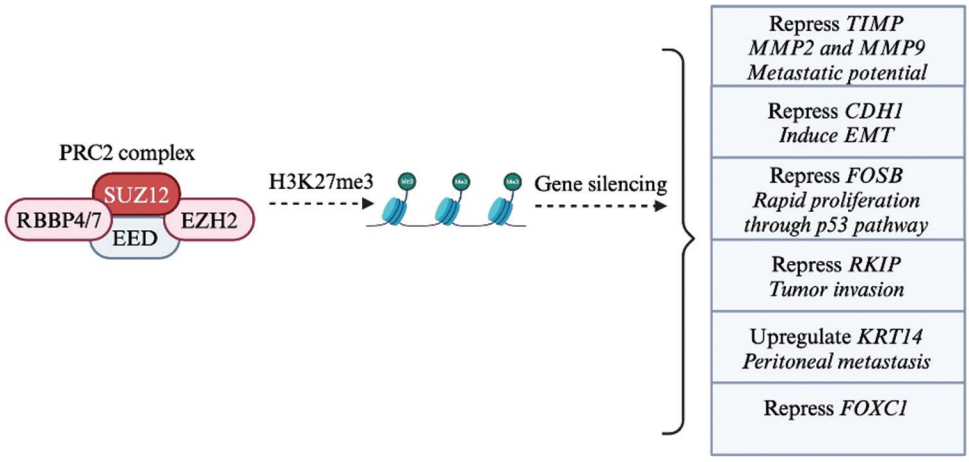

Figure 2. Enhancer of zeste homolog 2 (EZH2)-mediated H3K27me3 gene transcription. The polycomb repressive complex 2 complex consists of the core proteins EZH2, embryonic ectoderm development (EED), suppressor of zeste 12 (SUZ12), and retinoblastoma binding protein 4 and 7 (RBBP4/7).[122] Gene silencing in triple-negative breast cancer (TNBC) through EZH2-mediated H3K27me3 includes repression of tissue inhibitor of metalloproteinase 2 (*TIMP2)* transcription, which results in increased activity of matrix metalloproteinase 2 (MMP-2) and matrix metalloproteinase 9 (MMP-9) with a subsequent increased invasive activity of TNBC cells.[22] EZH2 suppresses epithelial-mesenchymal transition suppressor gene *CDH1*.[31] EZH2-mediated epigenetic inactivation of FOSB promotes TNBC cell proliferation by inactivating the p53 pathway.[32] EZH2 accelerates cell invasion, at least in part, through transcriptional repression of the metastasis suppressor Raf-1 kinase inhibitor protein (*RKIP)*.[31] EZH2 promotes keratin-14 (*KRT14*) transcription by attenuating the binding of repressor SP1 to its promoter, which promotes TNBC migration, invasion, and peritoneal metastasis.[35] Overexpression of EZH2 increases the level of H3K27me3 and inhibits the expression of forkhead box C1 (*FOXC1*).[33] Created in BioRender by Lukas, L (https://BioRender.com/q82a381).

include interaction with RelA/p65 and RelB subunits of nuclear factor-kappa B to activate the transcription of cytokines, such as TNF and IL6.[36,37] EZH2's transcriptional activation of RelB in TNBC has been shown to contribute to the maintenance of tumor-initiating cells.[36] It is hypothesized that EZH2 promotes breast cancer stem cells through the methylation and activation of STAT3.[36] EZH2 has been found to suppress the expression of transcription factor GATA3 and pro-apoptotic BH3-only protein BMF, thereby protecting TNBC cells from luminal differentiation and cell death.[38] Gonzalez *et al.*[24] identified reciprocal mechanistic cooperation between EZH2 and p38α, which promotes the growth and metastasis of TNBC.[24] EZH2 methylates p38a, increasing its protein stability and activity in TNBC.[24] This finding demonstrates that EZH2 functions not only through H3K27me3-mediated transcriptional silencing but also through direct methylation of the protein p38a.[24]

Tazemetostat, an EZH2 inhibitor that blocks the methyltransferase activity by competing with the methyl donor S-adenosyl-L-methionine (SAM),[39] was FDA-approved for the treatment of epithelioid sarcoma and follicular lymphoma.[40,41] However, despite its efficacy in preventing therapy relapse in lymphomas, other clinical trials showed minimal impact of treatment with tazemetostat and other catalytic inhibitors on solid tumors.[42] One notable study by Verma *et al.*[35] specifically evaluated the impact of tazemetostat on TNBC migration and metastasis and found that tazemetostat significantly inhibited the migration and invasion of TNBC cells *in vitro*. Furthermore, *in vivo* experiments demonstrated that tazemetostat treatment led to a marked reduction in peritoneal metastasis in mouse models, indicating its potential to suppress metastatic spread in solid tumors.[35] A phase II study of Tazemetostat in solid tumors harboring an *ARID1A* mutation is currently enrolling participants (NCT05023655).

Enhancers of zeste homolog 2 inhibitors, such as tazemetostat, do not affect the intrinsic protein stability of EZH2, but instead affect the catalytic ability of EZH2 by competing with the cofactor SAM and binding to the SET domain of EZH2.[42] However, in most solid tumors, the EZH2 protein itself, in addition to its role in H3K27me3-dependent growth and proliferation, is also involved in tumor proliferation.[42] Consequently, while EZH2 inhibitors have shown efficacy in certain malignant blood tumors, their effectiveness against solid tumors such as TNBC remains limited.[42] To block the proliferation of TNBC cells and inhibit primary tumor growth, it may be necessary to reduce EZH2 protein levels rather than solely inhibit its methyltransferase activity.[43] Wang *et al.*[42] found that although EZH2 is over-expressed in TNBC cells compared to normal breast cells, the anti-proliferative effect of EZH2 inhibitors on TNBC cells was minimal.[42] While these inhibitors can effectively reduce H3K27me3 repressive marks, they do not inhibit the proliferation

of most breast cancer cells because total EZH2 protein levels remain unaffected. This observation suggests that the expression of the EZH2 protein itself, rather than its methyltransferase activity, may be crucial for the occurrence and development of breast cancer, including TNBC.[42] Therefore, designing degradation molecules that selectively reduce EZH2 protein levels may offer an effective treatment strategy for EZH2-dependent tumors such as TNBC.[42] MS1943, an EZH2 selective degrader, has been shown to suppress TNBC tumor growth *in vivo*.[43] Combining enzymatic inhibition and depletion or degradation of EZH2 is another potential strategy for treating TNBC with high EZH2 expression. Mei *et al.*[44] showed that IHMT-337, an irreversible inhibitor of EZH2, exerts its effects through covalent modification of the EZH2 protein, leading to a sustained inhibition of its methyltransferase activity.[44] This inhibition results in the downregulation of target genes associated with cell proliferation and survival, particularly those involved in regulating cyclin-dependent kinase 4 transcription, thus highlighting the therapeutic potential of inhibiting both catalytic and non-catalytic function of EZH2 through protein degradation.[44] IHMT-337 and EPZ6438 were assessed for effects on TNBC cell line proliferation, and IHMT0337 was found to robustly suppress TNBC cell growth, whereas EPZ6438 had little to no effect on cell proliferation.[44] In pre-clinical models, both *in vitro* and *in vivo*, IHMT-337 inhibited TNBC cell proliferation.[44] Although inhibitors of methyltransferase activity of EZH2, such as Tazemetostat, may not be as effective in inhibiting TNBC cell proliferation, there remains merit in investigating combination strategies. Mei *et al.*[44] found that residual H3K27me3 persists after knockout of endogenous EZH2,[44] supporting other reports that EZH1 can target a subset of EZH2-regulated genes.[45] This functional redundancy allows EZH1 to partially compensate for the loss of EZH2.[46,47] Thus, combining an EZH2 inhibitor with an ICI may be a promising therapeutic strategy.[44]

3. Immune effects of enhancer of zeste homolog 2

Epigenetic dysregulation can affect the TME, influencing immune cell composition, cytokine signaling, and expression of immune checkpoints, ultimately contributing to immune evasion.[16] EZH2 plays a pivotal role in modulating immune cells and tumor cells within the TME, as shown in Figure 3. Anti-tumor immunity is driven by two main types of T cells: major histocompatibility complex class I (MHC-I)-restricted CD8$^+$ cytotoxic T cells and MHC-II-restricted CD4$^+$ helper T cells.[39] CD8$^+$ T cells release cytotoxic molecules, such as granzyme B and perforin, to directly kill tumor cells, whereas CD4$^+$ T cells secrete various cytokines, including

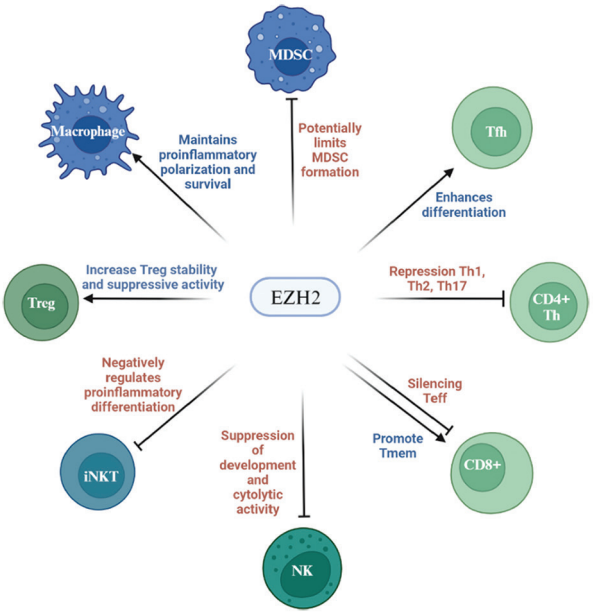

Figure 3. Enhancer of zeste homolog 2 (EZH2) immune effects. EZH2 mainly reduces anti-tumor immune cell effects within the tumor microenvironment. EZH2 restricts T helper (Th) subsets Th1, Th2, and Th17, promotes T follicular (Tfh) differentiation and function, and promotes CD4$^+$ T regulatory (Treg) stability and suppressive activity.[123] EZH2 promotes CD8$^+$ T memory (Tmem) precursors while reducing CD8$^+$ T effector (Teff) function.[123] EZH2 inhibits natural killer (NK) cells and negatively regulates invariant natural killer T cells (iNKT).[123] EZH2 maintains pro-inflammatory macrophage polarization and survival and potentially limits myeloid-derived suppressor cell (MDSC) formation.[123] Created in BioRender by Lukas, L. (https://BioRender.com/o93d285).

interferon-gamma (IFN-γ), tumor necrosis factor-alpha (TNF-α), and interleukin 2 (IL-2), to promote cytotoxic T-cell and natural killer (NK) cell anti-tumor responses.[9,13] EZH2-dependent gene silencing influences the effector differentiation status of T helper cell subsets and CD8$^+$ T cells following antigen stimulation.[48] Furthermore, EZH2 activity inhibits the differentiation and function of NK cells, indicating that targeting EZH2 could enhance both adaptive and innate cancer immunotherapy.[49]

In CD4$^+$ T cells, EZH2 binds to genes encoding the transcription factors T-bet, EOMES, and GATA3, restricting the differentiation and plasticity of T helper (Th) cells.[39] Loss of EZH2 results in increased Th1 and Th2 polarization[39] and promotes T-cell infiltration by enhancing the expression of chemokines CXCL9 and CXCL10.[39] EZH2 plays a crucial role in the formation of CD8$^+$ T memory precursors by activating Id3 while silencing Id2, EOMES, and PRDM1.[39,50] Although EZH2 regulates the function and survival of effector CD8$^+$ T cells by repressing the transcription of NUMB and FBXW7 through increased H3K27me3 deposition – thereby activating the Notch pathway – tumors can limit EZH2

expression in $CD8^+$ T cells through glycolysis restriction, which reduces the T-cell-mediated anti-tumor efficacy.[39,48]

Regulatory T cells (Tregs), identified as $CD4^+$, $CD25^+$, and, $FOXP3^+$ T cells, function to suppress inflammation and activation of other effector T cells (Teffs). In Tregs, EZH2 forms a complex with the FOXP3 transcription factor to maintain their activation state.[39] Inhibiting EZH2 in Tregs leads to unstable FOXP3 expression, granting Tregs pro-inflammatory properties, promoting the recruitment of $CD4^+$ and $CD8^+$ T cells, and increasing the production of IFN-γ and TNF-α, which enhances effective anti-tumor immunity.[39]

Natural killer cells express various cytokine receptors linked to chemotaxis and activation, allowing them to be recruited to the tumor site, where they are activated by cytokines, such as IL-12, to exert anti-tumor effects.[39,49] EZH2-expressing tumor cells exhibit decreased expression of the NKG2D ligand, which hinders NK cell activation and directly inhibits NK cell maturation and function.[39] Inhibiting EZH2 increases NK cell numbers, promotes their terminal maturation, and enhances their cytotoxicity.[39]

There are two main phenotypes of myeloid-derived suppressor cells (MDSCs): Monocytic MDSCs and polymorphonuclear MDSCs.[39] In tumors, monocytic MDSCs, such as monocytes, quickly differentiate into tumor-associated macrophages. EZH2-induced H3K27me3 reduces CCL2 expression and decreases macrophage infiltration, whereas EZH2 inhibition polarizes macrophages toward a more anti-tumor phenotype.[39] Despite these effects, EZH2 inhibitors often yield unsatisfactory results in clinical trials. One suggested explanation is the accumulation of MDSCs, which creates a more immune-suppressed TME and weakens the anti-tumor effect,[51] underscoring the importance of combination therapies.[39]

Cancer-associated fibroblasts (CAFs) are stromal components in the TME that facilitate tumor invasion and metastasis by producing growth factors, cytokines, and chemokines, that support cancer cell growth and create an immunosuppressive microenvironment.[39] The role of EZH2 in CAFs is somewhat conflicting; while EZH2 inhibition can suppress angiogenesis, the reduction in H3K27me3 levels in CAFs contributes to the maintenance of cancer cell stemness and growth.[39]

4. Immune escape and immunotherapy resistance in TNBC

4.1. Tumor-specific antigens (TSAs) and MHC expression

In TNBC, several immune evasion mechanisms contribute to resistance to immunotherapy. These mechanisms include the loss of TSAs, deficiencies in antigen presentation, and failure to initiate effective immune responses, which collectively hinder the efficacy of immunotherapeutic agents.[52,53] TNBC generates a greater number of neoantigens due to its high mutational burden and genome instability compared to other breast cancer subtypes.[52] The TME of TNBC typically exhibits a high density of TILs, and PD-L1 is commonly overexpressed in TNBC relative to other breast cancer subtypes.[52] The multicenter, non-randomized Phase Ib trial KEYNOTE-012 showed an overall response rate (ORR) of <20% in advanced PD-L1-expressing TNBC treated with pembrolizumab.[54] Conversely, the KEYNOTE-086 trial observed significantly higher ORRs and disease control rates in TNBC tumors with higher levels of TILs when treated with pembrolizumab.[55] This suggests that the presence of TILs is a critical factor influencing the success of immunotherapy in advanced TNBC.[55] Furthermore, alterations in MHC-1 expression, often due to downregulation or structural modifications, facilitate immune escape by impairing antigen presentation.[52] In TNBC patients resistant to ICIs, downregulation of human leukocyte antigen class 1 (HLA-1) has been frequently observed, potentially linked to mutations in HLA-1 encoding genes and the beta-2-microglobulin gene.[52] Transcription factors, such as NF-κB and NLRC5, along with various epigenetic mechanisms, play pivotal roles in regulating HLA-1 expression, with their ablation significantly affecting antigen presentation.[52] For instance, interferons (IFNs) can induce the expression of HLA-1 heavy chains and related components, whereas disruptions in these pathways can lead to HLA-1 downregulation.[52] In addition, TSAs arise from non-synonymous mutations, gene fusion, and other genomic alterations, and stimulate T-cell-mediated adaptive immunity; their abundance correlates with the tumor mutational burden (TMB).[52] Patients with high TMB are generally more responsive to ICI treatment due to the increased abundance of TSAs; however, PD-L1 expression does not consistently correlate with TMB across various cancer types.[52] Epigenetic changes, such as high EZH2 levels, can result in silencing of immune-related genes and facilitate immune escape by downregulating the expression and presentation of tumor antigens.[39,56,57]

Highlighting the important role of cytotoxic T cells as key effector cells in ICI-treated patients, mutations in genes encoding components of the MHC-I antigen processing pathway (APP) or the IFN-γ response pathway often result in immunotherapy resistance.[58] A genome-wide CRISPR/Cas9 screen has identified a function of PRC2 that coordinates the transcriptional silencing of the MHC-I APP, promoting evasion of T-cell-mediated immunity.[58] In cancers with low MHC-I expression, the promoters

of MHC-I APP genes exhibit both activating H3K4me3 and repressive H3K27me3 histone modifications. This combination silences the basal expression of MHC-I and limits its upregulation in response to cytokines.[58] The repression of genes by PRC2 is attributed to the H3K27me3 mark, a modification catalyzed by EZH2.[58] As demonstrated by Burr *et al.*,[58] treatment with EZH2 inhibitors greatly reduces H3K27me3 levels, resulting in the transcriptional activation of previously repressed MHC-I genes.[58]

Differentially methylated CpGs in promoter regions (within 3kb of the transcription start site) were analyzed to identify genes with unique, concordant gene expression across TNBC subtypes.[1] Despite an overall decrease in methylation, M-subtype TNBC tumors showed increased methylation and decreased expression in genes involved in IFN-γ signaling, immune checkpoint pathways (CD274, LAG3, and TIGIT), and MHC-mediated antigen processing and presentation (NLRC5, CIITA, HLA-A, HLA-B, and TAP1).[1] This subtype exhibited extensive hypermethylation in regions associated with immune signaling (such as IFN-γ signaling, IFN-γ response, T lymphocyte differentiation, TNF response, and immune cytokine signaling) and antigen processing and presentation.[1] Furthermore, EZH2 targets were found to be suppressed in these hypermethylated regions, suggesting the potential deregulation of PRC2.[1]

4.2. T-cell activation

Recruitment and activation of antigen-presenting cells (APCs), such as dendritic cells (DCs) and macrophages, are essential for initiating immune responses. Cancer cells can promote immune escape by downregulating chemokines that recruit APCs and inhibiting the danger signals that activate them.[52] For example, tumor-derived prostaglandin E2 can disrupt $CD8^+$ T-cell responses, facilitating immune evasion.[59] In addition, tumors can evade APC phagocytosis by upregulating "don't eat me" signals, such as CD47, whereas downregulating "eat me" signals, such as calreticulin (CRT).[60-62] In TNBC, glycosylation of B7-H4 stabilizes its expression, inhibiting CRT surface expression and allowing the tumor to escape immune destruction.[63]

The maturation of DCs is marked by the upregulation of costimulatory molecules, such as CD80, CD86, and CD40, which enables effective stimulation of T-cell proliferation and differentiation.[64,65] DCs have been observed to express high levels of PD-L1 whereas downregulating CD80 expression. This alteration prevents the activation of T cells through CD28, contributing to the reduced effectiveness of ICIs.[52,66,67] The interaction of CD80 and CD86 with CD28 on T cells is important for T-cell priming and the production of IL-2, which is vital for T-cell expansion.[68,69] Upregulation of PD-L1 on DCs can inhibit T-cell activation and promote immune evasion.[52]

Abnormal signaling pathways also contribute to immune escape in cancer, such as aberrant WNT/β-catenin signaling, which can prevent T-cell infiltration and suppress immune activation through various mechanisms, including the upregulation of PD-L1 in cancer stem cells.[70] Accumulation of β-catenin following WNT activation triggers the transcription of downstream target genes, such as *MYC*, which is associated with poor immune cell infiltration when highly expressed.[71-73] In TNBC, *MYC* is highly expressed and negatively correlates with the expression of key MHC-I genes (e.g., *BM2*), impairing antigen presentation.[74] MYC can also epigenetically repress *STING*, a gene involved in autonomous immune responses, leading to reduced production of chemokines (e.g., CCL5, CXCL10, and CXCL11), decreased recruitment of TILs, and impaired T-cell-mediated immune surveillance.[52,71] β-catenin activates the transcriptional repressor ATF3, which inhibits CCL4 transcription and subsequently the activation of $CD103^+$ DCs, diminishing the activation and infiltration of $CD8^+$ T cells and reducing the effectiveness of ICIs.[52,75-77]

The JAK-STAT pathway, activated by IFNs, plays a significant role in enhancing MHC expression on APCs, which is crucial for T-cell activation.[78] However, prolonged exposure to IFN-γ can exert selective pressure on tumors, resulting in the downregulation of components of the IFN-γ signaling pathway and facilitating immune evasion.[52,79] Furthermore, the loss of phosphatase and tensin homolog (PTEN) has been associated with decreased T-cell recruitment and function, contributing to resistance against ICIs.[80] PTEN is a critical regulator of the PI3K/Akt signaling pathway, which is essential for T-cell differentiation and function.[81] The loss of PTEN leads to enhanced PI3K/Akt signaling, negatively impacting T-cell persistence and expansion within the TME.[82] This dysregulation can result in an immunosuppressive environment that hinders effective anti-tumor immunity.

4.3. Programmed cell death ligand 1 expression

ICIs restore anti-tumor immunity by blocking the PD1/PD-L1 signaling axis, reactivating exhausted T cells in the TME.[52] PD-L1 expression can be regulated in five ways: (i) Chromatin changes, (ii) genomic changes, (iii) transcription factors and post-transcriptional regulation, (iv) translation and post-translational regulation, and (v) induction within the TME.[52] First, the *CD274* gene, which encodes PD-L1, is located on chromosome 9p24.1, and alterations in chromatin structure and

accessibility can directly influence its expression. Second, abnormal PD-L1 expression can arise from disruptions at any stage of the gene transcription and translation process, where the abnormal activation or inactivation of signaling pathways can impact immune function. Third, the excessive secretion of pro-inflammatory cytokines, such as IFN-γ, TNF-α, and interleukins in the TME, can induce PD-L1 expression in tumor cells through various signaling pathways, facilitating immune escape.[52,83,84] EZH2 can upregulate immune checkpoints on cancer cells; for example, EZH2 promotes hypoxia-inducible factor 1-alpha expression, which in turn upregulates PD-L1 in lung cancer cells.[39,85] Several strategies have been proposed to overcome drug resistance mechanisms in TNBC that bypass effective PD-L1 blockade: enhancing tumor immunogenicity, increasing antigen presentation by MHC, and regulating the recruitment and infiltration of immune effector cells. These approaches aim to boost the presence of TILs within the tumor, thereby restoring anti-tumor immune responses.[52]

5. Combination therapy strategies in TNBC

5.1. Enhancer of zeste homolog 2 inhibition and immunotherapy

The emerging field of epi-immunotherapy, which integrates epigenetic and immune therapies, can potentially make TNBC more responsive to ICIs by remodeling a suppressive TME. In non-TNBC solid tumors, EZH2 inhibition has been shown to enhance the response to immunotherapy. EZH2 inhibition has been demonstrated to increase MHC-I expression and overcome anti-PD-1 resistance, thereby suppressing tumor growth in a pre-clinical model of head and neck cancer.[86] In addition, EZH2 inhibitors and CRISPR-mediated EZH2 deficiency enhanced antigen presentation on tumor cells, promoted antigen-specific $CD8^+$ T-cell proliferation, increased IFN-γ production, and improved tumor cell cytotoxicity.[86] Furthermore, EZH2 inhibition also increased PD-L1 expression on the surfaces of hepatoma cells, improving the efficacy of anti-PD-L1 therapy.[87] In a pre-clinical model of non-small-cell lung cancer, EZH2 inhibition increased the efficacy of anti-PD-1 by elevating double-stranded RNA levels and inducing IFN pathway stress-mediated anti-tumor immunity.[39,88] The inhibition of EZH2 has been shown to upregulate antigen presentation genes and PD-L1.[40] Moreover, in an immunocompetent Lewis lung carcinoma tumor model, EZH2 inhibition caused tumor regression and enhanced $CD8^+$ T cells activity.[40]

Cytotoxic T-lymphocyte-associated protein 4 (CTLA-4) blockade has been shown to increase EZH2 expression in T cells in both humans and mice due to the activation of CD28 signaling.[39] For example, the anti-CTLA-4 antibody ipilimumab increases EZH2 expression in peripheral $CD4^+$ T cells, suggesting that inhibiting EZH2 in T cells may enhance the effectiveness of anti-CTLA-4 therapy.[89] Pre-clinical studies have shown that EZH2 inhibition can improve the anti-tumor efficacy of ipilimumab in mice inoculated with bladder cancer and melanoma.[39,90] Combining an EZH2 inhibitor with anti-CTLA-4, compared to anti-CTLA-4 monotherapy, reduced the percentage of $CD4^+$ $FoxP3^+$ Tregs and increased the percentage of intratumoral $CD4^+$ $ICOS^+$ $T\text{-}bet^+$ and $CD8^+$ $IFN\text{-}\gamma^+$ Teff cells in both bladder and melanoma models, resulting in an increased ratio of Teffs to Tregs.[90] As a result of these findings, several EZH2 inhibitors, such as tazemetostat and CPI-1205, are currently being studied in clinical trials, either as single agents or in combination with immunotherapies for various cancers,[91] including clinical trials combining tazemetostat with pembrolizumab for urothelial carcinoma.[91] Zingg *et al.*[92] found that subtoxic doses of EZH2 inhibitors could prevent immune resistance during immunotherapy, demonstrating that EZH2 inactivation synergizes with anti-CTLA-4 and IL-2 immunotherapy in melanoma pre-clinical models.[92]

Integrative analyses of TNBC multi-omics by Lehmann *et al.*[1] have identified characteristics of TNBC subtypes and subtype-specific genetic or pharmacologic vulnerabilities for future investigation. Pre-clinical data provide a strong rationale for using EZH2-inhibitory agents to restore MHC-I expression in immune-cold, PD-L1-negative, and M-subtype tumors, which exhibit the lowest levels of cell surface MHC-I expression.[1] MHC-I expression can be epigenetically silenced by PRC2 and restored by EZH2 inhibitors in mesenchymal cancer cell lines. Chromatin immunoprecipitation sequencing analysis following EZH2 inhibition has shown that increased MHC-I expression correlates with decreased promoter H3K27me3 occupancy at the MHC-I loci and the transactivator NLRC5.[1]

Vejmelkova *et al.*[93] assessed the therapeutic potential of Tazemetostat in treating pediatric malignant rhabdoid tumors characterized by the loss of integrase interactor 1 (INI1) protein.[93] In INI1-negative tumors, the loss of INI1 leads to aberrant EZH2 activity, resulting in the silencing of tumor suppressor genes and promoting oncogenesis. In this study, two patients received tazemetostat in combination with immunotherapy. One patient with a rhabdoid tumor of the ovary received tazemetostat as maintenance following resection, chemotherapy, and radiotherapy, alongside immunotherapy (nivolumab), achieving an event-free survival of 44 months. A second patient with relapsed atypical teratoid rhabdoid tumor underwent treatment consisting of metronomic therapy,

radiotherapy, tazemetostat, and immunotherapy (nivolumab and ipilimumab), achieving an overall survival of 37 months.[93] Chen *et al.*[94] described a case report of a patient with INI1 deficient-advanced squamous cell lung cancer exhibiting progressive disease while on maintenance pembrolizumab.[94] Unfortunately, the patient did not respond to sequential delivery of tazemetostat. In this case, molecular sequencing analysis did not reveal a *SMARCB1* deletion, suggesting that the loss of INI1 protein was due to epigenetic regulation rather than mutation.[94] Clinical trials evaluating tazemetostat in combination with immunotherapy are currently enrolling participants: Tazemetostat combined with pembrolizumab for urothelial carcinoma (NCT03854474), whereas another trial combines tazemetostat with durvalumab for advanced solid tumors (NCT04705818). NCT04705818 includes solid tumors with the presence of tertiary lymphoid structures, which are found in approximately 60% of breast cancer cases and are particularly common in TNBC.[95]

5.2. Radiotherapy

Since EZH2 inhibition appears to decrease cancer cell migration and tumor metastasis more than it reduces primary tumor growth in most solid tumors,[35] exploring combinations with radiation to achieve primary tumor control is warranted. Radiation also has immunomodulatory effects, with different radiation schemes inducing various lymphoid and myeloid responses, as well as modulating checkpoint expression.[96]

Radiotherapy induces DNA damage through direct ionization or indirectly through interactions between free radicals formed by ionization of water surrounding DNA, resulting in single- or double-strand breaks (DSBs).[97] Oxygen molecules react with these radicals, altering the chemical composition of DNA strand breaks and facilitating their recognition by DNA damage repair enzymes.[97] Under hypoxic conditions, radicals chemically react with free protons, reverting to their original form, which impedes the fixation of DNA damage and contributes to radioresistance.[97] In addition, hypoxia activates oxygen-sensitive signaling pathways, such as those mediated by hypoxia-inducible factor transcription factors, the unfolded protein response, and the mTOR pathway.[97] These pathways influence key biological processes, including mitosis, apoptosis, and angiogenesis, impacting radiosensitivity.[97] Hypoxia-induced global changes in histone modifications and DNA methylation, such as increased levels of H3K4me3 and decreased levels of H3K27me3, lead to transcriptional changes that also affect radiosensitivity.[97,98] Combining agents that inhibit both DNA methylation and histone acetylation may enhance radiosensitivity.[97] Inducing an anti-tumor immune response, overcoming tumor radioresistance, and generating anti-tumor non-targeted effects can significantly enhance the success of radiation treatments.[99]

In addition to its pivotal role in cellular processes, such as differentiation, proliferation, and tumor suppression, the SWI/SNF complex is crucial in the DNA damage response by propagating DNA damage signals and enabling DNA repair proteins to access damage sites.[100] Components of the SWI/SNF complex are essential for the non-homologous end joining (NHEJ) repair of DSBs in human cancer cells, suggesting that the SWI/SNF complex may contribute to resistance against therapeutic agents that induce DNA damage, including radiation.[100] *ARID1A*, a gene encoding the BAF250a protein, is a key component of the SWI/SNF complex that facilitates NHEJ by promoting the accumulation of Ku70/Ku80 proteins at DSBs, thereby conferring resistance to ionizing radiation.[100] The loss of *ARID1A* impairs checkpoint activation and DNA DSB repair, sensitizing cells to radiation.[100] Andrade *et al.*[100] showed that genetic inhibition of *ARID1A* leads to an accumulation of radiation-induced DSBs, sensitizing TNBC cells to radiation.[100] Bakr *et al.*[101] showed that the loss of *ARID1A* promotes the accumulation of micronuclei and activation of the cGAS-STING pathway, as well as increases the expression of immunomodulatory cytokines and chemokines from radiotherapy treatment. Notably, low *ARID1A* expression in cancer patients receiving radiotherapy was associated with higher infiltration of various immune cells.[101]

The interaction mechanism between EZH2 and radiation is not well understood.[39] Pre-clinical studies indicate that EZH2 inhibitors can enhance the radiosensitivity of glioma cells, atypical teratoma or rhabdoid tumor cells, and pancreatic cancer cells.[39,102-104] In a cohort of patients with nasopharyngeal cancer treated with radiation or chemoradiation, increased H3K27me3 expression was associated with chemoradioresistance.[39,105] Elevated EZH2 levels correlate with radiation resistance; however, pre-clinical evidence suggests that high-dose radiotherapy alone may reduce EZH2 protein expression *in vitro* and at the mRNA level *in vivo* through p53-mediated inhibition of transcription factor E2F1.[106-108] Klaus *et al.*[109] reported that radiation delivered concurrently with or after treatment with the EZH2 inhibitor tazemetostat induced robust antiproliferative activity and reduced clonogenic potential in tested atypical rhabdoid tumor cell lines.[109]

Gounder *et al.*[110] reported on a patient with *SMARCB1*/INI1-negative poorly differentiated chordoma treated with tazemetostat and sequential radiotherapy. It was found that EZH2 inhibition, evidenced by decreased H3K27me3 marks, led to a notable increase in intratumoral and

stromal infiltration by proliferative CD8⁺ T cells, FoxP3⁺ Tregs, and immune cells expressing checkpoint regulators PD-1 and LAG-3.[110] Following 4 weeks of tazemetostat treatment and subsequent radiotherapy to the primary tumor site, a complete response was observed at distant metastatic sites.[110] However, at the primary treatment site, which received a dose of 70 Gy in 35 fractions, only a partial response was noted. The authors speculated that radiotherapy at the sacrum likely depleted the TILs induced by tazemetostat, rendering the sacral mass less responsive to immunotherapy.[110] The patient was subsequently treated with ICIs. This strategy of EZH2 inhibition fostered a durable anti-tumor response, ultimately leading to T-cell exhaustion and checkpoint activation, suggesting that altering the epigenetic landscape may sensitize some tumors to checkpoint inhibitors.[110]

Radiotherapy can induce immunogenic cell death, characterized by the release of danger-associated molecular pattern antigens that trigger the uptake of antigens and activation of APCs, leading to the priming of cytotoxic lymphocytes and an adaptive immune response.[110] However, the precise contribution of EZH2 inhibition, radiotherapy, and PD-1/PD-L1 blockade on the immunologic and overall

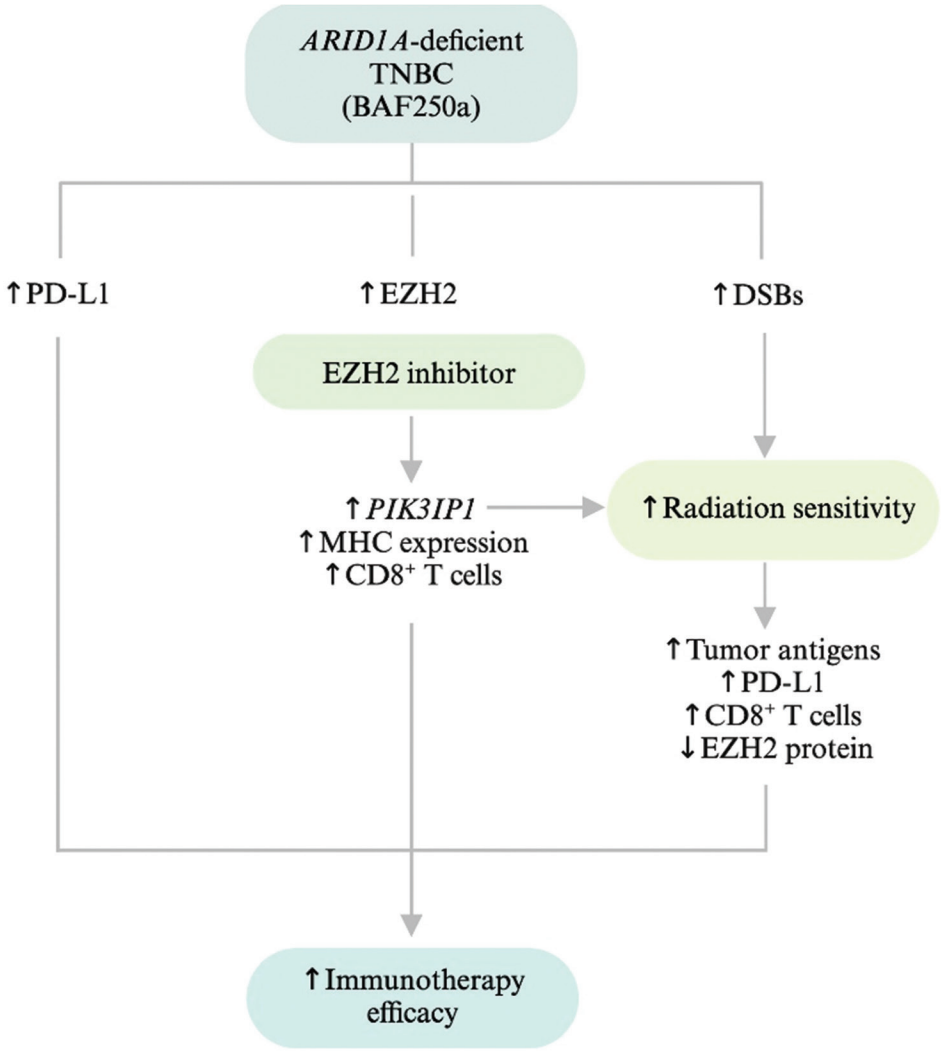

Figure 4. The proposed rationale for triple therapy of enhancer of zeste homolog 2 (EZH2) inhibition, radiation therapy, and immunotherapy in triple-negative breast cancer (TNBC). In AT-rich interactive domain 1A (*ARID1A*)-deficient TNBC (biomarker BAF250a), there is an increase in programmed cell death ligand 1 (PD-L1) expression, EZH2, and double-strand breaks (DSBs). EZH2 inhibition results in increased expression of *PIK3IP1*, major histocompatibility complex (MHC) expression, and CD8⁺ T cells. Increased *PIK3IP1* increases radiosensitivity, while radiation potentially increases tumor antigen release, PD-L1 expression, CD8⁺ T cells, and reduced EZH2 protein. Together, this combinational therapy may increase immunotherapy efficacy. Created in BioRender by Lukas, L. (https://BioRender.com/e14a778).

responses remain unclear, necessitating further research to elucidate the impact of tumor mutation burden or neoantigen load, T-cell receptor repertoire, and expansion of specific T cell clones on the immunologic and therapeutic responses to EZH2 inhibition and radiotherapy.[110] In the context of TNBC, PD-L1 expression was found to be increased in abscopal tumors following spatially fractionated radiotherapy (SFRT) in a murine TNBC model (4T1). The intratumoral immune cell composition in these abscopal tumors exhibited significant increases in activated $CD4^+$ and $CD8^+$ T cells.[111] SFRT, a novel radiation technique that applies ablative doses to tumor subvolumes while sparing surrounding tissues, results in highly heterogeneous dose deposition that may enhance the immune-rich infiltrate within the targeted tumor, promoting improved antigen presentation and activated T cells in non-irradiated tumors.[112] Different radiation regimens elicit distinct immune responses, and since SFRT consists of a heterogeneous dose distribution often delivered in a single fraction, its immune effects may differ from standard fractionation. In a murine model of pediatric glioblastoma, although both tazemetostat and standard fractionation radiotherapy given as monotherapies improved animal survival, the combination of tazemetostat with radiation did not further improve survival compared to either treatment alone, indicating a lack of additive or synergistic effects.[113] Although the mechanism of resistance was not further evaluated in the glioblastoma model, analysis of atypical teratoid/rhabdoid tumors and medulloblastoma remnant/recurrent tumors treated with cisplatin in combination therapies revealed reduced levels of EZH2 protein expression, H3K27me2, and H3K27me3, alongside a marked increase in the tumor cells exhibiting absence of or low EZH2 expression. This finding suggests that inter-tumoral heterogeneity may have contributed to tumor recurrence.[113] The immunocompromised animal model used in this study may not have adequately evaluated the immunomodulatory effects of radiation; thus, the combination therapies may have been insufficient to deplete the cells with no or low EZH2 expression. This limitation highlights the importance of evaluating immune effects and tumor heterogeneity in models of combination therapy, including single-cell sequencing and spatial single-cell analysis, to help understand drug resistance at the single-cell level.[113]

6. Conclusion

TNBC is a heterogeneous disease characterized by transcriptional diversity and varying immune cell compositions across its subtypes. ICIs have shown limited efficacy in TNBC, marked by a high incidence of primary resistance and the development of adaptive resistance. Therefore, strategies are needed to overcome this immunotherapy resistance, including combinations of ICIs with other anticancer agents, such as EZH2 inhibitors and radiotherapy, as proposed in Figure 4. The dysregulation of epigenetic mechanisms, particularly through the overexpression of EZH2, contributes to a suppressive TME that hampers effective T-cell responses. This is important in TNBC, where overexpression of EZH2 has been associated with increased PD-L1, but low TILs. By targeting EZH2, the TME could potentially be remodeled to enhance the infiltration and activity of TILs that are crucial for mediating anti-tumor immunity. In this context, BAF250a immunohistochemistry could serve as a useful biomarker. Patients with low BAF250a protein expression as a result of low *ARID1A* gene expression may benefit from EZH2 inhibition. This inhibition could upregulate PIK3IP1 expression, suppress tumor cell growth, and potentially restore previously repressed MHC-I expression, thereby improving the efficacy of immunotherapy.[1,6] Given that *ARID1A* mutations impair DNA repair pathways, this could lead to increased sensitivity to therapies that induce DNA damage, such as radiation.[114] The addition of radiotherapy may amplify the effects of immunotherapy through the release of tumor antigens, upregulation of PD-L1, and an increase in immune-rich infiltrate within the targeted volume of tumor, as well as potentially decreasing EZH2 protein expression. Despite the effectiveness of EZH2 inhibitors in reducing H3K27me3 repressive marks to improve response in other cancer types, they have not been observed to sufficiently inhibit the proliferation of most breast cancer cells as a monotherapy, possibly due to the lack of effects on total EZH2 protein levels.[42] This finding suggests that the protein expression of EZH2 itself, rather than its methyltransferase activity, may be more crucial in the development and progression of breast cancer, including TNBC, highlighting the potential use of EZH2 selective degraders, such as MS1943,[43] or agents that inhibit both the methyltransferase activity and degrade EZH2, such as IHMT-337.[44] Although EZH2 inhibitors are not as effective as a monotherapy in TNBC, given that residual H3K27me3 has been shown to persist in TNBC cells after knockout of endogenous EZH2, there is still merit in exploring combinations of EZH2 inhibitors, such as tazemetostat, with ICIs.[44]

Precision oncology utilizes the molecular profile of tumors to tailor more precise and personalized therapies for distinct patient groups who differ in both susceptibility to disease and responses to treatments.[115] Epigenetics, which influences gene expression and cellular phenotypes beyond the DNA sequence, plays an important role in this approach.[116] As such, epigenetic modifications are prime targets for therapeutic intervention.[116] When combined strategically with immunotherapy in TNBC, this approach

may provide a new population of resistant patients with treatments that could increase immunogenicity, manage tumor growth, improve survival, and enhance quality of life.

Acknowledgments

Figures created in BioRender.com by Evelina VanderSpek and Lauren Lukas.

Funding

None.

Conflict of Interest

The authors declare they have no competing interests.

Author contributions

Conceptualization: Lauren Lukas
Visualization: Lauren Lukas
Writing – original draft: Lauren Lukas
Writing – review & editing: All authors

Ethics approval and consent to participate

Not applicable.

Consent for publication

Not applicable.

Availability of data

Not applicable.

References

1. Lehmann BD, Colaprico A, Silva TC, *et al.* Multi-omics analysis identifies therapeutic vulnerabilities in triple-negative breast cancer subtypes. *Nat Commun*. 2021;12(1):6276.

   doi: 10.1038/s41467-021-26502-6

2. Loi S, Drubay D, Adams S, *et al.* Tumor-infiltrating lymphocytes and prognosis: A pooled individual patient analysis of early-stage triple-negative breast cancers. *J Clin Oncol*. 2019;37(7):559-569.

   doi: 10.1200/jco.18.01010

3. Yoshihara K, Shahmoradgoli M, Martínez E, *et al.* Inferring tumour purity and stromal and immune cell admixture from expression data. *Nat Commun*. 2013;4:2612.

   doi: 10.1038/ncomms3612

4. Li K, Wang B, Hu H. Research progress of SWI/SNF complex in breast cancer. *Epigenetics Chromatin*. 2024;17(1):4.

   doi: 10.1186/s13072-024-00531-z

5. Wu Q, Madany P, Akech J, *et al.* The Swi/SNF atpases are required for triple negative breast cancer cell proliferation. *J Cell Physiol*. 2015;230(11):2683-2694.

   doi: 10.1002/jcp.24991

6. Shen J, Ju Z, Zhao W, *et al.* ARID1A deficiency promotes mutability and potentiates therapeutic antitumor immunity unleashed by immune checkpoint blockade. *Nat Med*. 2018;24(5):556-562.

   doi: 10.1038/s41591-018-0012-z

7. Wang Y, Chen Z, Wu J, Yan H, Wang Y, He J. The mutation and low expression of arid1a are predictive of a poor prognosis and high immune infiltration in triple-negative breast cancer. *Curr Cancer Drug Targets*. 2023;59-68.

   doi: 10.2174/1568009623666230522115229

8. Sun D, Tian L, Zhu Y, *et al.* Subunits of ARID1 serve as novel biomarkers for the sensitivity to immune checkpoint inhibitors and prognosis of advanced non-small cell lung cancer. *Mol Med*. 2020;26(1):78.

   doi: 10.1186/s10020-020-00208-9

9. Kim YB, Ahn JM, Bae WJ, Sung CO, Lee D. Functional loss of ARID1A is tightly associated with high PD-L1 expression in gastric cancer. *Int J Cancer*. 2019;145(4):916-926.

   doi: 10.1002/ijc.32140

10. Sun M, Gu Y, Fang H, *et al.* Clinical outcome and molecular landscape of patients with ARID1A-loss gastric cancer. *Cancer Sci*. 2024;115(3):905-915.

    doi: 10.1111/cas.16057

11. Jung US, Min KW, Kim DH, Kwon MJ, Park H, Jang HS. Suppression of ARID1A associated with decreased CD8 T cells improves cell survival of ovarian clear cell carcinoma. *J Gynecol Oncol*. 2021;32(1):e3.

    doi: 10.3802/jgo.2021.32.e3

12. Tarantino P, Barroso-Sousa R, Garrido-Castro AC, *et al.* Understanding resistance to immune checkpoint inhibitors in advanced breast cancer. *Expert Rev Anticancer Ther*. 2022;22(2):141-153.

    doi: 10.1080/14737140.2022.2020650

13. Chen XY, Li B, Wang Y, *et al.* Low level of arid1a contributes to adaptive immune resistance and sensitizes triple-negative breast cancer to immune checkpoint inhibitors. *Cancer Commun (Lond)*. 2023;43(9):1003-1026.

    doi: 10.1002/cac2.12465

14. Duan R, Du W, Guo W. EZH2: A novel target for cancer treatment. *J Hematol Oncol*. 2020;13(1):104.

    doi: 10.1186/s13045-020-00937-8

15. Pasini D, Di Croce L. Emerging roles for polycomb proteins in cancer. *Curr Opin Genet Dev*. 2016;36:50-58.

    doi: 10.1016/j.gde.2016.03.013

16. Zhou L, Yu CW. Epigenetic modulations in triple-negative

breast cancer: Therapeutic Implications for tumor microenvironment. *Pharmacol Res*. 2024;204:107205.

doi: 10.1016/j.phrs.2024.107205

17. Wu F, Li N, Wu X, *et al.* EZH2 mutation is associated with the development of visceral metastasis by enhancing proliferation and invasion and inhibiting apoptosis in breast cancer cells. *BMC Cancer*. 2024;24(1):1166.

doi: 10.1186/s12885-024-12950-y

18. Glancy E, Wang C, Tuck E, *et al.* PRC2.1-and PRC2.2-specific accessory proteins drive recruitment of different forms of canonical PRC1. *Mol Cell*. 2023;83(9):1393-1411.e7.

doi: 10.1016/j.molcel.2023.03.018

19. Singh V, Nandi S, Ghosh A, *et al.* Epigenetic reprogramming of T cells: Unlocking new avenues for cancer immunotherapy. *Cancer Metastasis Rev*. 2024;43:175-195.

doi: 10.1007/s10555-024-10167-w

20. Alldredge JK, Eskander RN. EZH2 inhibition in ARID1A mutated clear cell and endometrioid ovarian and endometrioid endometrial cancers. *Gynecol Oncol Res Pract*. 2017;4:17.

doi: 10.1186/s40661-017-0052-y

21. Bitler BG, Aird KM, Garipov A, *et al.* Synthetic lethality by targeting EZH2 methyltransferase activity in arid1a-mutated cancers. *Nat Med*. 2015;21(3):231-238.

doi: 10.1038/nm.3799

22. Chien YC, Liu LC, Ye HY, Wu JY, Yu YL. EZH2 promotes migration and invasion of triple-negative breast cancer cells via regulating TIMP2-MMP-2/-9 pathway. *Am J Cancer Res*. 2018;8(3):422-434.

23. Hussein YR, Sood AK, Bandyopadhyay S, *et al.* Clinical and biological relevance of enhancer of zeste homolog 2 in triple-negative breast cancer. *Hum Pathol*. 2012;43(10):1638-1644.

doi: 10.1016/j.humpath.2011.12.004

24. Gonzalez ME, Naimo GD, Anwar T, *et al.* EZH2 T367 phosphorylation activates P38 signaling through lysine methylation to promote breast cancer progression. *iScience*. 2022;25(8):104827.

doi: 10.1016/j.isci.2022.104827

25. Gonzalez-Crespo I, Gomez-Caamano A, Pouso OL, Fenwick JD, Pardo-Montero J. A biomathematical model of tumor response to radioimmunotherapy with αPDL1 and αCTLA4. *IEEE/ACM Trans Comput Biol Bioinform*. 2023;20(2):808-821.

doi: 10.1109/tcbb.2022.3174454

26. Fujii S, Ito K, Ito Y, Ochiai A. Enhancer of zeste homologue 2 (EZH2) down-regulates RUNX3 by increasing histone H3 methylation. *J Biol Chem*. 2008;283(25):17324-17332.

doi: 10.1074/jbc.M800224200

27. Hirukawa A, Smith HW, Zuo D, *et al.* Targeting EZH2 reactivates a breast cancer subtype-specific anti-metastatic transcriptional program. *Nat Commun*. 2018;9(1):2547.

doi: 10.1038/s41467-018-04864-8

28. Borkiewicz L. Histone 3 lysine 27 trimethylation signature in breast cancer. *Int J Mol Sci*. 2021;22(23):12853.

doi: 10.3390/ijms222312853

29. Gong C, Yao S, Gomes AR, *et al.* BRCA1 positively regulates FOXO3 expression by restricting FOXO3 gene methylation and epigenetic silencing through targeting EZH2 in breast cancer. *Oncogenesis*. 2016;5(4):e214.

doi: 10.1038/oncsis.2016.23

30. Yang X, Karuturi RK, Sun F, *et al.* CDKN1C (P57) is a direct target of EZH2 and suppressed by multiple epigenetic mechanisms in breast cancer cells. *PLoS One*. 2009;4(4):e5011.

doi: 10.1371/journal.pone.0005011

31. Ren G, Baritaki S, Marathe H, *et al.* Polycomb protein EZH2 regulates tumor invasion via the transcriptional repression of the metastasis suppressor RKIP in breast and prostate cancer. *Cancer Res*. 2012;72(12):3091-3104.

doi: 10.1158/0008-5472.Can-11-3546

32. Zhang R, Li X, Liu Z, Wang Y, Zhang H, Xu H. EZH2 inhibitors-mediated epigenetic reactivation of fosb inhibits triple-negative breast cancer progress. *Cancer Cell Int*. 2020;20:175.

doi: 10.1186/s12935-020-01260-5

33. Zheng XJ, Li W, Yi J, *et al.* EZH2 regulates expression of FOXC1 by mediating H3K27me3 in breast cancers. *Acta Pharmacol Sin*. 2021;42(7):1171-1179.

doi: 10.1038/s41401-020-00543-x

34. Lu Y, Gu F, Ma Y, *et al.* Simultaneous delivery of doxorubicin and EZH2-targeting sirna by vortex magnetic nanorods synergistically improved anti-tumor efficacy in triple-negative breast cancer. *Small*. 2023;19(43):e2301307.

doi: 10.1002/smll.202301307

35. Verma A, Singh A, Singh MP, *et al.* EZH2-H3K27me3 mediated KRT14 upregulation promotes tnbc peritoneal metastasis. *Nat Commun*. 2022;13(1):7344.

doi: 10.1038/s41467-022-35059-x

36. Lawrence CL, Baldwin AS. Non-canonical EZH2 transcriptionally activates relb in triple negative breast cancer. *PLoS One*. 2016;11(10):e0165005.

doi: 10.1371/journal.pone.0165005

37. Lee ST, Li Z, Wu Z, *et al.* Context-specific regulation of NF-KB target gene expression by EZH2 in breast cancers. *Mol Cell*. 2011;43(5):798-810.

doi: 10.1016/j.molcel.2011.08.011

38. Schade AE, Perurena N, Yang Y, *et al.* AKT and EZH2 inhibitors kill $TNBC_S$ by hijacking mechanisms of involution. *Nature*. 2024;635:755-763.

doi: 10.1038/s41586-024-08031-6

39. Huang R, Wu Y, Zou Z. Combining EZH2 inhibitors with other therapies for solid tumors: More choices for better effects. *Epigenomics*. 2022;14(22):1449-1464.

doi: 10.2217/epi-2022-0320

40. Hoy SM. Tazemetostat: First approval. *Drugs*. 2020;80(5):513-521.

doi: 10.1007/s40265-020-01288-x

41. Von Keudell G, Salles G. The role of tazemetostat in relapsed/refractory follicular lymphoma. *Ther Adv Hematol*. 2021;12.

doi: 10.1177/20406207211015882

42. Wang C, Chen X, Liu X, *et al.* Discovery of precision targeting EZH2 degraders for triple-negative breast cancer. *Eur J Med Chem*. 2022;238:114462.

doi: 10.1016/j.ejmech.2022.114462

43. Ma A, Stratikopoulos E, Park KS, *et al.* Discovery of a first-in-class EZH2 selective degrader. *Nat Chem Biol*. 2020;16(2):214-222.

doi: 10.1038/s41589-019-0421-4

44. Mei H, Wu H, Yang J, *et al.* Discovery of IHMT-337 as a potent irreversible EZH2 inhibitor targeting CDK4 transcription for malignancies. *Signal Transduct Target Ther*. 2023;8(1):18.

doi: 10.1038/s41392-022-01240-3

45. Margueron R, Li G, Sarma K, *et al.* EZH1 and EZH2 maintain repressive chromatin through different mechanisms. *Mol Cell*. 2008;32(4):503-518.

doi: 10.1016/j.molcel.2008.11.004

46. Yoo KH, Oh S, Kang K, Hensel T, Robinson GW, Hennighausen L. Loss of EZH2 results in precocious mammary gland development and activation of STAT5-dependent genes. *Nucleic Acids Res*. 2015;43(18):8774-8789.

doi: 10.1093/nar/gkv776

47. Shen X, Liu Y, Hsu YJ, *et al.* EZH1 mediates methylation on histone H3 lysine 27 and complements EZH2 in maintaining stem cell identity and executing pluripotency. *Mol Cell*. 2008;32(4):491-502.

doi: 10.1016/j.molcel.2008.10.016

48. Zhao E, Maj T, Kryczek I, *et al.* Cancer mediates effector T cell dysfunction by targeting micrornas and EZH2 via glycolysis restriction. *Nat Immunol*. 2016;17(1):95-103.

doi: 10.1038/ni.3313

49. Guillerey C, Smyth MJ. NK cells and cancer immunoediting. *Curr Top Microbiol Immunol*. 2016;395:115-145.

doi: 10.1007/82_2015_446

50. He S, Liu Y, Meng L, *et al.* EZH2 phosphorylation state determines its capacity to maintain $CD8^+$ T memory precursors for antitumor immunity. *Nat Commun*. 2017;8(1):2125.

doi: 10.1038/s41467-017-02187-8

51. Huang S, Wang Z, Zhou J, *et al.* EZH2 Inhibitor GSK126 suppresses antitumor immunity by driving production of myeloid-derived suppressor cells. *Cancer Res*. 2019;79(8):2009-2020.

doi: 10.1158/0008-5472.Can-18-2395

52. Zheng Y, Li S, Tang H, Meng X, Zheng Q. Molecular mechanisms of immunotherapy resistance in triple-negative breast cancer. *Front Immunol*. 2023;14:1153990.

doi: 10.3389/fimmu.2023.1153990

53. Luo L, Wang Z, Hu T, *et al.* Multiomics characteristics and immunotherapeutic potential of EZH2 in pan-cancer. *Biosci Rep.* 2023;43(1).

doi: 10.1042/bsr2022223054

54. Nanda R, Chow LQ, Dees EC, *et al.* Pembrolizumab in patients with advanced triple-negative breast cancer: Phase Ib KEYNOTE-012 study. *J Clin Oncol*. 2016;34(21):2460-2467.

doi: 10.1200/jco.2015.64.8931

55. Loi S, Salgado R, Schmid P, *et al.* Association between biomarkers and clinical outcomes of pembrolizumab monotherapy in patients with metastatic triple-negative breast cancer: KEYNOTE-086 exploratory analysis. *JCO Precis Oncol*. 2023;7:e2200317.

doi: 10.1200/po.22.00317

56. Rosenthal R, Cadieux EL, Salgado R, *et al.* Neoantigen-directed immune escape in lung cancer evolution. *Nature*. 2019;567(7749):479-485.

doi: 10.1038/s41586-019-1032-7

57. Garrido F, Aptsiauri N, Doorduijn EM, Garcia Lora AM, van Hall T. The urgent need to recover mhc class I in cancers for effective immunotherapy. *Curr Opin Immunol*. 2016;39:44-51.

doi: 10.1016/j.coi.2015.12.007

58. Burr ML, Sparbier CE, Chan KL, *et al.* An evolutionarily conserved function of polycomb silences the MHC class I antigen presentation pathway and enables immune evasion in cancer. *Cancer Cell*. 2019;36(4):385-401.e8.

doi: 10.1016/j.ccell.2019.08.008

59. Bayerl F, Meiser P, Donakonda S, *et al.* Tumor-derived prostaglandin E2 programs CDC1 dysfunction to impair intratumoral orchestration of anti-cancer T cell responses. *Immunity*. 2023;56(6):1341-1358.e11.

doi: 10.1016/j.immuni.2023.05.011

60. Willingham SB, Volkmer JP, Gentles AJ, *et al.* The CD47-signal regulatory protein alpha (SIRPa) interaction is a

therapeutic target for human solid tumors. *Proc Natl Acad Sci U S A*. 2012;109(17):6662-6667.

doi: 10.1073/pnas.1121623109

61. Sikic BI, Lakhani N, Patnaik A, *et al.* First-in-human, first-in-class phase I trial of the anti-CD47 antibody HU5F9-G4 in patients with advanced cancers. *J Clin Oncol*. 2019;37(12):946-953.

doi: 10.1200/jco.18.02018

62. Obeid M, Tesniere A, Ghiringhelli F, *et al.* Calreticulin exposure dictates the immunogenicity of cancer cell death. *Nat Med*. 2007;13(1):54-61.

doi: 10.1038/nm1523

63. Song X, Zhou Z, Li H, *et al.* Pharmacologic suppression of B7-H4 glycosylation restores antitumor immunity in immune-cold breast cancers. *Cancer Discov*. 2020;10(12):1872-1893.

doi: 10.1158/2159-8290.Cd-20-0402

64. Zhang X, Chang A, Zou Y, *et al.* Aspirin attenuates cardiac allograft rejection by inhibiting the maturation of dendritic cells via the NF-κB signaling pathway. *Front Pharmacol*. 2021;12:706748.

doi: 10.3389/fphar.2021.706748

65. Li JG, Du YM, Yan ZD, *et al.* CD80 and CD86 knockdown in dendritic cells regulates Th1/Th2 cytokine production in asthmatic mice. *Exp Ther Med*. 2016;11(3):878-884.

doi: 10.3892/etm.2016.2989

66. Gaitonde P, Peng A, Straubinger RM, Bankert RB, Balu-Iyer SV. Phosphatidylserine reduces immune response against human recombinant factor VIII in hemophilia a mice by regulation of dendritic cell function. *Clin Immunol*. 2011;138(2):135-145.

doi: 10.1016/j.clim.2010.10.006

67. Wang L, Li Z, Ciric B, Safavi F, Zhang GX, Rostami A. Selective depletion of $CD11C^{+}$ $CD11b^{+}$ dendritic cells partially abrogates tolerogenic effects of intravenous mog in murine EAE. *Eur J Immunol*. 2016;46(10):2454-2466.

doi: 10.1002/eji.201546274

68. Zhou Y, Leng X, Luo X, *et al.* Regulatory dendritic cells induced by K313 display anti-inflammatory properties and ameliorate experimental autoimmune encephalitis in mice. *Front Pharmacol*. 2019;10:1579.

doi: 10.3389/fphar.2019.01579

69. Sim WJ, Malinarich F, Fairhurst AM, Connolly JE. Generation of immature, mature and tolerogenic dendritic cells with differing metabolic phenotypes. *J Vis Exp*. 2016;(112):54128.

doi: 10.3791/54128

70. Khramtsov AI, Khramtsova GF, Tretiakova M, Huo D, Olopade OI, Goss KH. Wnt/Beta-catenin pathway activation is enriched in basal-like breast cancers and predicts poor outcome. *Am J Pathol*. 2010;176(6):2911-2920.

doi: 10.2353/ajpath.2010.091125

71. Lee KM, Lin CC, Servetto A, *et al.* Epigenetic repression of sting by MYC promotes immune evasion and resistance to immune checkpoint inhibitors in triple-negative breast cancer. *Cancer Immunol Res*. 2022;10(7):829-843.

doi: 10.1158/2326-6066.Cir-21-0826

72. Lee JV, Housley F, Yau C, *et al.* Combinatorial immunotherapies overcome MYC-driven immune evasion in triple negative breast cancer. *Nat Commun*. 2022;13(1):3671.

doi: 10.1038/s41467-022-31238-y

73. Cancer Genome Atlas Network. Comprehensive molecular portraits of human breast tumours. *Nature*. 2012;490(7418):61-70.

doi: 10.1038/nature11412

74. Torrejon DY, Abril-Rodriguez G, Champhekar AS, *et al.* Overcoming genetically based resistance mechanisms to PD-1 blockade. *Cancer Discov*. 2020;10(8):1140-1157.

doi: 10.1158/2159-8290.Cd-19-1409

75. Spranger S, Bao R, Gajewski TF. Melanoma-intrinsic B-catenin signalling prevents anti-tumour immunity. *Nature*. 2015;523(7559):231-235.

doi: 10.1038/nature14404

76. Vu SH, Vetrivel P, Kim J, Lee MS. Cancer resistance to immunotherapy: Molecular mechanisms and tackling strategies. *Int J Mol Sci*. 2022;23(18):10906.

doi: 10.3390/ijms231810906

77. Liang X, Fu C, Cui W, *et al.* B-catenin mediates tumor-induced immunosuppression by inhibiting cross-priming of CD8+ T cells. *J Leukoc Biol*. 2014;95(1):179-190.

doi: 10.1189/jlb.0613330

78. Platanias LC. Mechanisms of type-I-and type-II-interferon-mediated signalling. *Nat Rev Immunol*. 2005;5(5):375-386.

doi: 10.1038/nri1604

79. Gao J, Shi LZ, Zhao H, *et al.* Loss of IFN-γ pathway genes in tumor cells as a mechanism of resistance to anti-CTLA-4 therapy. *Cell*. 2016;167(2):397-404.e9.

doi: 10.1016/j.cell.2016.08.069

80. Peng W, Chen JQ, Liu C, *et al.* Loss of pten promotes resistance to T cell-mediated immunotherapy. *Cancer Discov*. 2016;6(2):202-216.

doi: 10.1158/2159-8290.Cd-15-0283

81. Papa A, Pandolfi PP. The PTEN-PI3K axis in cancer. *Biomolecules*. 2019;9(4):153.

doi: 10.3390/biom9040153

82. Lin Z, Huang L, Li SL, Gu J, Cui X, Zhou Y. PTEN loss correlates with T cell exclusion across human cancers. *BMC Cancer*. 2021;21(1):429.

doi: 10.1186/s12885-021-08114-x

83. Garcia-Diaz A, Shin DS, Moreno BH, *et al.* Interferon receptor signaling pathways regulating PD-L1 and Pd-L2 expression. *Cell Rep.* 2017;19(6):1189-1201.

doi: 10.1016/j.celrep.2017.04.031

84. Wang X, Yang L, Huang F, *et al.* Inflammatory cytokines IL-17 and TNF-A up-regulate PD-L1 expression in human prostate and colon cancer cells. *Immunol Lett*. 2017;184:7-14.

doi: 10.1016/j.imlet.2017.02.006

85. Zhao Y, Wang XX, Wu W, *et al.* EZH2 Regulates PD-L1 expression via HIF-1α in non-small cell lung cancer cells. *Biochem Biophys Res Commun*. 2019;517(2):201-209.

doi: 10.1016/j.bbrc.2019.07.039

86. Zhou L, Mudianto T, Ma X, Riley R, Uppaluri R. Targeting EZH2 enhances antigen presentation, antitumor immunity, and circumvents anti-PD-1 resistance in head and neck cancer. *Clin Cancer Res*. 2020;26(1):290-300.

doi: 10.1158/1078-0432.Ccr-19-1351

87. Xiao G, Jin LL, Liu CQ, *et al.* EZH2 negatively regulates PD-L1 expression in hepatocellular carcinoma. *J Immunother Cancer*. 2019;7(1):300.

doi: 10.1186/s40425-019-0784-9

88. Qiu F, Yang Q, Sun W, Ruan K, Jiang N, Zhou J. EZH2 inhibition activates dsrna-interferon axis stress and promotes response to PD-1 checkpoint blockade in NSCLC. *J Cancer*. 2022;13(9):2893-2904.

doi: 10.7150/jca.73291

89. Li C, Wang Y, Gong Y, *et al.* Finding an easy way to harmonize: A review of advances in clinical research and combination strategies of EZH2 inhibitors. *Clin Epigenetics*. 2021;13(1):62.

doi: 10.1186/s13148-021-01045-1

90. Goswami S, Apostolou I, Zhang J, *et al.* Modulation of EZH2 expression in T cells improves efficacy of anti-CTLA-4 therapy. *J Clin Invest*. 2018;128(9):3813-3818.

doi: 10.1172/jci99760

91. Guo R, Li J, Hu J, *et al.* Combination of epidrugs with immune checkpoint inhibitors in cancer immunotherapy: From theory to therapy. *Int Immunopharmacol*. 2023;120:110417.

doi: 10.1016/j.intimp.2023.110417

92. Zingg D, Arenas-Ramirez N, Sahin D, *et al.* The histone methyltransferase EZH2 controls mechanisms of adaptive resistance to tumor immunotherapy. *Cell Rep.* 2017;20(4):854-867.

doi: 10.1016/j.celrep.2017.07.007

93. Vejmelkova K, Pokorna P, Noskova K, *et al.* Tazemetostat in the therapy of pediatric INI1-negative malignant rhabdoid tumors. *Sci Rep.* 2023;13(1):21623.

doi: 10.1038/s41598-023-48774-2

94. Chen X, Wu J, Pang G, Wei S, Wang P. Integrase interactor 1 (INI1) deficiency in a lung cancer patient presents nonresponse to immunotherapy and tazemetostat: A Case report. *Cureus*. 2023;15(8):e42934.

doi: 10.7759/cureus.42934

95. Narvaez D, Nadal J, Nervo A, *et al.* The emerging role of tertiary lymphoid structures in breast cancer: A narrative review. *Cancers* (*Basel*). 2024;16(2):396.

doi: 10.3390/cancers16020396

96. Grapin M, Richard C, Limagne E, *et al.* Optimized fractionated radiotherapy with anti-PD-L1 and anti-tigit: A promising new combination. *J Immunother Cancer*. 2019;7(1):160.

doi: 10.1186/s40425-019-0634-9

97. Smits KM, Melotte V, Niessen HE, *et al.* Epigenetics in radiotherapy: Where are we heading? *Radiother Oncol*. 2014;111(2):168-177.

doi: 10.1016/j.radonc.2014.05.001

98. Johnson AB, Denko N, Barton MC. Hypoxia induces a novel signature of chromatin modifications and global repression of transcription. *Mutat Res*. 2008;640(1-2):174-179.

doi: 10.1016/j.mrfmmm.2008.01.001

99. Trappetti V, Fazzari JM, Fernandez-Palomo C, *et al.* Microbeam radiotherapy-a novel therapeutic approach to overcome radioresistance and enhance anti-tumour response in melanoma. *Int J Mol Sci*. 2021;22(14):7755.

doi: 10.3390/ijms22147755

100. Andrade D, Mehta M, Griffith J, *et al.* HuR reduces radiation-induced DNA damage by enhancing expression of arid1a. *Cancers (Basel)*. 2019;11(12):2014.

doi: 10.3390/cancers11122014

101. Bakr A, Della Corte G, Veselinov O, *et al.* ARID1A regulates DNA repair through chromatin organization and its deficiency triggers DNA damage-mediated anti-tumor immune response. *Nucleic Acids Res*. 2024;52(10):5698-5719.

doi: 10.1093/nar/gkae233

102. Sak A, Kübler D, Bannik K, *et al.* Epigenetic silencing and activation of transcription: Influence on the radiation sensitivity of glioma cell lines. *Int J Radiat Biol*. 2017;93(5):494-506.

doi: 10.1080/09553002.2017.1270472

103. Alimova I, Birks DK, Harris PS, *et al.* Inhibition of EZH2 suppresses self-renewal and induces radiation sensitivity in atypical rhabdoid teratoid tumor cells. *Neuro Oncol*.

2013;15(2):149-160.

doi: 10.1093/neuonc/nos285

104. Agrawal R, Chen M, Bukhari Z, Ogunwobi OO, Haseeb MA, Martello LA. EZH2 Downregulation augments the effect of irradiation in reducing pancreatic cancer cell proliferation *in vitro*. *Ann Clin Lab Sci*. 2020;50(1):45-56.

105. Cai MY, Tong ZT, Zhu W, *et al.* H3K27me3 protein is a promising predictive biomarker of patients' survival and chemoradioresistance in human nasopharyngeal carcinoma. *Mol Med*. 2011;17(11-12):1137-1145.

doi: 10.2119/molmed.2011.00054

106. Kuser-Abali G, Gong L, Yan J, *et al.* An EZH2-mediated epigenetic mechanism behind P53-dependent tissue sensitivity to DNA damage. *Proc Natl Acad Sci U S A*. 2018;115(13):3452-3457.

doi: 10.1073/pnas.1719532115

107. Brenneman RJ, Sharifai N, Fischer-Valuck B, *et al.* Abscopal effect following proton beam radiotherapy in a patient with inoperable metastatic retroperitoneal sarcoma. *Front Oncol*. 2019;9:922.

doi: 10.3389/fonc.2019.00922

108. Wu C, Jin X, Yang J, *et al.* Inhibition of EZH2 by chemo- and radiotherapy agents and small molecule inhibitors induces cell death in castration-resistant prostate cancer. *Oncotarget*. 2016;7(3):3440-3452.

doi: 10.18632/oncotarget.6497

109. Klaus CR, Keats JA, Smith JJ, *et al.* Tazemetostat displays synergistic antiproliferative activity with backbone therapies in preclinical models of AT/RT and MRT. *Cancer Res*. 2017;77(13):1944.

doi: 10.1158/1538-7445.AM2017-1944

110. Gounder MM, Zhu G, Roshal L, *et al.* Immunologic correlates of the abscopal effect in a SMARCB1/INI1-negative poorly differentiated chordoma after EZH2 inhibition and radiotherapy. *Clin Cancer Res*. 2019;25(7):2064-2071.

doi: 10.1158/1078-0432.Ccr-18-3133

111. Johnsrud AJ, Jenkins SV, Jamshidi-Parsian A, *et al.* Evidence for early stage anti-tumor immunity elicited by spatially fractionated radiotherapy-immunotherapy combinations. *Radiat Res*. 2020;194(6):688-697.

doi: 10.1667/rade-20-00065.1

112. Lukas L, Zhang H, Cheng K, Epstein A. Immune priming with spatially fractionated radiation therapy. *Curr Oncol Rep.* 2023;25(12):1483-1496.

doi: 10.1007/s11912-023-01473-7

113. Qi L, Lindsay H, Kogiso M, *et al.* Evaluation of an EZH2 inhibitor in patient-derived orthotopic xenograft models of pediatric brain tumors alone and in combination with chemo- and radiation therapies. *Lab Invest*. 2022;102(2):185-193.

doi: 10.1038/s41374-021-00700-8

114. Park Y, Chui MH, Suryo Rahmanto Y, *et al.* Loss of ARID1A in tumor cells renders selective vulnerability to combined ionizing radiation and PARP inhibitor therapy. *Clin Cancer Res*. 2019;25(18):5584-5594.

doi: 10.1158/1078-0432.Ccr-18-4222

115. Neagu AN, Bruno P, Johnson KR, Ballestas G, Darie CC. Biological basis of breast cancer-related disparities in precision oncology era. *Int J Mol Sci*. 2024;25(7):4113.

doi: 10.3390/ijms25074113

116. Werner RJ, Kelly AD, Issa JJ. Epigenetics and precision oncology. *Cancer J*. 2017;23(5):262-269.

doi: 10.1097/ppo.0000000000000281

117. Durán M, Faull I, Lastra E, Laes JF, Rodrigo AB, Sánchez-Escribano R. ARID1A genomic alterations driving microsatellite instability through somatic MLH1 methylation with response to immunotherapy in metastatic lung adenocarcinoma: A case report. *J Med Case Rep.* 2021;15(1):89.

doi: 10.1186/s13256-020-02589-1

118. Goswami S, Chen Y, Anandhan S, *et al.* ARID1A mutation plus CXCL13 expression act as combinatorial biomarkers to predict responses to immune checkpoint therapy in mUCC. *Sci Transl Med*. 2020;12(548):eabc4220.

doi: 10.1126/scitranslmed.abc4220

119. Li L, Li M, Jiang Z, Wang X. ARID1A mutations are associated with increased immune activity in gastrointestinal cancer. *Cells*. 2019;8(7):678.

doi: 10.3390/cells8070678

120. Pignata S, Califano D, Lorusso D, *et al.* MITO END-3: Efficacy of avelumab immunotherapy according to molecular profiling in first-line endometrial cancer therapy. *Ann Oncol*. 2024;35(7):667-676.

doi: 10.1016/j.annonc.2024.04.007

121. Zhou H, Sun D, Song S, *et al.* Efficacy of immunotherapy in arid1a-mutant solid tumors: A single-center retrospective study. *Discov Oncol*. 2024;15(1):213.

doi: 10.1007/s12672-024-01074-1

122. Nutt SL, Keenan C, Chopin M, Allan RS. EZH2 function in immune cell development. *Biol Chem*. 2020;401(8):933-943

doi: 10.1515/hsz-2019-0436

123. Kim HJ, Cantor H, Cosmopoulos K. Overcoming immune checkpoint blockade resistance via EZH2 inhibition. *Trends Immunol*. 2020;41(10):948-963.

doi: 10.1016/j.it.2020.08.010

ACCSCIENCE PUBLISHING

Advances in Radiotherapy & Nuclear Medicine

ORIGINAL RESEARCH ARTICLE

Combining pan-immune-inflammation value and pretreatment tooth extractions in predicting osteoradionecrosis of the jaw: A pilot study

Efsun Somay[1]*, Erkan Topkan[2], Sükran Senyürek[3], Nilüfer Kılıç Durankuş[3], Düriye Öztürk[4], and Ugur Selek[3]

[1]Department of Oral and Maxillofacial Surgery, Faculty of Dentistry, Baskent University, Ankara, Turkey

[2]Department of Radiation Oncology, Faculty of Medicine, Baskent University, Adana, Turkey

[3]Department of Radiation Oncology, School of Medicine, Koc University, Istanbul, Turkey

[4]Department of Radiation Oncology, School of Medicine, Afyonkarahisar Health and Science University, Afyonkarahisar, Turkey

Abstract

Previously, we demonstrated that the pan-immune-inflammation value (PIV) and pretreatment tooth extraction (TE) were independent predictors of osteoradionecrosis of the jaws (ORNJ) in patients with locally advanced nasopharyngeal carcinoma (LA-NPC) undergoing concurrent chemoradiotherapy (C-CRT). This study aimed to determine if combining PIV and TE, termed the PIV-TE-ORNJ index, and could improve the prediction of ORNJ prevalence in the same scenario. We divided patients into two groups based on each factor, with the PIV and TE cutoffs at 833 and 4, respectively, as determined in our previous study. The novel PIV-TE-ORNJ index, which combined these factors, revealed four probable groups: Group 1, PIV < 833 and TE < 4; Group 2, PIV < 833 but TE ≥ 4; Group 3, TE < 4 but PIV ≥ 833; and Group 4, PIV ≥ 833 and TE ≥ 4. The medical records of 220 patients with LA-NPC were reviewed retrospectively. Comparisons between four groups revealed that the ORNJ rates for Groups 1 – 4 were 1.1%, 6.6%, 6.1%, and 43.8%, respectively ($P < 0.001$). Because the ORNJ rates in Groups 2 and 3 were interchangeable ($P = 0.91$), these groups were merged, and a three-tiered novel PIV-TE-ORNJ index was created: low risk, PIV < 833 and TE < 4; intermediate risk, PIV < 833 but TE ≥ 4, or TE < 4 but PIV ≥ 833; and high risk, PIV ≥ 833 and TE ≥ 4. Comparisons between the three groups demonstrated that the low- and high-risk groups had the lowest (1.1%) and highest (43.8%) ORNJ rates, respectively, whereas the ORNJ rate of the intermediate-risk group was in between (6.4%) ($P < 0.001$ for each). The PIV-TE-ORNJ index successfully stratified patients with LA-NPC into low-, intermediate-, and high-risk groups after C-CRT.

Keywords: Tooth extraction; Pan-immune-inflammation value; Nasopharyngeal cancer; Concurrent chemoradiotherapy; Osteoradionecrosis

***Corresponding author:**
Efsun somay
(esomay@baskent.edu.tr)

Citation: Somay E, Topkan E, Senyürek S, Durankuş NK, Öztürk D, Selek U. Combining pan-immune-inflammation value and pretreatment tooth extractions in predicting osteoradionecrosis of the jaw: A pilot study. *Adv Radiother Nucl Med*. 2025;3(1):46-56. doi: 10.36922/arnm.5799

Received: November 6, 2024

Revised: November 20, 2024

Accepted: December 20, 2024

Published online: January 17, 2025

1. Introduction

Locally advanced nasopharyngeal carcinomas (LA-NPCs) comprise approximately 70% of nasopharyngeal carcinomas (NPCs), for which concurrent chemoradiotherapy

(C-CRT) represents the current care standard.[1,2] C-CRT demonstrates significantly enhanced local control rates (>90%) and prolonged survival durations compared to radiotherapy (RT).[1] Nonetheless, a notable subset of patients subjected to this potent but potentially toxic treatment modality may suffer from severe delayed complications, including persistent dysphagia necessitating feeding tubes, trismus, and osteoradionecrosis of the jaw (ORNJ). Implementing more sophisticated intensity-modulated RT (IMRT) protocols reduces the incidence rates of these complications to a certain extent; however, they cannot eradicate them.[3-6]

ORNJ is a debilitating long-term complication of C-CRT in LA-NPC and other head-and-neck cancers. Its occurrence rate ranges from 2% to 22%, with over 70% of cases being identified within the initial 3 years after C-CRT.[7-10] ORNJ can occur spontaneously, and higher tumor stage, primary or nodal tumor invasion into the jaws, pretreatment alveolar surgery, non-IMRT techniques, tooth extractions (TEs) before and after treatment, and poor oral health are cited among the most common risk factors.[7,11,12] The fibro-atrophic theory is the most appreciated explanation of ORNJ formation. According to this theory, the detrimental vascular changes in the bone, conjoined with endothelial changes or loss, cause an inflammatory response that results in hypoxia, hypervascularity, and hypocellularity.[11,13] This mediator-induced inflammatory process is typically followed by abnormally high fibroblastic activity and incompetent bone repair, resulting in bone necrosis, *that is*, ORNJ.[11-14] As inflammatory cells and mediators play important roles in ORNJ development, their potential use in predicting the occurrence of ORNJ following RT or C-CRT warrants further investigation.

Prognostic indexes, such as the pan-immune-inflammation value (PIV = [platelet×monocyte×neutrophil]÷lymphocyte]), combine different indicators from the whole blood count and have garnered considerable attention as a practical and indirect method of assessing the overall inflammation extent in the body.[15] The PIV is an exceptional composite biomarker that integrates lymphocytes, platelets, monocytes, and neutrophils, objectively reflecting systemic inflammation and immunological activity. High PIVs frequently indicate persistent inflammation in individuals with atherosclerosis, vascular occlusive diseases, and several cancer.[16-19] In earlier research,[20,21] chronic systemic inflammation has been linked to arthritis and venous obstruction. Moreover, systemic inflammation has been connected to the activation of inflammatory mediators generated by neutrophil granulocytes and thrombocytes, such as tumor necrosis factor-α (TNF-α), interleukin-10 (IL-10), and vascular endothelial growth factor, which are crucial in tissue fibrosis.[16,22] Vascular thrombosis, hypoxia, and consequent fibrotic processes caused by radiation exposure can exacerbate localized damage by augmenting synthetic processes and the release of inflammatory chemokines and cytokines such as IL-1, IL-6, hypoxia-inducible factor-1 alpha (HIF-1α), insulin-like growth factor 2, and transforming growth factor-beta (TGF-ß).[23-26]

Although the association between post-RT TEs and the increased incidence of ORNJ is well-documented, the effect of pre-RT TE remains uncertain.[27-30] However, a recent study conducted by our team revealed a notable correlation between the occurrence of ≥4 pre-C-CRT TE and substantially high ORNJ rates (3.3% vs. 19.1% for ≥4 TE; $P = 0.003$) in patients with LA-NPC.[29] This finding underscores the potential significance of the level of mandibular trauma, potentially rendering the irradiated jaw site more susceptible to ORNJ development. Based on our previous findings, which indicated that high pretreatment PIV levels ≥833 and ≥4 TE were strong predictors of ORNJ rates after C-CRT, we will attempt to explore whether combining these specific parameters could better stratify these patients into different ORNJ risk groups. Consequently, this retrospective study aimed to determine whether this hypothesis is valid for LA-NPC cohorts who received IMRT-based C-CRT.

2. Patients and methods

2.1. Patients

Data were collected from the institutional medical records of 220 patients with LA-NPC who received comprehensive dental examinations and exclusive. C-CRT at the Dentistry Clinics and the Department of Radiation Oncology of Baskent University between January 2011 and December 2022. The inclusion criteria were as follows: patients aged 18 – 80 years, confirmed squamous cell NPC histopathology, clinical and/or radiologic evidence of LA-NPC according to the American Joint Committee on Cancer staging system (8th edition), no previous systemic chemotherapy or RT, accessible pre- and post-C-CRT panoramic radiographs, and complete blood count tests conducted before C-CRT. This study excluded patients with mandibular tumor invasion, prior diagnosis of osteoradionecrosis (ORNJ), or those who had used steroids within 30 days preceding C-CRT. Patients presenting with active systemic inflammatory conditions – including respiratory diseases, rheumatologic diseases, viral hepatitis, nephritic disorders, confirmed immunosuppressive disorders, collagen vascular diseases, or other chronic inflammatory conditions – were also ineligible for participation. These criteria were

established to mitigate any potential bias stemming from pre-existing immune-inflammatory conditions and the influence of medication use.

2.2. Baseline oral examination

Before undergoing C-CRT, each patient was examined for oral and dental pathologies, regardless of symptom status, per the American Dental Association and US Food and Drug Administration guidelines, and our institutional standards.[31] Following our institutional protocols, oral examinations included panoramic radiographs for each patient and followed the specifications advised by the manufacturer. The digital panoramic radiographs were obtained using the same X-ray machine (J Morita, Veraviewepocs 2D, Kyoto, Japan). An experienced oral and maxillofacial surgeon (ES) performed all clinical and radiological assessments.

2.3. Determination of pretreatment PIV and TE cutoffs

We opted not to set new PIV and TE cutoffs as 210 out of 220 patients in this study had also participated in our previous research published elsewhere. Therefore, the PIV and TE cutoffs used in this study to categorize patients into two groups for each factor were set at 833 (<833 vs. ≥833) and 4 (<4 vs. ≥4 extractions), respectively, based on our earlier work.[29]

2.4. Treatment details

Target volumes were defined using pre-C-CRT computed tomography (CT), 18F-fluorodeoxyglucose positron emission tomography-CT, and/or magnetic resonance imaging of the entire neck and nasopharyngeal primary, as mandated by our institutional standards for patients diagnosed with LA-NPC. The treatment approach employed was simultaneous integrated boost IMRT (SIB-IMRT), which was consistently applied to all patients. The methods for target volume definition, delineation, and prescribed SIB-IMRT doses adhered to those previously documented. The recommended RT doses for low-, moderate-, and high-risk planning target volumes were 54, 59.4, and 70 Gy, respectively. These doses were systematically administered daily over 33 days. The concurrent chemotherapy regimen consisted of three cycles of cisplatin, administered every 21 days, followed by an additional two cycles of a combination regimen involving cisplatin and 5-fluorouracil in the adjuvant setting. Supportive measures, such as nutritional supplements and antiemetic medications, were prescribed as required.

2.5. Follow-up oral examination

Dental and oral evaluations were performed during the follow-up appointments using the same protocol outlined in the "Baseline oral examination" section. ORNJ was diagnosed as per the following clinical and radiological criteria: "irradiated bone that fails to heal over 3 months without evidence of persisting, recurrent, or metastatic tumor."[31-35]

2.6. Statistical analysis

The descriptive characteristics are presented as the patient count and corresponding percentages or as the median and interquartile ranges. Nominal factors were contrasted using either Fisher's exact test or Pearson's Chi-squared test. The Mann–Whitney and Kruskal–Wallis tests were employed to compare continuous variables. This retrospective cohort study primarily aimed to identify any associations between post-C-CRT ORNJ rates and groups formed by merging pre-C-CRT. The combined groups were established using a pre-C-CRT PIV cutoff of 833 (<833 vs. ≥833) and pre-C-CRT TE groups (<4 and ≥4 extractions) identified in a previous study.[29] Briefly, in our previous investigation, receiver operating characteristic (ROC) curve analysis was employed to ascertain the optimal cutoff points for pre-C-CRT PIV measures and pre-C-CRT TE numbers that could divide the study cohort into two significantly discrete ORNJ risk groups for each variable under investigation. The cutoff points for pre-C-CRT PIV measures and pre-C-CRT TE numbers were 833 (area under the curve, 88.0%; sensitivity, 81.1%; specificity, 78.8%; and Youden index, 59.9) and 4 (the median pre-C-CRT value was determined as a cutoff point), respectively, which resulted in the formation of four groups: Groups 1 (PIV < 833 and TE < 4), 2 (PIV < 833 and TE ≥ 4), 3 (PIV ≥ 833 and TE < 4), and Group 4 (PIV ≥ 833 and TE ≥ 4). The optimal cutoff points for each variable were determined by identifying the points at which the J-index reaches its maximum value on the ROC curve.

Student's t-test, Chi-square test, or Spearman correlation tests were used to compare different groups as needed. The univariate analyses explored how patient, disease, and treatment variables might influence with ORNJ prevalence. The multivariate Cox proportional hazard model included only the statistically significant factors in the univariate analysis. All statistical tests were two-sided, and significance was considered at $P < 0.05$. Bonferroni corrections were used to correct treatment variables for multiplicity, which reduced the risk of random false-positive results when comparing three or more subgroups. The adjusted *P*-values obtained from this correction were then used to define the significance levels (significance level for Bonferroni corrected *P*-value for three possible comparisons was at 0.0167 [0.05÷3]).

3. Results

A retrospective review of the medical records of 220 patients with LA-NPC treated at our institution was conducted. The median age was 56 (range, 18 – 76) years, and 151 (68.6%) patients were male. Among the patients, 55.5% and 75.5% had a history of alcohol consumption and tobacco smoking, respectively. Most patients had T3 – 4 (67.3%) or N2 – 3 (80%) disease stage. Before starting C-CRT, all patients underwent at least one TE, with a median of three TEs (range, 1 – 11), indicating poor oral and dental health in the study participants. The median time from TEs to C-CRT initiation was 16 (range, 12 – 22) days (Table 1). The median time from C-CRT completion to ORNJ diagnosis was 20.8 (range, 12.4 – 27.6) months, resulting in an ORNJ incidence of 9.5%. All ORNJ cases were located in the posterior half of the affected jaw.

Out of the 220 patients in the present study, 210 were also part of our previous study. We used the pre-C-CRT PIV cutoff of 833 and the pre-C-CRT TE cutoff of 4 to divide the patients into two groups with significantly different rates of ORNJ. This resulted in the following groups: PIV < 833 (n = 154) and PIV ≥ 833 (n = 66), as well as TE < 4 (n = 127) and TE ≥ 4 (n = 93). When comparing the PIV and TE groups, ORNJ rates were significantly higher in the PIV ≥ 833 and TE ≥ 4 groups compared to their PIV<833 and TE<4 counterparts, respectively (2.6% vs. 25.8% for PIV ≥ 833; P < 0.001 and 3.14% vs. 22.4% for TE ≥ 4; P < 0.001).

As per the main objective of this study, the PIV and TE groups were combined, resulting in four distinct groups: Group 1, PIV < 833 and TE < 4; Group 2, PIV < 833 but TE ≥ 4; Group 3, TE < 4 but PIV ≥ 833; and Group 4, PIV ≥ 833 and TE ≥ 4 (Figure 1). When comparing these groups, the ORNJ rates were 1.1%, 6.6 %, 6.1%, and 43.8% for Groups 1 – 4, respectively. Given the indistinguishable ORNJ rates of Groups 2 and 3 (P = 0.91), these two groups were consolidated and a novel three-tiered ORNJ risk classification was formulated (Table 2: low risk (PIV < 833 and TE < 4), intermediate risk (PIV < 833

Table 1. Pretreatment and treatment characteristics

Characteristics	All patients (n=220)	Low-risk group (n=94)	Intermediate-risk group (n=94)	High-risk group (n=32)	P-value
Median age, years (range)	56 (18 – 76)	55 (18 – 76)	54 (18 – 76)	54 (18 – 76)	0.22
Age group, years (%)					
≤56	114 (51.8)	52 (55.3)	42 (44.7)	20 (62.5)	0.15
>56	106 (48.2)	42 (44.7)	52 (55.3)	12 (37.5)	
Sex, n (%)					
Female	69 (31.4)	28 (29.8)	32 (34.0)	9 (28.1)	0.75
Male	151 (68.6)	66 (70.2)	62 (66.0)	23 (71.9)	
Smoking status, n (%)					
Yes	166 (75.5)	70 (74.5)	69 (73.4)	27 (84.4)	0.44
No	54 (24.5)	24 (25.5)	25 (26.6)	5 (15.6)	
Alcohol consumption, n (%)					
Yes	98 (44.5)	43 (45.7)	41 (43.6)	14 (43.8)	0.95
No	122 (55.5)	51 (54.3)	53 (56.4)	18 (56.2)	
Median pre-C-CRT TE, n (range)	3 (1 – 11)	2 (1 – 3)	5 (4 – 9)	4 (1 – 11)	0.000*
Pre-C-CRT TE group, n (%)					
≥4	93 (42.3)	0 (0)	61 (64.9)	32 (100)	0.000*
<4	127 (57.7)	94 (100)	33 (35.1)	0 (0)	
Median time from TE to C-CRT, days (range)	16 (12 – 22)	17 (14 – 22)	16 (13 – 22)	16 (10 – 22)	0.43
T-stage, n (%)					
1 – 2	44 (20)	18 (19.1)	20 (21.3)	6 (18.8)	0.67
3 – 4	176 (80)	76 (80.9)	74 (78.7)	26 (81.2)	
N-stage, n (%)					
0 – 1	78 (32.7)	33 (35.1)	34 (36.2)	11 (34.4)	0.51
2 – 3	142 (67.3)	61 (64.9)	60 (63.8)	21 (65.6)	
Clinical Stage, n (%)					
III	79 (35.9)	33 (35.1)	35 (37.2)	11 (34.4)	0.42
IVA-B	141 (64.1)	61 (64.9)	59 (62.8)	19 (65.6)	

Abbreviations: C-CRT: Concurrent chemoradiotherapy; TE: Tooth extraction; T: Tumor; N: Node.

Table 2. Definition of the combined PIV and TE groups and PIV-TE-ORNJ index groups

Characteristics	Definition
Combined PIV and TE groups	
Group 1	PIV<833 and Pre-C-CRT TE<4
Group 2	PIV<833 and Pre-C-CRT TE≥4
Group 3	PIV≥833 and Pre-C-CRT TE<4
Group 4	PIV≥833 and Pre-C-CRT TE≥4
PIV-TE-ORNJ index groups	
Low risk	PIV<833 and Pre-C-CRT TE<4
Intermediate risk	PIV<833 and Pre-C-CRT TE≥4
High risk	or PIV≥833 and Pre-C-CRT TE<4
	PIV≥833 and Pre-C-CRT TE≥4

Abbreviations: PIV: Pan-immune-inflammation value; TE: Tooth extractions; ORNJ: Osteoradionecrosis of the jaws.

but TE ≥ 4 or TE < 4 but PIV ≥ 833); and high risk (PIV ≥ 833 and TE ≥ 4) (Table 3). When compared by three groups, the ORNJ rates stood at 43.8%, 6.4%, and 1.1% for the high-, intermediate-, and low-risk groups, respectively (Figure 2). The Bonferroni corrected *P*-values underscored the significant differences between the three groups ($P < 0.001$ for each comparison, Table 2). The comparison of risk groups showed that pre-C-CRT TE ≥ 4 was present in 100%, 64.9%, and 0% for the high-, intermediate-, and low-risk groups, respectively, suggesting a poorer oral health status that is significantly more common in the high- and intermediate-risk groups ($P < 0.001$).

In the univariate analysis, five additional factors were linked to a higher ORNJ incidence rate following definitive C-CRT. These factors included pre-C-CRT TEs ($P < 0.001$), post-C-CRT TEs ($P < 0.001$), a PIV ≥ 833 ($P = 0.001$), continued smoking ($P = 0.002$), and a mean mandibular dose of ≥56.4 Gy ($P < 0.001$). In the multivariate analysis, all six factors, including the three-tiered PIV-TE index, retained their independent significance concerning the ORNJ rates (Table 4).

4. Discussion

This retrospective cohort analysis sought to determine whether the combination of pre-C-CRT PIV levels and the number of TEs, specifically the PIV-TE-ORNJ index, could accurately predict the rates of ORNJ in patients treated for LA-NPC. This study originated from proven previous separate associations between these parameters and ORNJ rates. Our results confirmed the predictive validity of both PIV and TEs and illustrated that the PIV-TE-ORNJ index can categorize patients into three distinct risk groups for ORNJ occurrence, each exhibiting significantly different rates: high risk, 43.8%; intermediate risk, 6.4%; and low risk, 1.1% ($P < 0.001$).

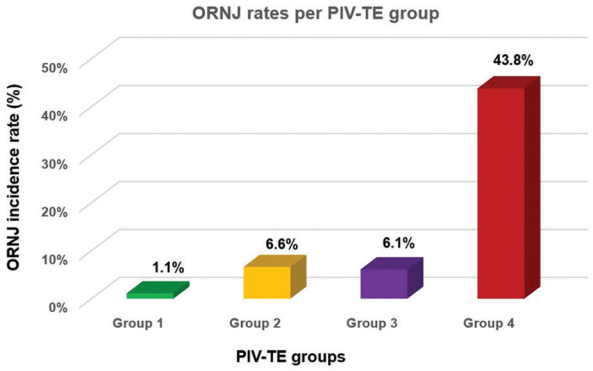

Figure 1. Combined pan-immune-inflammation value and pretreatment tooth extraction groups for osteonecrosis of jaw (Group 1, PIV < 833 and Pre-C-CRT TE < 4; Group 2, PIV < 833 and Pre-C-CRT TE ≥ 4, or PIV ≥ 833 and Pre-C-CRT TE < 4; and Group 3, PIV ≥ 833 and Pre-C-CRT TE ≥ 4).
Abbreviations: PIV: Pan-immune-inflammation value; TE: Tooth extractions; ORNJ: Osteoradionecrosis of the jaws.

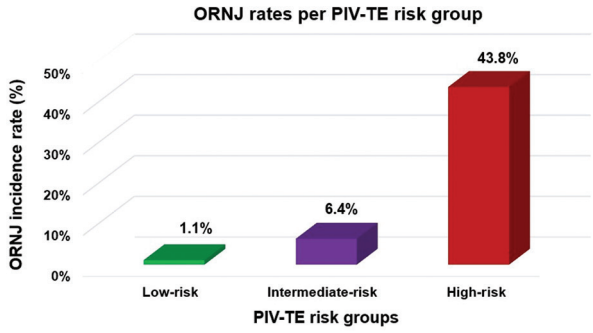

Figure 2. Osteoradionecrosis of the jaw rates for per PIV-TE-ORNJ index groups (Group 1, PIV<833 and Pre-C-CRT TE<4; Group 2, PIV<833 and Pre-C-CRT TE≥4; Group 3, PIV≥833 and Pre-C-CRT TE<4; and Group 4, PIV≥833 and Pre-C-CRT TE≥4).
Abbreviations: PIV: Pan-immune-inflammation value; TE: Tooth extractions; ORNJ: Osteoradionecrosis of the jaws.

Bone lysis can be observed as early as 4 h following RT. However, ORNJ appears to be primarily caused by radiation-induced damage to the endothelial cells, which results in progressive microvascular dysfunction, vascular obstruction, and low bone turnover attributable to an inadequate supply of oxygen and nutrients.[36] Adequate tissue oxygenation is essential for all the stages of the regenerative processes, including cell proliferation and growth, angiogenesis, collagen synthesis, and activation of the body's defense mechanisms against bacterial infections after any tissue injury, such as those caused by high doses of RT.[6,37] Following radiation-induced bone injury, proinflammatory cytokines such as TGF-ß, which promote fibrosis, and TNF-α, IL-1, and IL-6, are believed to initiate and exacerbate the development of ORNJ by activating a persistent chronic inflammatory phase.[35,38,39]

Table 3. Distribution of variables according to risk groups and results of their relationship

Characteristics	All patients (*n*=220)	Low-risk group (*n*=94)	Intermediate-risk group (*n*=94)	High-risk group (*n*=32)	*P*-value
Continued smoking, *n* (%)					
Yes	47 (21.4)	18 (19.14)	21 (22.34)	8 (0.25)	0.22
No	173 (78.6)	76 (80.86)	73 (77.66)	24 (0.75)	
Continued alcohol consumption, *n* (%)					
Yes	64 (29.01)	27 (28.72)	28 (29.80)	9 (28.13)	0.19
No	156 (70.99)	67 (71.28)	66 (70.2)	23 (71.87)	
Concurrent chemotherapy cycles, *n* (%)					
1	55 (0.25)	16 (0.25)	24 (25.53)	15 (46.9)	0.008
2 – 3	165 (0.75)	78 (0.75)	70 (74.47)	17 (53.1)	
Adjuvant chemotherapy cycles					
0	76 (34.54)	23 (24.5)	33 (35.1)	20 (62.5)	0.006
1 – 2	144 (65.46)	71 (75.5)	61 (64.9)	12 (37.5)	
Mean mandibular dose, Gy (range)	41.6 (18.4 – 74.8)	41.9 (18.4 – 74.2)	41.2 (19.3 – 73.7)	41.8 (19.1 – 74.8)	0.87
Mean mandibular dose group, *n* (%)					
<56.4	163 (74.1)	70 (74.5)	69 (73.4)	24 (0.75)	0.57
≥56.4	57 (25.9)	24 (25.5)	25 (26.6)	8 (0.25)	
Median post-C-CRT extracted teeth, n (range)	1 (0 – 5)	1 (0 – 1)	1 (0 – 5)	2 (0 – 5)	0.00*
Median C-CRT to ORN interval, mo. (range)	19 (12 – 24)	19 (19 – 19)	19 (15 – 24)	19 (12 – 24)	0.85
Post-CCRT TE, *n* (%)					
Absent	38 (17.3)	20 (21.3)	16 (17.0)	2 (6.3)	0.06
Present	182 (82.7)	74 (78.7)	78 (83.0)	30 (93.7)	
ORNJ, *n* (%)					
Absent	199 (90.5)	93 (98.9)	88 (93.6)	18 (56.3)	<0.001
Present	21 (9.5)	1 (1.1)	6 (6.4)	14 (43.8)	

Abbreviations: C-CRT: Concurrent chemoradiotherapy; Gy: Gray; ORNJ: Osteoradionecrosis of the jaws.

In a recent study by our group, PIV levels were associated with post-C-CRT ORNJ rates.[29] Herein, in line with our previous findings, we have corroborated that the incidence of ORNJ is significantly high in the group with PIV ≥ 833 compared with the group with PIV < 833 (25.8% vs. 2.6%, $P < 0.001$). This outcome indicates that PIV can be regarded as a pertinent biomarker for assessing the ORNJ risk in patients with LA-NPC who have received C-CRT.

A study demonstrated that TE functions as a catalyst in increasing ORNJ risk. Nonetheless, a significant debate exists concerning the optimal timing for TE enactment.[40,41] Consistent with the results of our previous and present studies, some researchers contend that TEs lead to a higher ORNJ risk due to radiation-related consequences, regardless of their timing. For example, Beech *et al*. found that pre-RT TEs, either alone or followed by post-RT TEs, increased the ORNJ risk.[28] Confirming the role of pretreatment TEs in ORNJ development, a recent meta-analysis by Jiang *et al*. elucidated a 4.16% risk of ORNJ associated with pre-RT TEs,[42] a figure that only marginally diverges from the 6.4% incidence of ORNJ observed within the intermediate-risk cohort in the present study. The increased risk of ORNJ following pre-RT TEs may be further aggravated by the severity of surgical damage to both soft tissues and bone. Multiple pretreatment TEs, which indicate poor oral health and significant trauma to the mandible, are clearly linked to a substantially higher risk of ORNJ. This heightened risk is likely due to decreased tissue blood flow and oxygenation in the severely injured mandible and tooth sockets after RT or C-CRT. In this respect, pre-C-CRT TE ≥ 4 was observed in 100% of the high-risk group, 64.9% of the intermediate-risk group, and 0% of the low-risk group. This finding highlights a significantly greater prevalence of suboptimal oral health status among the high- and intermediate-risk groups relative to the low-risk group ($P < 0.001$). Although further investigations are warranted, these results imply that in addition to increased trauma due to dental extractions, prolonged periods of compromised oral health and associated chronic local and systemic inflammation may have contributed to the elevated incidence of ORNJ within these patient subgroups.

The most prominent finding of this study was the creation of a new index by integrating previously established pretreatment PIV ≥ 833 and TE ≥ 4 to predict ORNJ rates after C-CRT in patients with LA-NPC, namely,

Table 4. Results of the univariate and multivariate analyses (ORNJ)

Characteristic	All patients (*n*=220)	ORN incidence (*n*=21)	Univariate *P*-value	Multivariate *P*-value
Age group, *n* (%)				
≤56 years	114 (51.8)	12 (10.5)	0.65	-
>56 years	106 (48.2)	9 (8.5)		
Sex, *n* (%)				
Female	69 (31.4)	7 (10.14)	0.81	-
Male	151 (68.6)	14 (9.27)		
Smoking history, *n* (%)				
Yes	166 (75.5)	15 (9.03)	0.60	-
No	54 (24.5)	6 (11.11)		
Alcohol consumption history, *n* (%)				
Yes	98 (44.5)	10 (10.2)	0.82	-
No	122 (55.5)	11 (9.01)		
Continued smoking, *n* (%)				
Yes	47 (21.4)	10 (47.62)	0.002	0.004
No	173 (78.6)	11 (52.38)		
Continued alcohol consumption, *n* (%)				
Yes	66 (0.30)	8 (38.1)	0.19	-
No	154 (0.70)	13 (61.9)		
T-stage group, *n* (%)				
1 – 2	44 (0.20)	3 (14.3)	0.18	-
3 – 4	176 (0.80)	18 (85.7)		
N-stage, *n* (%)				
0 – 1	78 (35.5)	6 (28.6)	0.23	-
2 – 3	142 (64.5)	15 (71.4)		
Clinical stage, *n* (%)				
III	79 (35.91)	6 (28.6)	0.27	-
IVA-B	141 (65.09)	15 (71.4)		
Concurrent chemotherapy cycles, *n* (%)				
1	55 (0.25)	5 (23.81)	0.88	-
2 – 3	165 (0.75)	16 (76.19)		
Adjuvant chemotherapy cycles, *n* (%)				
0	76 (34.55)	7 (33.3)	0.82	-
1 – 2	144 (65.45)	14 (66.7)		
Post-C-CRT TE, *n* (%)				
Absent	38 (17.3)	0 (0.0)	<0.001	<0.001
Present	182 (82.7)	21 (100.0)		
Pre-C-CRT TE group, *n* (%)				
≥4	76 (34.5)	17 (22.4)	<0.001	<0.001
<4	127 (65.5)	4 (3.14)		
PIV group, *n* (%)				
≥833	66 (30.0)	17 (25.8)	<0.001	0.001
<833	154 (70.0)	4 (2.6)		
PIV-TE-ORNJ group, *n* (%)*				
Low-risk group	94 (42.7)	1 (1.1)	0.006a	0.009a
Intermediate-risk group	94 (42.7)	6 (6.4)	<0.001[b]	<0.001[b]
High-risk group	32 (14.6)	14 (43.75)	<0.001[c]	<0.001[c]
MMD group, *n* (%)				
<56.4 Gy	163 (74.1)	4 (19.05)	<0.001	0.001
≥56.4 Gy	57 (25.9)	17 (80.95)		

Note: *Bonferroni corrected *P* values for each group (significant Bonferroni corrected *P*-value for three possible comparisons is 0.0167).
Abbreviations: T: Tumor; N: Node; C-CRT: Concurrent chemoradiotherapy; TE: Tooth extraction; PIV: Pan-immune-inflammation value; ORNJ: Osteoradionecrosis of jaws; MMD: Mean mandibular dose.

the PIV-TE-ORNJ index.[29] This novel three-tiered index effectively categorized patients into three distinct ORNJ risk groups: high risk (43.8%), intermediate risk (6.4%), and low risk (1.1%). In addition, although a 6.4% incidence of ORNJ in the intermediate-risk group was consistent with the literature,[7-10] the 43.8% ORNJ incidence observed in the high-risk group was significantly higher than that in any other research. This finding indicates that nearly one out of every two patients in the high-risk group will experience ORNJ at some point during post-C-CRT follow-up, emphasizing the importance of close dentistry follow-up visits, early commencement of prophylactic measures, adoption of non-traumatic or minimally traumatic dental extraction techniques, use of primary tissue closure after TEs, and more careful RT planning in the high-risk groups to keep organ-at-risk doses as low as possible.[43,44] This study also highlighted that the number of TEs serves as a more crucial indicator of the severity of mandibular trauma concerning ORNJ rather than the timing of TEs relative to the head and neck irradiation (pre- versus post-RT). This study revealed that the TE cutoff associated with increased ORNJ risk was ≥4, a finding consistent with the cutoff of >5 established by Tsai *et al.*,[45] that is, a 2.4% risk of ORNJ in patients who underwent ≤5 TEs following RT, whereas the risk increased to 12.1% in those who underwent >5 TEs (Z-score = 4.5062; $P < 0.0001$).

5. Limitations

This study has several limitations. First, the findings presented herein are based on a single institutional retrospective study with a modest cohort size, and they lack associated internal and external validation cohorts. Second, because the PIV is a dynamic biomarker with significant time-dependent fluctuations, the fittest cutoff may differ from the one presented here, which merely reflected single time-point measurements across all patients. Future studies into the PIV obtained during or after C-CRT may be valuable in identifying a more relevant PIV cutoff that may demonstrate a more reliable link with ORNJ rates. Third, the lack of *in vivo* oxygen measurements or vascular abnormalities necessitates considering blood flow measurements and evaluating the tissue oxygenation status in the treatment area before, during, and after C-CRT. This approach may prove valuable in identifying patients at a high risk of developing ORNJ. Fourth, in the absence of correlative analyses, we may have skipped the opportunity to clarify the potential links between ORNJ occurrence and levels of inflammatory biomarkers, such as HIF-1, VGEF, TNF-α, IL-1, IL-6, and TGF-β, which play critical roles in fibrosis formation and hypoxia and thus ORNJ. Fifth, because the study group had TEs before treatment, we were unable to compare the results between patients who had no TEs and those who had single or multiple TEs. However, this patient selection process was conducted intentionally to examine the effect of TE-related jaw trauma severity on the incidence rates of ORNJ. Specifically, we analyzed the correlation between the number of teeth extracted and ORNJ occurrence rather than exclusively focusing on the presence or absence of TE. All participants in this study exhibited poor oral health before C-CRT; therefore, the generalization of our results to all patients with LA-NPC is not feasible. However, given the nearly identical oral health conditions shared by nearly all participants, any associated bias will likely be minimal, if present at all. Considering all these facts together, the current findings are hypothesis-generating rather than concrete guidance until more extensive prospective research can corroborate them.

6. Conclusion

The findings of this retrospective study involving patients with LA-NPC suggest that the newly developed PIV-TE-ORNJ index could effectively categorize patients into three distinct ORNJ risk groups following C-CRT, offering a promising future for oncology practice. However, given the study's retrospective design and its limitation to a single center, further studies are needed to confirm these results before they can be incorporated into routine radiation and dental oncology practice.

Acknowledgments

None.

Funding

None.

Conflict of interest

The authors declare that they have no competing interests.

Author contributions

Conceptualization: All authors
Formal analysis: All authors
Investigation: All authors
Methodology: All authors
Writing–original draft: All authors
Writing–review & editing: All authors

Ethics approval and consent to participate

Baskent University Medical Faculty's Institutional Review Board (IRB No. DKA 19/39) approved the retrospective investigation before collecting patient data. This investigation was carried out in accordance with the principles outlined in the Helsinki Declaration and its later amendments. Before the C-CRT commenced,

all participants provided written informed consent for collecting and publishing associated outcomes, as required by our institution's policies and procedures.

Consent for publication

We ensured that all patients signed an informed consent form before the beginning of the evaluation, either themselves or their legally authorized representatives for acquisition and analysis of the patient's sociodemographic, dental, and medical records; blood samples, and publication of the outcomes.

Availability of data

Data cannot be shared publicly because it is owned and saved by the Baskent University Medical Faculty. However, for researchers who meet the criteria for access to confidential data, data are available from the Baskent University Institutional Data Access/Ethics Committee (contact through Baskent University Ethics Committee): contact address, adanabaskent@baskent.edu.tr.

References

1. Chen YP, Chan ATC, Le QT, Blanchard P, Sun Y, Ma J. Nasopharyngeal carcinoma. *Lancet*. 2019;394:64-80.

   doi: 10.1016/S0140-6736(19)30956-0

2. Su L, She L, Shen L. The current role of adjuvant chemotherapy in locally advanced nasopharyngeal carcinoma. *Front Oncol*. 2022;10:585046.

   doi: 10.3389/fonc.2020.585046

3. De Felice F, Musio D, Terenzi V, *et al*. Treatment improvement and better patient care: Which is the most important one in oral cavity cancer? *Radiat Oncol*. 2014;9:263.

   doi: 10.1186/s13014-014-0263-x

4. De Felice F, de Vincentiis M, Luzzi V, *et al*. Late radiation-associated dysphagia in head and neck cancer patients: Evidence, research and management. *Oral Oncol*. 2018;77:125-130.

   doi: 10.1016/j.oraloncology.2017.12.021

5. Pignon JP, le Maître A, Maillard E, MACH-NC Collaborative Group. Meta-analysis of chemotherapy in head and neck cancer (MACH-NC): An update on 93 randomised trials and 17,346 patients. *Radiother Oncol*. 2009;92:4-14.

   doi: 10.1016/j.radonc.2009.04.014

6. Meleca JB, Zhang E, Fritz MA, Ciolek PJ. Overview and emerging trends in the treatment of osteoradionecrosis. *Curr Treat Options Oncol*. 2021;22:115.

   doi: 10.1007/s11864-021-00915-3

7. Epstein JB, Wong FL, Stevenson-Moore P. Osteoradionecrosis: Clinical experience and a proposal for classification. *J Oral Maxillofac Surg*. 1987;45:104-110.

   doi: 10.1016/0278-2391(87)90399-5

8. Cheng VS, Wang CC. Osteoradionecrosis of the mandible resulting from external megavoltage radiation therapy. *Radiology*. 1974;112:685-689.

   doi: 10.1148/112.3.685

9. Rankow RM, Weissman B. Osteoradionecrosis of the mandible. *Ann Otol Rhinol Laryngol*. 1971;80:603-611.

   doi: 10.1177/000348947108000426

10. Reuther T, Schuster T, Mende U, Kübler A. Osteoradionecrosis of the jaws as a side effect of radiotherapy of head and neck tumour patients--a report of a thirty year retrospective review. *Int J Oral Maxillofac Surg*. 2003;32:289-295.

    doi: 10.1054/ijom.2002.0332

11. Kluth EV, Jain PR, Stuchell RN, Frich JC Jr. A study of factors contributing to the development of osteoradionecrosis of the jaws. *J Prosthet Dent*. 1988;59:194-201.

    doi: 10.1016/0022-3913(88)90015-7

12. Morrish RB Jr., Chan E, Silverman S Jr., Meyer J, Fu KK, Greenspan D. Osteonecrosis in patients irradiated for head and neck carcinoma. *Cancer*. 1981;47:1980-1983.

    doi: 10.1002/1097-0142(19810415)47:8<1980:aid-cncr2820470813>3.0.co;2-y

13. Marx RE. Osteoradionecrosis: A new concept of its pathophysiology. *J Oral Maxillofac Surg*. 1983;41:283-288.

    doi: 10.1016/0278-2391(83)90294-x

14. Garg H, Ramaraj PN, Palekar MG, Jain V. Changing trend in management of Osteoradionecrosis of the mandible: A case report. *Int J Appl Dent Sci*. 2018;4:271-274.

15. Guven DC, Sahin TK, Erul E, Kilickap S, Gambichler T, Aksoy S. The Association between the pan-immune-inflammation value and cancer prognosis: A Systematic review and meta-analysis. *Cancers*. 2022;14:2675.

    doi: 10.3390/cancers14112675

16. Saund DS, Pearson D, Dietrich T. Reliability and validity of self-assessment of mouth opening: A validation study. *BMC Oral Health*. 2012;12:48.

    doi: 10.1186/1472-6831-12-48

17. Lee LE, Ahn SS, Pyo JY, Song JJ, Park YB, Lee SW. Pan-immune-inflammation value at diagnosis independently predicts all-cause mortality in patients with antineutrophil cytoplasmic antibody-associated vasculitis. *Clin Exp Rheumatol*. 2021;129:88-93.

    doi: 10.55563/clinexprheumatol/m46d0v

18. Corti F, Lonardi S, Intini R, *et al*. The pan-immune-inflammation value in microsatellite instability-high metastatic colorectal cancer patients treated with immune checkpoint inhibitors. *Eur J Cancer*. 2021;150:155-167.

doi: 10.1016/j.ejca.2021.03.043

19. Fucà G, Beninato T, Bini M, *et al*. The pan-immune-inflammation value in patients with metastatic melanoma receiving first-line therapy. *Target Oncol*. 2021;16:529-536.

doi: 10.1007/s11523-021-00819-0

20. Zhang L, Xing R, Huang Z, *et al*. Synovial fibrosis involvement in osteoarthritis. *Front Med* (*Lausanne*). 2021;8:684389.

doi: 10.3389/fmed.2021.684389

21. Harth M, Nielson WR. Pain and affective distress in arthritis: Relationship to immunity and inflammation. *Expert Rev Clin Immunol*. 2019;15:541-552.

doi: 10.1080/1744666X.2019.1573675

22. Bhargava D, Jain M, Deshpande A, Singh A, Jaiswal J. Temporomandibular joint arthrocentesis for internal derangement with disc displacement without reduction. *J Maxillofac Oral Surg*. 2015;14:454-459.

doi: 10.1007/s12663-012-0447-6

23. Reher P, Doan N, Bradnock B, Meghji S, Harris M. Effect of ultrasound on the production of IL-8, basic FGF and VEGF. *Cytokine*. 1999;11:416-423.

doi: 10.1006/cyto.1998.0444

24. Albisinni S, Pretot D, Al Hajj Obeid W, *et al*. The impact of neutrophil-to-lymphocyte, platelet-to-lymphocyte and haemoglobin-to-platelet ratio on localised renal cell carcinoma oncologic outcomes. *Prog Urol*. 2019;29:423-431.

doi: 10.1016/j.purol.2019.05.008

25. Beresford MJ, Burcombe R, Ah-See ML, Stott D, Makris A. Pre-treatment haemoglobin levels and the prediction of response to neoadjuvant chemotherapy in breast cancer. *Clin Oncol* (*R Coll Radiol*). 2006;18:453-458.

doi: 10.1016/j.clon.2006.04.006

26. Mo CJ, Hu ZJ, Qin SZ, *et al*. Diagnostic value of platelet-lymphocyte ratio and hemoglobin-platelet ratio in patients with rectal cancer. *J Clin Lab Anal*. 2020;34:e23153.

doi: 10.1002/jcla.23153

27. Koga DH, Salvajoli JV, Alves FA. Dental extractions and radiotherapy in head and neck oncology: Review of the literature. *Oral Dis*. 2008;14:40-44.

doi: 10.1111/j.1601-0825.2006.01351.x

28. Beech NM, Porceddu S, Bats tone MD. Radiotherapy-associated dental extractions and osteoradionecrosis. *Head Neck*. 2017;39:128-132.

doi: 10.1002/hed.24553

29. Yilmaz B, Somay E, Topkan E, Kucuk A, Pehlivan B, Selek U. Utility of pre-chemoradiotherapy pan-immune-inflammation-value for predicting the osteoradionecrosis rates in locally advanced nasopharyngeal cancers. *Strahlenther Onkol*. 2023;11:910-921.

doi: 10.1007/s00066-023-02119-0

30. Khoo SC, Nabil S, Fauzi AA, Yunus SSM, Ngeow WC, Ramli R. Predictors of osteoradionecrosis following irradiated tooth extraction. *Radiat Oncol*. 2021;16:130.

doi: 10.1186/s13014-021-01851-0

31. White SC, Pharoah MJ. *Oral Radiology-E-Book: Principles and Interpretation*. 8th ed. St. Louis, Missouri: Elsevier; 2018.

32. Buglione M, Cavagnini R, Di Rosario F, *et al*. Oral toxicity management in head and neck cancer patients treated with chemotherapy and radiation: Dental pathologies and osteoradionecrosis (Part 1) literature review and consensus statement. *Crit Rev Oncol Hematol*. 2016;97:131-142.

doi: 10.1016/j.critrevonc.2015.08.010

33. Dhanda J, Pasquier D, Newman L, Shaw R. Current concepts in osteoradionecrosis after head and neck radiotherapy. *Clin Oncol* (*R Coll Radiol*). 2016;28:459-466.

doi: 10.1016/j.clon.2016.03.002

34. Chrcanovic BR, Reher P, Sousa AA, Harris M. Osteoradionecrosis of the jaws--a current overview--part 1: Physiopathology and risk and predisposing factors. *Oral Maxillofac Surg*. 2010;14:3-16.

doi: 10.1007/s10006-009-0198-9

35. Notani K, Yamazaki Y, Kitada H, *et al*. Management of mandibular osteoradionecrosis corresponding to the severity of osteoradionecrosis and the method of radiotherapy. *Head Neck*. 2003;25:181-186.

doi: 10.1002/hed.10171

36. Xu J, Zheng Z, Fang D, *et al*. Early-stage pathogenic sequence of jaw osteoradionecrosis *in vivo*. *J Dent Res*. 2012;91:702-708.

doi: 10.1177/0022034512448661

37. Chapchay K, Weinberger J, Eliashar R, Adler N. Anterior skull base reconstruction following ablative surgery for osteoradionecrosis: Case report and review of literature. *Ann Otol Rhinol Laryngol*. 2019;128:1134-1140.

doi: 10.1177/0003489419865558

38. Davis DD, Hanley ME, Cooper JS. Osteoradionecrosis. In: *StatPearls*. Treasure Island, FL: StatPearls Publishing; 2022. Available from: https://www.ncbi.nlm.nih.gov/books/NBK430818 [Last accessed on 2022 May 09].

39. Davì G, Patrono C. Platelet activation and atherothrombosis. *N Engl J Med*. 2007;357:2482-2494.

doi: 10.1056/NEJMra071014

40. Curi MM, Dib LL. Osteoradionecrosis of the jaws: A retrospective study of the background factors and treatment in 104 cases. *J Oral Maxillofac Surg*. 1997;55:540-544; discussion 545-546.

41. Schuurhuis JM, Stokman MA, Witjes MJ, Dijkstra PU,

Vissink A, Spijkervet FK. Evidence supporting pre-radiation elimination of oral foci of infection in head and neck cancer patients to prevent oral sequelae. A systematic review. *Oral Oncol*. 2015;51:212-220.

doi: 10.1016/j.oraloncology.2014.11.017

42. Jiang Y, Zhu X, Qu S. Incidence of osteoradionecrosis in patients who have undergone dental extraction prior to radiotherapy: A systematic review and meta-analysis. *J Oral Maxillofac Surg Med Pathol*. 2014;26:269-275.

doi: 10.1016/j.ajoms.2014.03.010

43. Jawad H, Hodson NA, Nixon PJ. A review of dental treatment of head and neck cancer patients, before, during and after radiotherapy: Part 1. *Br Dent J*. 2015;218:65-68.

doi: 10.1038/sj.bdj.2015.28

44. Sykes A J, Burt P A, Slevin N J, Stout R, Marrs J E. Radical radiotherapy for carcinoma of the oesophagus: An effective alternative to surgery. *Radiother Oncol*. 1998;48:15-21.

doi: 10.1016/s0167-8140(98)00037-1

45. Kuo TJ, Leung CM, Chang HS, *et al*. Jaw osteoradionecrosis and dental extraction after head and neck radiotherapy: A nationwide population-based retrospective study in Taiwan. *Oral Oncol*. 2016;56:71-77.

doi: 10.1016/j.oraloncology.2016.03.005

ACCSCIENCE PUBLISHING

Advances in Radiotherapy & Nuclear Medicine

ORIGINAL RESEARCH ARTICLE

The preventive and protective effects of aspirin on radiation-induced skin injury

Zhaoming Zhou[1,2], Yong Feng[1]*, and Wei Qiao[3]*

[1]Department of Radiation Oncology, Jiangsu Cancer Hospital and Jiangsu Institute of Cancer Research and the Affiliated Cancer Hospital of Nanjing Medical University, Nanjing, Jiangsu, China

[2]Department of Radiation Medicine, Guangdong Provincial Key Laboratory of Tropical Disease Research, School of Public Health, Southern Medical University, Guangzhou, Guangdong, China

[3]Department of Radiology, Jiangsu Cancer Hospital, Jiangsu Institute of Cancer Research and The Affiliated Cancer Hospital of Nanjing Medical University, Nanjing, Jiangsu, China

Abstract

Radiation-induced skin injury (RISI) is a frequent complication of radiotherapy that can severely hinder treatment and endanger patients' lives. Current treatments offer limited efficacy in reducing symptoms. This study explores the protective effect of aspirin (ASP) on RISI and its underlying mechanisms. As *in vivo* RISI models, 8 – 12-week-old C57BL/6 mice were irradiated with a single dose of 20 Gy X-rays to the skin of the right thigh, with sham-irradiated mice serving as controls. ASP was administered orally for 7 days before irradiation. Skin samples were collected on day 14 post-irradiation for single-cell RNA sequencing (sc-RNAseq). RISI severity was assessed daily using a modified RTOG/EORTC scoring system (scores ranging from 1 to 5.5). Our results showed that ASP delayed the onset of RISI and reduced its severity. The sc-RNAseq revealed an increased number of interfollicular epidermal cycling (IFE C) cells in irradiated skin, with some cells showing G2M cell cycle arrest. These IFE C cells exhibited elevated expression of stemness markers, indicating their importance in both RISI damage and subsequent repair. The ASP-treated group showed delayed skin injury onset and reduced peak severity compared to untreated controls. Furthermore, ASP appeared to promote homologous recombination repair of radiation-induced DNA damage, contributing to its protective effect. In conclusion, IFE C cells undergo G2M arrest to repair radiation-induced damage. ASP shows potential in preventing RISI, possibly through enhancing DNA repair. These findings suggest a novel therapeutic role for ASP in mitigating RISI.

Keywords: Radiation-induced skin injury; Single-cell RNA sequencing; Interfollicular epidermal cells; Aspirin; G2/M cell cycle arrest; DNA repair

***Corresponding authors:**
Yong Feng
(fengyong@njmu.edu.cn)
Wei Qiao
(13914707452@njmu.edu.cn)

Citation: Zhou Z, Feng Y, Qiao W. The preventive and protective effects of aspirin on radiation-induced skin injury. *Adv Radiother Nucl Med.* 2025;3(1):57-70. doi: 10.36922/arnm.5829

Received: November 9, 2024

Revised: December 9, 2024

Accepted: January 3, 2025

Published online: January 27, 2025

1. Introduction

Radiation-induced skin injury (RISI) is a common complication in patients undergoing radiotherapy, particularly in cancers that involve the skin or adjacent tissues. The severity of RISI can range from mild erythema to severe necrosis, posing a significant risk to patient well-being and potentially necessitating interruptions in the course of radiotherapy. Such disruptions can compromise the effectiveness of cancer treatment, leading to poorer outcomes for patients[1,2]. The clinical manifestations of RISI include

inflammation, desquamation, ulceration, and in severe cases, necrosis and fibrosis, all of which significantly reduce the quality of life for patients undergoing radiation therapy[1,3].

The pathophysiology of RISI involves complex interactions between radiation-induced DNA damage, inflammation, and impaired wound healing. Ionizing radiation leads to the generation of reactive oxygen species, causing extensive damage to cellular structures, particularly DNA. Double-strand breaks (DSBs) are the most lethal form of DNA damage caused by radiation, and inefficient repair of these lesions results in cell death or senescence. In addition, radiation disrupts the balance of cytokines, resulting in an inflammatory cascade that further exacerbates tissue injury and delays the healing process[1,4]. These challenges highlight the need for innovative therapies that not only address the symptoms of RISI but also target the underlying mechanisms of injury.

Current treatments for RISI remain largely inadequate, often failing to significantly alleviate the symptoms or reverse the damage caused by radiation. Standard care, which includes the use of corticosteroids, non-steroidal anti-inflammatory drugs, and advanced wound dressings, primarily focuses on managing symptoms rather than preventing the occurrence or progression of injury. These interventions provide limited benefit, particularly for severe cases, and do not effectively target the underlying DNA damage or inflammation that drives RISI[3]. The lack of effective preventative measures to protect the skin from radiation underscores the importance of identifying novel agents that can mitigate radiation-induced cellular damage and enhance the skin's innate repair mechanisms.

Recent research has suggested that aspirin (ASP), a non-steroidal anti-inflammatory drug, can help mitigate radiation-induced genotoxic effects through its ability to promote DNA repair. Specifically, ASP has been found to enhance homologous recombination, facilitating the repair of radiation-induced DSBs in DNA, which are a major contributor to cell damage and death following radiation exposure[5]. ASP has also been reported to inhibit the activity of pro-inflammatory pathways, which play a critical role in the inflammatory response to radiation[6]. By both promoting DNA repair and reducing inflammation, ASP may offer a multifaceted protective effect against RISI. This dual mechanism makes ASP an attractive candidate for further investigation as a prophylactic treatment for patients undergoing radiotherapy. ASP's role in DNA repair and inflammation modulation suggests that it could be particularly beneficial in the context of RISI, where both genotoxic stress and inflammation play key roles. Furthermore, previous studies have shown that the homologous recombination pathway is crucial for maintaining genomic stability in the face of radiation damage[7]. ASP's ability to facilitate this pathway may thus enhance cellular resilience to radiation, particularly in interfollicular epidermal (IFE) cells, which are essential for maintaining skin integrity and healing after injury.

Previous studies have demonstrated that ASP exhibits a dual mechanism: Reducing inflammation and promoting DNA repair in normal tissues while sensitizing cancer cells to radiotherapy through cyclooxygenase-2 (COX-2) pathway inhibition. These effects make ASP a promising adjunctive therapy for radiotherapy[8].

The objective of this study was to investigate the preventive and protective effects of ASP in a mouse model of RISI and to elucidate its potential mechanisms of action. We hypothesized that ASP could play a key role in mitigating the severity of RISI by promoting DNA repair in IFE cells, thereby enhancing cellular resilience to radiation-induced damage. By advancing our understanding of ASP's protective mechanisms, this study aims to contribute to the development of more effective strategies to protect patients from the adverse effects of radiation therapy.

2. Materials and methods

2.1. RISI mouse model

To establish the RISI model, we used 8 – 12-week-old female C57BL/6 mice (Guangdong Medical Laboratory Animal Center, China). Mice were maintained in a controlled animal facility under specific pathogen-free conditions, with a temperature of approximately 23°C in a 12-h light/dark cycle. The mice received sterile commercial rodent chow and water ad libitum. For the RISI model, the proximal right hind limb was shaved to expose the thigh skin. The mice were anesthetized using chloral hydrate and properly immobilized. Radiation was delivered using a Varian linear accelerator (6 MV, 3 Gy/min) to administer a single dose of 20 Gy X-ray irradiation to the thigh skin. Control mice underwent the same procedures, including shaving, anesthesia, and immobilization, but were not irradiated[9].

2.2. RISI scoring system

The severity of RISI was assessed using a modified scoring system based on the Radiation Therapy Oncology Group/European Organization for Research and Treatment of Cancer (RTOG/EORTC) grading criteria[10]. This modified system allows for a more detailed and statistically appropriate assessment of RISI severity, with scores ranging from 1 to 5.5. The detailed scoring system used in this study is shown in Table 1, which includes categories from normal skin (score = 1.0) to severe injury (score = 5.5),

Table 1. RISI evaluation criteria

Score	Description
1.0	Normal skin
1.5	Mild erythema and slight dryness
2.0	Moderate erythema and dryness
2.5	Prominent erythema and dry desquamation
3.0	Dry desquamation and slight crust formation
3.5	Dry desquamation, moderate crust formation, and mild epidermal exfoliation
4.0	Moist desquamation in plaques and moderate ulceration
4.5	Large, confluent moist desquamation, ulceration, and significant crusting
5.0	Open ulceration and full-thickness skin loss
5.5	Necrosis

Abbreviation: RISI: Radiation-induced skin injury.

encompassing levels of erythema, dryness, desquamation, and necrosis. Mice were observed daily to monitor the development of skin injury, and the scores were recorded to evaluate the progression of RISI. This refined scoring method enabled more precise differentiation of the injury stages.

2.3. Single-cell RNA sequencing (scRNA-seq)

At 14 days post-irradiation, the onset of injury became evident, and skin samples were collected from the irradiated regions of the experimental group mice and the sham-irradiated regions of the control group mice for scRNA-seq. The skin samples were separated into dermal and epidermal layers by treatment with Dispase II (Sigma-Aldrich, USA) at 37°C for 60 min. The layers were then minced and enzymatically digested in Liberase/DNase solution (Roche, Switzerland) to achieve cell dissociation. Single-cell suspensions were prepared using the Chromium Next GEM single-cell 3' reagent kit v3.1 (10× Genomics, USA), which were subsequently loaded onto the Chromium Controller, targeting the capture of roughly 6,000 cells per sample. Following lysis and reverse transcription, complementary DNA (cDNA) synthesis and library preparation were performed. Sequencing was conducted on the Illumina NextSeq500 platform (Illumina, USA).

2.4. Analysis of scRNA-seq data

Raw reads from each sample were processed using the "count" command of Cell Ranger software version 6.1.2 (10× Genomics, USA), aligning them to the mouse mm[11] (GRCm38) reference genome. The resulting report was evaluated to determine the quality of the samples based on metrics including cell numbers, average reads per cell, fraction of reads in cells, alignment rate, and sequencing saturation. Further filtering was applied to retain only high-quality cells, defined as those with over 200 expressed genes and <5% mitochondrial RNA content. Genes expressed in fewer than three cells were excluded from subsequent analyses. The datasets were normalized using the "LogNormalize" global scaling method. From each sample, 2,000 highly variable genes were selected for downstream analysis. Integration of datasets was performed using the Seurat Find Integration Anchors function followed by the IntegrateData function, using 1 – 40 dimensions. The integrated data were scaled, centered, subjected to dimensionality reduction using principal component analysis (PCA), and clustered at a resolution of 0.6 based on PCA1 – PCA40. Finally, the Uniform Manifold Approximation and Projection technique was used for data visualization.

2.5. Overall differential analysis between irradiated and control groups

To analyze the differences between the irradiated group and control group, t-Distributed Stochastic Neighbor Embedding (tSNE) plots were used to display cell population differences. Heatmaps were generated to present overall gene expression changes between groups. Enrichment analyses were conducted to identify the main pathways involved under different conditions. KEGG pathway enrichment analysis was performed using the enrich KEGG function from the clusterProfiler package[12], focusing on genes with significant changes between groups (*P*-value cutoff of 0.01). This analysis highlighted the key biological pathways affected by radiation treatment, including pro-inflammatory and DNA repair-related pathways. Visualization of enrichment results included dot plots, tree plots, and enrichment maps, which provided insights into the interconnected pathways affected by radiation. In addition, the Gene Set Enrichment Analysis (GSEA)[13] was employed to validate pathway activation and changes post-treatment, focusing on identifying upregulated and downregulated pathways and their impact on the overall cellular response.

2.6. Main cell type annotation and analysis

The identification of major cell types was conducted using classic cell markers such as *Epcam* for epithelial cells[14], *Col3a1* for fibroblasts[15], *Cd3d* for T cells[16], *Ly6c2* for monocytes[17], and *Pecam1* for endothelial cells[18]. These markers facilitated the classification of cells into their respective major categories. The proportions and counts of these cell types were analyzed to determine changes following irradiation. The analysis revealed shifts in cell population dynamics, indicating radiation-induced changes in cellular composition in the skin.

To understand the functional implications of these shifts, the Reactome pathway enrichment analysis was conducted. GSEA was used to evaluate pathway activations across different major cell types post-irradiation. Core pathways such as extracellular matrix organization, chemokine signaling, fatty acyl-CoA metabolism, Rho GTPase activity, and cornified envelope formation were identified. The average expression levels of core genes involved in these pathways were calculated for epithelial cells, fibroblasts, T cells, monocytes, and endothelial cells. The differential activation of these pathways was visualized to highlight the primary mechanisms impacted by radiation and to illustrate potential targets for ASP's protective effects.

2.7. Cell subtype annotation and analysis

For finer subclassification, specific marker genes were used to define each cluster[17]. For instance, IFE cells were identified based on *Krt10*, *Lor*, and *Pgsl1* expression, and further subdivided into IFE basal (IFE B), and IFE keratinized (IFE K) based on differential expression profiles. Similarly, the upper hair follicle (uHF) was distinguished using *Krt17*, *Krt79*, and *Cyb5r3*, and sebaceous gland (SG) markers included *Mgst1* and *Scd1*. For each of these clusters, additional gene markers were used to refine subclassification, incorporating well-established gene markers such as *Krt14*, *Krt15*, and *Lrig1* for infundibulum and bulge regions.

Further subclassification was performed by analyzing comprehensive gene expression profiles, which are visualized in the subsequent tSNE plots and heatmaps. Cluster-specific gene expression was validated with previously reported datasets, which include marker genes for dermal and epidermal skin cell types[19]. For clusters displaying ambiguous classifications, marker gene expression was further analyzed to provide a more precise categorization[19].

2.8. Pseudotime analysis

To further investigate the progression and differentiation of IFE cells during radiation-induced injury, pseudotime trajectory analysis was conducted using Monocle[20]. The scRNAseq data used for this analysis was composed of IFE cells, IFE B1, and IFE B2 cells. Gene expression data were extracted and organized into a cell data set object in Monocle, with further dimension reduction performed using DDRTree. Cells were then ordered along a pseudotemporal trajectory to model the progression of cellular states during injury and recovery. Differential gene expression analysis identified genes involved in radiation response pathways, with *Krt14*, *Krt10*, and *Mki67* serving as key markers for identifying cellular progression along the trajectory.

2.9. ASP treatment and evaluation of protective effects

To assess the protective effects of ASP on RISI, mice in the ASP treatment group were gavaged with ASP (20 mg/kg, once daily) for seven consecutive days before radiation exposure. The corresponding control group received an equal volume of saline. One day after the final gavage, both groups were irradiated with a single dose of 20 Gy X-ray to establish the RISI model. The severity of RISI was monitored daily post-irradiation, and the modified RISI scoring system was used to evaluate the effects of ASP treatment on the development and progression of skin injury.

3. Results

3.1. Overall differential analysis

The differential analysis of irradiated versus control groups revealed significant changes in cell clustering and gene expression patterns. The scRNA-seq data visualized through t-SNE plots showed a distinct separation between the control and irradiated groups, indicating substantial transcriptional reprogramming post-irradiation. Specifically, the control group included 5479 cells, whereas the irradiated group showed a reduction to 3543 cells, highlighting a significant decrease in cellular population after radiation exposure (Figure 1A). Heatmap visualization further illustrated marked differences in gene expression profiles, with notable clusters of genes either upregulated or downregulated between the two conditions. The contrasting colors of the heatmap emphasize the clear distinction in expression levels, suggesting major transcriptional changes following irradiation (Figure 1B). The differential gene expression analysis identified a significant number of differentially expressed genes (DEGs) between the irradiated and control groups. This set of DEGs includes both upregulated genes (n = 257) and downregulated genes (n = 500) (Table S1), which were further analyzed for pathway enrichment. Enrichment analysis showed that upregulated genes were predominantly involved in pathways such as "extracellular matrix organization" and "chemokine receptors bind chemokines" pathways, reflecting increased tissue remodeling and immune signaling activity. On the other hand, downregulated genes were enriched in pathways related to "Rho GTPases activate NADPH oxidases" and "fatty acid metabolism," indicating suppression of cellular processes linked to oxidative stress responses and lipid metabolism (Figure 1C). GSEA provided further validation for the differential pathway activation. The normalized enrichment scores (NES) indicate a shift in pathway activity between the two groups, with some pathways such

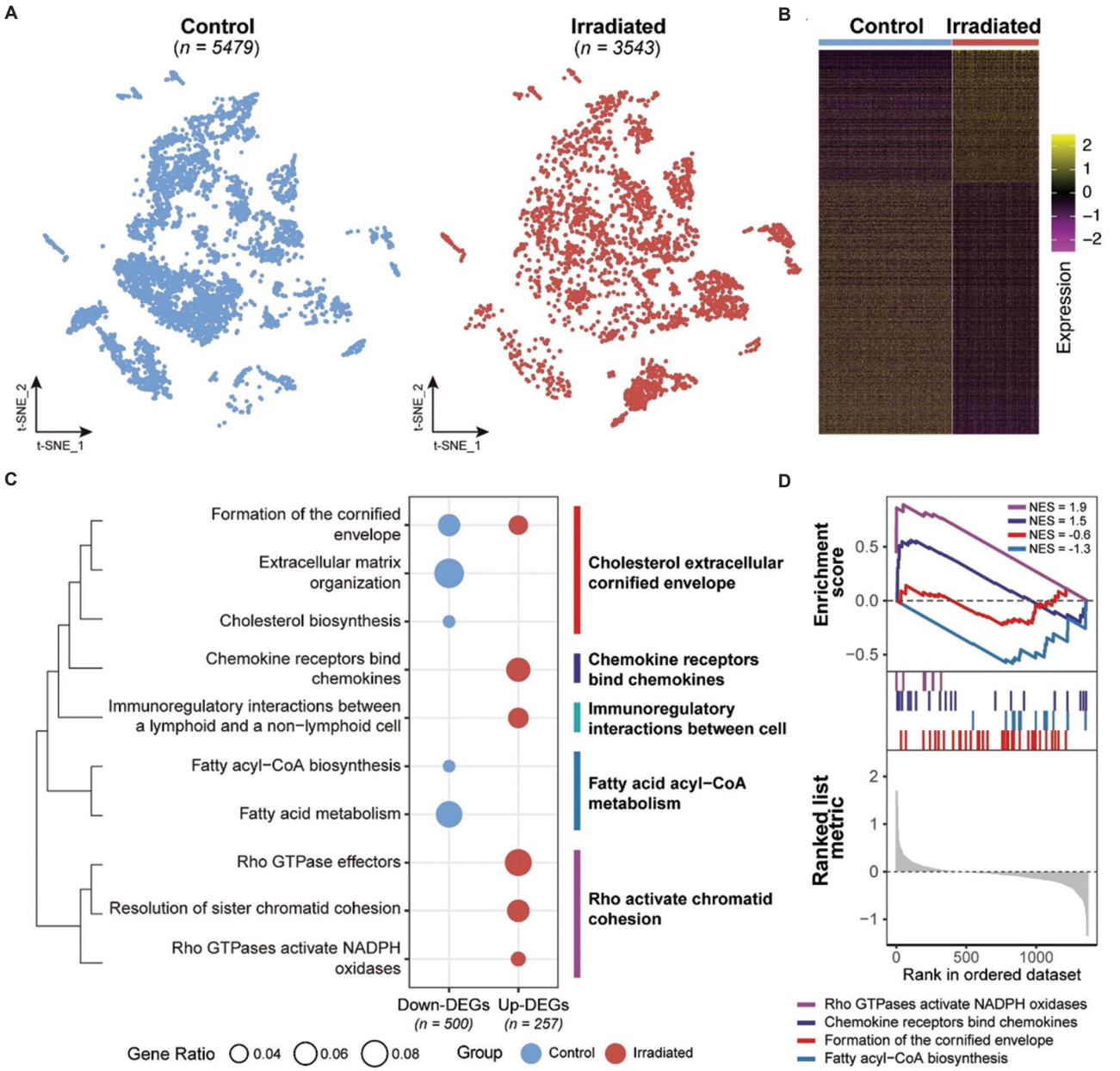

Figure 1. Overall differential analysis between control and irradiated groups. (A) t-SNE plots show the clustering of cells in control versus irradiated groups. The control group consisted of 5,479 cells, whereas the irradiated group had 3,543 cells. (B) Heatmap illustrating the differential gene expression patterns between control and irradiated conditions. Normalized expression levels of genes in the heatmap range from −2 to 2. (C) Enrichment analysis results of DEG between irradiated and control groups. Upregulated genes are enriched in pathways such as extracellular matrix organization and immune regulation, whereas downregulated genes are linked to cellular metabolic processes. (D) GSEA shows the specific upregulation or downregulation trends of major signaling pathways, with enrichment scores indicating pathway shifts following irradiation.
Abbreviations: DEG: Differentially expressed genes; GSEA: Gene set enrichment analysis; NES: Normalized enrichment score; t-SNE: t-Distributed stochastic neighbor embedding.

as "extracellular matrix organization" having an NES of +1.9, indicating substantial upregulation in the irradiated group. In contrast, pathways such as "Rho GTPases activate NADPH oxidases" showed an NES of −1.3, indicating post-irradiation downregulation. This analysis offers a detailed understanding of the specific biological pathways impacted by radiation, including the directionality of their modulation (Figure 1D).

3.2. Main cell type annotation and response to irradiation

Analysis of cell populations in irradiated versus control groups revealed notable differences in the composition of major skin cell types. A total of 9,022 cells were classified into major cell types, including epithelial cells, fibroblasts, T cells, monocytes, and endothelial cells, visualized using t-SNE. Epithelial cells constituted the largest population, followed by fibroblasts, T cells, and other types (Figure 2A). Comparing control and irradiated groups, the average number of cells within each type showed significant changes, with a marked reduction in the number of epithelial cells in the irradiated group (Figure 2B). The proportion of cell types also varied, suggesting that radiation exposure disproportionately affected specific cell populations, reducing epithelial content while maintaining more stable levels of T cells and monocytes. Marker gene analysis showed differential expression across cell types, with key markers such as *Epcam*, *Cd44*, *Ly6c2*, and *Pecam1* being particularly notable. For example, *Ly6c2*, which is related to immune response, displayed elevated levels in irradiated samples, indicating an increased presence of monocytes in response to radiation-induced inflammation (Figure 2C). The t-SNE visualizations focusing on the expression of key marker genes across different cell types demonstrated significant radiation-induced changes. Epithelial cells and fibroblasts exhibited an upregulation of genes associated with extracellular matrix remodeling, reflecting an attempt to repair radiation damage, potentially contributing to fibrosis as part of the skin's response (Figure 2D). Pathway analysis of DEGs across cell types highlighted the involvement of multiple key-signaling pathways, including "cornified envelope," "extracellular matrix," "chemokines," "fatty acyl-CoA synthesis," and "Rho GTPase" pathways. Notably, the "cornified envelope" and "extracellular matrix" pathways were significantly upregulated in irradiated epithelial cells, suggesting disruptions in skin barrier function and increased extracellular matrix activity – key features of the response to radiation injury (Figure 2E).

3.3. Cell subtype annotation analysis

The analysis of cell subtypes identified 13 distinct cell populations. This process was conducted in two major steps. Initially, using known skin cell markers, eight primary cell types were annotated, including IFE B, IFE differentiated (IFE D), IFE K, infundibulum basal (INFU B), outer bulge (OB), inner bulge (IB), SG, and LH (Figure S1A-C). In the next step, four of these major cell types underwent further characterization through comprehensive multigene expression analysis. This additional analysis allowed for finer differentiation of these groups, leading to the identification of specific subtypes[19]: IFE B was further differentiated into IFE B1 and IFE B2, IFE D was differentiated into IFE D1 and IFE D2, and the uHF was differentiated into uHFII, uHFIV, and uHFVI cells, resulting in a total of 13 annotated subtypes (Figure S1D-G, Figure 3B).

The t-SNE plot visualization (Figure 3A) clearly shows the separation between these 13 subtypes, with clusters highlighted for each cell population. A bar plot representation of cell numbers (Figure 3C) revealed variations in cell distributions between the control and irradiated groups, while the cell proportion plot (Figure 3D) depicted distinct changes in the prevalence of each subtype under irradiation conditions. Notably, despite the overall reduction in cell number post-irradiation, the number and proportion of IFE B1 cells were increased in the irradiated group compared to the control group. As this is an intriguing observation, subsequent analyses were primarily focused on the IFE B cell population.

Further analysis examined the cell cycle distribution of the two IFE B cell subtypes and revealed that the majority of cells in the G2M phase were present in the IFE B1 subpopulation (Figure 3E and F). Compared to other IFE B cells, IFE B1 cells exhibited higher expression levels of *Cdk1* and *Ccnb1*, leading us to define these actively cycling cells as IFE Cycling (IFE C) cells (Figure 3G and H). We then analyzed stem cell marker expression[21] across different IFE cell subtypes, revealing that IFE C cells exhibited the highest expression of the stem cell marker *Krt14*, suggesting the highest level of stemness within this subgroup (Figure 3I). In addition, comparing control and irradiated groups, we found that the expression of cell cycle markers *Cdk1* and *Ccnb1* was reduced post-irradiation, whereas the expression of the stemness marker Krt14 was elevated in the irradiated group (Figure 3J). Based on these observations, we hypothesize that IFE C cells serve as a reservoir for IFE cell populations. Upon irradiation, IFE C cells in mouse skin experience cell cycle arrest in the G2M phase. However, should these cells successfully bypass the G2M checkpoint, they could rapidly proliferate and differentiate to replenish epidermal cells in the skin.

3.4. Pseudotime analysis of IFE cells

A pseudotime analysis was performed on the major IFE cell populations to understand their differentiation trajectories. Figure 4 (A-C) shows the differentiation path of IFE subtypes, with IFE C cells positioned upstream in the differentiation process, confirming our previous hypothesis that IFE C serves as an origin cell type for further differentiation. The trajectory visualization highlights that IFE C cells are found at the beginning of the differentiation path, with subsequent transitions to other subtypes.

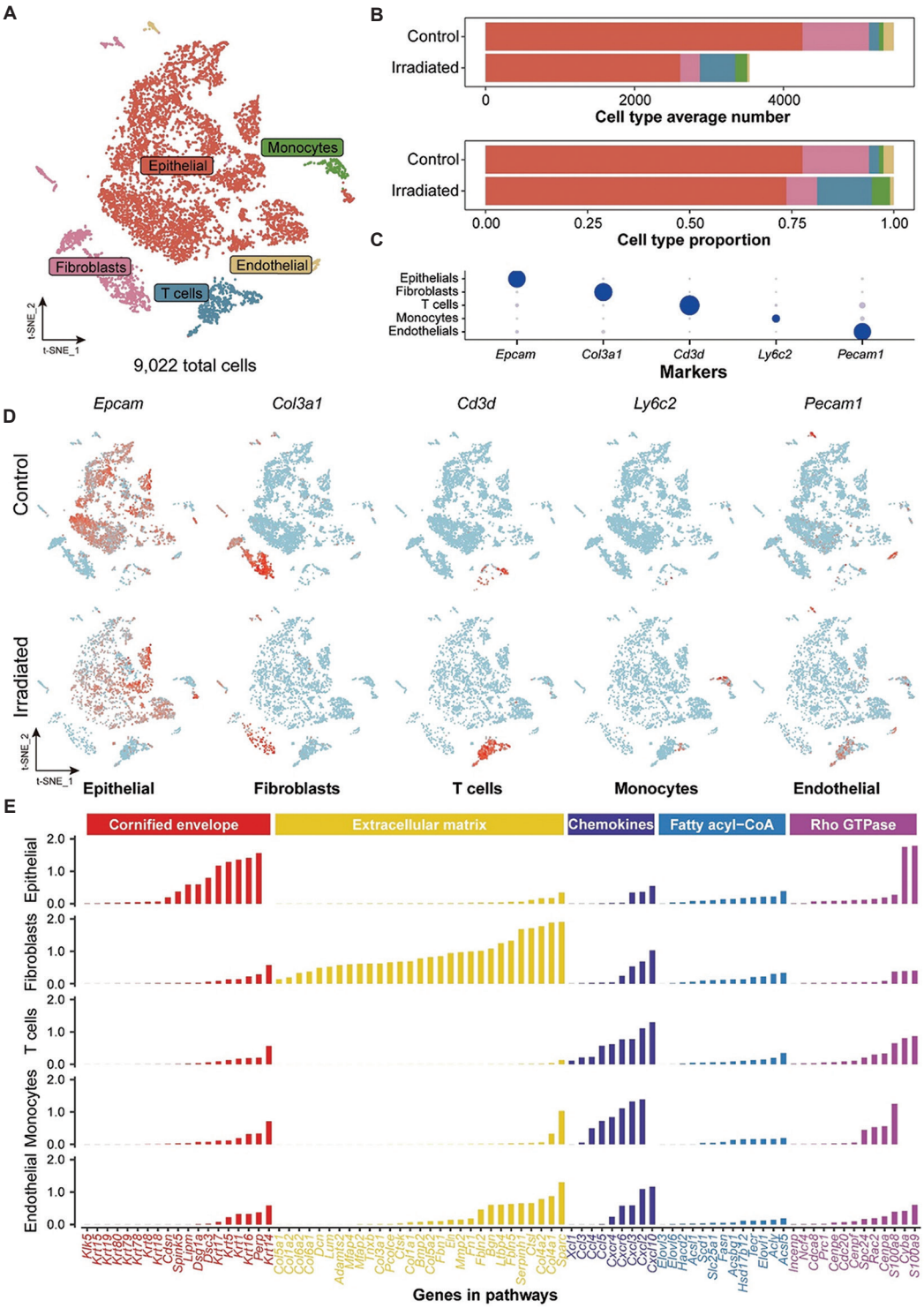

Figure 2. Cell type composition and differential gene expression in irradiated versus control groups. (A) t-SNE visualization of sc-RNAseq data shows distinct clustering of major skin cell types in irradiated and control conditions. Major cell types include epithelial cells, fibroblasts, T cells, monocytes, and endothelial cells. (B) Bar plot illustrates the number and average proportion of each cell type under control and irradiated conditions. (C) Dot plot of key markers, including *Cd34*, *Krt14*, *Ly6a*, and *Pecam1*, to demonstrate marker-specific expression across different clusters, helping to define cell identities. (D) t-SNE plots show the expression of specific marker genes across the cell types. Markers depicted include those important for epithelial identity, fibrosis, immune response, and endothelial function. (E) Pathway enrichment analysis for key upregulated and downregulated pathways among irradiated versus control samples. Abbreviations: sc-RNAseq: Single-cell RNA sequencing; t-SNE: t-Distributed stochastic neighbor embedding.

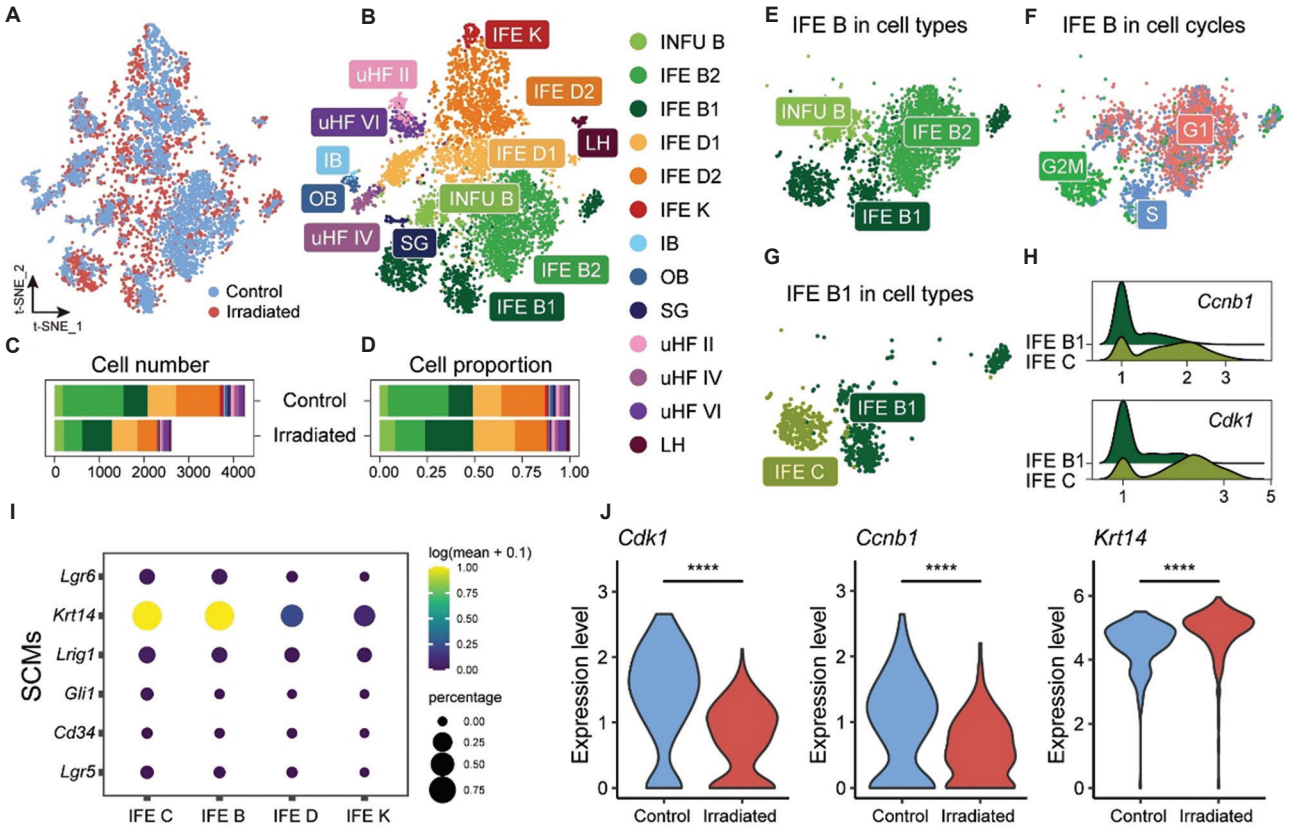

Figure 3. Detailed characterization and subtype analysis of irradiated versus control skin cells. (A) t-SNE plot comparing cell distributions in control (blue) and irradiated conditions (red). (B) t-SNE clustering shows the 13 identified cell subtypes, which include IFE B, IFE D, and others, after comprehensive cell characterization. (C) Bar plot represents the total number of cells in each subtype for control and irradiated conditions, with an increase observed in specific subtypes such as IFE B1 in irradiated skin. (D) Proportional distribution of each cell subtype across control and irradiated groups. (E-G) t-SNE plots highlighting the localization of IFE B cells among other epidermal cell types, the cell cycle distribution (G1, S, G2/M phases) in the IFE B population, and further stratification of the IFE B1 population into IFE C. (H) Density plots show the expression levels of cell cycle regulators *Cdk1* and *Ccnb1* in IFE B1 and IFE C cells. (I) Dot plot visualizes the expression of stem cell markers (Lrig1, Krt14, Lgr5, Gli1, and Cd34) across different epidermal cell types. (J) Higher expression of *Krt14* in irradiated samples whereas cycling genes *Cdk1* and *Ccnb1* show a decrease.

Note: ****indicates significance at $p<0.001$.

Abbreviations: IB: Inner bulge; IFE: Interfollicular epidermis; IFE B: IFE basal; IFE D: IFE differentiated; IFE K: IFE keratinized; INFU B: Infundibulum basal; LH: Langerhans cells; OB: Outer bulge; SG: Subcutaneous gland; SCMs: Stem cell markers; t-SNE: t-Distributed stochastic neighbor embedding; uHF: upper-hair follicle.

Further analysis of gene expression along pseudotime (Figure 4D) indicated distinct gene expression profiles associated with different pseudotime states, corresponding to different stages of differentiation. Clusters of genes such as those involved in skin development, response to radiation, and G2M cell cycle transition were identified as key players in these transitions. Cluster 1 (C1) genes, associated with skin development and keratinocyte differentiation, were highly expressed in early pseudotime, indicative of stemness and differentiation capability. Cluster 2 (C2) genes, including those related to response to radiation and cell cycle regulation, were more prominent in later stages.

In Figure 4E, the expression dynamics of key marker genes along the pseudotime trajectory are shown, with IFE C cells exhibiting high expression of stemness markers such as *Krt14*, whereas cycling markers such as *Cdk1* and *Ccnb1* decreased along the differentiation path. Notably, in irradiated conditions, these cycling markers were significantly reduced, while *Krt14* expression was elevated, suggesting a potential mechanism where radiation exposure induces cell cycle arrest but enhances stem cell properties of IFE C cells. This supports our hypothesis that IFE C cells act as progenitor cells and, upon successful progression past G2M arrest, possess the capacity to repopulate epithelial cells in the skin.

3.5. Molecular characterization of arrested and cycling cells within the irradiated IFE-C population

To further investigate the molecular differences between the G2M-arrested cells (Irra_Arrest) and those that have

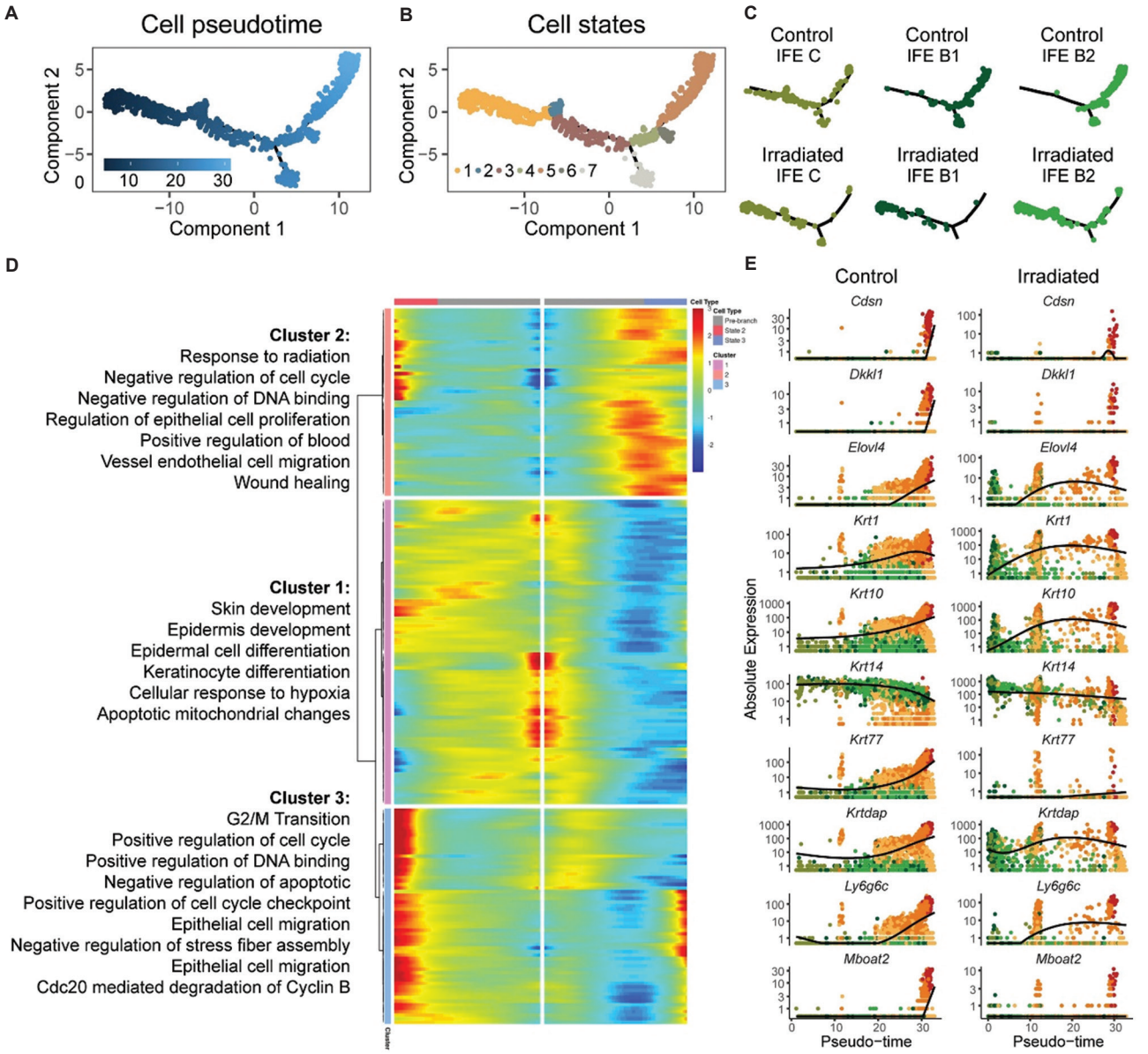

Figure 4. Pseudotime analysis of IFE cells. (A-C) Pseudotime trajectory of IFE subtypes shows differentiation pathways with IFE C cells positioned as upstream progenitors, highlighting their role in skin regeneration. (D) Heatmap shows gene expression along pseudotime. Cluster analysis reveals genes involved in skin development (Cluster 1), radiation response (Cluster 2), and G2M cell cycle transition (Cluster 3) at various differentiation stages. (E) Expression trends of key marker genes across pseudotime. Stemness markers such as *Krt14* are highly expressed in IFE C cells, whereas cycling markers such as *Cdk1* and *Ccnb1* decrease along differentiation, particularly post-irradiation.
Abbreviations: IFE: Interfollicular epidermis; IFE B: IFE basal; IFE C: IFE cycling.

progressed through the phase (Irra_Cycling) within the irradiated IFE-C population, we performed a Gene Set Variation Analysis (GSVA) using KEGG pathways (Figure S2). The results indicated significant pathway differences between the two subgroups of irradiated IFE-C cells.

The top pathways enriched in the Irra_Arrest group included those involved in immune response and inflammation, such as "natural killer cell-mediated cytotoxicity" and "cytokine-cytokine receptor interaction." These pathways are known to be related to immune activation and could imply a heightened immune response in the arrested cells as a consequence of radiation-induced stress. Other enriched pathways included those related to cell adhesion and signaling, such as "cell adhesion molecules" and "JAK-STAT signaling pathway," suggesting

that the arrested cells may be preparing for an immune-related response or stress adaptation.

In contrast, the Irra_Cycling cells showed significant enrichment in pathways related to metabolism, DNA repair, and cell cycle progression. Specifically, pathways such as "homologous recombination," "non-homologous end joining," "DNA replication," and "cell cycle" were highly enriched in cycling cells, suggesting a focus on cellular recovery, enhanced DNA repair mechanisms, and division. Notably, pathways such as "pyrimidine metabolism" and "purine metabolism" were also upregulated, pointing to active nucleotide synthesis needed for cell proliferation.

These distinct pathway differences suggest that irradiated arrested cells are largely engaged in immune and stress responses, whereas the corresponding cycling cells are focused on DNA repair and metabolic activity, aiming for proliferation and tissue recovery. We hypothesize that following irradiation, IFE C cells either enter an arrest state due to DNA damage or successfully repair the damage and re-enter the cell cycle. The activation of DNA repair pathways, such as homologous recombination and non-homologous end joining, likely promotes the recovery of these cells and contributes to the resolution of RISI (Figure S2).

3.6. ASP's effect on RISI progression

To further understand the impact of ASP on RISI, we evaluated RISI severity using daily recorded scores and performed additional analyses (Figure 5).

The trend of RISI scores over time indicated that the peak RISI score was significantly lower in the ASP-treated group compared to the untreated control group, demonstrating a reduction in injury severity by the treatment. Specifically, the peak RISI score in the untreated group was approximately 30, whereas the ASP-treated group peaked at around 20 (Figure 5A). The time taken for each group to reach a significant RISI score threshold (>3.5) showed no significant difference between the two groups (Figure 5B). However, the mean RISI scores between days 18 and 20 were notably lower in the ASP-treated group compared to the corresponding untreated controls, suggesting that ASP effectively reduced the injury severity during the peak period (Figure 5C). The duration for which the RISI score remained above the threshold of 3.5 was significantly shorter in the ASP-treated group than in the untreated group, indicating that ASP reduced the period of severe injury (Figure 5D).

These findings suggest that ASP pre-treatment provides a significant protective effect against RISI, reducing both the peak severity and the duration of high injury levels. This effect is likely mediated through the activation of DNA repair pathways and modulation of inflammatory responses.

4. Discussion

The findings of this study demonstrate that ASP pre-treatment has significant prophylactic effects against RISI in a mouse model. Our results indicate that ASP not only reduces the severity of RISI but also promotes the recovery of IFE cells through mechanisms that may involve enhanced DNA repair and modulation of cell cycle dynamics. This study represents a comprehensive effort to explore the protective effect of ASP at both the molecular and cellular levels, with implications for its potential clinical application as an adjunct therapy during radiotherapy.

One of the key findings in this study is the reduction in overall RISI severity in ASP-treated mice, as evidenced by delayed onset, reduced peak scores, and a shortened duration of high-severity injury. These effects are particularly striking when viewed alongside our comprehensive scoring system, which provides a detailed assessment of RISI progression. This detailed assessment allowed us to differentiate multiple phases of injury progression and identify the specific points at which ASP exerted its beneficial effects. The reduction in peak RISI severity and the shortened duration of high injury levels are likely driven by ASP's ability to modulate the inflammatory response and promote effective DNA repair (Figure 5). These observations are consistent with previous studies that have reported anti-inflammatory effects and DNA repair properties of ASP[5,22].

The differential gene expression analysis of irradiated versus control groups provided important insights into the molecular changes induced by radiation. The irradiated group exhibited significant transcriptional reprogramming, with a large number of genes associated with extracellular matrix organization and immune regulation being upregulated, while metabolic processes were downregulated. These findings suggest that radiation induces a stress response that shifts cellular focus from normal metabolic activity to survival and adaptation[23]. ASP treatment, by mitigating the inflammatory response and potentially reducing the extent of tissue damage, may help preserve the normal cellular environment, thereby preventing excessive tissue remodeling and fibrosis[24].

The cell subtype annotation analysis and pseudotime trajectory mapping provide additional insights into the role of ASP in protecting skin cells from radiation-induced damage. We observed that the IFE C cells, identified as the cycling population among the IFE subtypes, were located at the upstream end of the differentiation trajectory. This

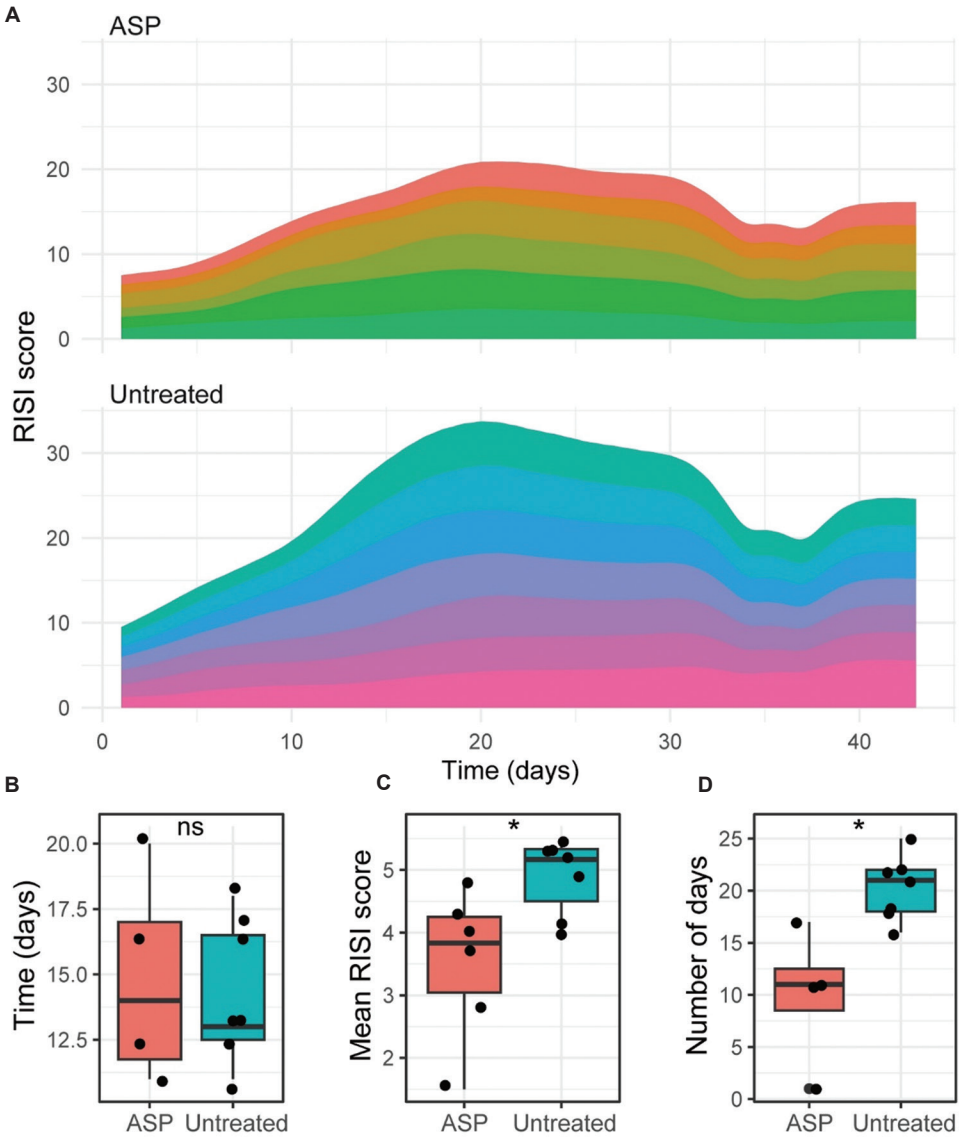

Figure 5. Effect of ASP on RISI. (A) Trend of RISI scores over time in ASP-treated versus untreated control groups. (B) Boxplot shows the time required for each group to reach an RISI score above the threshold (>3.5). No significant difference was observed between the groups. (C) Boxplot of mean RISI scores between days 18 and 20, with ASP-treated mice showing significantly lower scores compared to controls. (D) Duration of which irradiated mouse models show a RISI score above 3.5. ASP-treated mice showed a significantly shorter duration.
Note: *indicates significance at $p < 0.05$.
Abbreviations: ASP: Aspirin; ns: Not significant; RISI: Radiation-induced skin injury.

positioning suggests that IFE C cells act as progenitors for subsequent differentiation. Our results further show that radiation exposure caused a reduction in cycling markers such as *Cdk1* and *Ccnb1* while increasing the expression of the stemness marker, *Krt14*. This indicates that radiation exposure may induce G2M arrest in IFE C cells, leading to an enrichment of cells with stem-like properties. The observation that ASP-treated mice exhibited reduced RISI, suggests that ASP may help overcome radiation-induced cell cycle arrest and promote tissue regeneration.

In the context of radiation-induced cell cycle arrest, the GSVA highlighted critical differences between the arrested and cycling IFE C populations in irradiated conditions. The arrested cells showed increased activity in immune-related pathways such as "natural killer cell-mediated cytotoxicity" and "cytokine-cytokine receptor interaction" pathways. This implies that radiation-induced arrest is associated with an increased immune response, potentially reflecting a mechanism by which cells attempt to clear damaged components and maintain tissue integrity. On the other

hand, the cycling cells were enriched in pathways related to DNA repair, including "homologous recombination" and "non-homologous end joining" pathways, which are the primary repair mechanisms for DNA DSBs during most of the cell cycle[25,26]. These findings suggest that IFE C cells that successfully initiate DNA repair mechanisms can progress through the cell cycle and contribute to tissue recovery. ASP appears to promote this process, possibly by modulating the activity of DNA repair pathways and reducing oxidative stress as well as helping DNA repair[5].

The modified RISI scoring system based on the RTOG/EORTC criteria[10] proved to be highly effective for evaluating skin injury in this study. The scoring system allowed for a nuanced assessment of RISI severity, capturing changes in erythema, dryness, desquamation, and necrosis at various stages. The daily observation of mice and the detailed scoring system provided a robust dataset that highlighted differences in the temporal progression of RISI between ASP-treated and untreated groups. ASP-treated mice exhibited delayed onset and lower peak severity of RISI, underscoring the protective effects of ASP against radiation-induced damage. This refined scoring approach could be highly valuable in future pre-clinical studies investigating potential treatments for RISI.

ASP's role in normal tissue protection and tumor radiosensitivity is distinct. While it facilitates DNA repair in normal tissues, studies have shown its potential to enhance cancer cell radiosensitivity by downregulating COX-2 and inducing apoptosis[27]. This dual mechanism underlines its therapeutic potential in radiotherapy. ASP's protective effects against RISI are likely multifaceted, involving modulation of both immune response and cell cycle dynamics. Previous studies have shown that ASP can act as a radiosensitizer in certain cancer types by inhibiting key signaling pathways such as COX-2, which is involved in inflammation and tumor progression[8,28]. In the context of RISI, it is plausible that ASP's anti-inflammatory properties help to mitigate the inflammatory response following radiation, thus reducing tissue damage and improving overall skin health. Furthermore, our results suggest that ASP may enhance the DNA repair capacity of IFE C cells, thereby allowing them to overcome radiation-induced G2M arrest and re-enter the cell cycle, which is essential for tissue regeneration.

The increased proportion of IFE B1 cells observed in the irradiated group compared to the control group is an intriguing finding that warrants further investigation. The IFE B1 cells are characterized by higher expression levels of *Cdk1* and *Ccnb1*, indicating active cycling and proliferation. Following irradiation, the enrichment of IFE B1 cells may represent a compensatory mechanism aimed at maintaining epithelial integrity by promoting cell proliferation. ASP treatment appears to support this compensatory response by reducing the severity of radiation-induced damage and enabling these cells to proliferate and replace damaged tissue.

Our findings also raise important questions regarding the long-term impact of ASP treatment in the context of radiation exposure. While ASP has demonstrated clear benefits in reducing the severity of RISI in the short term, the potential effects on long-term skin health and carcinogenesis require further exploration. The use of ASP in clinical settings has been associated with reduced risk of certain cancers, and it will be important to determine whether these protective effects extend to radiation-induced carcinogenesis in skin tissue[27,29,30]. In addition, understanding the precise molecular mechanisms through which ASP enhances DNA repair and modulates the immune response will provide valuable insights into its potential applications in radiotherapy. Although scRNA-seq of ASP-treated samples was not performed in this study due to resource limitations, such analyses could offer detailed insights into the molecular pathways modulated by ASP. Future studies should investigate this direction to validate and expand upon the findings reported here. Besides, the presence of tumors can significantly alter signaling pathways, potentially modifying the efficacy of ASP in mitigating RISI. Investigating ASP's effects in tumor-bearing mouse models could provide clinically relevant insights and enhance the translational potential of our findings. This represents an important direction for future research.

5. Conclusion

Our study provides compelling evidence that ASP pre-treatment exerts a protective effect against RISI in a mouse model. This protection is probably mediated through multiple mechanisms, including modulation of the immune response, enhancement of DNA repair, and promotion of cell cycle re-entry in irradiated cells. These findings suggest that ASP could be a promising adjunct therapy for mitigating the side effects of radiotherapy, particularly in reducing skin toxicity. Future studies should focus on elucidating the detailed molecular mechanisms underlying these protective effects and exploring the potential of ASP in combination with other therapeutic agents to enhance skin recovery and reduce radiation-related complications.

Acknowledgments

None.

Funding

None.

Conflict of interest

The authors declare they have no competing interests.

Author contributions

Conceptualization: Zhaoming Zhou, Wei Qiao
Data curation: All authors
Formal analysis: Yong Feng
Funding acquisition: Wei Qiao
Investigation: Zhaoming Zhou
Methodology: Zhaoming Zhou
Project administration: Yong Feng
Resources: Wei Qiao
Software: Zhaoming Zhou
Supervision: Wei Qiao
Validation: Zhaoming Zhou
Visualization: Zhaoming Zhou
Writing – original draft: Zhaoming Zhou
Writing – review & editing: All authors

Ethics approval and consent to participate

This study did not include human participants, human data, or human tissue. The animal experiments were carried out in accordance with ethical procedures and the protocols were approved by the Ethics Committee for Laboratory Animals of the Southern Medical University (L2019074).

Consent for publication

Not applicable.

Availability of data

The data used in this study will be available from the corresponding author upon reasonable request.

References

1. Wei J, Meng L, Hou X, *et al*. Radiation-induced skin reactions: Mechanism and treatment. *Cancer Manag Res*. 2018;11:167-177.

   doi: 10.2147/CMAR.S188655

2. Brown KR, Rzucidlo E. Acute and chronic radiation injury. *J Vasc Surg*. 2011;53(15):15S-21S.

   doi: 10.1016/j.jvs.2010.06.175

3. Wang Y, Tu W, Tang Y, Zhang S. Prevention and treatment for radiation-induced skin injury during radiotherapy. *Radiat Med Prot*. 2020;1(2):60-68.

   doi: 10.1016/j.radmp.2020.02.004

4. Kim JH, Kolozsvary AJJ, Jenrow KA, Brown SL. Mechanisms of radiation-induced skin injury and implications for future clinical trials. *Int J Radiat Biol*. 2013;89:311-318.

   doi: 10.3109/09553002.2013.765055

5. Jiang H, Swacha P, Aung KM, Gekara NO. Aspirin protects against genotoxicity by promoting genome repair. *Cell Res*. 2023;33(4):325-327.

   doi: 10.1038/s41422-023-00783-6

6. Laube M, Kniess T, Pietzsch J. Development of antioxidant COX-2 inhibitors as radioprotective agents for radiation therapy-A hypothesis-driven review. *Antioxidants* (*Basel*). 2016;5(2):14.

   doi: 10.3390/antiox5020014

7. Li X, Heyer WD. Homologous recombination in DNA repair and DNA damage tolerance. *Cell Res*. 2008;18(1):99-113.

   doi: 10.1038/cr.2008.1

8. Kim KY, Seol JY, Jeon GA, Nam MJ. The combined treatment of aspirin and radiation induces apoptosis by the regulation of bcl-2 and caspase-3 in human cervical cancer cell. *Cancer Lett*. 2003;189(2):157-166.

   doi: 10.1016/S0304-3835(02)00519-0

9. Curras-Alonso S, Soulier J, Defard T, *et al*. An interactive murine single-cell atlas of the lung responses to radiation injury. *Nat Commun*. 2023;14(1):2445.

   doi: 10.1038/s41467-023-38134-z

10. Hoeller U, Tribius S, Kuhlmey A, Grader K, Fehlauer F, Alberti W. Increasing the rate of late toxicity by changing the score? A comparison of RTOG/EORTC and LENT/SOMA scores. *Int J Radiat Oncol Biol Phys*. 2003;55(4):1013-1018.

   doi: 10.1016/S0360-3016(02)04202-5

11. Gribov A, Sill M, Lück S, *et al*. SEURAT: Visual analytics for the integrated analysis of microarray data. *BMC Med Genomics*. 2010;3(1):21.

   doi: 10.1186/1755-8794-3-21

12. Yu G, Wang LG, Han Y, He QY. clusterProfiler: An R package for comparing biological themes among gene clusters. *OMICS*. 2012;16(5):284-287.

   doi: 10.1089/omi.2011.0118

13. Reimand J, Isserlin R, Voisin V, *et al*. Pathway enrichment analysis and visualization of omics data using g: Profiler, GSEA, Cytoscape and EnrichmentMap. *Nat Protoc*. 2019;14(2):482-517.

   doi: 10.1038/s41596-018-0103-9

14. Nguyen QH, Pervolarakis N, Blake K, *et al*. Profiling human breast epithelial cells using single cell RNA sequencing identifies cell diversity. *Nat Commun*. 2018;9:2028.

   doi: 10.1038/s41467-018-04334-1

15. Vorstandlechner V, Laggner M, Kalinina P, *et al*. Deciphering

the functional heterogeneity of skin fibroblasts using single-cell RNA sequencing. *FASEB J*. 2020;34(3):3677-3692.

doi: 10.1096/fj.201902001RR

16. Szabo PA, Levitin HM, Miron M, *et al*. Single-cell transcriptomics of human T cells reveals tissue and activation signatures in health and disease. *Nat Commun*. 2019;10(1):4706.

doi: 10.1038/s41467-019-12464-3

17. Paldor M, Levkovitch-Siany O, Eidelshtein D, *et al*. Single-cell transcriptomics reveals a senescence-associated IL-6/CCR6 axis driving radiodermatitis. *EMBO Mol Med*. 2022;14(8):e15653.

doi: 10.15252/emmm.202115653

18. Lehmann GL, Hanke-Gogokhia C, Hu Y, *et al*. Single-cell profiling reveals an endothelium-mediated immunomodulatory pathway in the eye choroid. *J Exp Med*. 2020;217(6):e20190730.

doi: 10.1084/jem.20190730

19. Joost S, Annusver K, Jacob T, *et al*. The molecular anatomy of mouse skin during hair growth and rest. *Cell Stem Cell*. 2020;26(3):441-457.e7.

doi: 10.1016/j.stem.2020.01.012

20. Morse M, Lennon N, Livak K. *Monocle: Cell Counting, Differential Expression, and Trajectory Analysis for Single-cell RNA-Seq Experiments*; 2016. Available from: https://www.semanticscholar.org/paper/monocle-%3a-cell-counting-%2c-differential-expression-%2c-morse-lennon/c7147e72a6ff07dacf7e72d9e2664d87d00f5b29 [Last Accessed on 2024 Nov 08].

21. Joost S, Zeisel A, Jacob T, *et al*. Single-cell transcriptomics reveals that differentiation and spatial signatures shape epidermal and hair follicle heterogeneity. *Cell Syst*. 2016;3(3):221-237.e9.

doi: 10.1016/j.cels.2016.08.010

22. Cuzick J, Otto F, Baron JA, *et al*. Aspirin and non-steroidal anti-inflammatory drugs for cancer prevention: An international consensus statement. *Lancet Oncol*. 2009;10(5):501-507.

doi: 10.1016/S1470-2045(09)70035-X

23. Sisakht M, Darabian M, Mahmoodzadeh A, *et al*. The role of radiation induced oxidative stress as a regulator of radio-adaptive responses. *Int J Radiat Biol*. 2020;96(5):561-576.

doi: 10.1080/09553002.2020.1721597

24. Dong Z, Yang L, Jiao J, *et al*. Aspirin in combination with gastrodin protects cardiac function and mitigates gastric mucosal injury in response to myocardial ischemia/reperfusion. *Front Pharmacol*. 2022;13:995102.

doi: 10.3389/fphar.2022.995102

25. Zhao B, Rothenberg E, Ramsden DA, Lieber MR. The molecular basis and disease relevance of non-homologous DNA end joining. *Nat Rev Mol Cell Biol*. 2020;21(12):765-781.

doi: 10.1038/s41580-020-00297-8

26. Ensminger M, Löbrich M. One end to rule them all: Non-homologous end-joining and homologous recombination at DNA double-strand breaks. *Br J Radiol*. 2020;93(1115):20191054.

doi: 10.1259/bjr.20191054

27. Alfonso L, Ai G, Spitale RC, Bhat GJ. Molecular targets of aspirin and cancer prevention. *Br J Cancer*. 2014;111(1):61-67.

doi: 10.1038/bjc.2014.271

28. Salehifar E, Hosseinimehr SJ, Thorat MA, Cuzick J. The use of cyclooxygenase-2 inhibitors for improvement of efficacy of radiotherapy in cancers. *Drug Discov Today*. 2016;21(4):654-662.

doi: 10.1016/j.drudis.2016.02.019

29. Thun MJ, Jacobs EJ, Patrono C. The role of aspirin in cancer prevention. *Nat Rev Clin Oncol*. 2012;9:259-267.

doi: 10.1038/nrclinonc.2011.199

30. Thorat MA, Cuzick J. Role of aspirin in cancer prevention. *Curr Oncol Rep*. 2013;15(6):533-540.

doi: 10.1007/s11912-013-0351-3

ACCSCIENCE PUBLISHING

Advances in Radiotherapy & Nuclear Medicine

ORIGINAL RESEARCH ARTICLE

Dosimetric analysis of the cone beam-focused gamma knife

Shan-Chuan Li[1,2], Shao-Run Gong[3], Xiao-Feng Zhang[2], Gang Li[3], Feng Zhang[2], Jun-Feng Wang[2]*, Shuang Zhang[2], Chun-Li Zhang[3], and Jun Li[3]

[1]Xi'an Zhenhe Medical Technology Company Limited, Xi'an, Shaanxi, China

[2]CNNC Cheng Imaging (Xi'an) Medical Equipment Company Limited, Xi'an, Shaanxi, China

[3]CNNC High Energy Equipment (Tianjin) Company Limited, Tianjin, China

Abstract

This study presents the first report on the fundamental dosimetric characterization of a novel image-guided radiosurgery system – the ZND-A Smart Knife (CNCI Co., Ltd, Xi'an, China). The dosimetric performance of this radiosurgery system was evaluated based on key parameters, including positioning reference point deviation, nominal focal point dose rate, focusing field size, dose gradient, and comprehensive error in dose calculation. The system employs "triple rotating and focusing" technique, and its dosimetric characteristics were measured. The maximum positioning reference point deviation for collimator #1 – 4 was 0.38 mm; the corresponding dose gradients were 3.1 mm, 3.4 mm, 5.4 mm, and 7.7 mm, respectively. In dose calculation, the maximum isocenter point dose deviation was 3.3%, and the area overlap ratio for the largest collimator (#4) reached 98.3%. These results demonstrate excellent dosimetric performance and clinical potential, confirming the safety and precision of the next-generation cone beam-focused gamma knife system.

Keywords: Cone beam-focused gamma knife; EBT3 film; Electrostatic meter; Radiation dosimetry; Stereotactic radiation therapy

***Corresponding author:**
Jun-Feng Wang
(wangjunfeng@cnci-ms.com)

Citation: Li S, Gong S, Zhang X, *et al*. Dosimetric analysis of the cone beam-focused gamma knife. *Adv Radiother Nucl Med*. 2025;3(1):71-81.
doi: 10.36922/arnm.6280

Received: November 19, 2024

1st revised: November 28, 2024

2nd revised: December 31, 2024

3rd revised: January 23, 2025

4th revised: February 5, 2025

Accepted: February 5, 2025

Published online: March 3, 2025

1. Introduction

With the rapid economic and social development in China, cancer incidence among Chinese residents has been increasing year by year. Thus, cancer prevention and treatment have become an important public health issue in China.[1] Stereotactic radiotherapy (SRT) is a method of treating tumors by irradiating the lesion, including potential surrounding regions, with multiple beams and angles to maximize therapeutic efficacy. It effectively addresses the limitations of conventional treatments, which may fail to deliver a radical dose to critical areas of the lesion.[2] Therefore, research and development, technological innovation, and measurement methodologies for SRT equipment have important implications for healthcare in China. This study conducts a comprehensive dosimetric characterization of the next-generation Gamma Knife system – the ZND-A Smart Knife – to validate its technical accuracy and operational safety for clinical deployment.

2. The principle and dose calculation model of ZND-A Smart Knife

2.1. Principle and components

The ZND-A Smart Knife is designed for SRT of solid tumors in the head and body as well as lesions that require radiosurgery. The equipment is shown in Figure 1.

ZND-A Smart Knife utilizes Cobalt-60 radioactive sources arranged in multiple concentric circles. By utilizing triple rotating and focusing of collimator, gamma-ray module, and drum, the system focuses 1.25 MeV average energy gamma rays onto the tumor or other pathological tissues. The therapeutic goal is achieved by leveraging both the damaging and inhibitory effects of gamma rays on tumors as well as the inherent radiosensitivity difference between tumor and healthy cells. Medical physicists make treatment plans based on tumor radiobiological principles, ensuring that normal tissue doses remain within acceptable levels. The Smart Knife's control system precisely positions the patient's tumor or other pathological tissue at the gamma-ray focal point based on the treatment plan made by Treatment Planning System (TPS). During repositioning, the stereotactic positioning system, guided by the image-guided system, ensures accurate realignment of the target. The radioactive sources deliver planned conformal irradiation at the target point. This integrated workflow ensures that tumors or other pathological tissues are precisely treated while sparing healthy structures.[3]

With the triple rotating and focusing technology, the maximum energy is deposited within the lesion region, while minimizing radiation exposure to normal tissue along the beam path.

In the interaction between gamma-ray and lesion, the relationship between the intensity of gamma rays and the depth of the medium is represented by the following equation:

$$I_t = I_0 e^{-\mu d} \quad \text{(I)}$$

where I_0 and I_t are the intensity of gamma rays before and after attenuation by medium, μ is the mass attenuation coefficient of the absorber medium, and d is the depth of measurement in medium (path length in medium).

As demonstrated by Equation I, the intensity of gamma rays gradually decreases with increasing penetration depth, depositing energy in the passing-through medium. Therefore, to deposit the maximum energy (dose) in the lesion region while minimizing radiation exposure to normal tissue along the beam path, the ZND-A Smart Knife radioactive sources are arranged in a concentric

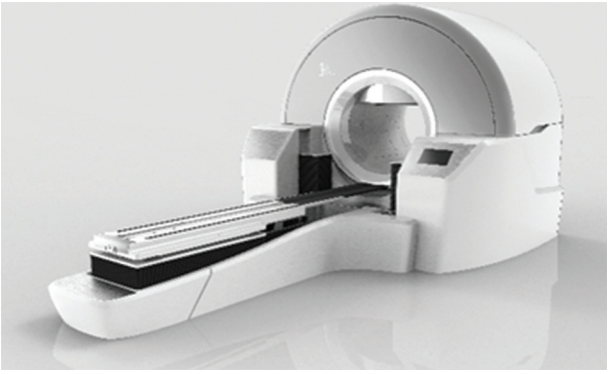

Figure 1. Gamma beam stereotactic radiotherapy system

circular pattern and installed in the gamma-ray module. The gamma rays produced by the radioactive sources are focused for the 1st time by the collimator. The gamma-ray module rotates around its own rotational axis. Due to the angular offset between the collimator axis and the module's rotational axis, a secondary focus is formed during rotation. As the module follows the rotating drum around drum's rotational axis, a tertiary focus is generated within the drum. Through this three-stage gamma-ray focusing, the equipment achieves a high focal-to-skin dose ratio and a steep dose gradient.[15]

2.2. Dose calculation model

The ZND-A Smart Knife uses isocentric irradiation, and the dose calculation is based on the Tissue Maximum Ratio (TMR) and Off-Axis Ratio (OAR) dose calculation model. The TMR and OAR are parameters decided by the collimator, source-to-axis distance, and machine-specific parameters in an actual installed machine. Thus, the TMR and OAR data have to be measured on the actual machine in the commissioning process. Then, the measured TMR and OAR baseline data would be imported to TPS for the TMR-OAR dose calculation model.

The coordinates of the dose calculation model are shown in Figure 2. The dose $D_p(X, Y, Z)$ of point $P(X, Y, Z)$ in the radiation field of ZND-A Smart Knife is represented by the following equation[4]:

$$D(X,Y,Z) = D_m(0,0,Z_m)\Delta TMR(0,0,Z)$$
$$\Delta\left(f + \frac{Z}{f} + Z_m\right)^2 \Delta OAR(0,Y,Z)\Delta OAR(X,0,Z) \quad \text{(II)}$$

where D_m $(0,0,Z_m)$ is the dose at the maximum dose point depth on the central beam axis; TMR $(0,0,Z)$ is the ratio of the dose at depth Z on the central beam axis in phantom to the dose at the same source-point distance and the reference depth of the maximum dose (Z_m); OAR

(*O,Y,Z*) and *OAR* (*X,O,Z*) are the ratios of doses at an off-axis point *(0, Y, Z)* and *(X,0, Z)* to the dose on the central beam axis at the same depth in a phantom; $\left(f+\frac{Z}{f}+Z_m\right)^2$ is a factor related to rotating focusing in space.

TMR is the ratio of the dose rate at a given point in phantom D_d to the dose rate at the same source-point distance and the reference depth of maximum dose D_m. As shown in Figure 3, the defining equation of TMR is represented by the following equation:

$$TMR(Z)=\frac{D_d}{D_m} \quad \text{(III)}$$

Where TMR is the ratio of the dose rate at a given point in phantom D_d to the dose rate at the same source-point distance and the reference depth of maximum dose D_m.

OAR is the ratio of the dose at an off-axis point to the dose on the central beam axis at the same depth in a phantom. It is a representation of dose distribution based on an isodose curve.

As shown in Figure 4, the definition of OAR at the X-axis is given by the following equation:

$$OAR(X,0,0)=\frac{D(X,Z)}{D(0,Z)} \quad \text{(IV)}$$

Equation II is the basic equation of our dose calculation model and algorithm. Based on the model, our algorithm rapidly and accurately calculates the planned dose using the measured OAR data, TMR data, and off-axis distance.[12]

3. Methods and materials

3.1. Dosimetry

The ZND-A Smart Knife is designed for tumors or other pathological tissues in the head and body. A standard spherical phantom made of polymethyl methacrylate (PMMA) was used for tests related to the head, while PMMA standard body phantom was used for tests related to the body. EBT3 GafChromic films (Ashland, Wilmington, U.S.) were used to measure radiation field profiles. PTW solid water phantom sets (PTW-Freiburg GmbH, Freiburg, Germany), PTW31010 (0.125cc) ionization chamber (PTW), PTW60019 (0.004cc) microDiamond detector (PTW), PTW UNIDOS Romeo electrometer (PTW), thermometer (Miaoguan, Pingyang, China) and DYM 3 barometer (Boji, Shanghai, China) were used in dose measurement. EPSON V850Pro scanner (Seiko Epson Corporation, Nagano, Japan) was used to scan the irradiated films. ImageJ image analysis software (Ver 1.54f; National Institute of Health, Bethesda, U.S.)

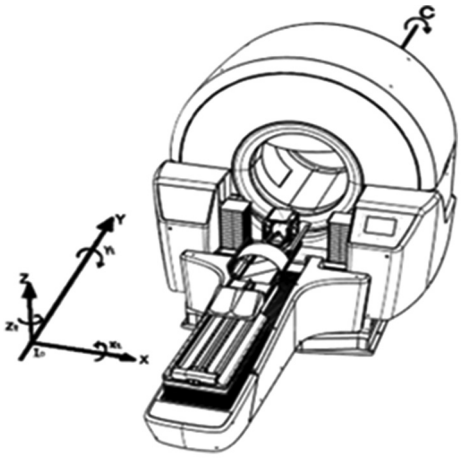

Figure 2. Coordinate system of gamma beam stereotactic radiotherapy system

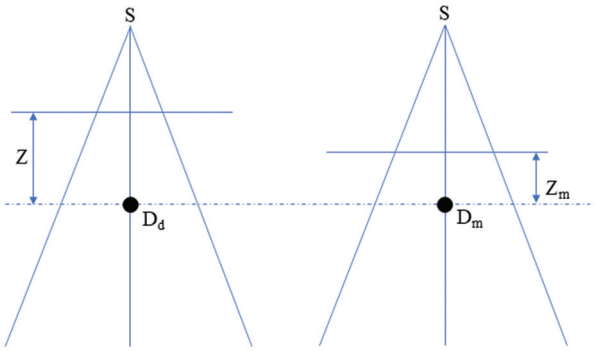

Figure 3. Tissue maximum ratio calculation. Notes: S is the source; Z is the depth on the central beam axis in phantom; Z_m is the maximum dose point depth on the central beam axis; D_d is the dose rate at a given depth Z in phantom; D_m is the dose rate at the same source-point distance and the reference depth of maximum dose.

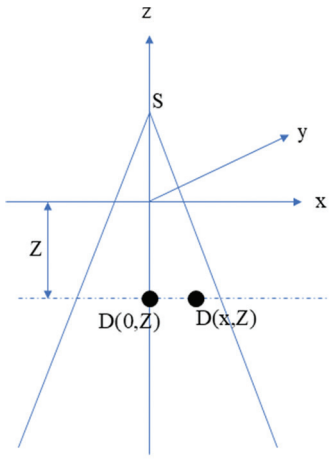

Figure 4. Off-axis ratio calculation. Notes: S is the source; Z is the depth on the central beam axis in phantom; D(0,Z) is the dose rate at point (0,Z) in phantom; D(X,Z) is the dose rate at point (X,Z) in phantom.

and MATLAB in-house program were used to process and analyze the data.

Based on the IAEA Technical Report of Series no. 277 *Absorbed Dose Determination in Photon and Electron Beams - An international Code of Practice* (TRS277) and JJG 1013-2006 *Verification Regulation of γ Radiation Source Used in Head Stereotactic Radiosurgery Therapy*, Equation (V) was used for calculation of absorbed dose to water.

$$D_{water} = M \times N_k \times (1-g) \times K_{att} \times K_m \times K_{TP} \times K_h \times K_s \times S_{w,air} \times P_u \times P_{cel} \quad (V)$$

where M is the reading of the dosimeter; N_k is the calibration coefficient in terms of air kerma by ionization chamber (unit = Gy); g is the fraction of the energy of the secondary electrons lost to bremsstrahlung in air, which is 0.0030 for Cobalt-60; K_{att} is the correction factor for the attenuation and scattering of photons in the ionization chamber material (including the buildup cap); K_m is the correction factor for the lack of air equivalence of the ionization chamber material; K_{TP} is the temperature and pressure correction factor, with a value of 0.997 when the relative humidity is 20% – 70% and the temperature is between 15°C and 25°C; K_s is the factor to correct the response of an ionization chamber for the lack of complete charge collection (due to ion recombination); $S_{w,air}$ is the stopping power ratio of water to air which is 1.136 for Cobalt-60; P_u is the perturbation correction factor; P_{cel} is the factor that corrects the response of an ionization chamber for the effect of the central electrode during in-phantom measurements in high-energy photon, electron, and proton beams.[9,16]

Due to the very small field sizes of Smart Knife's 1# and 2# collimators, the microDiamond detector (PTW60019) was calibrated by the ionization chamber (PTW31010) using the 4# collimator for measurements of small fields.[14]

3.2. Dosimetric performance test

China has national standards for gamma-ray beam SRT equipment for head and body treatments: YY 0831.1 – 2011[10] and YY 0831.2 – 2015.[11] The dosimetric performance of the ZND-A Smart Knife was tested, including the nominal absorbed dose rate at the focal point, positioning reference point deviation, radiation focusing field size, dose gradient, and comprehensive error in dose calculation. The test items and nominal values are summarized in Table 1.

4. Measurements and results

4.1. Measurements

4.1.1. Positioning reference point deviation

Gamma beam SRT is a technology used in clinical practice to treat tumors based on isocenter irradiation, where the radiation center and mechanical center coincide at one point. All implementations of the technique are based on the isocenter position, so the accuracy of the isocenter is a prerequisite for ensuring the accurate dose delivery to the tumor.

Using the PMMA standard phantom, the EBT3 Gafchromic film was placed in the phantom to separately measure the XOY and YOZ planes. The isocenter pinprick on the film holder was used to create reference holes on the irradiated film, serving as the mechanical center reference point. The irradiated film was then scanned with an Epson V850Pro scanner, exporting images in 16-bit grayscale. Figure 5 shows the film images of 1# collimator's XOY and YOZ planes, with the punched hole at the mechanical center, which serves as the positioning reference point. The threshold segmentation function of ImageJ was used to extract the radiation field center coordinates and the punched hole coordinates (mechanical center and positioning reference point). The deviations along the X, Y, and Z axes were acquired to calculate the positioning reference point deviation (ΔR) using Equation VI.[5,6]

$$\Delta R = \sqrt{\Delta X^2 + \Delta Y^2 + \Delta Z^2} \quad (VI)$$

4.1.2. Nominal focal point dose rate

The PMMA standard spherical phantom was mounted on the positioning frame, with its center aligned to the positioning reference point. The radiation detector was then inserted into the spherical phantom at a preset position, ensuring that the effective measurement point aligns with the phantom center. The treatment couch moved the spherical phantom to the preset irradiation position, after which it was irradiated for 2 min with each collimator sequentially. The dosimeter readings were recorded and the absorbed dose to water at the focal point D was calculated. The absorbed dose rate to water at the focal point was calculated according to Equation VII.

$$\dot{D} = \frac{D}{t} \quad (VII)$$

where is the absorbed dose rate to water at the focal point of this focusing field (unit = Gray per minute, Gy/min); D is the cumulative absorbed dose to water at the focal point of this focusing field in time t (unit = Gray, Gy); t is the time of irradiation (unit = minute, min).

A physicist can use Equation VI to derive the dose rate to water on the installation date from the dose rate to water on the measurement date.

$$\dot{D}_0 = \dot{D} \times e^{0.693 \times \Delta t / T_{1/2}} \quad (VIII)$$

Table 1. Physical performance of ZND-A Smart Knife

No.	Physical quantity	Item	Nominal value/requirements
1	Isocenter deviation		≤0.5mm
2	Nominal dose rate at the focal point	Head	The absorbed dose rate of the biggest radiation-focusing field ≥3.0 Gy/min
			The ratio of absorbed dose rates of the smallest to the biggest radiation-focusing fields ≥0.7
		Body	The absorbed dose rate of the biggest radiation-focusing field ≥2.0 Gy/min
			The ratio of absorbed dose rates of the smallest to the biggest radiation-focusing fields ≥0.6
3	Nominal radiation field (in diameter)	#1 Collimator	6 mm
		#2 Collimator	12 mm
		#3 Collimator	25 mm
		#4 Collimator	35 mm
4	Dose gradient	#1 Collimator	≤6 mm
		#2 Collimator	≤8 mm
		#3 Collimator	≤10 mm
		#4 Collimator	≤10 mm
5	Comprehensive error in dose calculation	Point dose	≤5%
		Area overlap ratio	≥90% (biggest radiation field)

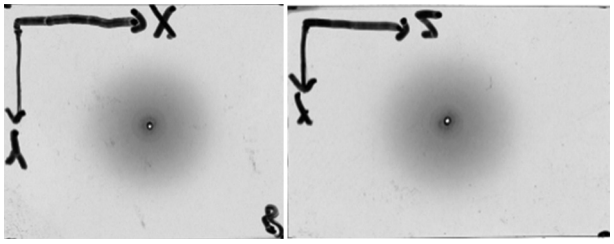

Figure 5. Films irradiated by 1# collimator. XOY and YOZ planes of the focusing field in phantom are shown.

where $\dot{D}_0$ is the dose rate to water at the focal point on the installation date; Δt is the number of years between installation date and measurement date; $T_{1/2}$ is the half-life of radioactive decay (= 5.27 years for Cobalt-60).

4.1.3. Film calibration

EBT3 is a specialized film that undergoes radiation-induced crosslinking, causing a color change that reflects the absorbed dose. Its advantages include no requirement for chemical development or a darkroom, water resistance, cuttability, a wide dose range, and an energy-independent dose response. EBT3 film exhibits varying grayscale levels depending on radiation exposure and must be calibrated for dose-grayscale correlation before use.

For the film calibration, EBT3 films were cut into small pieces to fit into the film holder in the spherical phantom. The films were exposed in the phantom using the biggest collimator, with doses ranging from 0 to 1000 cGy in 100 cGy increments. The irradiated films were then scanned by an EPSON V850 scanner to export 16-bit grayscale images. The grayscale-dose values were fitted to a second-order polynomial using ImageJ image analysis software, resulting in the calibration curve equation: $y = 2.1706E-6x^2 - 0.1625x + 3.03E3$. The grayscale-dose calibration curve is shown in Figure 6.

4.1.4. Focusing field size and dose gradient

EBT3 films were cut to match the same size with the 1#, 2#, 3#, and 4# collimators, with two films allocated for each collimator. For each collimator, one film was irradiated in the spherical phantom for the XOY plane, while another was irradiated for the YOZ plane. The irradiated films were then scanned using an EPSON V850 scanner to generate 16-bit grayscale images at a resolution of 400 dpi. Figure 7 displays images of the focusing field irradiated by the 1#, 2#, 3#, and 4# collimators. These images were analyzed using an in-house MATLAB program. The program uses the calibration curve equation to convert the image grayscale matrices into dose matrices for further evaluation. The focusing field size is defined by the 50% isodose curve area within the radiation field's dose distribution. The dose gradient of the focusing field is characterized by the distance between the 20% and 80% isodose curves within the radiation field's dose distribution.

4.1.5. TMR-OAR data

The TMR-OAR physical model is the core component of the TPS. It plays an essential part in calculating

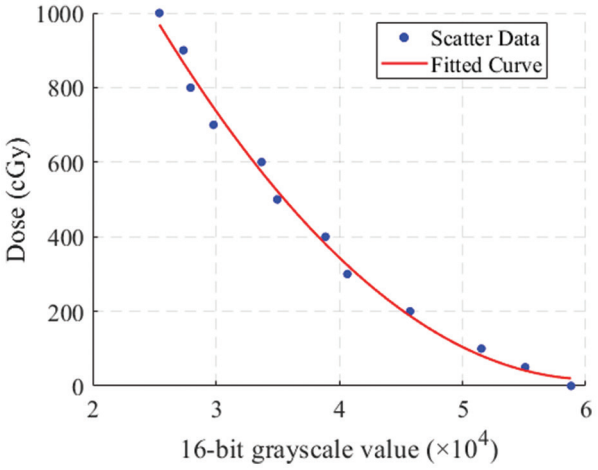

Figure 6. Grayscale-dose calibration curve

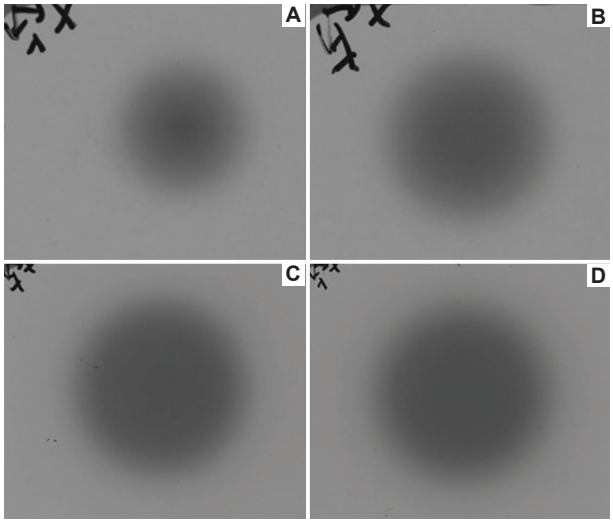

Figure 7. Irradiated films using different collimators. (A) 1# Collimator; (B) 2# Collimator; (C) 3# Collimator; (D) 4# Collimator.

dose distribution within tissue. The accuracy of the calculation depends on the accuracy of the measured data. To obtain accurate baseline data for the TMR and OAR physical models, a standard solid water phantom and microDaimond detector were used. The absorbed dose in tissue at different depths within the solid water phantom[7] was measured by adding or removing solid water plates in 30 mm increments. Using a MATLAB-based data processing program with linear interpolation, the absorbed dose was calculated for depths ranging from 5 to 300 mm with a 1 mm step, completing the TMR calculation.

The OAR measurement was performed using the standard solid water phantom and EBT3 film. The dose distribution at different depths was collected for different collimator sizes.[8] The OAR distribution of the ZND-A Smart Knife was accurately obtained by extracting dose distribution data at different depths using the MATLAB program, as shown in Figures 8 and 9. The TMR and OAR were imported into the TPS to evaluate the comprehensive error in dose calculation.

4.1.6. Comprehensive error in dose calculation

The comprehensive error in dose calculation is assessed to examine the comprehensive performance of TPS and radiotherapy equipment. It is evaluated by the relative percent deviation between the planned and measured doses at reference points, as well as the 50% isodose area overlap ratio between TPS calculation and film measurement.[9,10]

The evaluation process involves phantom, supplementary data (CT) scanner, and Gamma Knife. First, to scan the PMMA standard phantom on the positioning couch embedded with an N-line structure with the CT simulator or diagnostic CT scanner, generating

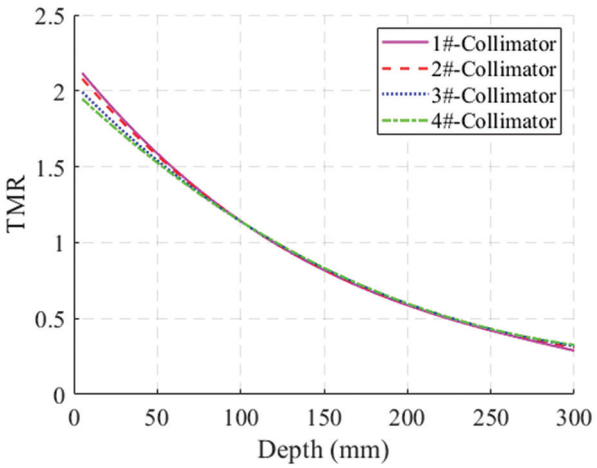

Figure 8. Tissue Maximum Ratio (TMR) of the four collimators at different depths

three-dimensional imaging data with spatial coordinates. Second, the TPS system analyzes the positioning image of the phantom and generates a dose verification plan tailored to the phantom, ensuring the accuracy of the dose calculations. Third, an ionization chamber and EBT3 film are placed in the phantom; the treatment control system then executes the dose verification plan, obtaining point dose and dose area data. Finally, ImageJ and MATLAB-based data-processing program are used to calculate the comprehensive error in dose calculation.[13]

The point dose deviation is calculated using the following equation:

$$\Delta P = \frac{P_1 - P_0}{P_0} \times 100\% \quad \text{(IX)}$$

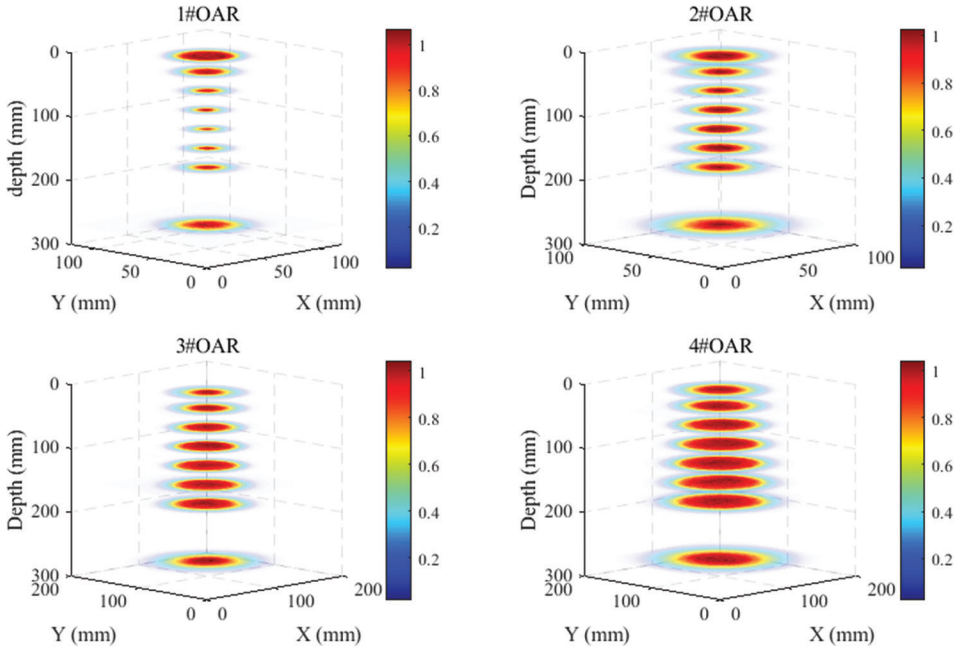

Figure 9. Off-Axis Ratio (OAR) of the four collimators at different depths

Where ΔP is the relative percent deviation between the planned and measured doses at a reference point; P_0 is the planned dose at the reference point in the PMMA standard spherical phantom (the calculated dose from TPS; unit = Gy); P_1 is the measured dose at the center of the PMMA standard spherical phantom, (unit = Gy).[17]

The 50% isodose area overlap ratio is calculated using the following equation:

$$\Delta S = \frac{S_c}{S_r + S_p - S_c} \times 100\% \quad \text{(X)}$$

where ΔS is the area overlap ratio; S_p is the area of 50% isodose curve in TPS; S_r is the area of 50% isodose curve in film measurement; S_c is the overlap area of S_p and S_r.[17]

4.2. Dosimetry analysis

Dosimetric performance is a fundamental requirement for the clinical treatment of gamma beam SRT equipment. Using the aforementioned methodology, the dosimetric performance of the ZND-A Smart Knife was evaluated, including positioning reference point deviation, radiation field gradient, and comprehensive error in dose calculation.

4.2.1. Positioning reference point deviation

The positioning reference point deviation measurement results are shown in Table 2. The maximum deviation of the ZND-A Smart Knife positioning reference point is 0.380 mm, which is less than the national standard and the technical agreement requirement of 0.5 mm.

Table 2. The positioning reference point deviation of ZND-A Smart Knife

Collimator	Plane	ΔX (mm)	ΔY (mm)	ΔZ (mm)	ΔR (mm)
#1	XOY	0.038	0.169	/	0.220
	YOZ	/	0.169	−0.130	
#2	XOY	0.159	0.095	/	0.198
	YOZ	/	0.095	0.067	
#3	XOY	0.166	0.335	/	0.380
	YOZ	/	0.335	−0.050	
#4	XOY	0.034	0.102	/	0.238
	YOZ	/	0.102	0.212	

Notes: ΔX, ΔY, ΔZ are the deviations along the X, Y, and Z axes; ΔR is the positioning reference point deviation.

4.2.2. Nominal focal point dose rate, focusing field size, and dose gradient

In clinical treatment, the radiation field, dose gradient, and dose rate are important factors influencing tumor control rate. The dose gradient directly affects the radiation exposure to healthy tissue, while the dose rate directly affects the treatment efficiency.

The radiation field size, dose gradient, and dose rate are shown in Table 3, where Str FFS represents the nominal radiation field, A represents the coordinate axis, FFS

Table 3. The radiation field, dose gradient, and dose rate of ZND-A Smart Knife

Collimator	Str FFS (mm)	A	FFS (mm)	DoseR (Gy/min)		DGOFF (mm)	
				Head	Body	L	R
#1	6	X	6.47	2.32	1.57	2.9	3.1
		Y	6.54			2.9	3.1
		Z	6.28			2.9	3.1
#2	12	X	11.30	3.11	2.30	3.3	3.3
		Y	11.17			3.3	3.3
		Z	11.55			3.4	3.1
#3	25	X	25.59	3.22	2.42	4.6	4.6
		Y	25.46			4.6	4.6
		Z	25.71			4.7	5.4
#4	35	X	33.59	3.48	2.62	6.6	6.7
		Y	33.59			6.6	6.7
		Z	34.41			6.4	7.7

Notes: Str FFS represents the nominal radiation field; A represents the coordinate axis; FFS represents the measured radiation field; DoseR represents the dose rate; DGOFF represents the dose gradient of the radiation field; and L and R represent the gradient values of the left and right half of the radiation field, respectively.

represents the measured radiation field, DoseR represents the dose rate, and DGOFF represents the dose gradient of the radiation field. L and R represent the gradient values of the left and right half of the radiation field, respectively. To ensure the accuracy of the radiation field and dose rate data acquisition, the film and ionization chamber were scaled and calibrated. The film dose scaling step is 100 cGy, and the dose range is 0 – 800 cGy. The maximum deviations between the nominal measured radiation fields for each collimator were 0.54 mm (9%), 0.83 mm (6.92%), 0.71 mm (2.84%), and 0.59 mm (1.69%); the dose gradients of the radiation fields were 3.1 mm, 3.4 mm, 5.4 mm, and 7.7 mm, which are much lower than the national standard requirements. The smaller dose gradient is expected to provide improved clinical tumor treatment benefits. In addition, the ratio of the minimum to maximum radiation focusing field dose rate in the head was 0.72, while in the body, it was 0.89. The maximum field dose rate reached 3.48 Gy/min, contributing to enhanced clinical treatment efficiency.

4.2.3. Comprehensive error in dose calculation

The ZND-A Smart Knife, based on the principle of cone beam focusing, has good dosimetric characteristics in clinical treatment, which are reflected in the small dosimetric comprehensive deviation. The TMR-OAR physical dose calculation model, based on the measured dosimetric characteristics of the equipment, promotes quick calculation of the dose and evaluates various biological features at any position of the target volume. The relative dose differences between the planned and measured doses at three reference points in space are shown in Table 4. The differences meet the national standards which is smaller than 5%.

Table 4. The point dose calculation of ZND-A Smart Knife

POS (mm)	Collimator	P_0 (Gy)	P_m (Gy)	Deviation (%)
0	#1	1.91	1.84	−3.36
	#2	3.98	4.06	2.03
	#3	3.98	4.05	1.85
	#4	3.93	3.95	0.60
30	#1	3.94	4.02	1.95
	#2	3.98	4.11	3.30
	#3	3.99	4.07	1.94
	#4	3.89	3.91	0.48
50	#1	3.95	4.00	1.24
	#2	3.97	4.08	2.90
	#3	3.99	4.05	1.64
	#4	3.84	3.84	0.10

Notes: POS represents the distance between the measurement point and the isocenter; P0 represents the calculated dose by the physical model; and Pm represents the actual measured dose.

As shown in Figure 10A, when the measurement reference point is at the isocenter, the deviation in point dose decreases as the collimator field size increases. When the measurement reference point is shifted 30 mm and 50 mm in the positive direction of the Y axis, the deviation of the point dose initially increases and then decreases as the collimator size increases. As shown in Figure 10B, the dose

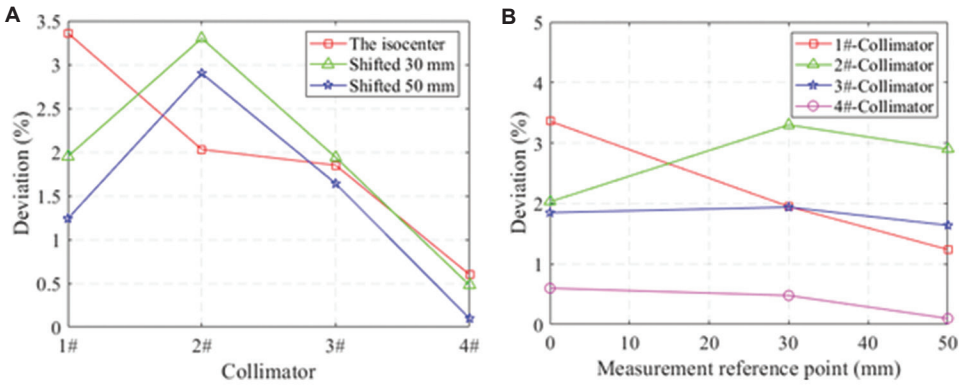

Figure 10. (A and B) ZND-A Smart Knife, deviation of point dose

calculation deviation of 1#, 3#, and 4# collimators decreases as the axial offset of the measurement point increases, while the dose calculation deviation of 2# collimator initially increases before decreasing as the axial offset increases.

This indicates that the inherent deviation trend of the dose distribution of the Smart Knife's collimators is decreasing within the irradiated space. The deviation at the isocenter is relatively the largest, indicating discrepancies in the physical model's baseline data acquisition process, mainly due to deviations in the TMR measurement at the same position (dose reference point), noise in OAR data processing, and misalignment of the field centers. Further research is needed to address this issue.

As shown in Table 5, the area overlap rate of the surface dose for the 4# collimator of 35 mm is 98.3%, where Col represents the collimator, S is the overlap area (mm^2), Sr is the film area, and Sp is the calculated area of the physical model, with the film resolution being 0.0635 mm. The measured dose area overlaps with the calculated area by 98.3%, exceeding the national standard and technical agreement requirement of >90%, indicating the excellent dose accuracy of the ZND-A Smart Knife and also reflecting the accuracy of the baseline physical data.

Table 5. The area overlap ratio of ZND-A Smart Knife

Collimator	S (mm^2)	S_r (mm^2)	S_p (mm^2)	Δ*S* (%)
#4	1064.55	1064.55	1083	98.30

Notes: S is the overlap area; S_r is the film area; and S_p is the calculated area of the physical model; and Δ*S* is the area overlap ratio.

5. Discussion

After the detailed measurements and analysis of the dosimetric performance of the ZND-A Smart Knife, the high dose rate, steep dose gradient, and accurate dose calculation are demonstrated. The high dose rate (up to 3.48 Gy/min) not only shortens the treatment time but also gives the potential for stereotactic radiosurgery. In addition, the deep dose gradient (3.1 mm – 7.7 mm) improves normal tissue sparing, potentially reducing radiotherapy toxicity and leading to improved treatment outcomes. Heck *et al.*[2] reported that a high dose rate and precise dose distribution can significantly increase tumor control rates while reducing damage to normal tissues. These dosimetric characteristics establish a solid foundation for clinical applications, especially in SRT.

With the detailed calculations and verifications of the dose distribution of the ZND-A Smart Knife based on the TMR-OAR physical model, the high accuracy of dose calculation has been demonstrated in this study. The maximum deviation in point dose calculation was only 3.3%, while the area coincidence rate reached 98.3%, confirming the reliability of the TPS. However, the study also found that as the measurement point moved away from the isocenter, the dose calculation deviation showed a trend, especially with the 2# collimator, where the deviation initially increased and then decreased with increasing off-axis distance. This deviation may be attributed to the accuracy of TMR and OAR data collection, isocenter positioning errors, and noise interference in data processing. Tham *et al.*[12] indicated that the accuracy of the physical model depends on precise data collection and processing, as even minor errors may lead to dose calculation deviations. Future research can further optimize data collection and processing methods to improve the overall accuracy of the TPS.

The remarkable performance of the ZND-A Smart Knife in aspects such as positioning reference point deviation, dose gradient, and dose calculation accuracy has fully demonstrated its reliability and promise of safety in clinical applications. In addition, automated quality control and artificial intelligence (AI) assistance can be considered to improve its stability and consistency in the future. Choi *et al.*[13] indicated that introducing machine-

specific reference correction factors can further improve the consistency of dose output, providing a direction for future improvements. Moreover, AI has the potential to enhance our understanding of machine capabilities (hardware) and refine algorithms (software) for dose calculation and treatment plan optimization.

6. Conclusion

To support the accuracy and safety evaluation of the dosimetry for the next-generation cone beam-focused gamma knife equipment, a measurement platform was established using PMMA standard phantoms, finger ionization chambers, and an electrometer. The physical properties and baseline data for the physical model were measured and analyzed, including the deviation of the positioning reference point, radiation field, dose gradient, and comprehensive error in dose calculation. Finally, based on the TMR-OAR physical model, the accuracy of the Smart Knife's comprehensive dose calculation was verified. The findings confirmed the high precision of the Smart Knife system, with a maximum positioning reference point deviation of only 0.38 mm. The measured dose gradients of 3.1 mm, 3.4 mm, 5.4 mm, and 7.7 mm demonstrated a steep dose falloff, ensuring excellent dose accuracy and effective radiation toxicity constraints. The maximum deviation in dose calculation was 3.3%, with the deviations at other measurement points remaining below 3%. The maximum area overlap rate of the maximum dose region within the radiation field reached 98.3%, exceeding national standards and technical agreement requirements. These results highlight the excellent dosimetric performance of the Smart Knife, confirming its safety, accuracy, and strong potential for clinical application.

Acknowledgments

The authors acknowledge the assistance received from Qi-Xing Han of CNNC Cheng Imaging (Xi'an) Medical Equipment Company, for the English translation of this article.

Funding

This research is funded by the CNNC research project "Smart Cobalt 60 cone beam-focused SRT system research and development".

Conflict of interest

All the authors are employees of CNNC.

Author contributions

Conceptualization: Shan-Chuan Li, Shao-Run Gong, Gang Li, Chun-Li Zhang, Jun Li

Formal analysis: Feng Zhang, Shuang Zhang

Investigation: Shan-Chuan Li, Xiao-Feng Zhang, Feng Zhang, Jun-Feng Wang, Shuang Zhang

Methodology: Shan-Chuan Li, Feng Zhang, Shuang Zhang

Writing – original draft: Shan-Chuan Li, Feng Zhang, Shuang Zhang

Writing – review & editing: Feng Zhang, Jun-Feng Wang

Ethics approval and consent to participate

Not applicable.

Consent for publication

Not applicable.

Availability of data

Data are available from the corresponding author upon reasonable request.

References

1. Qiu HB, Cao SM, Xu RH. An analysis of the temporal trends of cancer incidence, mortality, and burden in China based on global epidemiological data from 2020, with comparisons to data from the United States and the United Kingdom. *Cancer*. 2022;41(4):165-177.

   doi: 10.3321/j.issn.1000-467X.2022.4.ez202204003

2. Heck B, Jess-Hempen A, Kreiner HJ, Schöpgens H, Mack A. Accuracy and stability of positioning in radiosurgery: Long-term results of the Gamma Knife system. *Med Phys*. 2007;34(4):1487-1495.

   doi: 10.1118/1.2710949

3. Aland T, Kairn T, Kenny J. Evaluation of a Gafchromic EBT2 film dosimetry system for radiotherapy quality assurance. *Australas Phys Eng Sci Med*. 2011;34(2):251-260.

   doi: 10.1007/s13246-011-0072-6

4. Cao HB. *The Dosimetric Study of Body Gamma Knife*. Master's Thesis. Tsinghua University; 2015. Available from: https://cdmd.cnki.com.cn/Article/CDMD-10003-1015007280.htm [Last accessed on 2024 May 10].

5. Xu H, Liu M, Zhao QJ, Zheng Y, Lu JR. Applied research of Gamma knife detecting technique based on ImageL. *China Med Equip*. 2021;18(3):24-29.

   doi: 10.3969/J.ISSN.1672-8270.2021.03.006

6. Watanabe Y, Akimitsu T, Hirokawa Y, Mooij RB, Perera GM. Evaluation of dose delivery accuracy of Gamma Knife by polymer gel dosimetry. *J Appl Clin Med Phys*. 2005;6(3):133-142.

   doi: 10.1120/jacmp.v6i3.2110

7. Mao K, Kang J, Dai T, Han Y, Wang Z. Quality control of gamma ray stereotactic radiotherapy. *China Med*

Equip. 2015;(10):30-31, 32.

doi: 10.3969/J.ISSN.1672-8270.2015.10.009

8. Pai S, Das IJ, Dempsey JF, *et al*. TG-69: Radiographic film for megavoltage beam dosimetry. *Med Phys*. 2007;34(6 Part 1):2228-2258.

   doi: 10.1118/1.2736779

9. International Atomic Energy Agency. *Tehnical Report of Series no. 277 Absorbed Dose Determination in Photon and Electron Beams-An international Code of Practice.* 2nd ed. Austria: International Atomic Energy Agency; 1997.

10. National Technical Committee for Standardization of Medical Electrical Equipment, Subcommittee on Radiotherapy, Nuclear Medicine and Radiation Dosimetry Equipment (SAC/TC 10/SC 3). *YY 0831.1-2011, Stereotactic Radiotherapy System with Gamma Beam-Part 1: Multi-Source Stereotactic Radiotherapy System with Gamma Beam for Head Lesion*. China: State Food and Drug Administration; 2011.

11. National Technical Committee for Standardization of Medical Electrical Equipment, Subcommittee on Radiotherapy, Nuclear Medicine and Radiation Dosimetry Equipment (SAC/TC 10/SC 3). *YY 0831.2-2015, Stereotactic Radiotherapy System with Gamma Beam-Part 2: Multi-Source Stereotactic Radiotherapy System with Gamma Beam for Body Lesion*. China: State Food and Drug Administration; 2011.

12. Tham BZ, Aleman DM, Heaton RK, Nordström H, Coolens C. Physical dose validation of dynamic treatment for Gamma Knife radiosurgery. *Med Phys*. 2024;51(5):3635-3647.

    doi: 10.1002/mp.17034

13. Choi Y, Chun KJ, Kim ES, *et al*. Consistency of dose rates after applying machine-specific reference correction factors for the gamma knife 16 mm collimator field. *Med Phys*. 2023;50(6):3816-3824.

    doi: 10.1002/mp.16242

14. Kim TH, Yang HJ, Jeong JY, *et al*. Feasibility of isodose-shaped scintillation detectors for the measurement of gamma knife output factors. *Med Phys*. 2022;49(3): 1944-1954.

    doi: 10.1002/mp.15469

15. Mora G, Chibani O, Li J, Ma C. *SU-E-T-605: A New Design for a Rotating Gamma Knife. Monte Carlo Simulation. Poster Presented at: Fifty-Sixth annual meeting of the American Association of Physicists in Medicine, Austin, Texas*; 2014.

16. National Technical Committee on Ionizing Radiation Metrology. *JJG 1013-2006, Verification Regulation of γ Radiation Source Used in Head Stereotactic. Radiosurgery Therapy*. China: General Administration of Quality Supervision, Inspection and Quarantine of the People's Republic of China; 2006.

17. National Health and Family Planning Commission of the People's Republic of China. *WS 582-2017, Specifications for Testing of Quality Control in X and Γ Ray Stereotactic Radiotherapy System*. Beijing: National Health and Family Planning Commission of the People's Republic of China; 2017.

ACCSCIENCE PUBLISHING

Advances in Radiotherapy & Nuclear Medicine

MINI-REVIEW

Nanostructured materials as potent platforms for cancer chemoimmunotherapy

Himani Kalita[1,2]* and Manoj Patowary[3]

[1]Department of Chemistry, Indian Institute of Technology Guwahati, Guwahati, Assam, India

[2]Department of Chemistry, Savitribai Phule Pune University, Pune, Maharashtra, India

[3]Department of Applied Sciences and Humanities, School of Computing, MIT Art, Design and Technology University, Pune, Maharashtra, India

Abstract

Combinatorial chemoimmunotherapy has emerged as a potent approach in cancer treatment, offering the advantages of combining two treatment strategies (i.e., chemotherapy and immunotherapy), thereby reducing drug dosages and improving therapeutic outcomes. Nanomaterial-assisted drug delivery systems have garnered significant attention in chemoimmunotherapy for encapsulating and delivering therapeutic agents, as they can simultaneously target both cancer and immune cells, promoting drug accumulation with excellent therapeutic efficacy and minimal toxic side effects. This mini-review focuses on various aspects of immunotherapy and chemoimmunotherapy in cancer treatment and discusses several nanomaterial-assisted drug delivery systems used in chemoimmunotherapy.

Keywords: Chemoimmunotherapy; Immunotherapy; Cancer; Nanomaterial; Drug delivery; Therapeutics

***Corresponding author:**
Himani Kalita
(hkalita74@gmail.com)

Citation: Kalita H, Patowary M. Nanostructured materials as potent platforms for cancer chemoimmunotherapy. *Adv Radiother Nucl Med*. 2025;3(1):82-91.
doi: 10.36922/arnm.8150

Received: December 24, 2024

Revised: January 16, 2025

Accepted: February 3, 2025

Published online: February 18, 2025

1. Introduction

The immune system plays a crucial role in maintaining the body's health by eliminating harmful pathogens and generating appropriate responses to infections. It primarily functions by recognizing cell-surface pattern receptors, identifying pathogen-associated molecular patterns in the microbes, and detecting damage-associated molecular patterns in injured tissues.[1] Immunotherapy, therefore, stimulates white blood cells to identify tumor tissues and offers a potent strategy for cancer management, which remains a critical global healthcare issue. While conventional cancer treatments, such as radiotherapy and chemotherapy, exhibit excellent tumoricidal capabilities, they often cause toxicity to both cancer and healthy cells, potentially leading to severe hematologic toxicity and tissue dysfunction in patients.[2] Cancer immunotherapy, on the other hand, can specifically target tumor cells with mild side effects by leveraging the body's immune system to combat cancer. Furthermore, cancer immunotherapy has the potential to induce long-term antitumor responses in patients with advanced or metastatic cancers.[3] Metastasis has become a major challenge in clinical cancer care and is believed to involve a complex interplay between immune cells, cancer cells, and stromal cells at both the primary and metastatic sites.[4] Despite its advantages in specific tumor targeting with minimal side effects, immunotherapy faces several limitations, such as slow response,

low immune response rates, and high selectivity for certain tumor types.[5] In addition, it may sometimes cause impaired immune homeostasis[6] (Figure 1).

Chemotherapy, one of the principal conventional strategies in cancer therapy, utilizes various antineoplastic agents to combat cancer by either destroying tumor cells or inhibiting their proliferation. Chemotherapeutic drugs, such as cisplatin, doxorubicin, paclitaxel, methotrexate, and 5-fluorouracil, can easily circulate throughout the body through the bloodstream, making chemotherapy the preferred approach for metastatic cancers. The four most common mechanisms of action include antimetabolites, antimicrotubule agents, alkylating agents, and topoisomerase inhibitors.[7] Nevertheless, the non-specific targeting of chemotherapeutic drugs often results in systemic toxicity and severe side effects, such as vomiting, nausea, diarrhea, hair loss, fatigue, anemia, opportunistic infections, and neurotoxicity (both central and peripheral), as well as gastrointestinal issues. These treatments may also cause permanent damage to organs such as the heart, lungs, kidneys, and reproductive systems. In addition, chemotherapy sometimes fails due to factors, such as multi-drug resistance, immunosuppression, rapid drug clearance, and poor pharmacokinetics. These disadvantages highlight the urgent need for novel therapy modalities or the development of combination therapies.

Chemoimmunotherapy, which combines conventional chemotherapy and immunotherapy, presents a promising synergistic strategy to enhance antitumor efficacy and manage tumor progression, metastasis, and recurrence. While chemotherapeutic drugs were initially thought to be immunosuppressive, recent studies have shown that they can enhance the antitumor efficacy of immunotherapy by regulating the immunosuppressive microenvironment, promoting cross-presentation of tumor antigens, modulating the expression of tumor antigens or immune checkpoint molecules, and overcoming partial immunosuppression.[7] Chemotherapeutic agents eliminate cancer cells and generate cross-presented tumor antigens, making the tumor itself a source of antigens. Concurrent administration of immunotherapeutic agents enhances immune activation and antigen presentation; thereby inducing a potent antitumor immune response.[8] Furthermore, immunotherapy can overcome the limitations of chemotherapeutics, such as immunosuppression and low specificity, and increase the sensitivity of tumor cells to chemotherapy (Figure 2). Moreover, chemotherapy and immunotherapy have complementary, effective timelines. Chemotherapeutic drugs act quickly but for a short duration, whereas immunotherapeutic agents provide long-lasting antitumor effects. Immunotherapy can also address the shortcomings of chemotherapy,

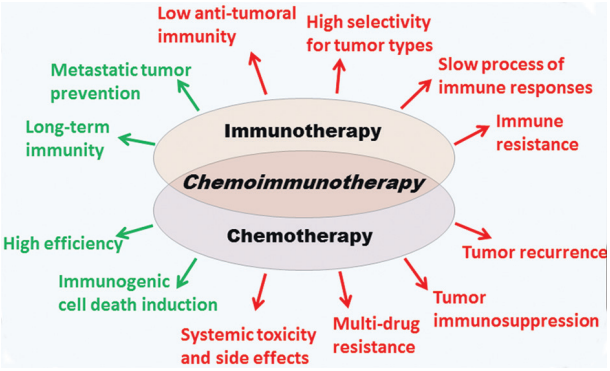

Figure 1. Advantages (indicated in green font) and disadvantages (indicated in red font) of immunotherapy and chemotherapy

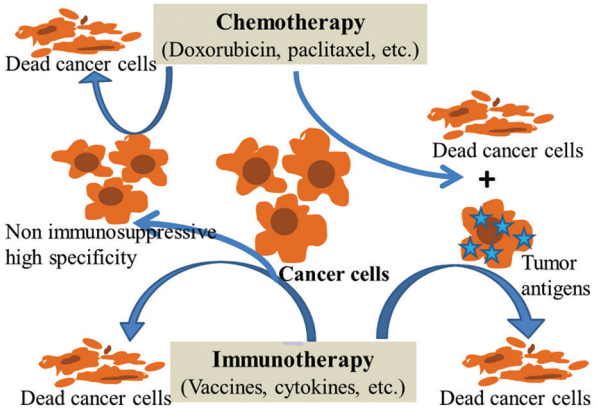

Figure 2. Schematic diagram illustrating the synergy between chemotherapy and immunotherapy

such as targeting chemotherapy-resistant cells and cancer stem cells. Although this combination strategy enhances therapeutic efficacy through synergistic effects, its effectiveness against solid tumors remains limited due to factors, such as varying physicochemical properties of drugs, insufficient tumor specificity, variability in delivery targets, and poor drug delivery efficacy.[7] Consequently, the development of vectors for the successful and simultaneous delivery of both drugs to target sites is crucial to achieving efficient synergistic combined treatment.

In recent years, nanomaterial-assisted drug delivery systems have gained significant attention in cancer treatment strategies. The systems are reported to improve the pharmacokinetics behavior of drugs *in vivo*, enhance drug stability, improve drug solubility and bioavailability, extend circulation time, enable targeted delivery, and control drug release. In addition, they offer advantages such as multi-drug co-delivery, cost efficiency, ease of synthesis, and scalability, making them highly promising for chemoimmunotherapy drug delivery. This mini-review discusses various aspects of immunotherapy and

chemoimmunotherapy in cancer treatment, as well as summarizes the different nanomaterial-assisted drug delivery systems employed in chemoimmunotherapy.

2. Cancer immunotherapy

Immunotherapy is a therapeutic strategy for treating cancer that enhances the patient's natural defense mechanisms to combat the disease. In recent years, cancer immunotherapy has gained significant attention as a powerful therapeutic approach. The cancer-immunity cycle, which underpins cancer immunity, consists of several key steps, including the release of cancer-cell antigens, presentation of these antigens by antigen-presenting cells, priming and activation of T cells, the transportation and infiltration of T cells into tumors, recognition of cancer cells by T cells, and the subsequent killing of cancer cells by cytotoxic T cells.[9] Therefore, it is theoretically possible to target each of these steps with various methods to achieve therapeutic benefits. Over the past few decades, numerous cancer immunotherapy strategies have been developed, including vaccines, adoptive cell therapy, therapeutic antibodies, and cytokine therapy[10] (Figure 3).

2.1. Cancer vaccines

The use of vaccines in cancer immunotherapy is an example of active immunotherapy, where the primary goal is to activate the effector functions of the immune system.[6] The principal function of vaccines, which may contain antigens or tumor cells, is to stimulate the immune system, eliminate the tumor, and prevent relapse. These vaccines introduce specific antigens expressed on the surface of cancer cells into the immune system. Recently, the structural analysis of cancer-cell-specific tumor-associated antigens has sparked significant interest in developing vaccines for cancer immunotherapy, aimed at preventing or treating cancer.

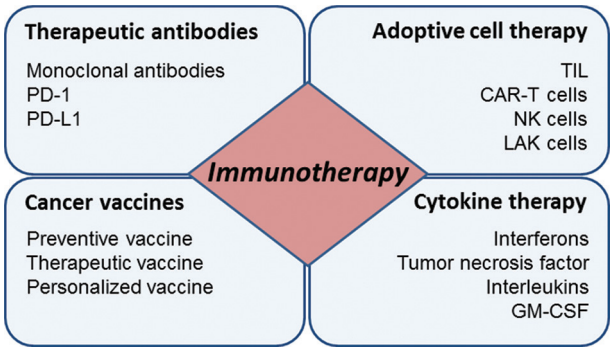

Figure 3. Various immunotherapy approaches for cancer treatment
Abbreviations: CAR-T: Chimeric antigen receptor T cells; GM-CSF: Granulocyte-macrophage colony-stimulating factor; LAK: Lymphokine-activated killer cells; NK: Natural killer cells; PD-1: Programmed cell death-1; PD-L1: Programmed death ligand-1; TIL: Tumor-infiltrating lymphocytes.

For instance, vaccines against the hepatitis B virus are used to reduce the incidence of hepatocellular carcinoma in patients with chronic liver disease.[11] Similarly, vaccines targeting human papillomavirus are employed to prevent cancers of the vagina, cervix, and throat.[12] For therapeutic purposes, Sipuleucel-T (Provenge) was developed as the first commercial cancer vaccine for treating prostate cancer. This is a dendritic cell-based vaccine.[13] On the contrary, talimogene laherparepvec (T-VEC; Imlygic) is an oncolytic herpes simplex virus vaccine used to treat metastatic melanoma.[14] In addition, several other cancer vaccines are currently being developed and undergoing clinical trials, including the GVAX lung cancer vaccine (CG 8123), glycoprotein 100 (GP 100) vaccines, and the NY-ESO-1 plasmid deoxyribonucleic acid vaccine (pPJV7611), among others. Cancer vaccines are often combined with adjuvants to activate the immune system and generate robust immune responses against cancer. These adjuvants typically include microbes and microbial derivatives (e.g., cytosine-phosphate-diester guanine), cytokines/endogenous immunomodulators (e.g., granulocyte-macrophage colony-stimulating factor), viral vectors (e.g., adenovirus, vaccinia virus), mineral salts (e.g., alum), oil emulsions or surfactants (e.g., Montanide).[9]

2.2. Adoptive cell therapy

Adoptive cell therapy is another cancer immunotherapy strategy that enhances the immune system's ability to combat cancer cells. In this approach, T cells are collected from the patient's tumor tissue or blood and then engineered *ex vivo* into highly active, tumor-specific T cells. These modified T cells are then injected back into the patient for cancer treatment.[15] These T cells primarily include tumor-infiltrating lymphocytes, chimeric antigen receptor T cells, natural killer cells, and lymphokine-activated killer cells.[16] Compared to other cancer immunotherapy strategies, adoptive cell therapy offers the advantage of generating large numbers of anticancer T cells *ex vivo*, which can specifically recognize and destroy tumor cells. Two types of adoptive cell therapy using chimeric antigen receptor T cells, Kymriah® and Yescarta®, have already been approved by the United States Food and Drug Administration (FDA) and European Medicines Agency for cancer treatment.

2.3. Therapeutic antibodies

Immune checkpoint therapy is another cancer immunotherapy technique that employs targeted antibodies to activate the immune response and destroy cancer cells. These therapeutic antibodies bind to specific antigen sites and either block or stimulate critical immune checkpoints that regulate the immune system. This reactivation of immune cells enhances their

ability to kill cancer cells while minimizing systemic toxicity. Commonly used therapeutic antibodies include monoclonal antibodies such as programmed death 1 (PD-1) antibodies and programmed death ligand-1 (PD-L1) antibodies.[17] Numerous monoclonal antibodies have been approved by the FDA and are currently used in cancer treatment. For instance, Rituximab (the first anti-B-lymphocyte antigen monoclonal antibody) is used to treat blood cancers, Trastuzumab (an anti-human epidermal growth factor receptor 2 monoclonal antibody) is used in the treatment of breast cancer, and Cetuximab (an anti-epidermal growth factor receptor monoclonal antibody) is used to treat metastatic colorectal cancer. Monoclonal antibodies can be used alone or in combination with other anticancer agents. For instance, Kadcyla, an FDA and European Medicines Agency-approved antibody-drug conjugate comprising Trastuzumab and the chemotherapy drug Emtansine is used to treat metastatic breast cancer.[18]

2.4. Cytokine therapy

Cytokines are chemical messengers or signaling proteins in the immune system. These small, soluble proteins are released by various cells, such as T cells, mast cells, B cells, and macrophages.[8] Cytokines can improve the patient's immune response either by directly inducing apoptosis through pro-apoptotic and anti-proliferative signals or indirectly by activating cytotoxic immune cells, thereby eradicating cancer cells. Numerous cytokines have been studied and applied in cancer therapy to date, including interferons, tumor necrosis factor, interleukins, and granulocyte-macrophage colony-stimulating factor. Interferon alpha was the first cytokine approved by the FDA for leukemia cancer immunotherapy in 1986.[19] It was later used for treating lymphoma, melanoma, and AIDS-related Kaposi's sarcoma. Aldesleukin (Proleukin®), a synthetic interleukin, was approved for the treatment of melanoma and kidney cancer.[20]

Although immunotherapy offers significant advantages in cancer treatment, it faces certain challenges in some patients or tumor types, including weak immunogenicity of therapeutic vaccines, off-target side effects, and immune-related adverse events.

3. Cancer chemoimmunotherapy

Chemotherapy is one of the most commonly used traditional approaches for cancer treatment, utilizing toxic compounds to inhibit the proliferation of rapidly growing cancer cells. However, these chemotherapy drugs also affect other fast-growing healthy cells, such as those in the bone marrow, hair follicles, and gastrointestinal tract, leading to toxic side effects, such as severe nausea, hair loss, and bowel issues. In addition, chemotherapy faces challenges such as poor pharmacokinetics and the development of multiple drug resistance. As a result, chemotherapy is often combined with other therapeutic techniques, such as radiotherapy, surgical treatment, and immunotherapy, to enhance its efficacy. Among these combinations, the integration of chemotherapy with immunotherapy – termed chemoimmunotherapy – has emerged as a potent synergistic strategy for improving antitumor efficacy, and numerous products are currently undergoing pre-clinical and clinical trials.

Chemotherapeutic drugs are expected to induce immunomodulation within the tumor microenvironment, primarily by triggering immunogenic tumor cell death, inhibiting the expression of immune checkpoints, maintaining the suppressive influence of T cells, promoting the infiltration of tumor-killing cells, enhancing intrinsic tumor cell immunogenicity, downregulating the immunosuppressive microenvironment, and influencing the function of other cells, such as dendritic cells and myeloid-derived suppressor cells.[7,21] Although chemoimmunotherapy holds significant potential for tumor management and reducing recurrence rates, conventional dosing methods may reduce its effectiveness due to inadequate accumulation, low circulation time, induction of toxicity, and insufficient infiltration in tumor tissues under physiological conditions. In this regard, nanotechnology has emerged as a promising tool to address several of these challenges by lowering drug doses and reducing the frequency of administration, leading to safer chemoimmunotherapy treatments. In recent decades, the application of multifunctional nanomaterial-assisted drug delivery systems has become increasingly popular in chemoimmunotherapy due to their adjustability and versatility, thereby helping to resolve various cancer-related issues.

4. Nanomaterial-assisted drug delivery systems

Nanomaterials have been increasingly adopted in chemoimmunotherapy due to their significant advantages, including multi-drug co-delivery, precise targeting, controlled drug release, promotion of immune responses, and sensitivity to stimuli (such as pH, redox, enzymes, heat, magnetic fields, and light). These nanomaterials improve the stability, solubility, bioavailability, and circulation time of drugs, thereby enhancing their pharmacokinetic properties *in vivo*. As a result, they increase therapeutic effects while minimizing toxic side effects. Furthermore, they offer the advantages, such as facile synthesis, cost-efficiency, and scalability for large-scale production. Numerous nanomaterial-assisted drug delivery systems

have been designed and studied for use as vectors in chemoimmunotherapy, including lipid nanocarriers,[22] polymeric nanocarriers,[23] dendrimers,[24] metallic and inorganic nanoparticles,[25] and biomimetic nanoparticles[26] (Figure 4). The following sections discuss several of these nanomaterial-assisted drug delivery systems.

4.1. Lipid nanocarriers

Lipid-based nanocarriers exhibit excellent solubility in aqueous media and are capable of loading both hydrophilic and lipophilic drugs while minimizing systemic toxicity. This feature makes them one of the most commonly approved types of nanodrug carriers. They possess several advantageous properties, including good biodegradability, biocompatibility, non-immunogenicity, a large surface-area-to-mass ratio, long-term stability, high encapsulation efficiency for poorly water-soluble drugs, high versatility, controlled release, affordable scalability for manufacture, and low toxicity.[27,28] In addition, lipid nanocarriers can be administered through various routes, such as oral, parenteral, transdermal, intranasal, and ocular applications.[28] Lipid nanocarriers typically consist of nanostructured lipid vectors, solid lipid nanoparticles, lipid-nucleic acid complexes, and others. Recently, lipid nanoparticles have been approved by the FDA for the non-viral delivery of nucleic acid therapeutics, such as the coronavirus disease 2019 messenger RNA vaccines and Patisiran (approved in 2020 and 2018, respectively).[29] Several other lipid nanocarrier-based therapeutics are currently undergoing clinical trials for various human diseases. Yong *et al.*[30] used RNA-interference-loaded lipid nanoparticles to develop a dual-targeted therapeutic vector for tumor myeloid cells and cancer cells. This vector, which inhibits heme oxygenase-1, enhances chemoimmunotherapy by sensitizing tumor cells to chemotherapeutics through increased immunogenic cell death and reprogramming tumor myeloid cells to a distinct phenotype. This cascade, in turn, activates a cluster of differentiation 8-positive ($CD8^+$) cytotoxic T cells. In addition, heme oxygenase-1 inhibition alters tumor macrophage differentiation. In a recent study, glutathione-responsive prodrug-based hybrid lipid-polymer nanoparticles were developed as a synergistic antitumor chemoimmunotherapy vector.[31] These nanoparticles were composed of 2-bromopalmitate (a lipid alternative), 1,2-stearoyl-sn-glycerol-3-phosphoethanolamine-N-[methoxy(polyethylene glycol)-2000] (a stabilizer polymer), and polyphosphoester-based camptothecin prodrug (a cationic helper polymer). These prodrug nanoparticles were shown to induce PD-L1 degradation by inhibiting palmitoylation for immune checkpoint blockade therapy. The nanoparticles significantly prevented melanoma progression by enhancing cytotoxic $CD8^+$ T cell-mediated antitumor immune responses and promoting the infiltration and activation of intra-tumoral lymphocytes.

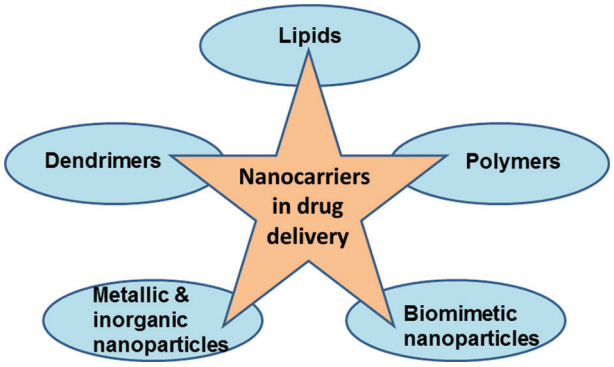

Figure 4. Various nanomaterial-assisted drug delivery systems used in chemoimmunotherapy

4.2. Polymeric nanocarriers

Polymers, particularly polymeric micelles, have been widely studied as nanovectors in chemoimmunotherapy for the co-delivery of multiple drugs, due to their unique core-shell architecture. These polymeric micelles are formed through the spontaneous self-assembly of amphiphilic block copolymers in aqueous solutions, resulting in thermodynamically stable colloidal structures. In these micelles, hydrophobic drugs can be either chemically coupled or physically encapsulated within the hydrophobic core, while hydrophilic drugs can be loaded through chemical conjugation or physical interactions. In addition, multifunctional polymer micelles can be easily obtained through surface modifications of the polymers, enhancing the efficient loading of both hydrophobic and hydrophilic drugs. Wei *et al.*[32] developed two types of targeting micelles for the simultaneous delivery of anticancer drug doxorubicin and imiquimod (R837) to tumor cells and tumor-associated macrophage through intravenous and intratumoral injections, respectively. This approach aimed to achieve synergistic chemoimmunotherapy for breast cancer. The micelles were constructed using phenylboronic acid-poly(ethylene glycol)-poly(ε-caprolactone) and acetylated chondroitin sulfate-protoporphyrin as the polymers. Similarly, low molecular weight heparin and D-α-tocopheryl succinate were developed into polymeric micelles for the co-delivery of doxorubicin and Toll-like receptor (TLR) 7 agonist imiquimod for the treatment of orthotopic and metastatic breast cancer.[33] Recently, reactive oxygen species (ROS)-responsive polymer prodrug-based nanoparticles have been explored for chemoimmunotherapy. These nanoparticles contain

the immunogenic inducer paclitaxel and indoleamine 2,3-dixoygenase 1 blocker 1-methyl-D,L-tryptophan. The polymeric nanocarriers were composed of poly(ethylene glycol) as the hydrophilic segment, with enzyme cleavable 1-methyl-D,L-tryptophan ester, and oxidation-sensitive phenyl peroxalate ester as hydrophobic blocks.[34] The copolymer self-assembles into prodrug-based nanoparticles, which release paclitaxel in response to intracellular ROS, thereby inducing immunogenic cell death. The generated ROS further promotes nanoparticle disassembly and the continued release of paclitaxel, enhancing the therapeutic effects.

4.3. Dendrimers

Dendrimers are well-known drug nanocarriers with both hydrophobic and hydrophilic components. They are hyperbranched, spherical polymers that can be easily functionalized through surface conjugation and exhibit stable structures at all concentrations.[35] Their unique properties – including hydrophobic or hydrophilic cavities in the interior, well-defined structure, size monodispersity, compact globular shape, numerous internal cavities, a large number of controllable "peripheral" functionalities, good versatility, high water solubility, superior biocompatibility, and high ratio of surface groups to molecular volume – make dendrimers excellent drug delivery vectors. Due to their unique structure and properties, drug molecules can either be physically encapsulated in the internal cavities of dendrimers through non-covalent interactions or chemically conjugated to the peripheral functional groups through covalent interactions. In addition, the peripheral functional groups allow for the attachment of different solubilizing groups and targeting moieties on the surface in a multivalent fashion. Dendrimeric products such as Stratus® CS Acute Care Diagnostic System and Starburst® have already been approved by the FDA and are commercially available for healthcare.[36] Both of these are tectodendrimers, which are superstructured dendrimers with a high-generation core and low-generation shell. Recently, Song *et al.*[37] developed pH-sensitive core-shell tectodendrimers for the simultaneous co-delivery of CD47 siRNA and doxorubicin to tumor cells for synergistic chemoimmunotherapy of breast cancer. The developed nanovector could simultaneously compress siRNA and physically load doxorubicin with good loading efficacy, and it could rapidly release the drug in the acidic tumor microenvironment.

4.4. Metallic and inorganic nanoparticles

Metallic and inorganic nanoparticles have been widely utilized as nanocarriers for delivering therapeutics due to their excellent characteristics, including non-immunogenicity, good stability, ease of synthesis, ease of functionalization, inertness, and high drug-loading capacity. In addition, some nanoparticles exhibit remarkable magnetic, thermal, and optical properties, while others can be designed in various sizes, structures, and geometries, such as nanorods, nanospheres, nanoshells, and nanostars. Numerous metallic and inorganic nanoparticles have been studied as nanovectors for delivering therapeutics to targeted tumor sites in chemoimmunotherapy. For example, gold nanoparticle vesicles co-loaded with the immune inhibitor BLZ-945 and the anticancer drug SN38 were developed for chemoimmunotherapy against primary and metastatic cancers, incorporating photoacoustic imaging in the second near-infrared window.[38] The gold nanoparticle vesicles were synthesized through the self-assembly of nanogapped gold nanoparticles with poly(ethylene glycol) and poly(SN38-co-4-vinylpyridine). The vesicles exhibited dual biologically responsive properties, being both pH- and redox-sensitive. In another study, a multifunctional nanoparticle formulation with an iron oxide core was developed as a nanovector for the targeted and simultaneous co-delivery of the cytotoxic agent doxorubicin and TLR3 agonist polyinosinic: polycytidylic acid to both breast cancer and dendritic cells. This formulation utilized an endoglin-binding peptide to target both triple-negative breast cancer cells and vasculature endothelium.[39] The nanoparticles induced tumor apoptosis through multiple mechanisms, such as direct cancer cell killing and dendritic cell-mediated innate and T cell-mediated adaptive immune responses. Recently, black phosphorus nanoparticles were co-loaded with low-dose doxorubicin and BMS-202 (a PD-L1 blocker) for the chemoimmunotherapy of lung cancer. Drug release from the composite occurred upon mild photothermal heating at 40°C.[40] In this system, low-dose doxorubicin-induced oxidative stress and activated the high mobility group box 1/receptor for advanced glycation end product/nuclear factor kappa light chain enhancer of activated B cells/PD-L1 pathway. The drug-loaded composite demonstrated improved cancer cell toxicity and promising synergism in the presence of tumor-associated macrophages.

4.5. Biomimetic nanoparticles

Biomimetic nanoparticles, which are prepared by mixing or coating biocompatible materials with biomaterials to mimic the functions of natural structures and processes, can camouflage themselves as autologous components. These features allow them to circumvent rapid clearance by the immune system, thereby prolonging circulation

time and enhancing drug delivery efficiency. Due to their resemblance in size, morphology, and surface properties to natural structures, biomimetic nanoparticles exhibit superior biocompatibility, good bioavailability, excellent targeting, enhanced therapeutic efficacy, significant *in vivo* interactions, and minimal toxic side effects. To date, numerous biomimetic nanoparticles mimicking natural structures have been studied as nanovectors for therapeutic delivery in chemoimmunotherapy, including those derived from macrophages,[41] peptides,[42] erythrocytes,[43] and cell membranes.[44]

Cell membrane biomimetic nanoparticles typically consist of a cell membrane coating on functional nanoparticles, where the membrane proteins remain bioactive. This bioactivity allows the nanoparticles to evade the immune system, resulting in prolonged blood circulation time and efficient tumor targeting. Wang *et al.*[45] developed a biomimetic tumor-targeting nanomedicine comprising gemcitabine-loaded poly(lactic-co-glycolic acid) nanoparticles coated with the bio-engineered cancer cell membrane. These membranes retain tumor-associated antigens and express peptides targeting M2-like macrophages for the chemoimmunotherapy of pancreatic cancer. The developed nanomedicine was further combined with an immune checkpoint inhibitor (PD-L1 antibody), which synergistically enhances the immunotherapeutic effect by removing PD-L1$^+$ macrophage and downregulating PD-L1. In a similar study, a combined therapeutic system was developed that included a prodrug (doxorubicin conjugated to D-α-tocopherol polyethylene glycol 1000 succinate with a targeting peptide-ligand cyclin arginylglycylaspartic acid) and a nanoparticle-based vaccine (mannose-inserted erythrocyte membrane-enveloped poly[D,L-lactide-co-glycolide]-SS-hgp nanoparticles) for synergetic chemoimmunotherapy of lung cancer.[46] Hou *et al.*[47] developed an M1-type macrophage-based drug delivery vehicle carrying sorafenib-loaded lipid nanoparticles for chemoimmunotherapy. In this system, M1-type macrophages act as both the delivery vehicle for sorafenib and as a therapeutic tool for immunotherapy. In addition, PD-L1 binding peptide-conjugated nanoparticles loaded with the anticancer drug doxorubicin and exhibiting pH-sensitive characteristics were developed for the chemoimmunotherapy of colon cancer.[48] The released peptide conjugate at the tumor site blocks PD-1/PD-L1 interactions, preventing immune escape and stimulating enhanced immune response.

5. Conclusion

Nanomaterial-assisted drug delivery systems have emerged as a promising approach in cancer chemoimmunotherapy, with a bright future ahead. Extensive research has been conducted on their design, development, and evaluation for the chemoimmunotherapy of various cancers, which could ultimately be translated into clinical applications. While chemoimmunotherapy still faces challenges in cancer treatment, nanosized drug delivery systems are expected to play a vital role in harnessing their exceptional advantages. However, several challenges remain for nanosized drug delivery systems, including unavoidable drug leakage, complex manufacturing processes, instability, and undefined safety in excipients. These issues must be addressed to enhance the clinical translation prospects of these systems. Thus, there is an urgent need for nanomaterial-assisted drug delivery systems that offer simple formulation, an established preparation process, and good biocompatibility from a commercial transformation perspective. We hope that this mini-review inspires researchers to explore new perspectives on nanomaterial-assisted drug delivery systems for cancer chemoimmunotherapy.

Acknowledgments

None.

Funding

None.

Conflict of interest

The authors declare that they have no competing interests.

Author contributions

Conceptualization: Himani Kalita
Writing – original draft: Himani Kalita
Writing – review & editing: Manoj Patowary

Ethics approval and consent to participate

Not applicable.

Consent for publication

Not applicable.

Availability of data

Not applicable.

References

1. Shams F, Golchin A, Azari A, *et al*. Nanotechnology-based products for cancer immunotherapy. *Mol Biol Rep*. 2022;49:1389-1412.

   doi: 10.1007/s11033-021-06876-y

2. Yang Z, Ma Y, Zhao H, Yuan Y, Kim BY. Nanotechnology

platforms for cancer immunotherapy. *Wiley Interdiscip Rev Nanomed Nanobiotechnol*. 2019;12:e1590.

doi: 10.1002/wnan.1590

3. Bockamp E, Rosigkeit S, Siegl D, Schuppan D. Nano-enhanced cancer immunotherapy: Immunology encounters nanotechnology. *Cells*. 2020;9:2102.

doi: 10.3390/cells9092102

4. Zhang P, Meng J, Li Y, *et al*. Nanotechnology-enhanced immunotherapy for metastatic cancer. *Innovation (Camb)*. 2021;2(4):100174.

doi: 10.1016/j.xinn.2021.100174

5. Wang J, Li L, Xu ZP. Enhancing cancer chemo-immunotherapy: Innovative approaches for overcoming immunosuppression by functional nanomaterials. *Small Methods*. 2024;8:e2301005.

doi: 10.1002/smtd.202301005

6. Akkın S, Varan G, Bilensoy E. A review on cancer immunotherapy and applications of nanotechnology to chemoimmunotherapy of different cancers. *Molecules*. 2021;26:3382.

doi: 10.3390/molecules26113382

7. Lang X, Wang X, Han M, Guo Y. Nanoparticle-Mediated synergistic chemoimmunotherapy for cancer treatment. *Int J Nanomedicine*. 2024;19:4533-4568.

doi: 10.2147/IJN.S455213

8. Bagherifar R, Kiaie SH, Hatami Z, *et al*. Nanoparticle-mediated synergistic chemoimmunotherapy for tailoring cancer therapy: Recent advances and perspectives. *J Nanobiotechnology*. 2021;19:110.

doi: 10.1186/s12951-021-00861-0

9. Mu W, Chu Q, Liu Y, Zhang N. A review on nano-based drug delivery system for cancer chemoimmunotherapy. *Nanomicro Lett*. 2020;12:142.

doi: 10.1007/s40820-020-00482-6

10. Gupta SL, Basu S, Soni V, Jaiswal RK. Immunotherapy: An alternative promising therapeutic approach against cancers. *Mol Biol Rep.* 2022;49:9903-9913.

doi: 10.1007/s11033-022-07525-8

11. Stanley M. Tumour virus vaccines: Hepatitis B virus and human papillomavirus. *Philos Trans R Soc Lond B Biol Sci*. 2017;372:20160268.

doi: 10.1098/rstb.2016.0268

12. Kamolratanakul S, Pitisuttithum P. Human papillomavirus vaccine efficacy and effectiveness against cancer. *Vaccines (Basel)*. 2021;9(12):1413.

doi: 10.3390/vaccines9121413

13. Sutherland SIM, Ju X, Horvath LG, Clark GJ. Moving on from sipuleucel-T: New dendritic cell vaccine strategies for prostate cancer. *Front Immunol*. 2021;12:641307.

doi: 10.3389/fimmu.2021.641307

14. Ferrucci PF, Pala L, Conforti F, Cocorocchio E. Talimogene laherparepvec (T-VEC): An intralesional cancer immunotherapy for advanced melanoma. *Cancers (Basel)*. 2021;13(6):1383.

doi: 10.3390/cancers13061383

15. Du S, Yan J, Xue Y, Zhong Y, Dong Y. Adoptive cell therapy for cancer treatment. *Exploration* (*Beijing*). 2023;3:20210058.

doi: 10.1002/EXP.20210058

16. Lasvergnas J, Naigeon M, Chouahnia K, Zelek L, Chaput N, Duchemann B. Adoptive cell therapies in thoracic malignancies. *Cancer Immunol Immunother*. 2022;71:2077-2098.

doi: 10.1007/s00262-022-03142-3

17. Robert C, Soria JC, Eggermont AMM. Drug of the year: Programmed death-1 receptor/programmed death-1 ligand-1 receptor monoclonal antibodies. *Eur J Cancer*. 2013;49:2968-2971.

doi: 10.1016/j.ejca.2013.07.001

18. Dhillon S. Trastuzumab emtansine: A review of its use in patients with HER2-positive advanced breast cancer previously treated with trastuzumab-based therapy. *Drugs*. 2014;74:675-686.

doi: 10.1007/s40265-014-0201-0

19. Lin FC, Young HA. Interferons: Success in anti-viral immunotherapy. *Cytokine Growth Factor Rev*. 2014;25:369-376.

doi: 10.1016/j.cytogfr.2014.07.015

20. Murer P, Brannetti B, Rondeau JM, *et al*. Discovery and development of ANV419, an IL-2/anti-IL-2 antibody fusion protein with potent CD8+ T and natural killer cell-stimulating capacity for cancer immunotherapy. *MAbs*. 2024;16:2381891.

doi: 10.1080/19420862.2024.2381891

21. Emens LA. Chemoimmunotherapy: Reengineering tumor immunity. *J Cancer*. 2010;16:295-303.

doi: 10.1007/s00262-012-1388-0

22. Wang T, Suita Y, Miriyala S, Dean J, Tapinos N, Shen J. Advances in lipid-based nanoparticles for cancer chemoimmunotherapy. *Pharmaceutics*. 2021;13(4):520.

doi: 10.3390/pharmaceutics13040520

23. You K, Wang Q, Osman MS, *et al*. Advanced strategies for combinational immunotherapy of cancer based on polymeric nanomedicines. *BMEMat*. 2024;2:e12067.

doi: 10.1002/bmm2.12067

24. Liu S, Li J, Gu L, Wu K, Xing H. Nanoparticles for

chemoimmunotherapy against triple-negative breast cancer. *Int J Nanomedicine*. 2022;17:5209-5227.

doi: 10.2147/IJN.S388075

25. Mao W, Yoo HS. Inorganic nanoparticle functionalization strategies in immunotherapeutic applications. *Biomater Res*. 2024;28:0086.

doi: 10.34133/bmr.0086

26. Zang S, Huang K, Li J, *et al*. Metabolic reprogramming by dual-targeting biomimetic nanoparticles for enhanced tumor chemo-immunotherapy. *Acta Biomater*. 2022;148:181-193.

doi: 10.1016/j.actbio.2022.05.045

27. Plaza-Oliver M, Santander-Ortega MJ, Lozano MV. Current approaches in lipid-based nanocarriers for oral drug delivery. *Drug Deliv Transl Res*. 2021;11:471-497.

doi: 10.1007/s13346-021-00908-7

28. Dabholkar N, Waghule T, Rapalli VK, *et al*. Lipid shell lipid nanocapsules as smart generation lipid nanocarriers. *J Mol Liq*. 2021;339:117145.

doi: 10.1016/j.molliq.2021.117145

29. Suzuki Y, Ishihara H. Difference in the lipid nanoparticle technology employed in three approved siRNA (Patisiran) and mRNA (COVID-19 vaccine) drugs. *Drug Metab Pharmacokinet*. 2021;41:100424.

doi: 10.1016/j.dmpk.2021.100424

30. Yong SB, Ramishetti S, Goldsmith M, *et al*. Dual-targeted lipid nanotherapeutic boost for chemo-immunotherapy of cancer. *Adv Mater*. 2022;34:e2106350.

doi: 10.1002/adma.202106350

31. Tan X, Wang C, Zhou H, *et al*. Bioactive fatty acid analog-derived hybrid nanoparticles confer antibody-independent chemo-immunotherapy against carcinoma. *J Nanobiotechnology*. 2023;21:183.

doi: 10.1186/s12951-023-01950-y

32. Wei X, Liu L, Li X, *et al*. Selectively targeting tumor-associated macrophages and tumor cells with polymeric micelles for enhanced cancer chemo-immunotherapy. *J Control Release*. 2019;313:42-53.

doi: 10.1016/j.jconrel.2019.09.021

33. Wei J, Long Y, Guo R, *et al*. Multifunctional polymeric micelle-based chemo-immunotherapy with immune checkpoint blockade for efficient treatment of orthotopic and metastatic breast cancer. *Acta Pharm Sin B*. 2019;9(4):819-831.

doi: 10.1016/j.apsb.2019.01.018

34. Song J, Cheng M, Xie Y, Li K, Zang X. Efficient tumor synergistic chemoimmunotherapy by self-augmented ROS-responsive immunomodulatory polymeric nanodrug. *J Nanobiotechnology*. 2023;21:93.

doi: 10.1186/s12951-023-01842-1

35. Mekonnen TW, Darge HF, Tsai HC, *et al*. Combination of ovalbumin-coated iron oxide nanoparticles and poly(amidoamine) dendrimer-cisplatin nanocomplex for enhanced anticancer efficacy. *Colloids Surf B Biointerfaces*. 2022;213:112391.

doi: 10.1016/j.colsurfb.2022.112391

36. Mittal P, Saharan A, Verma R, *et al*. Dendrimers: A new race of pharmaceutical nanocarriers. *Biomed Res Int*. 2021;2021:8844030.

doi: 10.1155/2021/8844030

37. Song C, Ouyang Z, Liu J, *et al*. Core-shell tecto dendrimers co-deliver drug/gene for immunomodulation of macrophages and dendritic cells and checkpoint blockade-promoted breast cancer chemoimmunotherapy. *Nano Today*. 2024;58:102437.

doi: 10.1016/j.nantod.2024.102437

38. Zhu R, Su L, Dai J, *et al*. Biologically responsive plasmonic assemblies for second near-infrared window photoacoustic imaging-guided concurrent chemo-immunotherapy. *ACS Nano.* 2020;14:3991-4006.

doi: 10.1021/acsnano.9b07984

39. Mu QG, Lin G, Jeon M, *et al*. Iron oxide nanoparticle targeted chemo-immunotherapy for triple negative breast cancer. *Mater Today (Kidlington)*. 2021;50:149-169.

doi: 10.1016/j.mattod.2021.08.002

40. Xu HZ, Chen FX, Li K, *et al*. Anti-lung cancer synergy of low-dose doxorubicin and PD-L1 blocker co-delivered via mild photothermia-responsive black phosphorus. D*rug Deliv Transl Res*. 2025;15:269-290.

doi: 10.1007/s13346-024-01595-w

41. Zhao Y, Zheng Y, Zhu Y, Li H, Zhu H, Liu T. Docetaxel-loaded M1 macrophage-derived exosomes for a safe and efficient chemoimmunotherapy of breast cancer. *J Nanobiotechnology*. 2022;20:359.

doi: 10.1186/s12951-022-01526-2

42. Wang Y, Xie L, Li X, Wang L, Yang Z. Chemo-immunotherapy by dual-enzyme responsive peptide self-assembling abolish melanoma. *Bioact Mater*. 2024;31:549-562.

doi: 10.1016/j.bioactmat.2023.09.006

43. Su L, Hao Y, Li R, *et al*. Red blood cell-based vaccines for ameliorating cancer chemoimmunotherapy. *Acta Biomater*. 2022;154:401-411.

doi: 10.1016/j.actbio.2022.10.001

44. Jiang X, Wu L, Zhang M, *et al*. Biomembrane nanostructures: Multifunctional platform to enhance tumor chemoimmunotherapy via effective drug delivery. *J Control Release*. 2023;361:510-533.

doi: 10.1016/j.jconrel.2023.08.002

45. Wang M, Hu Q, Huang J, *et al*. Engineered a dual-targeting biomimetic nanomedicine for pancreatic cancer chemoimmunotherapy. *J Nanobiotechnology*. 2022;20:85.

doi: 10.1186/s12951-022-01282-3

46. Bao Y, Hu Q, Wang X, *et al*. Chemo-immunotherapy with doxorubicin prodrug and erythrocyte membrane-enveloped polymer nano-vaccine enhances antitumor activity. *Biomed Pharmacother*. 2020;129:110377.

doi: 10.1016/j.biopha.2020.110377

47. Hou T, Wang T, Mu W, *et al*. Nanoparticle-loaded polarized-macrophages for enhanced tumor targeting and cell-chemotherapy. *Nanomicro Lett*. 2020;13:6.

doi: 10.1007/s40820-020-00531-0

48. Zhu W, Bai Y, Zhang N, *et al*. A tumor extracellular pH-sensitive PD-L1 binding peptide nanoparticle for chemo-immunotherapy of cancer. *J Mater Chem B*. 2021;9:4201-4210.

doi: 10.1039/d1tb00537e

ACCSCIENCE PUBLISHING

Advances in Radiotherapy & Nuclear Medicine

SHORT COMMUNICATION

Positron emission tomography/computed tomography in B-cell non-Hodgkin's lymphoma at Hanoi Oncology Hospital

Phuong Pham Cam[1,2,3], Thai Pham Van[1,3]*, Thang Nguyen Van[4], and Nien Vu Thi[2]

[1]The Nuclear Medicine and Oncology Center, Bach Mai Hospital, Hanoi, Vietnam

[2]Department of Oncology and Nuclear Medicine, University of Medicine and Pharmacy, Vietnam National University, Hanoi, Vietnam

[3]Department of Nuclear Medicine, Hanoi Medical University, Hanoi, Vietnam

[4]Department of Nuclear Medicine, Hanoi Oncology Hospital, Hanoi, Vietnam

Abstract

This study aimed to review ^{18}fluoro-2-deoxy-d-glucose positron emission tomography/computed tomography (^{18}FDG PET/CT) imaging characteristics of B-cell non-Hodgkin's lymphoma (NHL) at Hanoi Oncology Hospital. PET/CT helps accurately assess the NHL stage compared with other diagnostic imaging methods, such as CT and magnetic resonance imaging. In this retrospective descriptive study, 86 newly diagnosed B-cell NHL cases were histopathologically and immunohistochemically examined at Hanoi Oncology Hospital between January 2018 and December 2022. Patients underwent ^{18}FDG PET/CT for pretreatment staging. The stages before and after PET/CT were evaluated and compared. Before PET/CT, 26 (30.2%), 29 (33.7%), 15 (17.5%), and 16 (18.6%) patients were in stages I, II, III, and IV, respectively. After PET/CT, the rates of Stage I, II, III, and IV cases were 22.1%, 26.8%, 20.9%, and 30.2%, respectively. PET/CT results increased the stage in 21/86 patients (24.4%). The proportion of patients with advanced stages after PET/CT in the rapidly progressing histopathology group was higher (25%) than the slowly progressing histopathology group (21.4%), and the difference was not significant. Therefore, PET/CT is critical for accurately determining the disease stage of B-cell NHL, thereby helping to detect additional lesions missed by conventional imaging diagnostic tools.

Keywords: B-cell non-Hodgkin's lymphoma; ^{18}FDG PET/CT; Pre-PET/CT stage; Post-PET/CT stage

***Corresponding author:**
Thai Pham Van
(phamvanthai@hmu.edu.vn)

Citation: Cam PP, Van TP, Van TN, Thi NV. Positron emission tomography/computed tomography in B-cell non-Hodgkin's lymphoma at Hanoi Oncology Hospital. *Adv Radiother Nucl Med*. 2025;3(1):92-96.
doi: 10.36922/arnm.4813

Received: September 10, 2024

Revised: October 17, 2024

Accepted: November 8, 2024

Published online: December 9, 2024

1. Introduction

Non-Hodgkin's lymphoma (NHL) is a group of malignant lymphoproliferative diseases with complex clinical manifestations, histopathology, and prognosis. According to GLOBOCAN 2022, NHL ranks 10th in Vietnam concerning new incidence among common cancers, of which B-cell lymphoma accounts for most of the cases.[1]

The cancer stage must be assessed for appropriate treatment. The NHL diagnosis is based on clinical examination and paraclinical tests such as biopsy for pathology,

immunohistochemistry, ultrasonography, computed tomography, and ^{18}fluoro-2-deoxy-d-glucose positron emission tomography/computed tomography (18FDG PET/CT).

Most patients with NHLs have increased glucose metabolism; thus, whole-body PET/CT with ^{18}FDG provides molecular-level metabolic images by PET and can be combined with anatomical images by CT. Consequently, it can accurately detect lesions in tumors and lymph nodes with a much higher sensitivity and specificity than conventional imaging methods. Compared with other imaging methods, PET/CT can assess the NHL stage more accurately. Reportedly, ^{18}FDG PET/CT has sensitivity and specificity up to 99%–100% in diagnosing B-cell NHL stage.[2] Therefore, this study aimed to fully evaluate the role of ^{18}FDG PET/CT in B-cell NHL.

2. Methods

In this retrospective descriptive study, 86 patients newly diagnosed with B-cell NHL who had not previously been treated were histopathologically and immunohistochemically examined at Hanoi Oncology Hospital between January 2018 and December 2022. Patients with severe diseases, two or more types of cancer, and high blood sugar ≥11.1 mmol/L before PET/CT, did not agree to participate in the study, and those with incomplete information were excluded.

Patients fasted for at least 6 h before the scan. Patients with blood glucose levels before the scan that did not exceed 11.1 mmol/L received an intravenous dose of ^{18}FDG of 0.14 – 0.15 mCi/kg. After ^{18}FDG injection, patients rested in the waiting room. After 45 – 60 min, patients underwent full-body PET/CT using the GE PET/CT system. The results were processed using specialized software, read, and agreed on by two nuclear medicine specialists. Information about age, sex, pathology type, lesion location, lesion size injury, and maximum standard uptake value of the injury were recorded.

The data were analyzed using IBM SPSS Statistics version 20 (IBM Corp., Armonk, NY, USA). Normally distributed quantitative variables were expressed as mean ± standard deviation and non-normally distributed variables as median. The t- and Mann–Whitney tests were used to compare two means and medians, respectively.

3. Results

Patient characteristics are summarized in Table 1.

A total of 86 patients were recruited, of whom 55.8% were men. The median age of the patients was 58.1 years. Most patients had rapidly progressive pathology (n = 72).

Table 1. Patients' characteristics

Parameters	Category	Number (n=86)	Percentage
Sex	Male	48	55.8
	Female	38	44.2
Pathological classification	Rapid progression	72	83.7
	Slow progression	14	16.3
Stage before PET/CT	I	26	30.2
	II	29	33.7
	III	15	17.4
	IV	16	18.7
Stage after PET/CT	I	19	22.1
	II	23	26.8
	III	18	20.9
	IV	26	30.2
Changing stage	Unchanged	65	75.6
	Increased stage*	21	24.4
	Decreased stage**	0	0

Notes: *Increased stage: upstaging is the presence of additional suspicious lesions on PET/CT compared with other imaging methods that changes the stage per Ann Arbor classification. The criterion for determining a positive PET/CT result is the presence of focal ^{18}FDG increased uptake as determined by standard uptake value (SUV) and/or lymph nodes on CT measuring ≥10 mm. SUV of 2.5 is the diagnostic threshold, distinguishing between benign and malignant lesions. **Decreased stage: downstaging is defined as lesions that are suspicious on other imaging methods but not on PET/CT, which change the stage per Ann Arbor classification.
Abbreviation: ^{18}FDG: 18fluoro-2-deoxy-d-glucose; PET/CT: Positron emission tomography/computed tomography.

The PET/CT stages before and after the procedure differed (Table 1). The number of patients in Stages III and IV increased after PET/CT compared with that before the scan. The Stage III rate increased to 20.9%, particularly Stage IV, which remarkably increased to 30.2%. After PET/CT, the stage increased in 24.4% of the patients and remained the same in 75.6%; none of the patients had a lowered stage.

After PET/CT, the patients were distributed as follows: three patients from stage I were reassigned to Stage II, three from Stage I to Stage III, one from Stage I to Stage IV, five from Stage II to Stage III, four from Stage II to Stage IV, and five from Stage III to stage IV. None of the patients lowered the stage (Figure 1).

The post-PET/CT increase rate of the slow-progressing histopathological group was lower (21.4%) than that of the rapid-progressing histopathological group (25%). However, this difference was not significant with $P > 0.05$ (Table 2).

4. Discussion

For B-cell NHL, accurate determination of disease stage is crucial for selecting appropriate treatment methods,

Table 2. Stage changes on each histopathological group

Histopathological group	Unchanged	Increased stage	Decreased stage	Summary	*P*-value
Rapidly progressing group[a]					
n	54	18	0	72	0.776
%	75.0	25.0	0	100	
Slowly progressing group[b]					
n	11	3	0	14	
%	78.6	21.4	0	100	

Notes: [a]The rapidly progressing group includes diffuse large B-cell NHL, Stage III follicular NHL. Burkitt's lymphoma and T-cell NHL do not belong to the aforementioned two types. Clinical manifestations are usually remarkable during diagnosis. Treatment should be immediately performed with a strong regimen. [b]The slowly progressing group includes chronic lymphocytic leukemia/small cell lymphoma, follicular lymphoma (stages I and II), marginal zone lymphoma (node, spleen, and MALT body), sezary syndrome/Mycosis fungoides, and primary poorly differentiated large T-cell lymphoma. The disease typically has no clinical manifestations during diagnosis and is often discovered accidentally. The disease progresses slowly. The initial response to treatment is good; however, the recurrence risk is high.
Abbreviation: NHL: Non-Hodgkin's lymphoma.

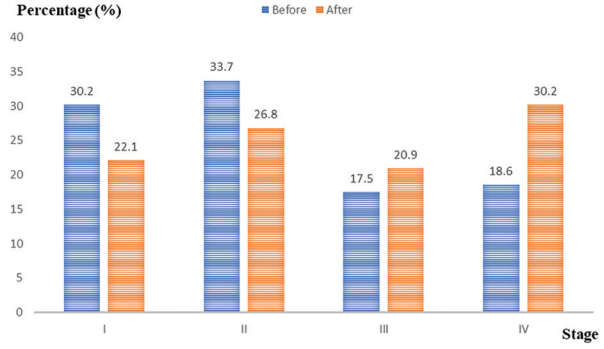

Figure 1. Disease stage before and after PET/CT
Abbreviation: PET/CT: Positron emission tomography/computed tomography.

disease prognosis, and treatment effectiveness. Compared with other common diagnostic imaging methods, PET/CT provides more information about the extent of disease spread. PET/CT can rapidly and accurately detect extranodal malignant lymphoma organizations in the liver, spleen, soft tissue, etc., due to the higher-than-normal absorption of ^{18}FDG of these organizations.

In Vietnam, several studies have examined the value of ^{18}FDG PET/CT in diagnosing the lymphoma stage. Pham *et al.* found that PET/CT changed the disease stage in 25.2% of patients, with the stage increasing in 22.8% and decreasing in 2.4%.[3] In addition, Nguyen Huu Thuong showed similar results: PET/CT changed the stage in 21.4% of the patients, of which the stage increased in 19.6% and decreased in 1.8%.[4] However, when only considering extranodal lymphomas, Mai and Le found that PET/CT changed the stage (increased stage) in more than half of the patients (52.6%).[5]

The role of PET/CT in assessing the stage of lymphoma has also been reported in the literature. According to Kasireddy *et al.*, the PET stages were higher and lower than the CT stages in 27 (14%) and 3 (1%) patients, respectively.[6] In Metser's *et al.* multicenter study of 850 patients (male = 467; female = 383), PET/CT increased the stage in 150/850 (17.6%) patients and led to a change in treatment strategies in 224/850 (26.4%).[7] In Raanani *et al.*'s study of 68 patients with NHL, PET/CT detected ^{18}FDG hyper-uptake lesions in normal-sized lymph nodes (usually <10 mm) and the most common extranodal locations, including the liver, spleen, cortical bone, bone marrow, and skin. These locations were missed on CT. In addition, a few cases of paravertebral lesions in the lung were read as benign on CT; however, on PET/CT, these lesions had increased ^{18}FDG uptake and were related to NHL. PET/CT increased the stage in 31% of patients, only 1% were downstaged, and the treatment strategy in 25% changed after PET/CT.[8] Omar *et al.* found that PET/CT changed the stage from II to IV in 25% of the patients, no lymph node lesions measured <10 mm, and all lesions were detected. The new lesions were all outside the lymph nodes.[9] In a multicenter, multinational study by Barrington *et al.*, involving 1,171 patients with lymphoma, PET/CT changed the stage in 19.9% of the patients, of which the stage increased in 13.6% and downstaged in 6.3%. Among patients with increased stage, additional extranodal lesions were discovered in 74.2% (most common in the bone marrow, lung, liver, pleura, and multiple sites), and new lesions were detected in 22%. Lesions with normal size but increased ^{18}FDG uptake on PET/CT, splenic lesions with increased ^{18}FDG uptake without structural abnormalities on CT, and other lesions that were unclear on CT had increased ^{18}FDG uptake on PET/CT (3.8%). In patients with lower stages, the most common cases were large lymph node and spleen lesions on anatomical images on CT; however, their ^{18}FDG uptake levels were in the normal range in PET/CT. In addition, some lesions in the lungs,

bone marrow, and adrenals demonstrated abnormalities on CT but had ^{18}FDG absorption levels at the physiological threshold.[10] Particularly, studies have shown the important role of PET/CT in assessing bone marrow lesions in NHL. Biopsy of all bone marrow lesions is impossible, and the assessment of bone marrow invasion based on CT or magnetic resonance imaging (MRI) is difficult. Thus, PET/CT with 64 molecular metabolism images can show lesions with increased ^{18}FDG uptake very early. According to Adams *et al*., PET/CT can detect bone marrow lesions with a sensitivity of 70.8 – 90.8%, specificity of 99.0 – 100%, and area under the receiver operating characteristic curve of up to 99.83%. Compared to bone marrow biopsy results, PET/CT gave false-negative results in 3.1% of the patients and false-positive results in 12.5% ($P < 0.05$).[11] Similarly, Li *et al*. compiled research based on 36 published reports and revealed that PET/CT has a sensitivity of 93 – 99% and specificity of 98 – 99% in detecting bone marrow invasive lesions in NHL, whereas bone marrow biopsy had a lower sensitivity of 34 – 55% and specificity of 92 – 100%.[12] Berthet *et al*. studied 142 cases of diffuse large B-cell lymphoma, and ^{18}FDG PET/CT showed higher sensitivity than bone marrow biopsy (94% vs. 24%, $P < 0.001$). The negative report of PET/CT was also higher than that of bone marrow biopsy (98% vs. 80%, $P < 0.01$).[13]

Compared with MRI, PET/CT has a comparable ability to accurately diagnose lesions. However, in slowly progressing lymphoma, MRI could detect lesions that barely capture ^{18}FDG on PET/CT. Wang *et al*. examined 338 patients and showed that in those with rapidly progressing lymphomas, PET/CT and MRI had the same accuracy rates in determining the disease stage (98%, $P < 0.05$), and in slowly progressing disease, PET/CT only had a diagnostic accuracy rate of 87%, whereas MRI recorded up to 96%. Among these, many slowly progressing histopathological lesions could not nearly capture ^{18}FDG.[14] Similarly, Maccioni *et al*. evaluated MRI as a good imaging diagnostic tool for lymphoma stages, and the results between MRI and ^{18}FDG PET/CT were very similar.[15] ^{18}FDG PET/CT is still the "gold standard" in accurately assessing the stage of B-cell lymphoma.

Herein, before PET/CT, 86 patients were staged according to the Ann - Arbor classification based on the ultrasound, CT, and MRI findings: 30.2%, 33.7%, 17.5%, and 18.6% of the patients were in Stages I, II, III, and IV, respectively. After PET/CT, patients were restaged based on the lesion number and locations identified on PET/CT images. After PET/CT, among patients with Stage 1 disease, three patients had additional lymph node damage on the same side of the diaphragm, changing the stage to II; another lymph node damage on the same side of the diaphragm was noted in three patients; therefore, the stage was changed to III; additional lesions in two extranodal organs were noted in one patient, which progressed to Stage IV. Among patients in Stage II, additional lesions were found on the diaphragm side in five patients; therefore, they were restaged to III, and ≥2 additional extranodal organs were detected in four patients, changing their stage to IV. Among patients with Stage III disease, five progressed to Stage IV due to the additional spread of extranodal lesions was noted. Thus, PET/CT results showed a change in stage (increased stage) in 21 of the 86 patients (24.4%). The rate of stage change between the rapidly and slowly progressing histopathology groups was not significantly different. Thus, our research results were not much different from the research results of others in Vietnam and worldwide. Therefore, ^{18}FDG PET/CT is a very valuable method in diagnosing the B-cell lymphoma stage. Accurate assessment of the disease stage helps doctors select appropriate treatment methods with the highest effectiveness. In addition, PET/CT is very valuable in monitoring, evaluating treatment response, and predicting B-cell NHL. Before PET/CT, 26 (30.2%), 29 (33.7%), 15 (17.5%), and 16 (18.6%) patients were in Stages I, II, III, and IV, respectively. After PET/CT, the rates of Stages I, II, III, and IV cases were 22.1%, 26.8%, 20.9%, and 30.2%, respectively. The rate of patients with increased stage after PET/CT scan in the rapidly progressing histopathology group was higher (25%) than in the slowly progressing histology group (21.4%), and the difference was not significant.

5. Conclusion

PET/CT plays an important role in accurately determining the disease stage of B-cell NHL, helping detect additional lesions missed on conventional imaging diagnostic tools.

Acknowledgments

The authors thank the patients and the colleagues who made this work possible.

Funding

None.

Conflict of interest

Phuong Pham Cam is an Editorial Board Member of this journal but was not in any way involved in the editorial and peer-review process conducted for this paper, directly or indirectly. Separately, other authors declared that they have no known competing financial interests or personal relationships that could have influenced the work reported in this paper.

Author contributions

Conceptualization: Phuong Pham Cam, Thai Pham Van
Investigation: Thang Nguyen Van, Nien Vu Thi, Phuong Pham Cam, Thai Pham Van
Methodology: Thang Nguyen Van, Thai Pham Van
Writing–original draft: Thang Nguyen Van, Nien Vu Thi, Phuong Pham Cam
Writing–review & editing: Phuong Pham Cam, Thai Pham Van

Ethics approval and consent to participate

This study was approved by Hanoi Medical University (certificate of approval No. 4670/QĐ-ĐHYHN). This is a retrospective, non-interventional study thus ethics approval is not required.

Consent for publication

Informed consent was obtained from the patients to publish their data.

Availability of data

Not applicable.

References

1. Bray F, Laversanne M, Sung H, *et al*. Global cancer statistics 2022: GLOBOCAN estimates of incidence and mortality worldwide for 36 cancers in 185 countries. *CA Cancer J Clin*. 2024;74(3):229-263.

   doi: 10.3322/caac.21834

2. Fueger BJ, Yeom K, Czernin J, *et al*. Comparison of CT, PET, and PET/CT for Staging of patients with indolent non-Hodgkin's lymphoma. *Mol Imaging Biol*. 2009;11(4):269-274.

   doi: 10.1007/s11307-009-0200-9

3. Pham VT, Thieu TH, Mai TK, *et al*. Evaluate the role of 18F-FDG PET/CT in diagnosing the stage of non-Hodgkin's lymphoma. *Vietnam J Oncol*. 2018;5:75-79.

4. Nguyen HT, Nguyen KL, Nguyen HN, *et al*. The role of 18FDG PET/CT in assessing stage and response to treatment of malignant non-Hodgkin's lymphoma. *J Milit Med Pharm*. 2022;6:107-117.

5. Mai HS, Le NH. FDG PET/CT in stage assessment Stage and response to treatment of extranodal non-Hodgkin lymphoma. *Vietnam J Radiol*. 2022;25:58-64.

   doi: 10.55046/vjrnm.25.642.2016

6. Kasireddy S, Nirmal S, Kathal R, *et al*. A systematic review of the role of PET-CT imaging in the assessment of treatment response and its predictive value for survival outcomes in adult patients with newly diagnosed Hodgkin lymphoma: A comparison with conventional imaging techniques. *Research Square [Preprint]*; 2024.

   doi: 10.21203/rs.3.rs-3837903/v1

7. Metser U, Prica A, Hodgson DC, *et al*. Effect of PET/CT on the management and outcomes of participants with Hodgkin and aggressive non-Hodgkin lymphoma: A multicenter registry. *Radiology*. 2019;290(2):488-495.

   doi: 10.1148/radiol.2018181519

8. Raanani P, Shasha Y, Perry C, *et al*. Is CT scan still necessary for staging in Hodgkin and non-Hodgkin lymphoma patients in the PET/CT era? *Ann Oncol*. 2006;17(1):117-122.

   doi: 10.1093/annonc/mdj024

9. Omar NN, Alotaify LM, Abolela MS. PET/CT in initial staging and therapy response assessment of lymphoma. *Egypt J Radiol Nucl Med*. 2016;47(4):1639-1647.

   doi: 10.1016/j.ejrnm.2016.07.009

10. Barrington SF, Kirkwood AA, Franceschetto A, *et al*. PET-CT for staging and early response: Results from the response-adapted therapy in advanced hodgkin lymphoma study. *Blood*. 2016;127(12):1531-1538.

    doi: 10.1182/blood-2015-11-679407

11. Adams HJA, Kwee TC, Keizer B, *et al*. FDG PET/CT for the detection of bone marrow involvement in diffuse large B-cell lymphoma: Systematic review and meta-analysis. *Eur J Nucl Med Mol Imaging*. 2014;41(3):565-574.

    doi: 10.1007/s00259-013-2623-4

12. Li Z, Li C, Chen B, *et al*. FDG-PET/CT versus bone marrow biopsy in bone marrow involvement in newly diagnosed paediatric lymphoma: A systematic review and meta-analysis. *J Orthop Surg Res*. 2021;16(1):482.

    doi: 10.1186/s13018-021-02521-3

13. Berthet L, Cochet A, Kanoun S, *et al*. In newly diagnosed diffuse large B-cell lymphoma, determination of bone marrow involvement with 18F-FDG PET/CT provides better diagnostic performance and prognostic stratification than does biopsy. *J Nucl Med*. 2013;54(8):1244-1250.

    doi: 10.2967/jnumed.112.114710

14. Wang D, Huo Y, Chen S, *et al*. Whole-body MRI versus 18F-FDG PET/CT for pretherapeutic assessment and staging of lymphoma: meta-analysis. *Onco Targets Ther*. 2018;11:3597-3608.

    doi: 10.2147/OTT.S148189

15. Maccioni F, Alfieri G, Assanto GM, *et al*. Whole body MRI with diffusion weighted imaging versus 18f-fluorodeoxyglucose-PET/CT in the staging of lymphomas. *Radiol Med*. 2023;128(5):556-564.

    doi: 10.1007/s11547-023-01622-9

ACCSCIENCE PUBLISHING

Advances in Radiotherapy & Nuclear Medicine

CASE SERIES

The role of ^{18}F-fluorodeoxyglucose positron emission tomography/computed tomography in the detection of brown tumors: A case series

Salah Nabih Oueriagli*, Ayoub Dribla*, Omar Ait Sahel, Yassir Ben Ameur, and Abderrahim Doudouh

Department of Nuclear Medicine, Mohammed V Military Teaching Hospital, Souissi University, Rabat, Morocco

Abstract

We present two cases of chronic hemodialysis patients with suspicious lytic pelvic bone lesions in the context of secondary hyperparathyroidism (HPT). Bone biopsies were inconclusive. ^{18}F-fluorodeoxyglucose positron emission tomography/computed tomography (^{18}F-FDG PET/CT) scans revealed highly hypermetabolic lytic lacunar bone lesions scattered throughout the skeleton. Pathological ^{99m}Tc-hexakis-methoxy-isobutyl-isonitrile (^{99m}Tc-MIBI) uptake in the cervical region suggested parathyroid tissue involvement, while whole-body ^{99m}Tc-MIBI scintigraphy did not reveal pathological uptake. Brown tumors were strongly suspected based on clinical and laboratory evidence of HPT, ruling out malignancy. Our cases suggest the superior sensitivity of ^{18}F-FDG PET/CT in detecting and characterizing brown tumors compared to whole-body ^{99m}Tc-MIBI scintigraphy. This examination offers crucial insights into characterizing brown tumors based on morpho-metabolic criteria, minimizing inaccurate diagnosis of this pathological condition.

Keywords: Brown tumors; Positron emission tomography/computed tomography; ^{18}F-fluorodeoxyglucose; Hyperparathyroidism

***Corresponding authors:**
Salah Nabih Oueriagli (salah.nabihoueriagli@gmail.com)
Ayoub Dribla (ayoubdribla10@gmail.com)

Citation: Oueriagli SN, Dribla A, Sahel OA, Ameur YB, Doudouh A. The role of 18F-fluorodeoxyglucose positron emission tomography/computed tomography in the detection of brown tumors: A case series. *Adv Radiother Nucl Med*. 2025;3(1):97-102.
doi: 10.36922/arnm.3540

Received: April 30, 2024

1st revised: June 14, 2024

2nd revised: June 23, 2024

Accepted: June 27, 2024

Published online: January 16, 2025

1. Background

Brown tumors represent a rare manifestation of hyperparathyroidism (HPT), a condition characterized by excessive secretion of parathyroid hormone (PTH), leading to abnormalities in bone metabolism. Despite their non-neoplastic nature, these tumors can inflict significant morbidity due to their deleterious effects on bone structure and function. Within the realm of diagnosing and detecting brown tumors, ^{18}F-fluorodeoxyglucose positron emission tomography/computed tomography (^{18}F-FDG PET/CT) assumes a pivotal role. Through two clinical case reports, we highlight the role of this hybrid imaging technique in detecting the morpho-metabolic aspect of brown tumors.

2. Case presentation

2.1. Case 1

A 40-year-old female, undergoing chronic hemodialysis for 6 years, had a history of invasive ductal carcinoma of the right breast with contralateral recurrence in 2013.

Following conservative treatment, an increase in CA15-3 levels at 73 U/mL (reference value <31.3 U/mL) and diffuse bone pain in 2018 suggested metastatic recurrence. Bone scintigraphy indicated metabolic super scan with heterogeneous uptake in the skull. In addition to mediastinal and left internal mammary lymph node involvement, a CT scan revealed lytic lesions in the spine, sternum, and pelvic bones. PET-CT scan showed metabolically active metastatic lesions in the left lung, liver segment IV, mediastinal lymph nodes, and left internal mammary chain. Bone lesions appeared hypermetabolic with lacunar lytic foci. The spine showed slightly more intense and heterogeneous uptake, particularly with hypermetabolic chondrocostal and lower jaw lesions, resembling a metabolically active, extensively remodeled skeleton (Figure 1). A weakly hypermetabolic retrothyroid left focus with maximum standardized uptake value (SUV_{max}) = 3.3 suggested a parathyroid formation, necessitating additional ultrasound and parathyroid scintigraphy. Concurrently, the phosphocalcic assessment showed a total calcium level of 116 mg/L (reference range: 80 – 105 mg/L) and a phosphorus level of 42 mg/L (reference range: 25 – 50 mg/L). The PTH level was abnormally elevated at 1214 pg/mL (reference range: 15 – 68 pg/mL), confirming the diagnosis of secondary HPT. A cervical ultrasound revealed a centimetric retrothyroid left mid-lobe nodular formation suggestive of a parathyroid nodule at this level. Whole-body scan with 99mTc-MIBI show no definite suspicious focus suggestive of brown tumors, except for physiological radiopharmaceutical uptake in the parotid, submaxillary, hepatobiliary, and digestive regions (Figure 2A). ^{99m}Tc-hexakis-methoxy-isobutyl isonitrile (^{99m}Tc-MIBI) parathyroid scintigraphy showed a pathologically retained focus of ^{99m}Tc-MIBI in the left mid-lobe, with slightly delayed washout compared to the rest of the thyroid parenchyma, suggesting pathological parathyroid tissue, consistent with the results of cervical ultrasound (Figure 2B). Whole-body scanning at the end of the examination showed two areas of very low and

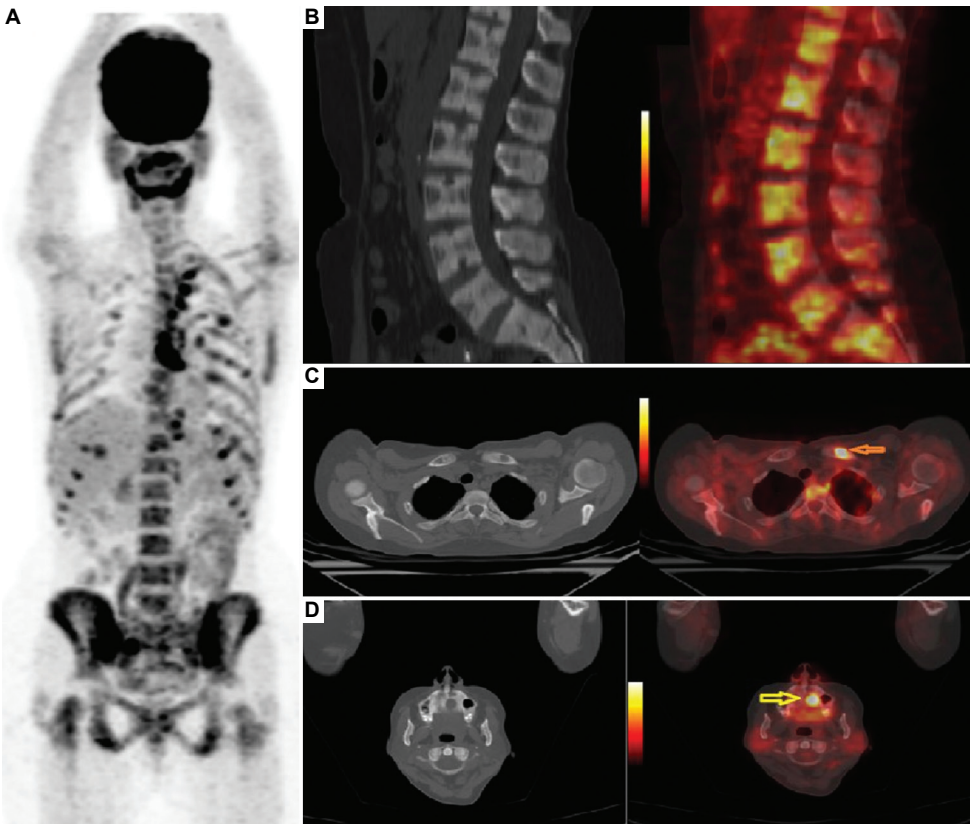

Figure 1. Hypermetabolic uptake in the spine, chondrocostal regions, and lower jaw. (A) 3D Maximum Intensity Projection (MIP) image show heterogeneous and diffuse hypermetabolism throughout the axial skeleton, particularly intense lower mandibular hypermetabolism and staggered, symmetrical hypermetabolic foci in the right and left chondrocostal joints, presumably metabolic in origin, related to the patient's known chronic hemodialysis state. (B) Sagittal CT and PET/CT fusion images of the lumbar spine show multiple hypermetabolic lacunar foci corresponding to brown tumors. (C) CT and PET/CT fusion images show a rounded, hypermetabolic lytic lesion with regular contours in the inner third of the left clavicle (orange arrow). (D) CT and PET/CT fusion images show a hypermetabolic lower mandibular lacuna (yellow arrow). (B-D) Images corresponding to brown tumors.
Abbreviation: PET/CT: Positron emission tomography/computed tomography.

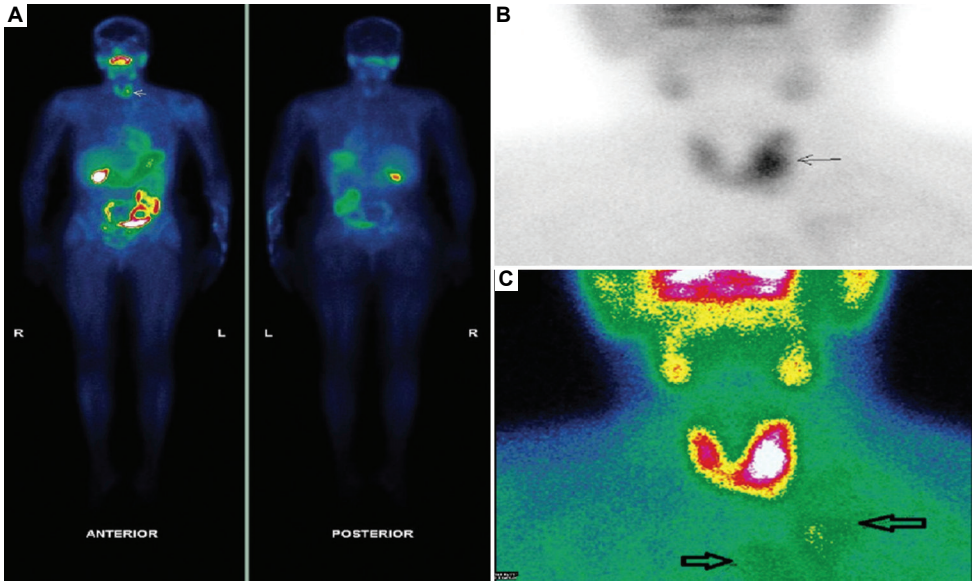

Figure 2. ^{99m}Tc-MIBI whole-body scan, parathyroid scintigraphy, and cervical static acquisition show physiological uptake, a pathologic focus in the left mediolobar region, and low uptake near the clavicle and manubrium, respectively, suggestive of brown tumors. (A) Whole-body scan with ^{99m}Tc-MIBI show no definite suspicious focus suggestive of brown tumors, except for physiological radiopharmaceutical uptake in the parotid, submaxillary, hepatobiliary, and digestive regions. (B) Parathyroid scintigraphy showing a pathologic retention focus of ^{99m}Tc-MIBI in the left mediolobar region consistent with the retrothyroid nodule visualized on cervical ultrasound (indicated by the arrow). (C) Anterior cervical static acquisition following whole-body scan showing two areas of very low and heterogeneous ^{99m}Tc-MIBI uptake adjacent to the inner third of the left clavicle and the sternal manubrium, presumably corresponding to brown tumors on PET/CT examination (indicated by the arrow).
Abbreviation: PET/CT: Positron emission tomography/computed tomography.

heterogeneous ^{99m}Tc-MIBI uptake corresponding to the inner third of the left clavicle and the sternal manubrium (Figure 2C). A comparison of images in PET/CT and ^{99m}Tc-MIBI scintigraphy suggested that these uptake areas corresponded presumably to brown tumors. Thus, given these clinical, biological, and radiological findings, the diagnosis of brown tumors was established, especially in the absence of signs of malignancy on bone biopsies performed on the patient.

2.2. Case 2

A 21-year-old female with chronic renal failure due to congenital urological malformation presented to the rheumatology department with pelvic pain, lumbalgia, and weight loss. X-rays revealed lytic lacunar images in both iliac wings and L3. Biological tests showed an inflammatory syndrome, elevated C-reactive protein 60.8 mg/L, and increased gamma globulins. Phosphocalcic assessment indicated slightly elevated corrected calcium of 2.53 mmol/L and normal phosphorus levels, but significantly increased PTH levels. Cervical ultrasound revealed two centimetric hypoechoic heterogeneous well-vascularized nodular formations at the lower poles, suggestive of bilateral parathyroid nodules. ^{99m}Tc-MIBI parathyroid scintigraphy confirmed pathological parathyroid tissue near the lower poles of both thyroid lobes. Whole-body scanning at the end of the examination did not show any pathological uptake of ^{99m}Tc-MIBI elsewhere in the body. CT scan revealed spondylodiscitis at L2 – L3 and lacunar images in both iliac wings suggestive of renal osteodystrophy. The bone scan showed no suspicious foci. Lumbar magnetic resonance imaging (MRI) confirmed spondylodiscitis and bone biopsies yielded inconclusive results. PET/CT scan revealed metabolically active lytic foci in the axial and peripheral skeleton, particularly in the pelvis and lumbar spine at the level of L2 and L3 (Figure 3), suggesting a neoplastic origin, but the symmetric nature of lesions and lacunar contours favored brown tumors. The diagnosis was confirmed by the absence of malignancy in bone biopsies and clinical-biological arguments related to secondary HPT. The subsequent management consisted of conservative medical treatment of HPT and appropriate antibiotic therapy with biological and radiological follow-up.

3. Discussion

Brown tumors are benign lytic bone lesions, often encountered in the context of secondary HPT or hypersecreting parathyroid carcinoma.[1] They are much more common in women over 50 and can affect the entire skeleton, particularly the bones of the face, long bones of the upper and lower limbs, pelvis, and ribs.[2] They can cause

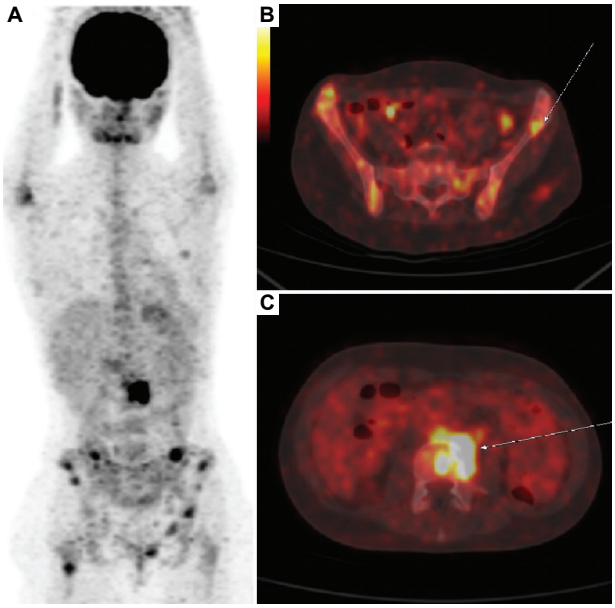

Figure 3. Hypermetabolic uptake is seen in the right humeral head, lumbar spine (L2 and L3), iliac wings, and right femoral diaphysis corresponding to brown tumors. Multiple hypermetabolic lytic foci in both iliac wings and a focus in the lumbar spine at L2 are suggestive of spondylodiscitis. (A) 3D Maximum Intensity Projection (MIP) image showing hypermetabolic foci in the right humeral head, the lumbar spine at the level of L2 and L3, the iliac wings, and the upper end of the right femoral diaphysis, corresponding to morphological images of brown tumors. (B) PET/CT fusion image of the pelvis in the sagittal section showing multiple hypermetabolic lytic lacunar foci in both iliac wings, corresponding to brown tumors. (C) PET/CT fusion image of the lumbar spine at the level of L2 in the sagittal section highlighting a hypermetabolic focus in the body of L2 associated with diffuse and heterogeneous hypermetabolism of the lateral wall of L2 and adjacent areas suggestive of spondylodiscitis focus.
Abbreviation: PET/CT: Positron emission tomography/computed tomography.

intense inflammatory pain and swelling, exposing the patient to a high risk of fractures.[1] In a neoplastic context, their presence can pose a differential diagnostic problem with unrecognized bone metastases, which is illustrated by the case of a 69-year-old woman who presented with pain in her right clavicle. A CT scan revealed a pathological fracture of the right clavicle, associated with multiple osteolytic lesions, and a left cervical mass. An ^{18}F-FDG PET/CT showed significant FDG uptake in the cervical mass and osteolytic lesions, suggesting metastatic parathyroid cancer,[3] or, in rare cases, with a primary giant cell tumor of polyostotic nature. Their positive diagnosis relies on a convergence of clinical-biological arguments related to HPT and histopathological findings, but above all on the contribution of imaging after ruling out a neoplastic origin.

Standard radiographs are usually sufficient for identifying brown tumors, but they may lack specificity in their description. Additional imaging modalities, such as CT, MRI, and/or PET/CT become necessary in cases of diagnostic uncertainty, multifocality, or involvement of adjacent soft tissues.

In general, ^{99m}Tc-MIBI scintigraphy remains the gold standard for pre-operative localization of hyperfunctional parathyroid lesions in primary, secondary, or tertiary HPT.[4] In cases of known bone lesions, it is feasible to combine cervical and mediastinal exploration with a whole-body analysis, which allows mapping of the lesions throughout the skeleton in a single examination.[5] In a study by Zhao and Wang, whole-body ^{99m}Tc-MIBI scintigraphy performed in the context of primary (63 patients) and secondary (16 patients) HPT showed bone hyperfixations corresponding to brown tumors in 4% of cases (3/79). These hyperfixations are not constant, differ from one patient to another, and are not specific to brown tumors but reflect bone hypermetabolism related to osteoclastic cell proliferation.[6] The radiopharmaceutical accumulates in mitochondrial cells and reflects cell proliferation and multinucleation of osteoclasts within the bone. The heterogeneity of fixation of bone lesions with ^{99m}Tc-MIBI can be explained by the difference in cellularity and mitochondrial content within brown tumors in the same patient,[7] as in the case of our first patient where the pathological foci found on whole-body scanning with ^{99m}Tc-MIBI were of low and heterogeneous uptake, located differently, and fewer in number than those found on PET/CT.

PET/CT with ^{18}F-FDG has been used in this context, marking its superiority. Few clinical observations in line with this advancement have been reported in the literature.[7-10] This can be explained by the limited number of patients and the decreasing prevalence related to systematic biological screening of hypercalcemia.[11] A case of brown tumors reported in the literature involving a patient with secondary and then tertiary HPT concluded the superiority of ^{18}F-FDG PET/CT for detecting diffuse bone lesions compared to ^{99m}Tc-MIBI scintigraphy.[7] Undoubtedly, ^{18}F-FDG is a non-specific tracer of glucose metabolism whose accumulation is higher in neoplastic cells. Foci of uptake in bone can be seen during PET/CT examination and have a benign nature, notably inflammatory foci (active osteoarthritis, fracture, synovitis, etc.), infectious foci (osteomyelitis, prosthetic infection, arthritis, spondylodiscitis, etc.), and some benign bone pathologies such as brown tumors, giant cell bone tumors, and Paget's disease in case of malignant transformation. During this examination, brown tumors appear as multiple lytic lacunar foci with regular contours, highly metabolically active, single or multiple, scattered throughout the axial and peripheral skeleton, particularly in long bones, facial bones, and the pelvis. These lacunar

foci are sometimes symmetrical, distinguishing them from osseous metastases, which are, by nature, randomly distributed throughout the skeleton. Despite these morpho-metabolic criteria, it is impossible to definitively rule out the neoplastic origin of these lacunar foci, and histological methods remain the only guarantee to confirm the diagnosis of brown tumors. Sometimes, in the face of repeated bone biopsies free of malignancy, the convergence of clinical-biological arguments related to secondary HPT and the morpho-metabolic aspect of these tumors are sufficient for clinicians to diagnose brown tumors.[2]

In our cases, parathyroid scintigraphy complemented by whole-body scanning did not show clear pathological uptake of ^{99m}Tc-MIBI outside the usual sites of cervical and/or mediastinal uptake: Bone sites suspected of being brown tumors. Similarly, bone scintigraphy with radiobiphosphonates performed for diagnostic purposes in the neoplastic context failed to highlight these lytic foci. This suggests that both methods lack the sensitivity to detect multiple brown tumors scattered throughout the axial and peripheral skeleton. Our two clinical cases thus suggest that ^{18}F-FDG PET/CT may be more sensitive for detecting bone lesions in the context of brown tumors than whole-body ^{99m}Tc-MIBI scintigraphy. This examination provides key insights into characterizing brown tumors based on morpho-metabolic criteria, minimizing inaccurate diagnosis of pathological condition.

4. Conclusion

The two clinical cases we present are consistent with other cases reported in the literature, suggesting the superiority of ^{18}F-FDG PET/CT for the detection of brown tumors compared to whole-body ^{99m}Tc-MIBI scintigraphy and/or bone scintigraphy with radiobiphosphonates. Histological methods remain the reference to confirm the diagnosis and rule out a neoplastic origin of these lytic foci.

Acknowledgments

None.

Funding

None.

Conflict of interest

The authors declare that they have no competing interests.

Author contributions

Conceptualization: Ayoub Dribla, Yassir Ben Ameur
Investigation: Ayoub Dribla, Omar Ait Sahel
Methodology: Salah Nabih Oueriagli, Ayoub Dribla
Writing – original draft: Ayoub Dribla, Salah Nabih Oueriagli
Writing – review & editing: Salah Nabih Oueriagli, Abderrahim Doudouh

Ethics approval and consent to participate

All procedures performed in studies involving human participants were in accordance with the ethical standards of the institutional and/or national research committee and with the 1964 Helsinki Declaration and its later amendments or comparable ethical standards. For this case series, formal consent to participate is not required.

Consent for publication

Written informed consent was obtained from the patients for publication of this case series and any accompanying images.

Availability of data

Authors make available to all scientists, documents described in the manuscript, including new software, databases, and all relevant raw data.

References

1. Ullah E, Ahmad M, Ali SA, Redhu N. Primary hyperparathyroidism having multiple Brown tumors mimicking malignancy. *Indian J Endocrinol Metab*. 2012;16:1040-1042.

   doi: 10.4103/2230-8210.103037

2. Penhaat MG, Drui D, Ansquer C, Mirallie E, Maugars Y, Guillot P. Contribution of ^{18}FDG PET/CT for the detection of brown tumors in a case of primary hyperparathyroidism. Rhum Rev. 2016;83:386.389.

   doi: 10.1016/j.rhum.2016.05.013

3. Tsukamoto S, Kawabata K, Kawamura H, Takata K, Hosono M. Differentiating brown tumor from bone metastasis in parathyroid cancer using 18F-FDG PET and 99mTc-MIBI SPECT. *Clin Nucl Med*. 2024;49(5):444-446.

   doi: 10.1097/RLU.0000000000005115

4. Greilsamer T, Blanchard C, Christou N, *et al*. Management of thyroid nodules incidentally discovered on MIBI scanning for primary hyperparathyroidism. *Langenbecks Arch Surg*. 2015;400:313-318.

   doi: 10.1007/s00423-015-1286-y

5. Santiago Chinchilla A, Ramos Font C, Muros de Fuentes MA, *et al*. False negative of the scintigraphy with 99mTc-sestamibi in parathyroid carcinoma with associated brown tumors. Contributions of the 18F-FDG-PET/CT. *Rev Esp Med Nucl*. 2011;30:174-179.

   doi: 10.1016/j.remn.2010.08.006

6. Zhao Y, Wang Q. Bone uptake of Tc-99m MIBI in patients

with hyperparathyroidism. *Ann Nucl Med*. 2014;28:349-355.

doi: 10.1007/s12149-014-0818-9

7. Gedik GK, Ata O, Karabagli P, Sari O. Differential diagnosis between secondary and tertiary hyperparathyroidism in a case of a giant-cell and brown tumor containing mass. Findings by (99m)Tc-MDP, (18)F-FDG PET/CT and (99m) Tc-MIBI scans. *Hell J Nucl Med*. 2014;17:214-217.

doi: 10.1967/s002449910147

8. Sager S, Aliyev A, Halac M, Oztürk T. Positron emission tomography/computed tomography imaging of brown tumors mimicking multiple skeletal metastases in patient with primary hyperparathyroidism. *Indian J Endocrinol Metab*. 2012;16:850-852.

doi: 10.4103/2230-8210.100682

9. Zanglis A, Andreopoulos D, Zissimopoulos A, Baziotis N. Multiple brown tumors with Tc-99mMDP superscan appearance and negative Tc-99mMIBI uptake. *Clin Nucl Med*. 2006;31:640-643.

doi: 10.1097/01.rlu.0000237968.88074.fb

10. Geysen A, Van Laere K, Verscuren R. Detection of unexpected brown tumors due to hyperparathyroidism diagnosed by 18F-FDG PET/CT. *Clin Nucl Med*. 2021;46(1):e16-e17.

doi: 10.1097/RLU.000000000003380

11. Heimburger C, Andres E, Rust E, *et al*. Morpho-functional imaging in a patient with hyperparathyroidism and multifocal maxillary brown tumor. *Rev Med Interne*. 2013;34:377-381.

doi: 10.1016/j.revmed.2013.02.007

ACCSCIENCE PUBLISHING

Advances in Radiotherapy & Nuclear Medicine

BRIEF REPORT

Utility of fluorine-18 fluorodeoxyglucose positron emission tomography in the etiological diagnosis of unexplained inflammatory syndromes: A retrospective study of 25 cases

Salah Oueriagli Nabih*, Omar Ait Sahel, Yassir Benameur, Meryem Aboussabr, Ikram Zahfir, and Abderrahim Dousouh

Department of Nuclear Medicine, Military Teaching Hospital, University Hassan II, Rabat, Morocco

Abstract

Positron emission tomography integrated with computed tomography using 2-deoxy-2-[fluorine-18]fluoro-D-glucose (^{18}F-FDG PET/CT) plays a critical role in the localization, diagnosis, and management of infectious diseases and inflammatory disorders. This hybrid imaging modality provides morpho-metabolic information that aids in defining the etiology of unexplained inflammatory syndromes and assessing treatment response. A key advantage of ^{18}F-FDG PET/CT is its ability to provide a comprehensive, "all in one" diagnostic solution, particularly in cases where localizing symptoms are absent, facilitating the identification of metastatic and/or septic foci. Recently, there has been increasing recognition among clinicians of its potential in diagnosing, characterizing, and assessing inflammatory disorders. This study evaluates the clinical utility of ^{18}F-FDG PET/CT in identifying the etiology of inflammatory syndromes by analyzing 25 patients with unexplained inflammatory disorders. The findings highlight the high reproducibility, sensitivity, and specificity of this imaging modality in this context.

Keywords: ^{18}F-FDG PET/CT; Unexplained inflammatory syndromes; Predictive values

***Corresponding author:**
Salah Oueriagli Nabih
(hmimV@gmail.com)

Citation: Nabih SO, Sahel OA, Benameur Y, Aboussabr M, Zahfir I, Dousouh A. Utility of fluorine-18 fluorodeoxyglucose positron emission tomography in the etiological diagnosis of unexplained inflammatory syndromes: A retrospective study of 25 cases. *Adv Radiother Nucl Med*. 2025;3(1):103-108.
doi: 10.36922/arnm.5895

Received: November 13, 2024

1st revised: December 16, 2024

2nd revised: January 15, 2025

Accepted: January 16, 2025

Published online: February 28, 2025

1. Introduction

Since its introduction in Morocco in 2010, ^{18}F-fluorodeoxyglucose positron emission tomography/computed tomography (^{18}F-FDG PET/CT) has played a crucial role in the localization, diagnosis, and management of infectious diseases and inflammatory disorders, particularly in cases where paraclinical examinations fail to provide a definitive diagnosis. Delayed diagnosis in such cases can lead to unfavorable medical and economic consequences. The adoption of this hybrid imaging technique has significantly improved the specificity of disease detection. As a result, there has been a growing interest in employing ^{18}F-FDG PET/CT for the detection of inflammation and infections. Notably, the mechanisms underlying ^{18}F-FDG uptake and metabolic trapping are fundamentally similar in both inflammatory and neoplastic cells. In both cases, cellular accumulation occurs due to the upregulation of membrane transporters (GLUT1 and GLUT5), increased cellular energy consumption, and inability to metabolize ^{18}F-FDG. A comprehensive literature review indicates that the most common

etiologies of unexplained inflammatory syndromes include vasculitis, neoplastic processes, granulomatous diseases, and infections affecting the cardiovascular, gastrointestinal, and pulmonary systems.

2. Methods

2.1. Patient recruitment

This retrospective study included 25 consecutive patients with unexplained inflammatory syndrome who underwent ^{18}F-FDG PET/CT at our institution between January 2019 and December 2024. Inflammatory syndrome was defined as a persistent elevation of C-reactive protein beyond the normal range for a minimum duration of 3 weeks. All patients presented with febrile syndrome and had negative morphological findings on conventional imaging.

2.2. ^{18}F-FDG PET/CT

All ^{18}F-FDG PET/CT scans were performed using an integrated PET/CT scanner (GE Discovery STE8, GE Healthcare, USA). Patients fasted for at least 8 h before imaging, without any premedication. Blood glucose levels and body weight were measured before ^{18}F-FDG injection, ensuring that all patients had blood glucose levels below 6.27 mmol/L. A net dose of 3 MBq/kg of ^{18}F-FDG was administered intravenously, with an average uptake time of 45 – 60 min. Based on patient body weights ranging from 50 to 80 kg, and after accounting for residual syringe activity, the mean net injected dose was 193 MBq. Image acquisition began 45 min post-injection, covering the region from the head to the upper thighs, with a scan duration of 3 min per bed position. PET images were reconstructed using vendor-provided algorithms that applied ordered subset expectation maximization, employing two iterations, 28 subsets, and a 128 × 128 reconstruction matrix. Attenuation correction was achieved using CT data acquired during the same session. CT imaging was performed from the skull base to the upper thighs, with imaging parameters set at 120 mA current, 140 kV voltage, and a table speed of 13.5 mm/rotation. Axial CT images were reconstructed with a slice thickness of 3.75 mm. All PET/CT studies were independently reviewed by two nuclear physicians. These experts analyzed PET-only, CT-only, and fused PET/CT images in combined sessions. Fused PET/CT images were primarily used to localize lesions and differentiate pathological ^{18}F-FDG uptake from physiological uptake in adjacent organs. Metabolic activity at abnormal ^{18}F-FDG uptake sites was assessed qualitatively and semi-quantitatively. The maximum standardized uptake value (SUVmax) within the volume of interest was calculated using Equation I:

$$SUV_{max} = \frac{\text{Measured activity within the volume of interest}\left(\frac{\text{MBq}}{\text{mL}}\right)}{\text{Injected dose of}^{18}\text{F-FDG(MBq)} \Big/ \text{Patient's body weight(g)}} \quad \text{(I)}$$

To ensure accuracy and reliability in SUV measurements, a rigorous in-house quality control program was implemented. This program included weekly calibrations conducted by the service team. It involved radioactive ^{18}F-FDG PET/CT sources, calibration phantoms, standardized protocols, detailed result analysis, and regular staff training to maintain optimal equipment performance and reliable imaging results. On PET/CT images, sites of abnormal ^{18}F-FDG uptake were documented based on uptake intensity and anatomical location. These findings were further evaluated by comparing the intensity of abnormal intake to that of physiological ^{18}F-FDG uptake in the liver.

2.3. Histopathological and descriptive analyses

Histopathological examination was considered the gold standard for confirming the etiology of inflammatory syndrome. Biopsy was performed in patients with accessible pathological ^{18}F-FDG uptake. Descriptive analyses, including patient age, sex, PET value, and histological confirmation, are represented in Table 1.

3. Results

A total of 25 patients with suspected unexplained inflammatory syndrome were included in this study. The mean age at the time of ^{18}F-FDG PET/CT imaging was 55 years (range: 11 – 82 years). There was a male predominance, with 15 males (60%) and 10 females (40%), resulting in a sex ratio of 1.5. Among the study population, 9 patients (9/25; 36%) presented with unexplained long-term fever (≥38.5°C for at least 3 weeks). ^{18}F-FDG PET/CT was positive in 15 patients (60%) and negative in 10 patients (40%). Patients with a positive PET/CT result subsequently underwent biopsy confirmation whenever possible. However, two patients had inaccessible uptake, precluding morphological confirmation (Table 1). In this study, the specificity and sensitivity of ^{18}F-FDG PET/CT for diagnosing inflammatory syndrome were 81% and 93%, respectively. The positive and negative predictive values (NPV) were 86% and 90%, respectively, while the false-positive and false-negative rates were 7% and 19%, respectively (Table 2).

4. Discussion

Inflammatory syndrome can manifest in two phases: acute or chronic, depending on its duration. Acute inflammation

Table 1. PET-CT findings of the study population

Patient	Sex	Age	Suspicions uptake	SUVmax	^{18}F-FDG PET-CT	Biopsy
1	M	61	-	-	(–)	N/A
2	M	59	Multiple lytic bone uptake	2.3 – 4.3	(+)	+ (Pulmonary adenocarcinoma)
3	M	56	Muscular uptake	3.2 – 5.4	(+)	– Physiological uptake
4	F	72	-	-	(–)	N/A
5	M	72	Vascular hypermetabolism of neck and mediastinum	5.3	(+)	+ (Horton)
6	F	56	Mediastinal lymph-nodes	3.6 – 14.8	(+)	+ (Sarcoidosis)
7	M	31	Sigmoid uptake	9.4	(+)	– (Physiological uptake)
8	M	50	Rectal uptake	14.2	(+)	+ (Rectal adenocarcinoma)
9	F	82	Skeletal muscle uptake	4.5 – 5.6	(+)	+ (Polymyositis)
10	M	62	Vascular hypermetabolism of the neck and mediastinum	3.2 – 4.5	(+)	+ (Horton)
11	M	64	Hypermetabolic sub-centimeter pulmonary nodule	5.9	(+)	+ (Pulmonary adenocarcinoma)
12	M	33	-	-	(–)	N/A (encephalitis)
13	F	26	-	-	(–)	N/A
14	M	64	Multiple hypermetabolic pulmonary nodules	2.9 – 6.0	(+)	+ (Pulmonary adenocarcinoma)
15	F	71	-	-	(–)	N/A
16	F	62	Cardiac hypermetabolic focus	5.7	(+)	N/A (endocarditis)
17	F	62	-	-	(–)	N/A (Horton under corticosteroid therapy)
18	M	33	-	-	(–)	N/A
19	M	32	Recto-sigmoid uptake	16.4	(+)	+ (Active ulcerative colitis)
20	M	56	Vascular hypermetabolism of the neck and mediastinum	3.2 – 4.5	(+)	+ (Horton)
21	M	50	Cardiac hypermetabolic focus	19.0	(+)	None(Endocarditis)
22	F	75	-	-	(–)	N/A
23	F	68	-	-	(–)	N/A
24	F	74	Mediastinal lymph-nodes uptake	4.5 – 10.3	(+)	+ Non-Hodgkin lymphoma
25	M	11	-	-	(–)	N/A

Notes: F: Female; M: Male; (+): Positive; (–): Negative; N/A: Not available.
Abbreviation: PET-CT: Positron emission tomography-computed tomography.

is characterized by an early vascular response, including vasodilation and plasma protein exudate resulting from endothelial damage. This increase in endothelial permeability allows leukocytes (mainly neutrophils and some monocytes) to escape from the vascular environment into the tissue parenchyma. Leukocyte migration is facilitated by chemotactic factors linked to bacterial infections or necrotic tissue. When the underlying cause of acute inflammation is resolved, the associated vascular and tissue changes subside within a few days. However, certain inflammatory processes

persist for several weeks or even months, evolving into chronic inflammation, where vascular congestion is less pronounced. During this phase, neutrophils in the exudate either undergo apoptosis or migrate back into the vascular environment. They are gradually replaced by macrophages and lymphocytes, leading to fibrotic changes in the affected tissues.[1] When phagocytic cells (primarily neutrophils, eosinophils, and monocytes) are exposed to certain stimuli, they metabolize large amounts of glucose through aerobic or anaerobic glycolysis, a phenomenon known as the "respiratory explosion." This process triggers cellular defense mechanisms, including migration, microbicide production, and phagocytosis.[2] Consequently, cellular uptake of ^{18}F-FDG increases, a process further enhanced by cytokine- and growth factor-induced upregulation of glucose transporters.[1,2] There is no fundamental difference between the mechanisms of ^{18}F-FDG uptake and metabolic trapping in inflammatory and neoplastic cells (Figure 1). In both cases, radiotracer accumulation occurs due to increased expression of membrane transporters, elevated cellular energy consumption, and inability to metabolize fluorinated glucose.

Furthermore, there is no inherent limitation to the use of SUVmax as a semi-quantitative index in ^{18}F-FDG PET/CT. This is due to the potential for intense ^{18}F-FDG uptake in highly active inflammatory or infectious pathologies, such as sarcoidosis or tuberculosis. Conversely, low or absent ^{18}F-FDG uptake may occur in patients undergoing empirical corticosteroid or antibiotic therapy, leading to false-negative results. An example from our study is a patient with Horton's disease under corticosteroid treatment, who exhibited a negative ^{18}F-FDG PET scan.

^{18}FDG PET/CT is a valuable tool for identifying the etiology of inflammatory syndromes, with a wide range of indications. This includes gastrointestinal infections, such as inflammatory colitis, Crohn's disease, and ulcerative colitis (Figure 2), as well as granulomatous diseases such as sarcoidosis and tuberculosis. In this context, ^{18}F-FDG PET/CT demonstrates high sensitivity but relatively lower specificity.[3,4]

In infectious diseases, ^{18}F-FDG PET/CT is particularly effective in diagnosing diabetic foot infections, osteomyelitis, and prosthetic joint infections, with high specificity. Beyond enabling etiological diagnosis, it also facilitates assessments of infection extent and therapeutic monitoring, underscoring its significant medico-economic value.[5-10]

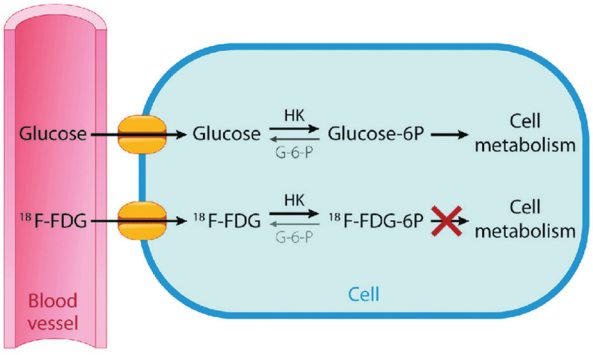

Figure 1. Abnormal uptake and metabolic scavenging of 2-deoxy-2-[fluorine-18]fluoro-D-glucose (^{18}F-FDG) in inflammatory or neoplastic cells, comparing to glucose. Available via license: "https://creativecommons.org/licenses/by-nc-nd/4.0/

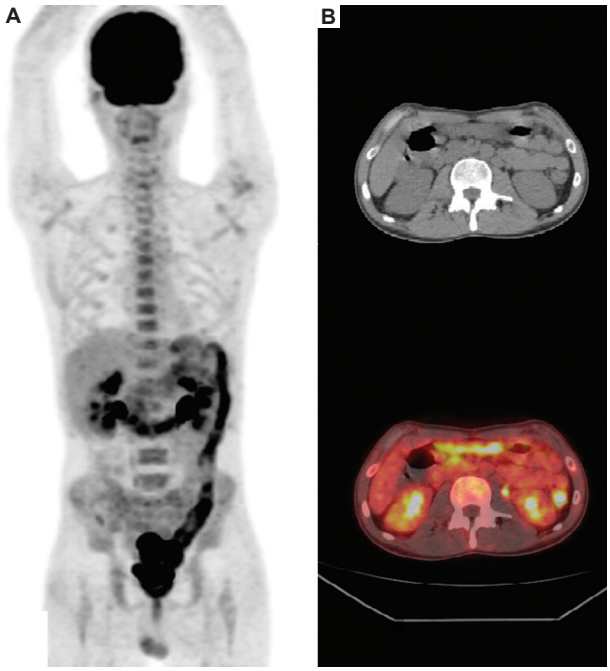

Figure 2. (A) Maximum intensity projection showing physiological and pathological uptake of ^{18}F-FDG. (B) CT image and fusion image in axial sections showing intense recto-sigmoid uptake (SUVmax = 16.4). Normal digestive uptake due to Biguanide use was ruled out. Biopsy of digestive tract confirmed active ulcerative colitis.

Table 2. Predictive values of PET-CT for the etiological diagnosis of unexplained inflammatory syndromes in 25 patients

Metric	PET-CT (+) (%)	PET-CT (–) (%)	Se (%)	Sp (%)	PPV (%)	NPV (%)	FPR (%)	FNR (%)
Value	60	40	93	81	86	90	7	19

Notes: (+): Positive; (–): Negative.
Abbreviation: PET-CT: Positron emission tomography-computed tomography; Se: Sensitivity; Sp: Specificity; PPV: Positive predictive value; NPV: Negative predictive value; FPR: False-positive rate; FNR: False-negative value.

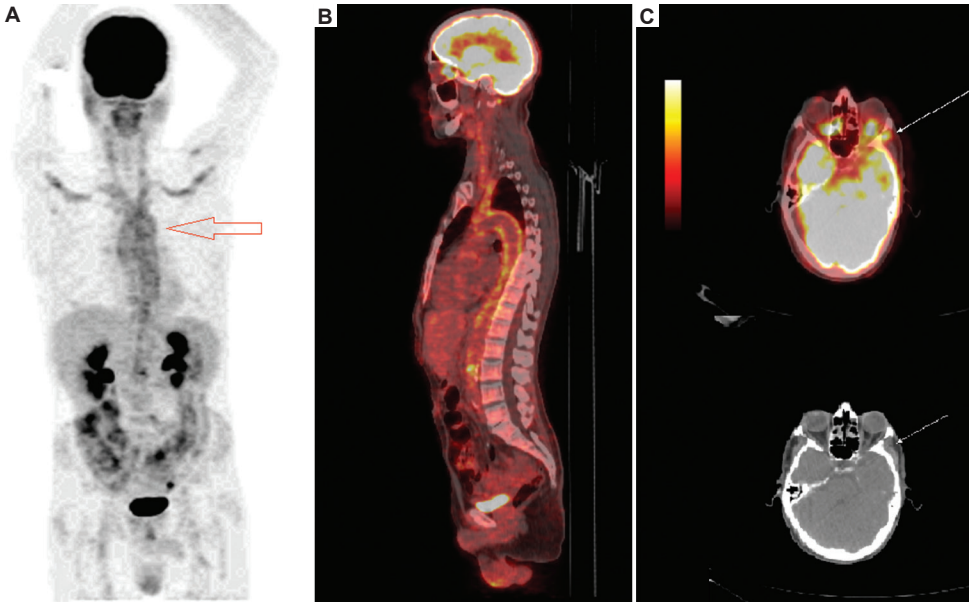

Figure 3. 18F-FDG PET scan of a patient follow-up for suspected vasculitis. (A) Maximum intensity projection and (B) fusion image in the sagittal section showing moderate vascular hypermetabolism of the neck and mediastinum (SUVmax = 5.3) with a characteristic "crossbow appearance" (red arrow). (C) Fusion image in the axial section showing suspected hypermetabolic uptake in the left temporal artery (SUVmax = 4.5), compatible with Horton's disease.

In endocarditis, ^{18}F-FDG PET/CT is a highly sensitive imaging technique capable of detecting prosthetic valve infections and infections associated with cardiac stimulators, particularly in cases where blood cultures and conventional morphological imaging yield negative results.[11]

^{18}F-FDG PET/CT is also instrumental in investigating fever of unknown origin (FUO). FUO is defined as a febrile syndrome persisting for at least 3 weeks, with temperatures reaching ≥38.8°C, and no definitive diagnosis after conventional explorations.[12,13] The etiologies of FUO are diverse, with infectious causes accounting for approximately 25% of cases, followed by neoplastic causes (lymphomas, solid tumors) in 15 – 25% of cases. Other etiologies include granulomatous diseases, vasculitis, pulmonary embolisms, and polypharmacy-induced fever.[14] ^{18}F-FDG PET/CT has been shown to be highly effective in detecting the etiology of FUO, with a sensitivity and specificity of approximately 90%. Notably, its NPV approaches 95%.[14]

In vascular pathology, ^{18}F-FDG PET/CT plays a crucial role in diagnosing vasculitis, including Horton's arteritis, Takayasu arteritis, rhizomelic pseudo-polyarthritis, inflammatory arteritis, and active atheromatous plaques. The technique provides high PPV and NPV, making it a valuable diagnostic tool. In this context, PET/CT enables early, infra-radiological diagnosis based on the morpho-metabolic characteristics of ^{18}F-FDG uptake and facilitates therapeutic monitoring, guiding treatment decisions such as corticosteroid therapy, statins, and other targeted therapies (Figure 3).[15]

While PET/CT remains a valuable tool for the assessment of vascular inflammation, PET/magnetic resonance imaging (MRI) offers additional advantages in the assessment of cardiac and vascular pathologies. This hybrid imaging modality combines the high sensitivity of ^{18}F-FDG for detecting inflammatory and infectious diseases with the superior specificity of MRI for diagnosing cardiovascular conditions.

5. Conclusion

Our study presents findings that are consistent with existing literature regarding the role of ^{18}F-FDG PET/CT in evaluating unexplained inflammatory syndromes. Despite the predominant use of ^{18}F-FDG PET/CT in nuclear medicine for oncological indications, this imaging technique remains underutilized in non-oncological applications, as evidenced by the limited number of patients included in our study. These findings should further encourage clinicians to consider integrating ^{18}F-FDG PET/CT into the diagnostic workup of patients with unexplained inflammatory syndromes, thereby expanding its routine clinical applications.

Acknowledgments

None.

Funding

None.

Conflict of interest

The authors declare that they have no competing interests.

Author contributions

Conceptualization: Salah Oueriagli Nabih, Meryem Aboussabr, Ikram Zahfir,
Formal analysis: Salah Oueriagli Nabih, Meryem Aboussabr.
Investigation: Omar Ait Sahel, Yassir Benameur
Methodology: Salah Oueriagli Nabih
Writing – original draft: Salah Oueriagli Nabih
Writing – review & editing: Salah Oueriagli Nabih, Abderrahim Doudouh

Ethics approval and consent to participate

All procedures performed in studies involving human participants were in accordance with the ethical standards of the Institutional and/or National Research Committee and with the 1964 Helsinki Declaration and its later amendments or comparable ethical standards. For this interesting image, formal consent is not required.

Consent for publication

Written informed consent was obtained from all patients for publication.

Availability of data

Authors make available to all scientists, documents described in the manuscript, including new software, databases, and all relevant raw data.

References

1. Kubota R, Yamada S, Kubota K, Ishiwata K, Tamahashi N, Ido T. Intratumoral distribution of fluorine-18-fluorodeoxyglucose *in vivo*: High accumulation in macrophages and granulation tissues studied by microautoradiography. *J Nucl Med*. 1992;33(11):1972-80.
2. Mochizuki T, Tsukamoto E, Kuge Y, *et al*. FDG uptake and glucose transporter subtype expressions in experimental tumor and inflammation models. *J Nucl Med*. 2001;42(10):1551-1555.
3. Prabhakar HB, Rabinowitz CB, Gibbons FK, O'Donnell WJ, Shepard JA, Aquino SL. Imaging features of sarcoidosis on MDCT, FDG PET, and PET/CT. *AJR Am J Roentgenol*. 2008;190(3 Suppl):S1-S6.

   doi: 10.2214/AJR.07.7001
4. Zhuang H, Alavi A. 18-fluorodeoxyglucose positron emission tomographic imaging in the detection and monitoring of infection and inflammation. *Semin Nucl Med*. 2002;32(1):47-59.

   doi: 10.1053/snuc.2002.29278
5. Dumarey N, Egrise D, Blocklet D, *et al*. Imaging infection with 18F-FDG-labeled leukocyte PET/CT: Initial experience in 21 patients. *J Nucl Med*. 2006;47(4):625-632.
6. Rini JN, Palestro CJ. Imaging of infection and inflammation with 18F-FDG-labeled leukocytes. *Q J Nucl Med Mol Imaging*. 2006;50(2):143-146.
7. Park IN, Ryu JS, Shim TS. Evaluation of therapeutic response of tuberculoma using F-18 FDG positron emission tomography. *Clin Nucl Med*. 2008;33(1):1-3.

   doi: 10.1097/RLU.0b013e31815c5128
8. Bleeker-Rovers CP, Vos FJ, Corstens FH, Oyen WJ. Imaging of infectious diseases using [18F] fluorodeoxyglucose PET. *Q J Nucl Med Mol Imaging*. 2008;52(1):17-29.
9. Bleeker-Rovers CP, Vos FJ, Wanten GJ, *et al*. 18F-FDG PET in detecting metastatic infectious disease. *J Nucl Med*. 2005;46(12):2014-2019.
10. Jamar F, Buscombe J, Chiti A, *et al*. EANM/SNMMI guideline for 18F-FDG use in inflammation and infection. *J Nucl Med*. 2013;54(4):647-658.

    doi: 10.2967/jnumed.112.112524
11. Salomäki SP, Saraste A, Kemppainen J, *et al*. 18F-FDG positron emission tomography/computed tomography in infective endocarditis. *J Nucl Cardiol*. 2017;24(1):195-206.

    doi: 10.1007/s12350-015-0325-y
12. Bleeker-Rovers CP, De Kleijn EM, Corstens FH, Van der Meer JW, Oyen WJ. Clinical value of FDG PET in patients with fever of unknown origin and patients suspected of focal infection or inflammation. *Eur J Nucl Med Mol Imaging*. 2004;31(1):29-37.

    doi: 10.1007/s00259-003-1338-3
13. Meller J, Sahlmann CO, Scheel AK. 18F-FDG PET and PET/CT in fever of unknown origin. *J Nucl Med*. 2007;48(1):35-45.
14. Blockmans D, Knockaert D, Maes A, *et al*. Clinical value of [(18)F]fluoro-deoxyglucose positron emission tomography for patients with fever of unknown origin. *Clin Infect Dis*. 2001;32(2):191-196.

    doi: 10.1086/318480
15. Hao R, Yuan L, Kan Y, Li C, Yang J. Diagnostic performance of 18F-FDG PET/CT in patients with fever of unknown origin: A meta-analysis. *Nucl Med Commun*. 2013;34(7):682-688.

    doi: 10.1097/MNM.0b013e328361cd0e

Our Journals

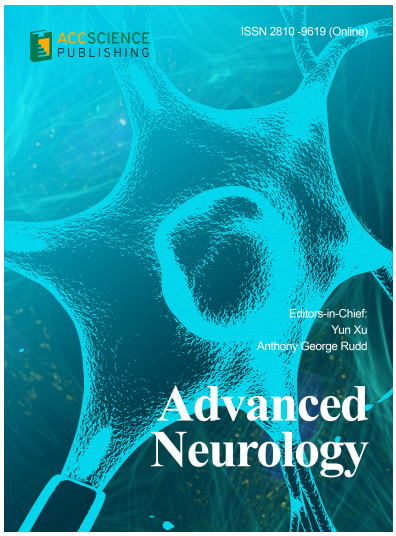

Advanced Neurology is a peer-reviewed and open-access journal that aims to publish and disseminate novel research in the breadth of neurology and neuroscience. The journal aims to advance our understanding in the nervous system and provide a platform to neuroscientists and physicians to showcase their findings in original fundamental and clinical research as well as to present new ideas that highlight the changes in the neurological clinical practice.

Advanced Neurology covers subject areas, including but not limited to the following:

- Neurological disorders
- Neurodegenerative disease
- Cerebrovascular disease
- Epilepsy and movement disorders
- Neuroimmune disease
- Neurological infections
- Muscle disease
- Molecular and cellular neuroscience
- Systems neuroscience
- Cognitive neuroscience
- Computational modeling of nervous system

Global Translational Medicine is a quarterly journal that focuses on medicine, biological sciences, and biomaterials engineering. The goal of *Global Translational Medicine* is to provide a platform to researchers for showcasing their latest research works in translational medicine so as to advance the field towards the betterment of human health. Despite the advancement of omics and new technologies, the process of transforming these technologies and scientific research results into effective therapies and putting them into clinical use still has a long way to go. *Global Translational Medicine* provides a platform to fill the gaps in preclinical and inter-disciplinary research, to promote clinical translation of scientific research results, and to contribute to the conception of new and improved preventive measures as well as diagnostic and therapeutic techniques of diseases.

Global Translational Medicine covers the following themes: cardiovascular disease, metabolism/diabetes/obesity, neuroscience/neurology, cancer, biomaterials and their applications in medicine, proteomics/metabolomics, pharmacogenomics, biomarkers, bioinformatics and data mining, animal and clinical research, and medical methods arising from interdisciplinary crossover.

Start a new journal

Write to us via email if you are interested to start a new journal with AccScience Publishing. Please attach your CV, professional profile page and a brief pitch proposal in your email. We shall inform you of our decision whether we are interested to collaborate in starting a new journal.

Contact: info@accscience.com

https://accscience.com/journal/ARNM

Contact
www.accscience.com
8 Burn Road, #15-03 Trivex, Singapore 369977
Email: editorial@accscience.com
Phone: +65 8182 1586